COO-3158-62
Report #2952

DIRECT OBSERVATION OF THE POINT-DEFECT STRUCTURE OF DEPLETED-ZONES IN ION-IRRADIATED METALS

by

Ching-Yeu Wei

Ph.D. Thesis
January 1978

Research Group:
Prof. D. N. Seidman
MSE

DISCLAIMER

ACKNOWLEDGEMENT

The author wished to thank Professor David N. Seidman for serving as his major advisor and for his enthusiastic assistance and continuous encouragement throughout the course of this work. The author also wishes to thank Professors J. M. Blakely and B. M. Siegel for serving as his minor advisors and for their useful discussions.

Special thanks are accorded to Mr. R. F. Whitmarsh for his enthusiastic technical assistance and Mrs. K. J. Pratt for the photographic work.

Special thanks are also extended to Dr. G. Ayrault and Dr. H. P. Huo and A. Wagner for their useful discussions.

A deep indebtedness is due to the author's wife for the numerous personal sacrifies she made to allow the completion of this work. The indebtedness is also due to the author's parents for their continuous encouragement.

This work was supported by the United States Atomic Energy Commission. Additional support was received from the Advanced Research Projects Agency and the National Science Fundation through the use of the technical facilities of the Materials Science Center at Cornell University.

TABLE OF CONTENTS

Page

LIST OF TABLES

LIST OF FIGURES

Figure Page

DIRECT OBSERVATION OF THE POINT-DEFECT STRUCTURE OF DEPLETED-ZONES IN ION-IRRADIATED METALS

Ching-Yeu Wei

Cornell University 1978

The point-defect structure of individual depleted zones has been studied systematically, for the first time, in great detail. Four-pass zone-refined tungsten field-ion microscope (FIM) specimens were irradiated in-situ at 10 K with 30 keV Cr^+, Mo^+ or W^+ ions to a total dose of $(2 \text{ to } 10)\times10^{12}$ ion cm^{-2} and examined by the pulse field-evaporation technique at 10 K. The experimental conditions were arranged such that each depleted zone was created by a single incident-ion. The number of vacant lattice sites within a depleted zone was compared with a modified Kinchin-Pease model. The radial distribution function was determined for each depleted zone; it was found that the vacant lattice sites within the volume of each depleted zone tended to exist in a highly clustered state. It was found that the diameter D of each depleted zone was described by the equation $D \simeq \langle y^2\rangle^{1/2}$ where $\langle y^2\rangle^{1/2}$ is the second moment of the theoretical distribution curve, of the fraction of incident ion energy deposited in atom motion, transverse to the direction of the incident ion-beam. The spatial distribution of self-interstitial atoms (SIAs) in a specimen irradiated with 30 keV Cr^+ ions and in a specimen irradiated with 18 keV Au^+ ions, at 10 K, was determined.

A low bound to the average range of replacement collision sequences (RCSs) was found to be 175± 85 A. A detailed FIM study was also made of the vacancy structure of a (220) platelet created by a single 30 keV W^+ ion in a platinum-4.0 at.% gold alloy; the specimen was irradiated at 40 K and then isochronally warmed to 100 K. The (220) platelet was found to consist of 31 vacant lattice sites, lying in four (220) planes, and clustered in a disc-shaped region which is ∿20 A in diameter. It was suggested on the basis of our observation of this platelet that prismatic dislocation loops lying on (220) type planes, observed by transmission electron microscopy, in ion or fast neutron irradiated platinum can form as a result of the direct collapse of (220) type vacancy platelets.

I. INTRODUCTION

One of the most persistent problems in the field of radiation damage is that of understanding quantitatively the nature of the displacement spike; i.e., the total number and the spatial distribution of vacant lattice sites (VLSs) and self-interstitial atoms (SIAs) produced as the result of the impact of an energetic particle in the range of incident energies from 25 eV to 14 MeV. For many metals the irradiation with fission neutrons results in the production of primary knock-on atoms (PKAs) with an energy distribution between ∿10 and 100 keV. Hence the study of displacement spikes produced by PKAs in this energy range will contribute to a better understanding of the damage caused by fission neutrons.

The theoretical evolution of a displacement spike starts with the work of Brinkman(1-2) in the mid-fifties. Brinkman suggested that a displacement spike occurs in the lattice of a heavy metal when the energy of the PKA falls to a value such that it displaces almost every atom it encounters; at this value of energy the mean free path between atomic collisions is of the order of an interatomic distance. The Brinkman displacement spike consists of a central void-like region surrounded by a mentle of SIAs; the number of SIAs is equal to the number of VLSs in the void-like region. In this model all the SIAs are located within a few interatomic distances of the surface of the central void-like region. Subsequently Seeger,(3-4) in the late fifties and early sixties, pointed out that the periodicity of the ordered crystal lattice must be considered and in particular that both energy transport by focusons and focused replacement collision sequences(RCSs)* in close-packed crystallographic directions could play a role in the creation of the displacement spike which we will refer to as a depleted zone.†

In the late fifties and early sixties Vineyard and coworkers(7-9) introduced molecular dynamic calculations, employing fast computers, to simulate atomic collisions in crystalline solids. They assembled a small fcc crystallite of copper (∿500 or 1000 atoms), employing a reasonable interatomic potential, and introduced a low-energy (≤2 keV) PKA into this lattice. The computer then solved the many-body interactions by incrementally integrating the classical equations of motion of all the atoms present. The results of their simulation experiments were able to show the existence of both focusons and RCSs in the <100>, <110> and <111> directions in the fcc copper lattice. Similar results were also obtained for the bcc α-iron lattice. The fundamen-

---

* The focuson(5) is an energy packet that propagates down a row of atoms; it transfers momentum, but not mass. The RCS(6) involves both the propagation of momentum and mass along a close-packed atomic row.

† The term depleted zone is used in preference to displacement spike or cascade, although they are all often used synonymously in the literature.

tal problem of their many-body calculation is the size of the crystallite that can be stored and manipulated by the computer which was then available to them. Hence, this many-body calculation was primarily used to simulate a small depleted zone produced by a low-energy PKA.

In addition to the many-body computer-simulation model of a depleted zone, produced by a low-energy PKA, there is also a very extensive literature employing the binary-collision computer-simulation technique(10-12) to treat a high-energy (≥5 keV) PKA. This approximation had been used extensively by Beeler(13-16) to study the spatial distribution of VLSs and SIAs in individual depleted zones produced in a stationary lattice at 0 K (i.e., no zero-point energy atomic vibrations). After an energetic atom made a collision with a stationary lattice atom, each atom carried away a fraction of the initial incident energy as determined by the pairwise interaction, while a small displacement energy (E_d) was lost to the lattice per collision. All moving atoms were followed until further displacement collision were impossible. Any SIA that was within a 30 site recombination volume around a VLS was allowed to recombine athermally, but no point-defect migration was allowed. The results of this simulation showed the depleted zone to consist of a large vacancy-rich central core surrounded by an SIA cloud. The same technique, with certain modifications, had also been employed by Doran(17) and Doran and Burnett (18) and Robinson and Torrens(19-20) to study, among other things, the effects of thermal vibrations, choice of the interatomic potential, inelastic energy losses and displacement threshold criterion on the point-defect concentration in a depleted zone produced in a number of different metals (copper, iron and gold). Holmes and Robinson(21) have also considered the problem of RCSs in association with depleted zones employing the binary-collision model. The basic problem of the binary-collision model is that this model is not appropriate for the energy range below 100 eV where focusons and RCSs could play an important role in determining the final spatial arrangement of SIAs around each depleted zone. Nevertheless, the binary-collision computer-simulation does provide qualitative physical insight into the point-defect structure of a depleted zone.

So far, only two field-ion microscope (FIM)(22) studies, which can be directly compared with the computer simulation have been performed. Beavan et al.(23) irradiated pure tungsten with 20 keV W^+ ions at 18 K (below the Stage I SIA long-range migration peak(24-25)). Two depleted zones were detected and analyzed in two different specimens. A depleted zone detected in the (222) plane had a vacancy concentration of ∿8.7 at.% and the local SIA concentration was ∿0.92 at.%. The SIAs found locally were located on the peripheral surface of the zone. In the lattice surrounding this depleted zone there were 25 SIAs. It was shown that 12 of these 25 SIAs could have been propagated away from the depleted zone along <111> directions and 11 along <011> directions. For <011> directions the propagation distances were between 45 and 150 A, while for the <111> directions these distances were between 45 and 85 A. This result constituted direct evidence for the existence of RCSs. The upper and lower limit in both cases was determined by a sampling problem and not the intrinsic range of RCSs. The other depleted zone detected in the (141) plane had an irregular geometry which was elongated along the $[10\bar{1}]$ direction. This depleted zone was found to consist of 81 VLSs and the vacancy concentration was ∿10 at.%. The SIAs were found on the outer surface of this depleted zone and the SIA concentration was ∿0.5 at.%. The depleted zone in the (141) plane was found to intersect the initial surface and therefore it was not clear whether this depleted zone was a partial or a total depleted zone.

Wilson and Seidman(26) irradiated pure tungsten with 20 keV W^+ ions at 473 K (towards the top of Stage II(27)). They detected a depleted zone near the (222) plane and found it to consist of 41 VLSs clustered in a cubic region ∿13 A on a side. No contrast effects which could be attributed to SIAs were found in or near the depleted zone or in the lattice surrounding it. If only first nearest-neighbor VLSs were considered then the distribution of cluster sizes was as follows: (1) three mono-VLSs; (2) one di-VLS; (3) one tri-VLS; (4) one hexa-VLS; and (5) one cluster of 27 VLSs. The depleted zone exhibited a definite degree of elongation along the $[\bar{1}10]$ direction when the VLSs were projected onto the (002) plane. Finally, the vacancy concentration in this depleted zone was ∿33 at.%.

Other FIM experiments on vacancy-type radiation damage have been done on the metals tungsten, iridium and platinum by Galligan and co-workers(28-30), Buswell,(31-32) Pétroff and Washburn,(33) and Ralph and co-workers.(34-37) The emphasis of most of these studies had been on characterizing the distribution of the vacancy damage produced at room temperature and, in a few experiments, at 78 K. These studies have been useful in demonstrating that three basic morphological-types of vacancy damage exist in the primary state of damage. These three basic types are: (1) depleted zones; (2) compact vacancy clusters or voids; and (3) dislocation loops. The voids may be considered to be depleted zones with a very high local vacancy concentration $(c_v)^*$. The dislocation loops were initially depleted zones with a high local value of c_v that have collapsed into the lower-energy dislocation loops.

The important result that emerges from the FIM research on both tungsten and iridium is that the dislocation-loop portion of the damage accounts for only a small fraction of the

---

* It is the author's opinion that it is difficult to differentiate voids from depleted zones in the FIM micrographd without actually reconstructing them in three dimensions as described in sect.V.4.1.

vacancy population. The largest fraction of the vacancy population (90% in the case of tungsten) is in the form of depleted zones (with a vacancy concentration of between 1 and 20 at.%) and compact clusters or voids. These observations offer an explanation of why the yield factor (Y), where

$$Y = \frac{\text{observable vacancy contrast-effects (number per cm}^2\text{)}}{\text{ion dose (number of ion per cm}^2\text{)}}$$

measured by the transmission electron microscope (TEM) technique is often considerably less than unity. For example, in the case of copper irradiated with 30 keV Cu^+ ions at room temperature Y is 0.3,(38) and in the case of tungsten irradiated at room temperature it is 0.1.(39-40) The understanding of these low values of Y is extremely important because the TEM technique has been used extensively to study vacancy damage in both ion or neutron-irradiated metals.(40-44) The observation of the primary radiation-damage state by TEM depends heavily on the ability of the vacancy-rich core of a depleted zone to collapse into a dislocation loop with sufficient strain-field contrast to make itself visible in a TEM image. A vivid illustration of this point comes from some recent work of English and Eyre(45) on iron. They irradiated α-iron at room temperature with 40 to 240 keV Fe^+, Ni^+, Ge^+, Kr^+, Xe^+ and W^+ ions. They found that the defect yield is a strong function of the mass of the incident ions, increasing from zero for Fe^+ ions to ∿20% for W^+ ions. In particular, when iron was irradiated with ≤240 keV Fe^+ ions at room temperature no dislocation loops were observed. An explanation of this observation is simply that with increasing ion mass the depleted zones becomes more compact, the vacancy supersaturation is higher and therefore depleted zones have a higher propability to collapse athermally into dislocation loops.

The high-resolution TEM technique(46) had been extensively applied to the study of the damage state of irradiated materials. A relatively well-developed theory of image formation(47) coupled with the commercial availability of TEMs had strongly aided the application of this technique to the study of radiation damage in both metals(41-43) and non-metals.(48) The TEM results have given us a good deal of physical insight into the character (i.e., SIA or VLS) and spatial arrangement of the damage in the irradiated state of materials; it is also an extremely useful technique for determining the size distribution and average number density of the observed damage. Unfortunately, the TEM is not at present capable of resolving the individual VLSs or SIAs in and around a depleted zone, and therefore the FIM with its atomic resolution is better suited for a detailed study of the spatial distribution of point defects produced as a result of the bombardment of solids with energetic particles.

In this thesis several aspects of work have been performed and are briefly described as follows:

(1) In Chapter III a novel Faraday cup was described

which allows the simultaneous observation and measurement of ion-beam currents. The Faraday cup was constructed around a Galileo channel electron-multiplier array (CEMA) which served as the basis of an internal image intensification system (a gain of $\geq 10^4$) for the observation of the ion beam: the CEMA also acted as a collector for the ion current which was measured by a Keithley 602 electrometer. The ion current was integrated by a simple and inexpensive dosimeter; the electronic circuit for the dosimeter is described. The application of the Faraday cup to the observation and measurement of a 30 keV Ar^+ ion beam is presented as an illustrative example. We have also employed this Faraday cup to observe and measure 30 keV Cr^+, Mo^+ or W^+ and 18 keV Au^+ ion beams employed for the in-situ irradiation of FIM specimens.

(2) In Chapter IV a detailed FIM study of the vacancy structure of a (220) platelet created by a single 30 keV W^+ ion in a platinum-4.0 at.% gold alloy was described; the specimen was maintained at 40 K (below substage II_B) during the in-situ irradiation at $\sim 2 \times 10^{-9}$ Torr. Prior to the pulsed field-evaporation dissection of the specimen at 40 K it was warmed isochronally to 100 K (above substage II_C). The (220) platelet was found to consist of 31 VLSs, lying in four (220) planes, and clustered in a disc-shaped region which is ∿20 A in diameter. If only first nearest-neighbor VLSs were considered then the distribution of cluster sizes was as follows:

(1) two mono-VLSs; and (2) one jumbo VLS cluster containing 29 VLSs. The range of the VLS concentration within the (220) vacancy platelet is ∿35 to 44 at.%. Employing the modified Kinchin-Pease equation it was calculated that the displacement efficiency (κ) for this platelet is 0.12. It is suggested that the prismatic dislocation loops lying on (220) type planes, observed by transmission electron microscopy, in ion or fast-neutron irradiated platinum can form as a result of the direct collapse of (220) type vacancy platelets.

(3) In Chapter V we presented a first systematic study of the point-defect structure of a depleted zone created by a single 30 keV W^+, Mo^+ or Cr^+ ion at 10 K in tungsten. The dependence of the point-defect structure of a depleted zone on the mass of the incident ion was studied in great detail. First, a three-dimensional drawing of each depleted zone was constructed from the FIM micrographs. Second, the number of VLSs within a depleted zone was compared with the modified Kinchin-Pease model. Third, the radial distribution function was determined for each depleted zone. It was found that the VLSs within the volume of the depleted zone tended to form clusters. Fourth, the experimental diameter of each depleted zone was compared with the Winterbon-Sigmund-Sanders (WSS) theory.(107) It was suggested that the quantity $\langle y^2\rangle^{\frac{1}{2}}$*

---

* The quantity $\langle y^2\rangle^{\frac{1}{2}}$ is the second moment of the elastic ion-energy deposition curve along the direction perpendicular to the incident ion.

is a better estimate of the size of a single depleted zone as opposed to the quantity $2<y^2>^{\frac{1}{2}}$ originally suggested by Westmoreland and Sigmund.(84) Finally, the observed spatial distributions of SIAs in a specimen irradiated with 30 keV Cr^+ ions and in a specimen irradiated with 18 keV Au^+ ions were determined and a lower bound of the RCS chain length in tungsten was determined to be 175 ±85 A.

II. EXPERIMENTAL DETAILS

II.1. The Ultra-High Vacuum FIM and the Irradiation Facility

The FIM is attached to the left-hand side of our accelerator system via a three-stage differentially-pumped flight tube$^{(51-52)}$ (see fig. 1). This arrangement allows for the *in-situ* irradiation of the FIM specimen at a background pressure of $\leq 2\text{x}10^{-9}$ Torr in the FIM with a pressure of Ne, Ar or Xe ranging between (2 to 10)$\text{x}10^{-6}$* Torr measured above the diffusion pump which evacuates the Hill-Nelson sputtered-metal ion-source.

After being accelerated to 30 keV** the ion beam was translated horizontally or vertically by two sets of parallel plates and was chemically analyzed by an electromagnet in the horizontal direction. This colimated ion beam was made to pass through the three-stage differentially-pumped flight tube and subsequently to enter the FIM to bombard the specimen. A special Faraday cup was then employed to simultaneously monitor the profile and intensity of the ion beam. Two sets of parallel plates seated in the flight tube above the third differential pump were used to steer and raster the ion beam. The horizontal deflection plates received a variable dc voltage

---

* All pressures reported in this thesis have been converted from guage pressure to real pressure.

** This was the most common irradiation energy employed in our studies.

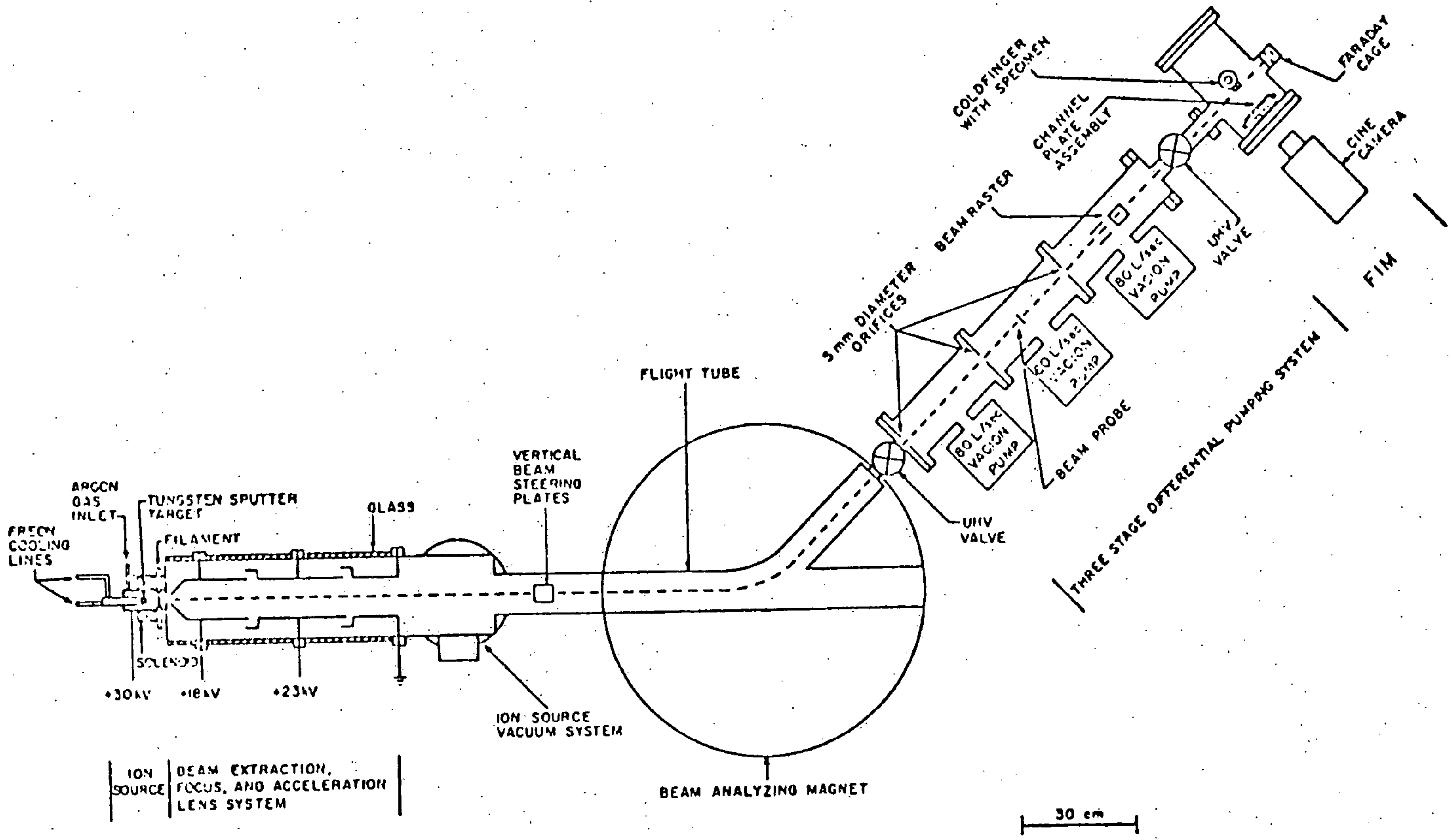

Figure 1. An overall view of the experimental apparatus.

of 1 kV maximum which carried a 200 V saw-tooth wave form at 2 khz. A variable dc voltage of 1 kV maximum and a 200 V saw-tooth signal at 200 hz were applied to the vertical plates. This beam-steering system was found to be extremely useful to adjust the position of the ion beam relative to the specimen. Details regarding the design of the Faraday cup are given in Chapter III.

II.2. Data Recording System and Ciné Film Analysis

The FIM images were observed with the aid of an internal image-intensification system based on a Galileo 76 mm diameter channel electron-multiplier array (CEMA) and the FIM images produced in this manner were recorded on 35 mm ciné film with the aid of an Automax ciné-camera equipped with a 1000 ft. film chamber. Each FIM image was recorded after a field-evaporation pulse had been initiated. The recorded and developed ciné film was analyzed with a Vanguard motion analyzer which is equipped with x-y cross-hairs, a position readout(74) and a zeroing device. The zeroing device is capable of zeroing the position readout of any point on the ciné film, this feature allowed us to directly read the coordinate of any point on the ciné film with respect to any zeroed point. The position readout of the motion analyzer was interfaced to a Houston Omnigraphic 2000 x-y recorder via a unity-gain buffer which is used to lower the output impedance of the position readout of the motion analyzer. The positions of any atomic and vacant sites detected in the FIM micrographs were then transferred to a sheet of graph paper by the x-y recorder. The zeroing device on the motion analyzer and the x-y recorder was extremely useful for reconstructing the point-defect structure of the depleted zone in three-dimension from the two-dimensional FIM micrographs.

III. A NOVEL FARADAY CUP FOR THE SIMULTANEOUS OBSERVATION AND MEASUREMENT OF ION-BEAM CURRENTS

III.1. Introduction

For the past few years we have employed energetic (∿10-45 keV) positively-charged metal ion-beams to irradiate metal field-ion microscope (FIM) specimens.(49-57) The irradiations have been performed *in-situ* under ultra-high vacuum (∿(0.2 to 2)x10^{-9} Torr) conditions in a stainless steel FIM; the FIM specimen is attached to the tail of a continuous-transfer liquid-helium cryostat via a copper FIM specimen holder that is clamped to a sapphire piece that serves to electrically isolate the specimen holder from the cryostat.(58) The main problems with the *in-situ* irradiations were the alignment and observation of the ion beam with respect to the FIM tip and the accurate measurement of the ion dose. Prior to the use of the design described in this chapter we had employed a phosphor screen to first align and observe the ion beam and then a separate Faraday cup to measure the ion dose. This arrangement had the following deficiencies: (1) it was cumbersome; (2) it was time consuming; and (3) the photon yield per incident heavy-ion on the phosphor is small(59) making it difficult to visually observe a heavy-metal or gas ion-beam (e.g., 30 keV Ar^+, Cr^+, Mo^+ or W^+).

To correct these problems we have designed and constructed a Faraday cup which allows us to both continuously and simultaneously monitor the ion-beam cross-section and ion dose.

At the heart of the present system is a Galileo channel-electron multiplier array (CEMA) which serves as the basis of an internal image intensification system to observe the ion beam and also as an ion-beam collector in the Faraday cup. This design overcomes the major problem inherent to a conventional Faraday cup design; i.e., the inability to simultaneously observe the profile of the ion beam and to measure the ion dose. The present paper describes this novel Faraday cup which corrects the above mentioned problem; in addition, a simple dosimeter is described which gives a direct readout of the integrated flux (i.e., the dose). The use of this Faraday cup to measure and observe an ion current of $2\mathrm{x}10^{-9}$ amp of 30 keV Ar^+ ions is presented as an illustrative example of the capabilities of the present design. In addition, we have also used the present design to observe and measure 30 keV Cr^+, Mo^+ or W^+ and 18 keV Au^+ ion beams during the in-situ irradiation of tungsten FIM specimens. There appears to be no fundamental limitation on the application of this design to the observation and measurement of all the elements in the periodic table that one can make into positively or negatively charged ion-beams.

III.2. Design and Performance of the Faraday Cup

III.2.1. The Faraday Cup and the Channel Electron Multiplier Array

Figure 2 shows a cross-sectional top view of the Faraday cup (right-hand side) and its relationship to the FIM specimen

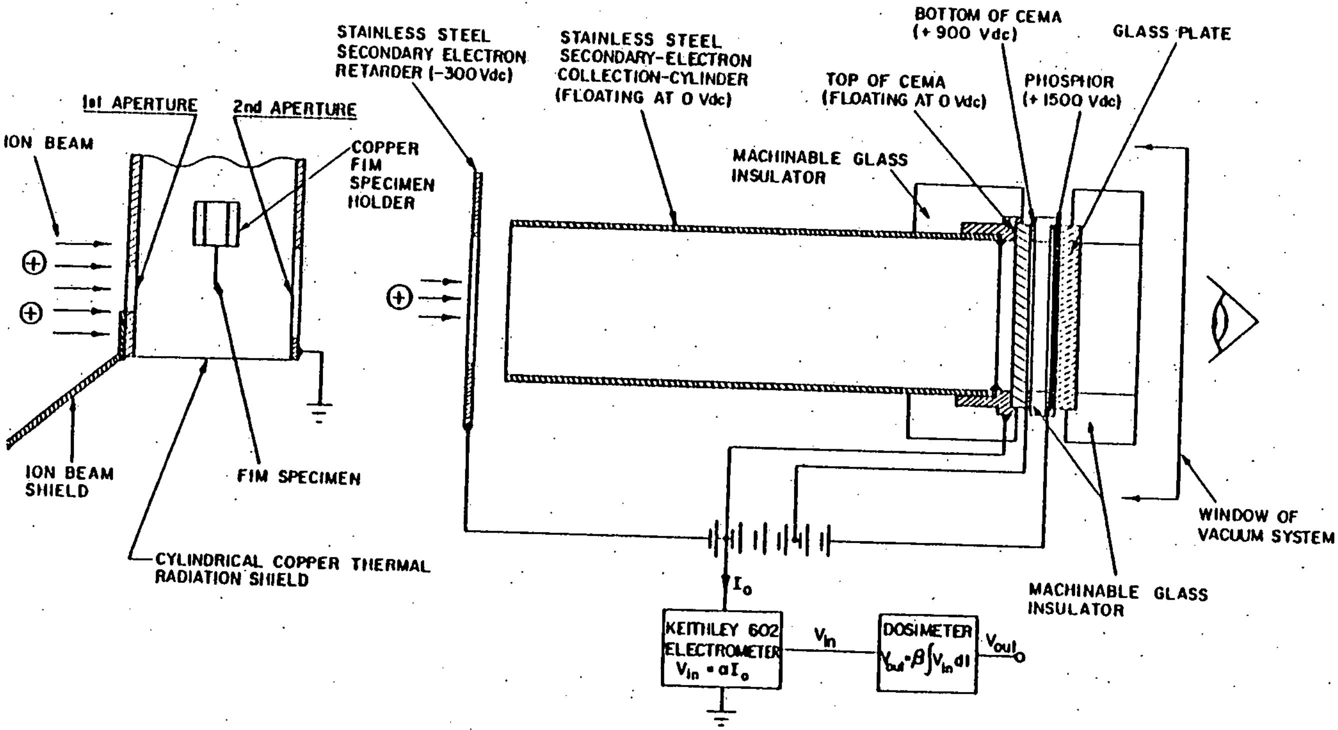

Figure 2: A schematic diagram (top view) showing the relationship of the FIM specimen (left-hand side of the figure) to the Faraday cup (right-hand side of the figure).

(left-hand side). The FIM specimen was in the form of an ∿1 cm long wire (∿0.13 to 0.20 mm in diameter) which was sharply pointed and was mounted on an hexagonal-shaped copper FIM specimen holder. The FIM specimen and its holder are surrounded by a cylindrical copper thermal radiation-shield which contains two apertures; the first aperture defined the cross-sectional area of the ion beam that impinged on the FIM specimen. The second aperture was made larger in diameter than the first one to avoid an ion-beam shadowing effect. In addition, a piece of gold metal was attached to the cylindrical thermal copper radiation-shield on the side of the first aperture to further shield the Faraday cup from any portion of the ion beam which may have accidentally by-passed the first aperture.

The ion beam that passes through the second aperture of the cylindrical copper thermal radiation-shield next enters the Faraday cup as it passes through an annular stainless steel ring that served the role of a secondary-electron retarder; the latter was biased at -300 Vdc. The secondary-electron retarder prevents electrons that are produced inside the secondary-electron collection-cylinder, floating at 0 V, from escaping from the Faraday cup and it also prevents stray electrons from entering the Faraday cup. The long stainless steel secondary-electron collection-cylinder serves to recapture any secondary-electrons that were released by the ion beam. Finally the ion beam(60) was collected on the front surface of the CEMA, which was also floating at 0 V, and it is measured with a Keithley 602 electrometer. The incident ion-beam current was also converted to an electron current by the CEMA.(61) The back surface of the CEMA was maintained at +900 Vdc; the voltage drop of 900 Vdc across the CEMA produces a gain of $\sim 10^4$. The CEMA was separated from a P-1 phosphor screen(62), deposited on a glass plate, by a 1.6 mm thick annular ring fabricated from Corning No. 2598 machinable glass. The electron current produced by the CEMA was accelerated and proximity focused onto the phosphor screen which was maintained at +1500 Vdc; the glass plate, on which the phosphor was deposited, was coated with a conducting layer of tin oxide.(63-64) The visible light given off by the phosphor is observed through an ∿2.5 cm diameter glass window on the FIM. An example of the observational capability of the CEMA portion of the Faraday cup is shown in fig. 3. Figure 3a shows the cross-sectional image of a 30 keV Ar^+ ion beam at a current density of $\sim 4\times10^{-9}$ amp cm^{-2}. Figure 3b shows an FIM specimen which was biased at ∿600 Vdc to give a shadowgraph of the tip in the ion beam; this technique has been found to be extremely useful for rapidly aligning the FIM specimen with respect to the ion beam.

III.2.2. Measurement of the Positive Ion Current

The problem of measuring the total ion current (I_i) is best explained with the aid of the approximate equivalent

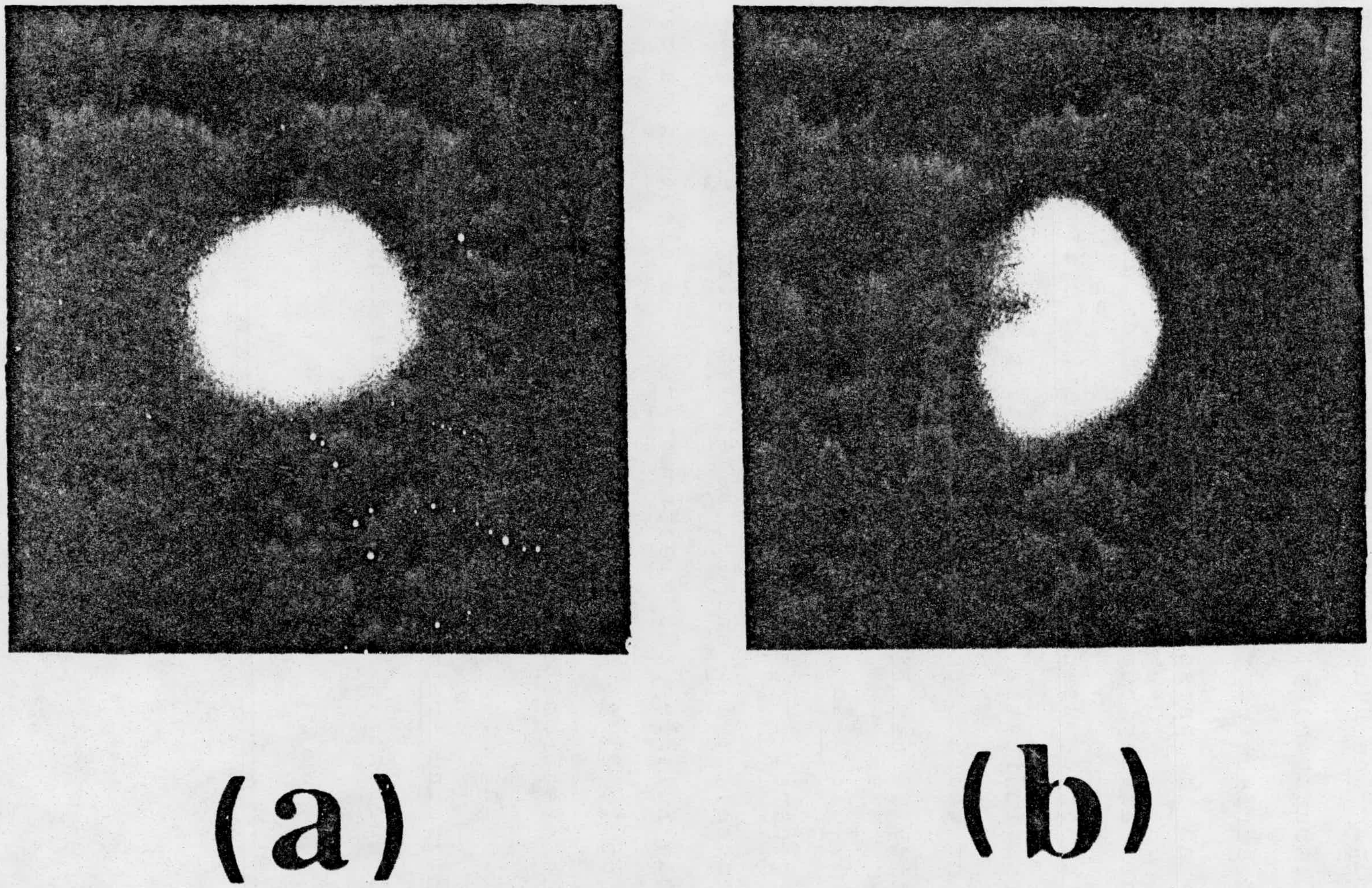

Figure 3: (a) A photograph of the image of a 30 keV Ar$^+$ ion beam with the FIM tip at earth potential; the current is $2\text{x}10^{-9}$ amp on an area of 0.5 cm^2.

(b) In this case the FIM tip is at a potential of +600 Vdc and the shadow of conically-shaped tip is readily seen; same Ar$^+$ ion current. Both images were recorded on Polaroid 3000 ASA film.

circuit, shown in fig. 4, for the irradiation system and the Faraday cup. The numbered points 0 to 3, at the top of the circuit, correspond to the secondary-electron retarder (0), the front surface of the CEMA (1), the back surface of the CEMA (2) and the phosphor screen (3). The total ion current enters the Faraday cup at the point 0 from the irradiation system; the diode used in the irradiation system portion of the diagram indicates symbolically that a reverse positive-ion current was not possible in this portion of the circuit. The quantity I_i can divide itself into three separate ion currents I_{i1}, I_{i2} and I_{i3} at the points 1, 2 and 3 respectively; in general it is expected that $(I_{i2} + I_{i3}) << I_{i1}$. The ion currents I_{i1}, I_{i2} and I_{i3} rejoin at point F and flow through the Keithley 602 electrometer. The electron current in the loop 1, 2, 3, V_3, V_2 and F, denoted I_e, is <u>not</u> measured by the electrometer whereas the leakage currents $I_{\ell 1}$, $I_{\ell 2}$ and $I_{\ell 3}$ flowing from points V_1, V_2 and V_3, respectively, to the earth ground <u>are</u> measured by the electrometer. Therefore the total current I_o measured by the electrometer (EM) is given by

$$I_o = \sum_{j=1}^{3} I_{ij} - \sum_{k=1}^{3} I_{\ell k} \tag{1a}$$

$$= I_i - \sum_{k=1} (V_k/R_{\ell k}) \tag{1b}$$

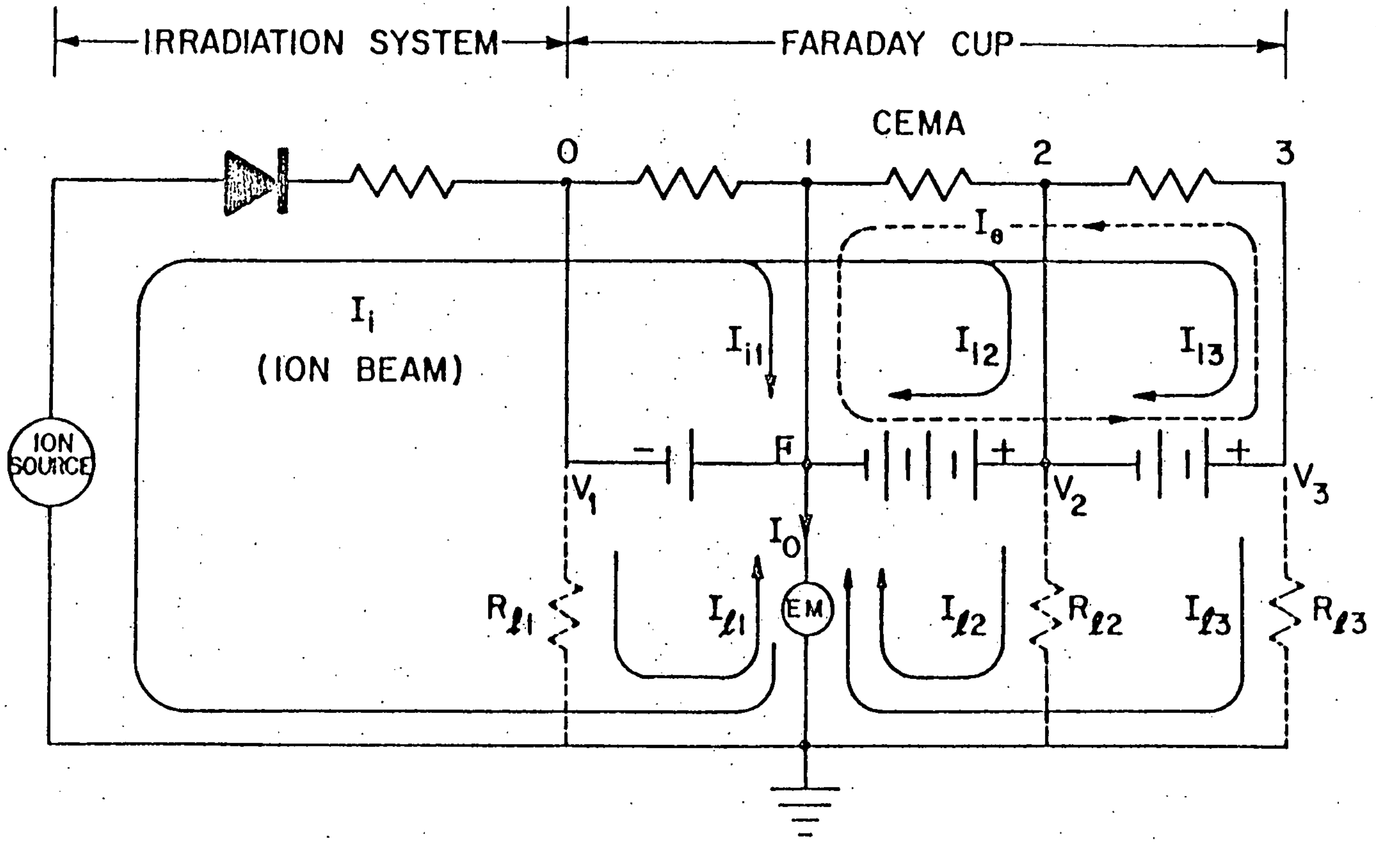

Figure 4: An equivalent circuit for the irradiation system and the Faraday cup; the ion-beam current is I_i and the current measured by the electrometer (EM) is I_o. In practice I_o is almost equal to I_i since the leakage resistance ($R_{\ell 1}$, $R_{\ell 2}$ and $R_{\ell 3}$) is very large (10^{15} Ω).

where V_k is the voltage at the points V_1, V_2, and V_3 respectively and $R_{\ell k}$ is the insulation resistance between the point V_k and the earth ground. Employing eq. (1b) it can be shown (assuming that $3R_\ell \simeq R_{\ell 1} \simeq R_{\ell 2} \simeq R_{\ell 3}$) that R_ℓ should be greater than 10^{14} Ω if the total leakage current $(\sum_{k=1}^{3} I_{\ell k})$ is required to be less than 10^{-11} amp; this value of 10^{-11} amp corresponds to 1% of a typical minimum value, for our research, of I_i $= 10^{-9}$ amp. In practice the leakage current was minimized by employing Corning machinable glass No. 2598 to insulate the Faraday cup from the surrounding wall of the FIM; this machinable glass has a volume resistivity of $\sim 10^{17}$ Ω-cm at 25°C. It was estimated that R_ℓ is greater than 10^{15} Ω.

The three required voltages (-300, 900 and 1500 Vdc) for the Faraday cup (see figs. 2 and 4) were provided by six Burgess U-200 dry cell batteries which were mounted in a specially constructed plexi-glass box. Inside the FIM the leads from the Faraday cup were spark-welded to four Ceramseal feedthrough which were mounted on a standard 2-3/4 inch diameter doublesided Varian Conflat flange. Outside the FIM we employed MHV connecters and polyethylene cable to provide maximum electrical insulation. Control experiments have demonstrated that the total leakage current was always less than 3×10^{-12} amp and that a value of 1×10^{-12} amp was very typical; the latter value was only 0.1% of the minimum ion current of 1×10^{-9} amp used in a typical charged particle irradiation in our research.

III.3. A Simple Dosimeter

The current I_o, which is essentially equal to the quantity I_i, was measured by a Keithley 602 electrometer. Since an important physical quantity, for every irradiation, is the total dose (i.e., the integrated flux); a simple and inexpensive dosimeter was constructed to integrate the I_i with respect to time. The Keithley 602 electrometer converts I_o to an equivalent voltage (V_{in}); this electrometer provided an output voltage of 1 Vdc for full-scale meter deflection on any current range.

Figure 5 shows the schematic diagram for the dosimeter(65) which is essentially an analog integrator. An adjustable voltage source was connected to the non-inverting input of the difference amplifier to diminish the self-integration of the integrator to less than 10 μV sec^{-1}. The multiplier stage was used to calibrate the output voltage (V_{out}); the quantity V_{out} was given by the equation

$$V_{out} = \beta \int V_{in}(t)dt \qquad (2)$$

where β was an adjustable constant with the dimensions of sec^{-1}.

Let us now consider an example of how eq. (2) was used in practice. The object was to obtain a value of V_{out} which was proportional to the total dose; for example, for $I_o = 10^{-9}$ amp, an irradiation time of 600 sec and an ion-beam cross-sectional area of 0.5 cm^2 the dose is 0.75×10^{13} ion cm^{-2}; thus

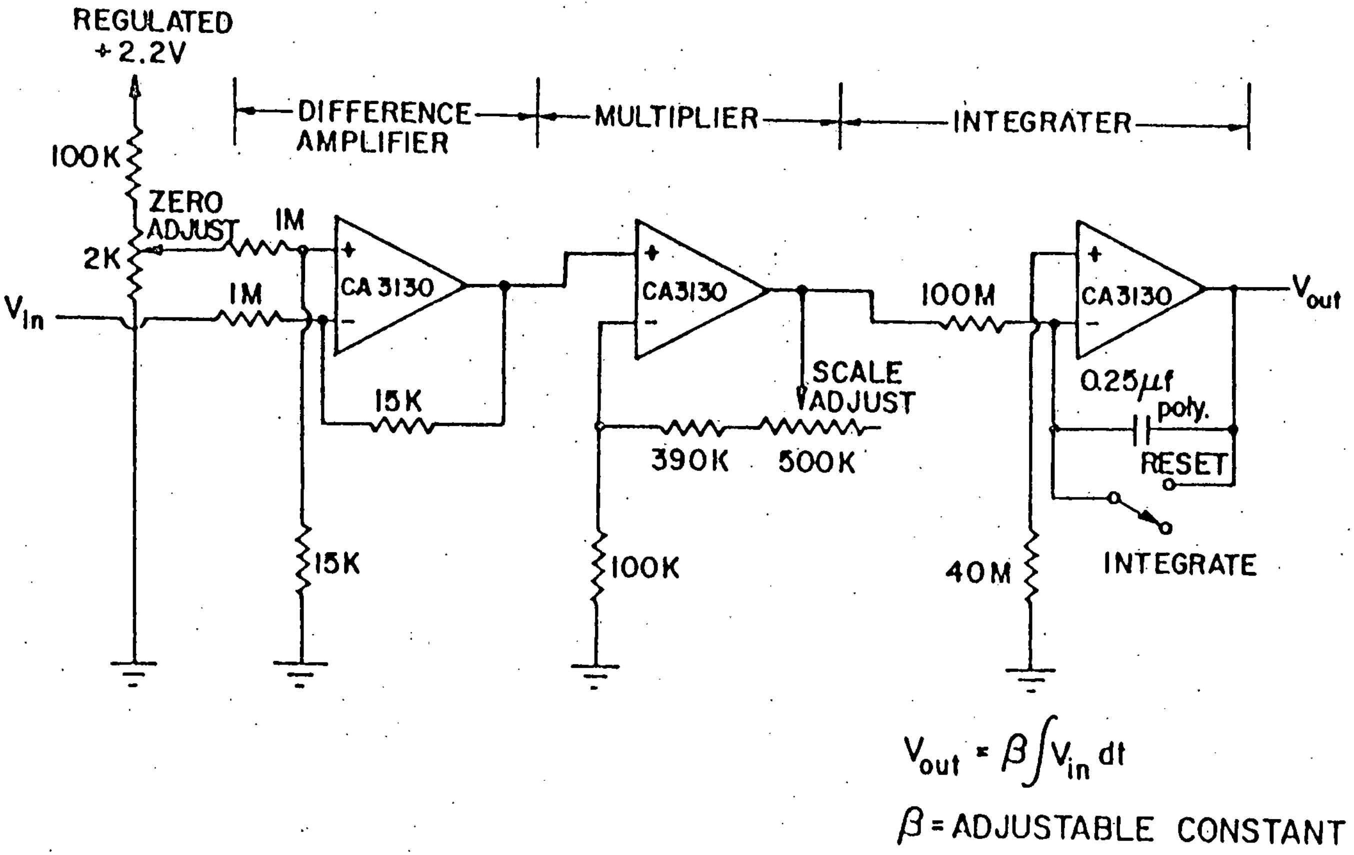

Figure 5: The electronic circuit for the dosimeter used to measure the integrate flux during an irradiation. The input voltage V_{in} is provided by the Keithley 602 electrometer (see fig. 2).

we calibrated the dosimeter to obtain $V_{out} = 0.75$ Vdc. For $I_o = 10^{-9}$ amp the value of V_{in} was 0.33 Vdc using the 3×10^{-9} amp range on the electrometer; therefore, employing

$$V_{out} = 3.75\times10^{-3} \int V_{in}(t)dt \qquad (3)$$

for this scale of the electrometer and for the cross-sectional area of 0.5 am^2; we note that I_o need not be constant for eq. (2) to be valid. The dosimeter can, of course, be calibrated in a similar manner for any other ion-beam cross-sectional area or current scale of the electrometer. The dosimeter was found to be particularly useful in terminating the ion irradiation at some pre-determined dose.

IV. DIRECT OBSERVATION OF THE VACANCY STRUCTURE OF A (220) PLATELET IN AN ION IRRADIATED PLATINUM-4.0at.% GOLD ALLOY

IV.1. Introduction

The point-defect structure of the primary state of damage of irradiated metals can, at present, only be studied experimentally by the field-ion microscope (FIM) technique. The FIM technique provides us with an exact picture of the arrangement of vacant lattice-sites and self-interstitial atoms (SIAs) within and around a depleted zone created by a single primary knock-on atom.(66-67) The present chapter represents an extension of our earlier research on the body-centered cubic metal tungsten(23,26) to a face-centered cubic platinum-4.0at.% gold alloy. There is earlier qualitative work on depleted zones in fast-neutron irradiated platinum by Attardo and Galligan(28, 68) and Inal and Galligan;(29) the main emphasis in this work was in determining size distributions whereas our emphasis is on the spatial distribution of vacant lattice sites within and around individual depleted zones.

In the research on tungsten we studied the point-defect structure of depleted zones created at both 18 K (Stage I) and 473 K (near the top of Stage II); see Schilling, Sonnenberg and Dibbert(69) for a discussion of Stage II in the Pt(Au) system. The work presented here describes the vacant lattice-site structure of a depleted zone that had collapsed into a four-layer vacancy platelet on a (220) plane. The (220) vacancy platelet was created in the Pt-4.0 at.% Au alloy by a single 30 keV W^+ ion at 40 K (below substage II_B); the specimen was subsequently annealed to 100 K (above substage II_C) prior to its examination at 40 K. The (220) vacancy platelet represents an energy state that is intermediate in energy between a three-dimensional compact vacancy cluster and a dislocation loop. The possibility of stable multi-layer vacancy platelets dose not seem to have been considered in the theoretical literature on this subject. It is suggested on the basis of our observation of this platelet that prismatic dislocation loops, observed in transmission electron microscopy studies of ion or fast-neutron irradiated Pt, can form directly from the collapse of vacancy platelets on {220} type planes. And that the vacancy supersaturation within a platelet required for collapse into a dislocation loop can be exceedingly large. Finally, we present, for the first time, the application of the OR TEP program(70) to provide a stereographic drawing of the vacancy platelet.

IV.2. Experimental Details

IV.2.1. Specimen Chemistry and Preparation

The Pt-4.0 at.% Au alloy was prepared at Cornell University and the gold concentration was determined to be 4.0±0.3 at.% by the analytical chemistry laboratory of the Materials Science Center and the U.S. Testing Laboratory (see Table I of Chen and Balluffi.(71) The alloy was drawn into 0.13 mm diameter wire and electropolished in a molten salt solution of $NaNO_3$ and ∿20 % by wt. NaCl, maintained at 350°C, to remove any surface contamination. The wires were next annealed by resistively heating them in air at ∿1400 K and then air quenched by rapidly terminating the heating current. Sharply-pointed FIM specimens were prepared by the standard electropolishing-technique(72) at 3 to 4 Vdc, in the above described molten salt-solution, at 623 K. The procedure consisted of dipping a wire specimen, at regular intervals, into the salt bath to a depth of ∿5 mm and rapidly removing it after 0.2 sec. Next the FIM specimen was field-evaporated continuously in the FIM at ∿125 K and then pulsed field-evaporated at $\lesssim$ 70 K to a final end-form at a background pressure of 1×10^{-4} Torr Ne.

IV.2.2. The Irradiation Procedure

The specimens were irradiated in-situ in a bakeable ultra-high vacuum FIM which is attached to a Hill-Nelson sputtered-metal ion-source via a three-stage differentially-pumped flight-tube (see fig. 1). This arrangement allowed for an in-situ irradiation at $\sim 2\times10^{-9}$ Torr with a pressure of $(2 \text{ to } 5)\times10^{-6}$ Torr argon measured above the diffusion pump which evacuates the ion source. The alloy was irradiated at 40 K with a magnetically analyzed 30 keV W^+ ion beam to a dose of $\sim 1\times10^{13}$ ion cm^{-2} and the flux of ions at the specimen position was $\sim 3\times10^{10}$ $cm^{-2}sec^{-1}$; at this value of the flux the time required to form an adsorbed monolayer was greater than the irradiation period. After the 40 K irradiation the specimen was annealed isochronally to 100 K.(57)

The specimen temperature was monitored with a miniature platinum resistance thermometer (PRT) mounted near the tail of the cryostat. For further details regarding temperature measurement, the sputtered-metal ion-source and the irradiation facility see our earlier publications.(73, 52, 54)

IV.2.3. Data Recording System and Ciné Film Analyzer

The neon FIM images were observed with the aid of an internal image-intensification system based on a Galileo 76 mm diameter channel electron-multiplier array(61) and the FIM images produced in this manner were recorded on 35 mm film with the aid of an Automax ciné-camera equipped with a 1000 ft. film chamber. The recorded and developed ciné film was analyzed with a Vanguard motion analyzer which is equipped with x-y cross-hairs and a position readout;(74) the motion analyzer was interfaced to a Houston Omnigraphic 200 x-y recorder. This latter feature was extremely useful for reconstructing the point defect structure of the depleted zone discussed in this chapter. Each FIM image was recorded after a field-evaporation pulse had been initiated; the pulse height and duration were adjusted so that one atom, on the average, was removed per pulse on the (420) plane.

IV.3. The Arrangement of Atoms in the $(75\bar{1})$ plane

The vacancy platelet (depleted zone A) discussed in this chapter was detected in the $(75\bar{1})$ plane of an FIM specimen with a [100] orientation. This plane is located on the $[\bar{1}1\bar{2}]$ zone inbetween the (220) and $(53\bar{1})$ planes (see fig.6a).† The interplanar spacing for the $(75\bar{1})$ plane is $a_o/\sqrt{75}$* and there are a series of equally spaced planes between the zeroth plane and the 75th plane.** The atomic arrangement within the $(75\bar{1})$ plane and the stacking of the $(75\bar{1})$ planes is a bit complicated, hence we consider this plane in detail.

The crystallography of the $(75\bar{1})$ plane is not given in Nicholas' atlas(78), hence we constructed a ball model of a

---

† The Miller indices (hkl) of the physical planes must be of unmixed parity for an fcc lattice. If the Miller indices are of mixed parity it is a simple matter to convert them to unmixed parity.

* The lattice parameter of the fcc cell is denoted by a_o; for the Pt-4.0 at.% Au alloy a_o = 3.921 A.(76)

** The number of planes in an identity period (N_{hkl}) is given by the expression $N_{hkl} = QQ^*(h^2 + k^2 + l^2)/2$ where Q is one if h, k, l are all odd and Q is 2 if h, k, l are of mixed parity; and Q^* is one if h + k + l is even, while Q^* is 2 if h + k + l is odd. It is important to note that in making this calculation one must use the Miller indices (hkl) before they have been converted into unmixed parity. We alao note that the Jaswon and Dove(77) statement "that the stacking pattern of the primitive cubic (hkl) planes constitutes a congruence modulo $h^2 + k^2 + l^2$" is not <u>generally</u> correct.

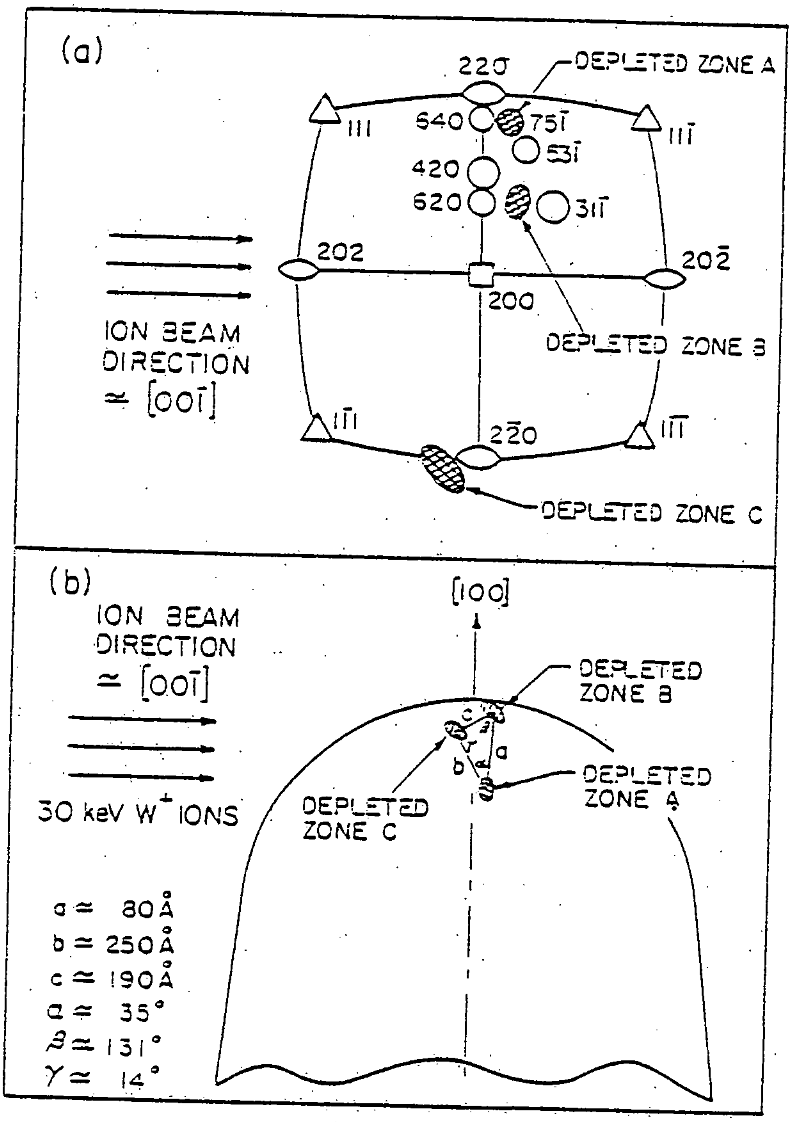

Figure 6: (a) A partial 200 stereographic projection showing the location of depleted zones A, B and C; depleted zone A is the (220) vacancy platelet.
(b) A schematic cross-sectional view of the FIM tip which contained depleted zones A, B and C; the plane of projection is the (020) plane. This figure is drawn to scale.

$(75\bar{1})$ plane according to the procedure developed by Moore and Nicholas.(75) A photograph of this ball model, built on a (200) plane, is shown in fig. 7; the dark balls indicate the atoms in the outermost (zeroth) layer. The visible atoms, within the primitive unit cell, from different layers are indicated by the numbers 1, 2, 3, 4 and 5. The balls marked with an x indicate one $(11\bar{1})$ plane that intersects the $(75\bar{1})$ plane. The ball model was used to determine the primitive mesh and the stacking sequence of planes zero to five. Figure 8 shows the primitive mesh (plane zero) of the $(75\bar{1})$ plane and the positions of the atoms of planes 1 to 5 that project within the primitive mesh; the Appendix A and Table 9 give more details concerning fig. 8.†

IV.4. Procedure for the Construction of a Depleted Zone

In this section the basic procedure used to reconstruct a depleted zone in three-dimensions, from the FIM micrographs, is explained. The steps employed were as follows:

1. The positions of all atoms and vacant sites on the zeroth layer were determined employing the x-y cross-hairs on the motion analyzer in conjunction with the x-y recorder. All the cartesian coordinates were read with respect to a common fiducial mark which had been engraved in the phosphor screen portion of the internal image-intensification system.

---

† We have generally followed the scheme of Nicholas(78) in presenting crystallographic information.

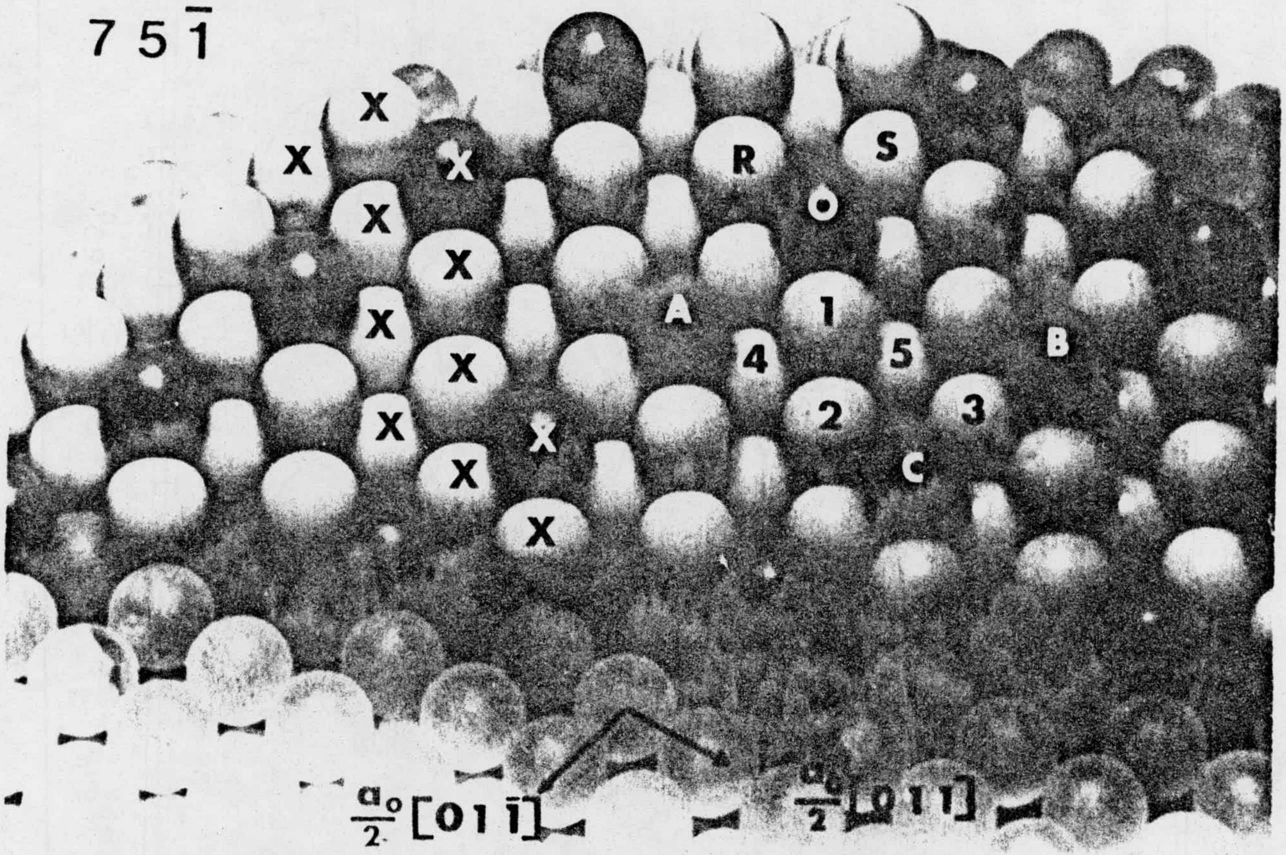

Figure 7: A photograph of a ball model of the $(75\bar{1})$ plane built on a (200) plane. The dark balls indicate atoms which are in the outermost (zeroth) layer; the visible atoms within one primitive unit cell, from different layers, are indicated by the numbers 1, 2, 3, 4 and 5. The balls marked with an x indicate one $(11\bar{1})$ plane that intersects the $(75\bar{1})$ plane.

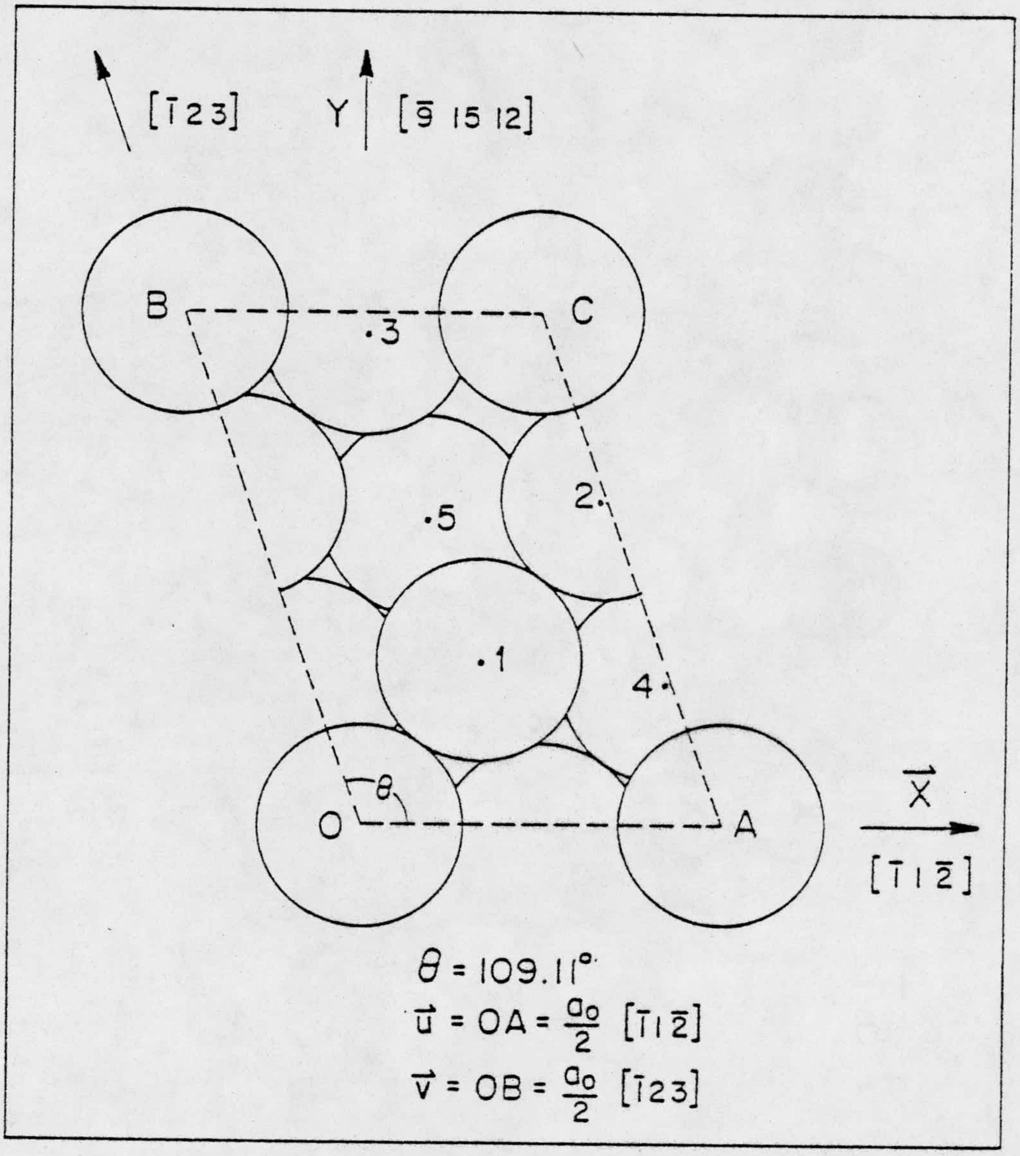

Figure 8: The primitive mesh (OABC) of the $(75\bar{1})$ plane and the projection of the atoms that lie within this primitive mesh for layers 1 to 5.

This procedure eliminated all errors in the positions of atoms caused by the slippage of film in either the ciné camera or the motion analyzer.

2. An atom or vacant site in the zeroth layer was arbitrarily chosen as the origin atom for this layer; the atom labeled 0(0,0,0) in fig. 9 was taken to be an origin atom. A schematic diagram showing the positions of the atoms in two successive $(75\bar{1})$ planes, which had been recorded as outlined in step 1, is shown in fig. 9. The atomic sites in the zeroth and first layers are represented by solid black circles and open circles respectively. The vector $\frac{a_o}{2}[\bar{1}1\bar{2}]$ which lies along the intersection of the $(75\bar{1})$ and $(53\bar{1})$ planes was chosen as the u-axis. Similarly, the vector $\frac{a_o}{2}[\bar{2}31]$ which lies along the intersection of the $(75\bar{1})$ and (640) planes was used to determine the vector $\frac{a_o}{2}[\bar{1}23]$ which was taken to be the v-axis (see fig. 9). The vector $(a_o/75)[75\bar{1}]$ which is normal to the $(75\bar{1})$ plane was taken to be the Z-axis (see the Appendix A). All of the vectors used so far are in the standard orthogonal coordinate system. Next the coordinates of the atomic sites were indexed with respect to the vectors $\vec{u}$, $\vec{v}$ and $\overrightarrow{OZ}$ $\{(a_o/75)\ [75\bar{1}]\}$; for example, the sites O, A and B in the zeroth layer have local coordinates (0,0,0), (1,0,0) and (0,1,0) respectively. The origin for the first layer (O') is uniquely assigned to the atomic site which is projected within the unit primitive cell of the zeroth layer (see fig. 9); O'_p denotes the projection of O' onto the zeroth layer then

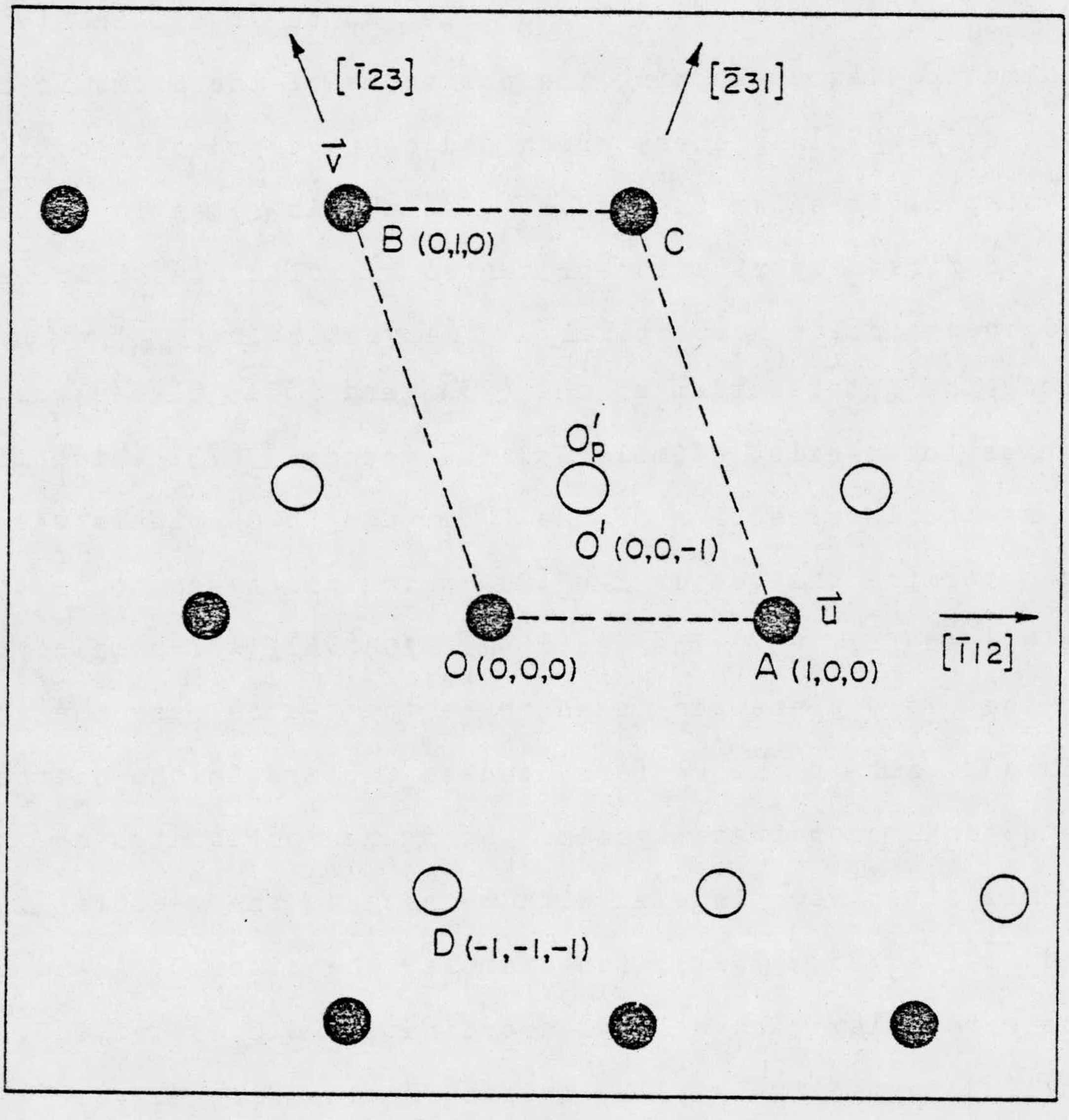

Figure 9: A drawing of the atom positions in the zeroth and first layers of the $(75\bar{1})$ plane. The figure is used to explain how the (220) vacancy platelet was recpnstructed from the FIM image; see sect.IV. for the details.

$\overline{O'_pO'} = [00\bar{1}]$. Hence, $\overrightarrow{O'_pD} = \overrightarrow{O'_pO'} + \overrightarrow{O'D} = [00\bar{1}] + [\bar{1}\bar{1}0] = [\bar{1}\bar{1}\bar{1}]$, so that the coordinates of D are (-1,-1,-1) relative to O'_p. The local coordinates of other atomic sites in the first layer, relative to O'_p, were derived in a similar manner. The practical advantage of this local coordinate system was that all the vacant lattice sites had integral coordinates.

3. Finally the coordinates of an atomic site, such as D, relative to the origin O in the zeroth layer, were obtained by adding the shift vector $\vec{t} = [t_x t_y 0]$ to $\overrightarrow{O'_pD}$. The shift vector is the projection of $\overrightarrow{OO'}$ onto $(75\bar{1})$ and is given by $\vec{t} = (a_o/150)\ [61\ 85\ \bar{2}]$ (see the Appendix A). Extending this procedure the positions of all the atomic sites observed can then be transformed back to an orthogonal coordinate system with O as its origin. In practice all the required transformations were carried out in our laboratory with the aid of a Nova 1220 minicomputer.

IV.5. Results

In only one out of three ion-irradiated Pt(Au) specimens did we find a mapable and isolated depleted zone in the bulk of a specimen; this specimen had an average radius of curvature of $\sim$190 A. We shall momentarily call this depleted zone DZA; this position in the FIM tip, relative to the two other depleted zones detected, is shown in fig. 6. It is noted that DZA is located $\sim$30 A down from the initial surface and $\sim$90 A from the irradiated surface of the specimen. Depleted zone B is located near the $(93\bar{1})$ plane and depleted zone C is located near the $(2\bar{2}0)$ plane. Depleted zones B and C were found only one or two interplanar spacings from the irradiated surface of the specimen. The DZA detected in the $(75\bar{1})$ plane was found to consist of 31 vacant lattice sites* clustered in a disc-shaped region, ∿20 A in diameter lying near a (220) plane. Thus DZA has the morphology of a vacancy platelet with a (220) habit plane; thus we call it a (220) vacancy platelet.

Figure 10 shows a series of ten FIM micrographs of ten successive $(75\bar{1})$ planes; they were chosen from a total of $1.2\text{x}10^3$ frames of 35 mm ciné film which were recorded and analyzed in the reconstruction of the (220) vacancy platelet. The $(75\bar{1})$ plane and the surrounding planes are indexed in frame 1; the frame number of the ciné film is located in the right-hand corner below each micrograph and the layer number is preceeded by the letter n (e.g., n = 1) in the upper left-hand corner above each micrograph. Frames 1, 235, 292 and 898 show atomically perfect planes in layers 1, 3, 4 and 10 respectively; the other frames exhibit $(75\bar{1})$ planes containing vacant lattice-sites. The position of each atom in the $(75\bar{1})$ plane is indicated schematically below each micrograph by a solid black-dot and a vacant lattice-site is indicated by an

---

* One contrast effect produced by a gold atom is a single dark atom site;(71) this contrast effect is identical to that of a vacant lattice site. Hence, the 31 vacant sites detected represent an upper limit to the vacancy population in the platelet.

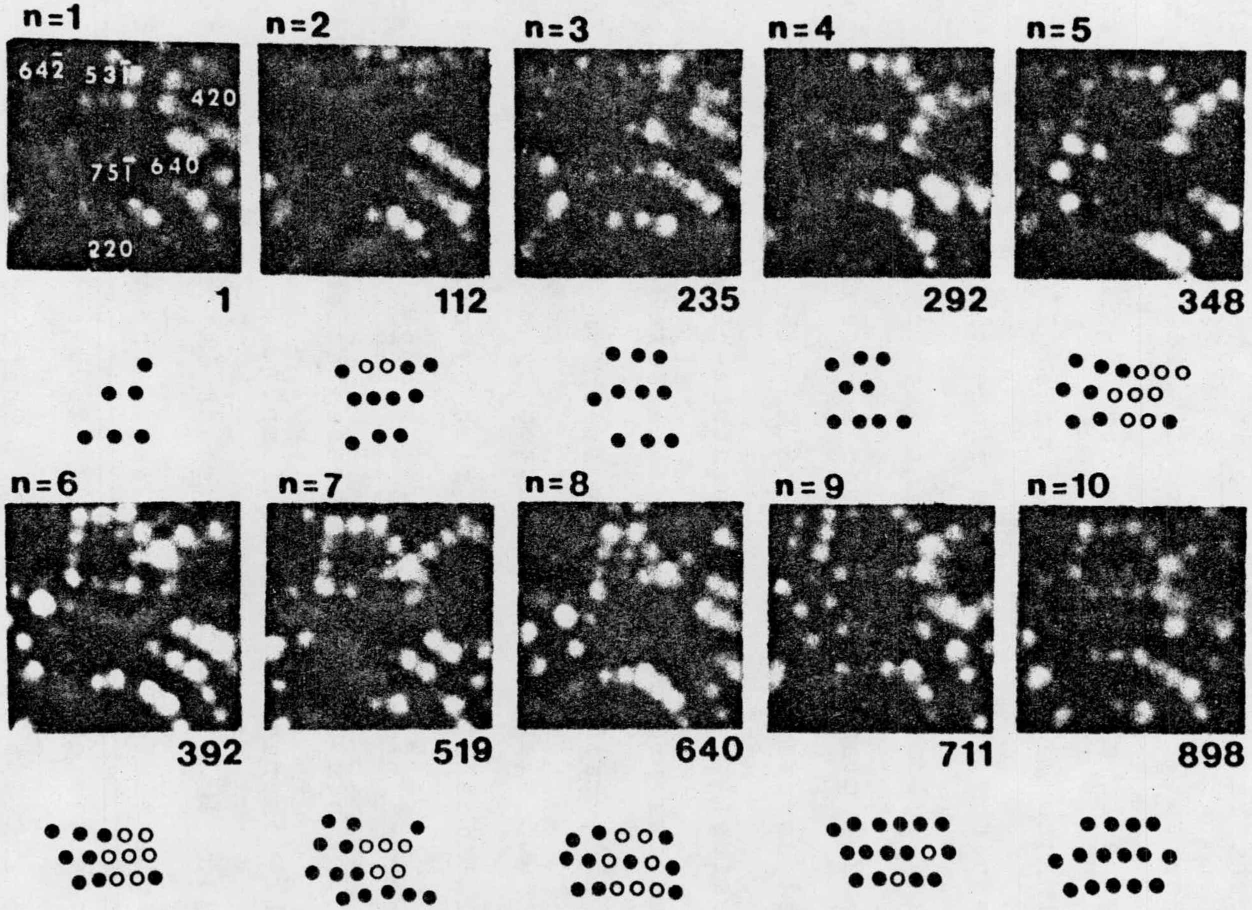

Figure 10: A series of ten FIM micrographs out of 898 recorded during the atom-by-atom dissection of the (220) vacancy platelet. The solid black dots indicate normal lattice atoms and the open circles indicate vacant lattice sites.

open circle. Because of the small size of the $(75\bar{1})$ plane we have been forced to include ledge atoms in analyzing the (220) vacancy platelet; a missing atom in the ledge was only counted as a vacant lattice site if <u>no</u> atom was detected in this site during the entire atom-by-atom dissection process of this plane.

Figure 11 shows a projection of all the vacant sites contained in the vacancy platelet on a (220) plane; this plane was chosen for the projection since the habit-plane of this disc-like agglomerate of vacant lattice sites is very close to the (220) plane. The number(s) associated with the open-circle(s) corresponds to the (220) plane in which the vacant sites reside; the doubly concentric-circle indicates that two vacancies project to the same site. An isometric drawing of the (220) vacancy platelet is shown in fig. 12. The boundary of each slab was constructed by connecting the outermost vacant lattice sites in each slab by straight line-segments; the thickness of each slab is two (220) interplanar spacings (2.77 A). This isometric representation of DZA shows its plate-like character rather clearly.

Figure 13 exhibits the vacant lattice-sites in the (220) vacancy platelet in a second way. The vacant lattice-sites were projected onto the $(0\bar{2}0)$, (200) and (002) planes in figs. 13a, 13b and 13c respectively. The projection onto the (002) plane in fig. $\bar{1}3$c shows very clearly that the habit plane is a (220) plane. Figure 13d is a photograph of a ball-model of the (220) vacancy platelet; each ball represents a vacant

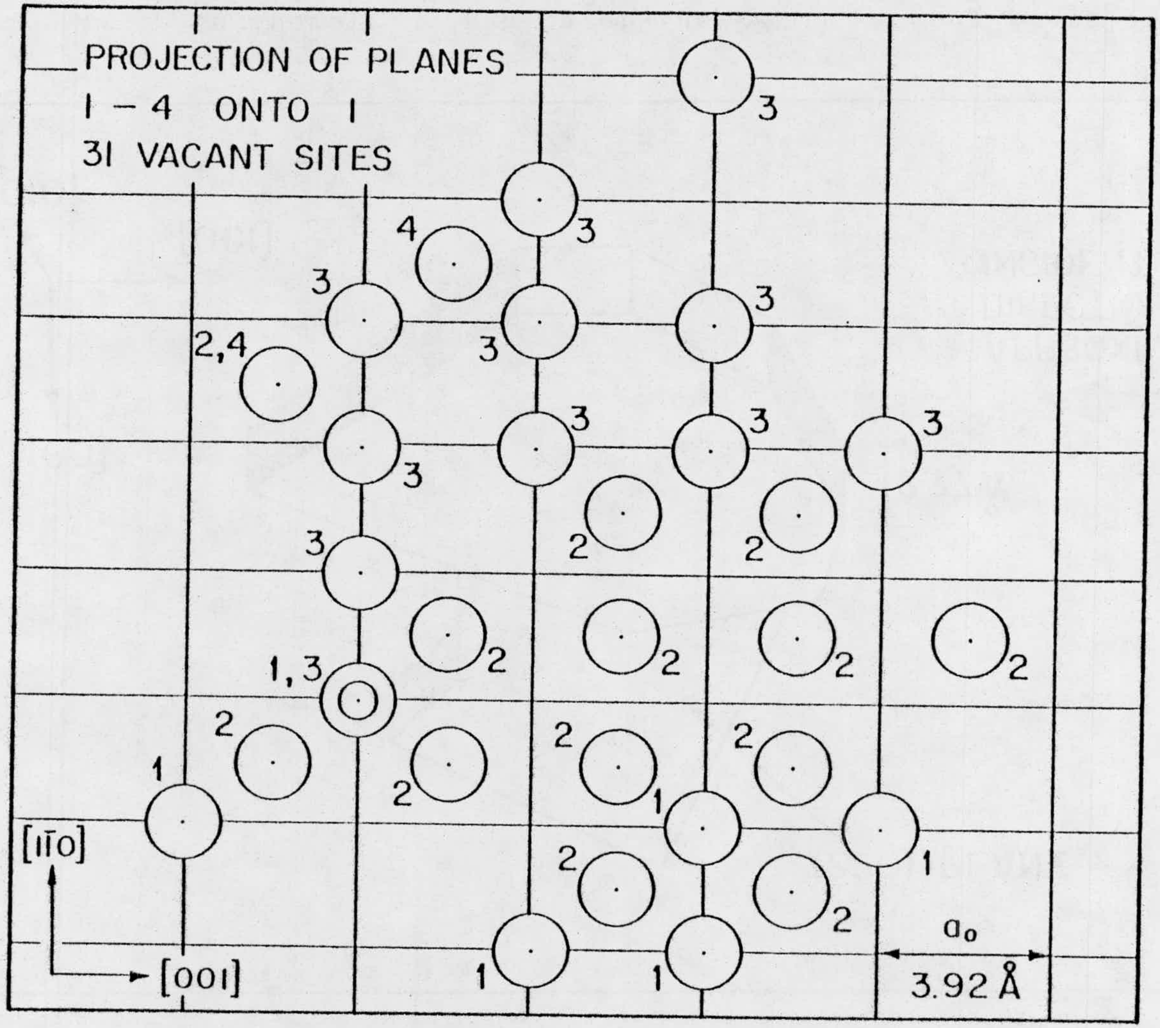

Figure 11: The projection of all the vacant lattice sites contained within the (220) vacancy platelet projected onto a (220) plane.

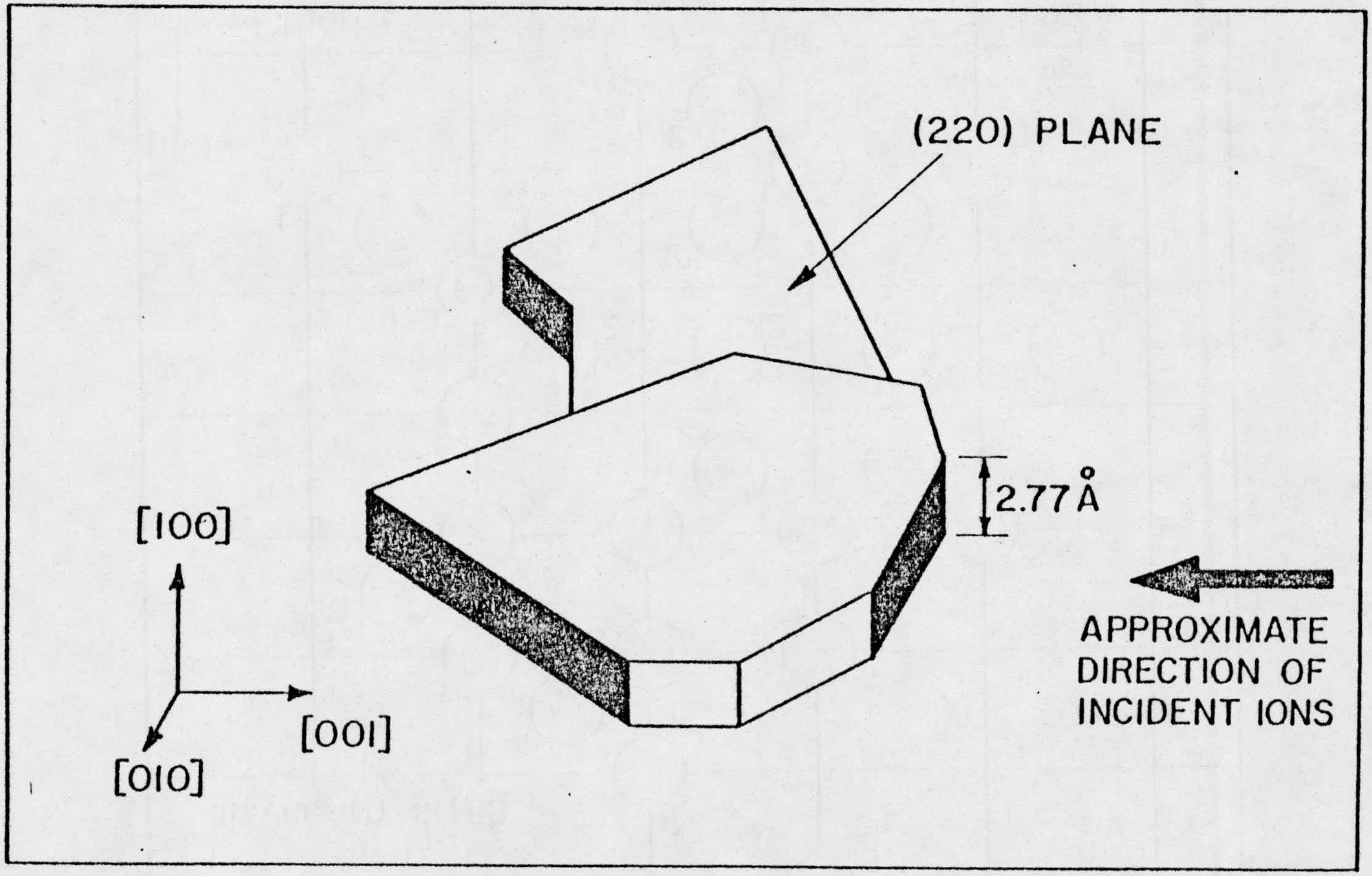

Figure 12 : An isometric drawing of the (220) vacancy platelet constructed from the maps shown in fig. 13.

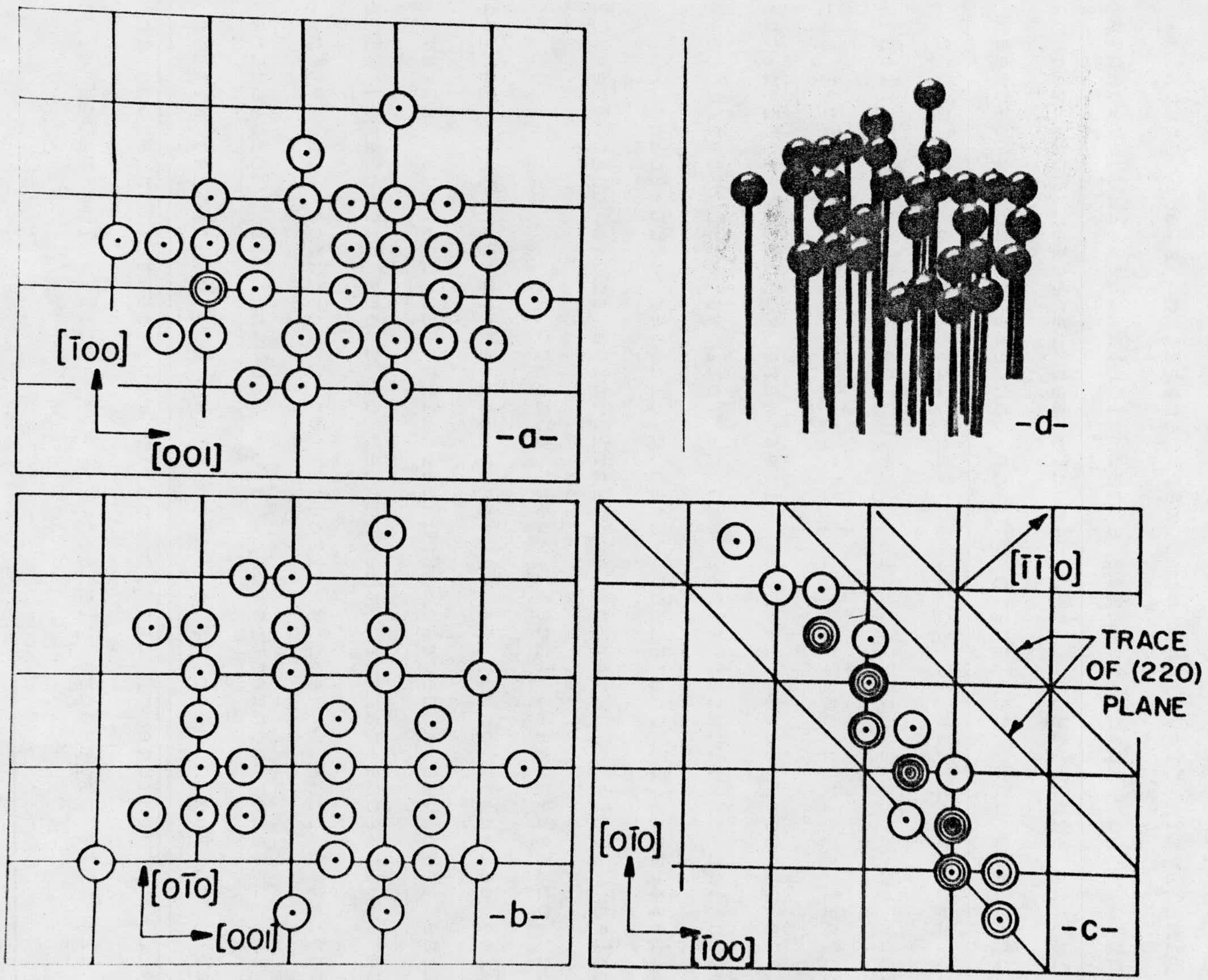

Figure 13: Projections of the vacant lattice sites onto the $(0\bar{2}0)$, (200) and (002) planes in figs. 13a, 13b and 13c respectively. Fig. 13d is a photograph of a ball model taken along approximately a $[\bar{1}00]$ direction; each ball represents a vacant lattice site.

lattice-site and the surrounding lattice atoms have been omitted for clarity. The photograph in fig. 13d was taken along approximately a $[\bar{1}00]$ direction.

Finally in fig. 14 a computer generated* stereographic drawing of the vacant lattice sites within the (220) vacancy platelet is exhibited. The open circles represent the vacant lattice-sites and the length of the connecting bonds between vacant lattice-sites is equal to the first nearest-neighbor distance ($a_o/\sqrt{2}$) in the fcc lattice. The viewing direction is approximately along an $[0\bar{1}1]$ direction. If only first nearest-neighbors vacant lattice sites were considered then the distribution of cluster sizes was as follows: (1) two monovacancies; and (2) one jumbo vacancy cluster containing 29 vacancies. This cluster size distribution shows that the (220) vacancy platelet was, indeed, very compact.

The calculation of the vacancy concentration in a depleted zone involves a degree of uncertainty as one must always estimate, in some manner, the number of atoms associated with the depleted zone. We now discuss two procedures for estimating the vacancy concentration (c_v). In the first procedure we employed the number of atomic sites (80) contained within the $\sim$1200 A^3 volume of the isometric representation shown in fig. 12; this procedure yielded $c_v \simeq 39$ at.%. The value of c_v

---

* The OR TEP program, developed at the Oak Ridge National Laboratory to provide isometric drawings and stero-displays of large complex organic and biological molecules, was used to make fig. 14.

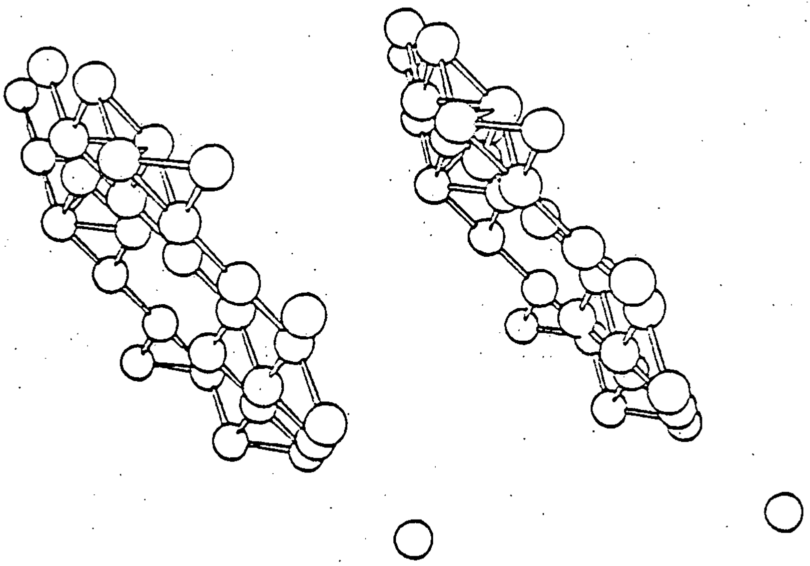

Figure 14: A computer generated stereographic pair of the (220) vacancy platelet. Each open circle represents a vacant lattice site and the bond length connecting any two vacant lattice sites is equal to the first nearest neighbor distance ($a_o/\sqrt{2}$). The viewing direction is approximately along an $0\bar{1}\bar{1}$ direction.

was lowered to 35 at.% if it was corrected for the gold solute atoms which display the same contrast effect as a vacant lattice site. The second procedure involved calculating c_v in each (001) plane passing through the platelet and then averaging over all (001) planes contained within the depleted zone. The number of atomic sites counted in the calculation of c_v was contained within a rectangle whose borders were determined by the four outermost vacant lattice sites in each (001) plane. This procedure was repeated for the (100) and (010) planes. The average value of c_v obtained in this manner is ∿44 at.%. Thus the possible range of c_v is ∿35 to 44 at.% employing the above two counting procedures.

IV.6. Discussion

IV.6.1. Probability that the (220) Platelet was Created by One Incident Ion

Employing the same geometric argument as the one used earlier(23, 26) it was estimated that the maximum number of ion hits on the cross-sectional area of the platelet (∿30 A^2) was 0.03. This value was an upper bound because the calculation neglected the spread in the range of the incident ions. Since the estimated number of ion hits on the cross-sectional area was approximately 33 times less than unity we concluded that the vacancy platelet was created by a single incident-ion.

IV.6.2. The Number of Vacancies in the (220) Platelet

The model used most frequently to calculate the number of

Frenkel pairs ($\langle\nu\rangle$) produced by a primary knock-on atom (PKA) is the modified Kinchin-Pease$^{(79)}$ amorphous solid model. The modified expression for $\langle\nu\rangle$ is given by:

$$\langle\nu\rangle = \kappa\langle\hat{E}\rangle/2\bar{E}_d \qquad (4)$$

where $\langle\hat{E}\rangle$ is the average damage energy, κ is the displacement efficiency and $\bar{E}_d$ is the average displacement threshold energy. The quantity $\langle\hat{E}\rangle$ is related to the incident ion energy E_o by the equation

$$\hat{E} = E_o - \hat{Q} \qquad (5)$$

where $\hat{Q}$ is the total energy lost from a collision cascade through inelastic processes. In the present situation E_o is 30 keV, $\hat{Q}$ is 7.26 keV and $\bar{E}_d$ is 44 eV; the value of $\hat{Q}$ was calculated for the Ta^+ on Au situation employing the recent extensive tabulation of Winterbon.$^{(80)}$ The value of $\bar{E}_d$ was taken from the tables compiled by Lucasson$^{(81)}$; we emphasize that this $\bar{E}_d$ represents an <u>average</u> threshold energy rather than the minimum energy (33 eV) required to produce a displacement in platinum. For the (220) vacancy platelet the value of $\langle\nu\rangle$ was equal to 31, hence κ was equal to 0.12. This value is considerably less than the value of $\sim$0.8 to 0.9 found both from computer simulation studies$^{(20)}$ and analytical solutions.$^{(82)}$ This factor of $\sim$ 7 between the calculated and experimental value of κ can be attributed to the following causes: (1) the known straggling of the damage energy$^{(83)}$; (2) fluctuations in the value of $\langle\nu\rangle$ for a given $\hat{E}^{(20)}$; and (3) the enhanced recombination of SIAs and vacancies due to the fact that the specimen was annealed to 100 K (end of substage II_c) prior to its examination at 40 K.

IV.6.3. The Diameter of the Platelet

An estimate of the expected cascade size in Pt-4.0 at.% Au† was made employing the tabulations given by Winterbon.(80) The diameter of the cascade ($D_\perp$) was taken to be given by $2(\langle y^2\rangle)^{1/2}$(84) where $\langle y^2\rangle$ is the second moment of the damage distribution curve* (i.e., the distribution of the fraction of ion energy deposited in atom motion). The value $\langle y^2\rangle$ was obtained in the following manner: (1) the mean damage depth ($\langle x\rangle$) was calculated (∿35 A); (2) the relative damage straggling ratio ($\langle \Delta x^2\rangle/\langle x\rangle^2$) was calculated (0.39); and finally (3) the relative transverse damage straggling ratio ($\langle y^2\rangle/\langle \Delta x^2\rangle$) was calculated using the results of steps 1 and 2 (0.51). Employing the above numbers the value of $D_\perp$ was determined to be ∿16 A. This value can be compared to the experimental value of ∿20 A for the (220) platelet. The experimental and theoretical values are in reasonable agreement††, hence it appears that Westmoreland and Sigmund's method provides a useful approach for obtaining an approximate estimate of the size of a cascade (also see Jenkins and Wilkens(85)).

---

† The present situation of 30 keV W^+ on Pt-4.0 at.% Au was modeled for 30 keV Ta^+ on Au.

* This is the damage distribution which is perpendicular to the direction of the incident ions.

†† The agreement is surprisingly good considering that the specimen was annealed to the top of substage II_c(100 K).

We further note that the (220) vacancy platelet was located ∿90 A in from the irradiated surface; this value is a factor of 2.6 greater than the mean damage depth of ∿35 A and the quantity $[90 - \langle x \rangle]$A is five times greater than one standard deviation $(\langle \Delta x^2 \rangle)^{1/2} = 11$ A . Thus the (220) vacancy platelet lies in the extreme tail end of the damage distribution profile or alternatively it was produced as a result of a dechanneling event; note that the incident ion beam was approximately parallel to the $[00\bar{1}]$ direction (see fig. 6a). In a computer simulation study of depleted zones in copper Robinson and Torrens(20) have found that the channeled atoms are associated with a reduced number of displacements and a large loss of energy by inelastic processes; thus this may be a fourth possible reason for the small number of vacancies in the (220) platelet and hence the small calculated value of κ in eq. (4) (see sect. IV.6.2.).

IV.6.4. Stability of the (220) Vacancy Platelet

The subject of the relative stability of the different possible morphologies of vacancy clusters in quenched or irradiated metals has been the subject of several theoretical treatments(86-87) as well as numerous experimental investigations(88,43) by a variety of techniques.

The FIM technique has been useful in demonstrating that there are at least three basic morphological types of vacancy clusters in the primary damage state of irradiated metals(67); the simpler primary damage state (a random distribution of

Frenkel pairs) produced by MeV electrons is excluded from this categorization. The three basic morphological types are: (1) depleted zones; (2) very compact three-dimensional vacancy-clusters or voids; and (3) dislocation loops. The above categorization was based on FIM observations of 10 MeV proton, fast neutron or heavy ion (50-150 keV W^+, W^{+2}, Zn^+, Hg^+, Ar^+ and Xe^+) irradiated specimens of tungsten, iridium and platinum; the irradiations were generally performed at either room temperature or 78 K (see Seidman(67) for the references from which the above categorization was made). The vacancy concentration stored in the dislocation loops, in the above metals, only represented a small fraction of the total vacancy concentration in the irradiated metals; in the case of tungsten it was ∿10%. This is an important result since the transmission electron microscope (TEM) studies of irradiated metals depend heavily on the ability of the vacancy-rich core of a depleted zone to collapse into a dislocation loop; the latter defect is imaged via strain-field contrast in a TEM image.(43) With care it is also possible to observe voids by the TEM technique; although the voids are best observed in an out-of-focus state.(89) In conclusion the FIM observations provide a simple explanation for the low values of the yield-factor(40,46) determined by the TEM technique, for a number of ion-irradiated metals; that is, of the three basic morphological types only the dislocation loops have been, in general, observed by the TEM experiments. Thus an appreciable fraction of the radiation damage is often i a state of aggregation that is not resolved in the TEM image. This conclusion is corroborated, in the case of platinum, by Schindler's TEM observation(90) that the yield-factor for platinum irradiated with 60 keV Au^{++} ions is only 0.1.

The (220) vacancy platelet reported and analyzed in this chapter must represent an energy state that is intermediate in energy between a three-dimensional compact vacancy cluster (or void) and a dislocation loop. It is interesting to observe that the platelet-like structure exists over four (220) planes (see figs. 12 to 14); this possibility does not appear to have been considered theoretically in the literature.† On the theoretical side Johnson(87) has predicted that a single-layer vacancy-platelet on a {111} plane, in nickel, is stable to collapse into a perfect dislocation loop up to 180 vacancies. While Savino and Perrin(91) have calculated by a computer simulation technique that a (111) planar vacancy aggregate, in copper, of as few as six vacancies can readily collapse into a more stable configuration. In addition there have been three TEM studies of both fast-neutron irradiated Pt(92-93) and 60 keV Au^{++} ion-irradiated(90) platinum. In all three cases prismatic dislocation loops (i.e., with an $(a_o/2)<110>$ type Burgers vector) were detected; in Schindler's research he determined that 90% of the dislocation loops observed had an $(a_o/2)<110>$ type Burgers vector (the remaining

---

† To the best of our knowledge only the possibility of a single-layer vacancy-platelet had been considered in the theoretical literature.

10% of the dislocation loops were Frank loops). Furthermore in unpublished research Schindler (private communication) had determined the habit plane of the prismatic dislocation loops to be of the {110} type. Thus we would like to suggest, on the basis of our observations in this Pt-4.0 at.% Au alloy and the TEM research on irradiated Pt, that the prismatic loops observed, in the TEM studies, formed directly as the result of the collapse of vacancy platelets on the {220} type planes. That is, the vacancies need not have first collapsed onto a {111} type plane to form a Frank dislocation loop with an $(a_o/3)\langle 111\rangle$ type Burgers vector and then unfaulted as a result of the dislocation reaction(94)

$$(a_o/3)\,[111] + (a_o/6)\,[11\bar{2}] \rightarrow (a_o/2)\,[110] \qquad (6)$$

to form a prismatic dislocation loop.

The final point that we would like to note is the high degree of stability with respect to collapse into a prismatic dislocation loop, of the present vacancy platelet, despite the fact that the local vacancy concentration of 35 to 44 at.% corresponds to a local supersaturation, at 100 K, of $\sim$(5 to 6) $\times 10^{74}$ and therefore to a chemical potential of $\sim$1.5 eV per vacancy within the platelet. Thus it would appear that even greater values of the supersaturation, within a platelet, are necessary for it to collapse into a prismatic dislocation loop in the case of platinum.

V. PRIMARY DAMAGE STATE OF ION-IRRADIATED PURE TUNGSTEN

V.1. Introduction

In this chapter we present the first systematic study of the point-defect structure of depleted zones created by a single 30 keV W^+, Mo^+ or Cr^+ ion at 10 K in tungsten. The dependence of the point-defect structure of a depleted zone on the mass of the incident ion was studied in great detail. First, we applied the OR TEP(70) program to provide a three-dimensional drawing of each depleted zone. Second, the number of VLSs within each depleted zone was compared with the modified Kinchin-Pease model.(20, 79) Third, the radial distribution function was determined for each depleted zone. It was found that the VLSs within the volume of a depleted zone tended to form clusters. Fourth, the experimental diameter of each depleted zone was compared with the WSS theory.(107) Finally, the observed spatial distributions of SIAs in a specimen irradiated with 30 keV Cr^+ ions and in a specimen irradiated with 18 keV Au^+ ions were measured and a lower bond of the RCS chain length in tungsten was determined to be 175±85 A.

V.2. Experimental Details

V.2.1. Specimen Preparation

Four-pass zone-refined single crystal rods 1.0 to 1.5 mm in diameter and 20 cm in length were prepared by the electron-beam zone-melting technique at Cornell University. They were first reduced to a 0.5 mm diameter rod by electropolishing at 30 Vdc in a solution of 20 g NaOH in one liter of a 60-40 mixture of glycerol and water, with air bubbled through the electrolyte.(95) The thinned rods were then polished and sectioned into 2 cm lengths o.1 mm diameter in a 1N NaOH electrolyte at 9 Vdc. A sectioned rod specimen was mounted in the specimen holder and polished into a sharply-pointed FIM tip by the ac drop-off technique. Typically, the specimen was immersed vertically into a layer of 1 N NaOH aqueous solution floated on the top of CCl_4. A 4 Vac potential was then applied to the specimen with respect to a stainless-steel cathode until a slightly necked region was produced at the interface between the NaOH and CCl_4. The specimen was then lifted slightly and the neck was allowed to propagate inward until the lower section of the wire dropped off. At this point the specimen had a thin and long taper. Once again the specimen was polished by the procedure described above, but before the lower section of the wire dropped off the voltage was switched to ∿3 Vac pulse controlled by a momentary push-button switch. The pulse was terminated when the lower section was observed to drop off.

A specimen produced by this ac drop-off technique usually imaged at a potential of 3 to 4 kV in the FIM; this corresponded to a tip radius of ∿100 A. The initial end-form of the electropolished tip was extremely rough on the atomic scale. An atomically smooth end-form was obtained by combining dc and pulsed field-evaporation at 78 K.

V.2.2. Experimental Procedure

After the specimen was field evaporated to a tip radius of 200 to 400 A, it was cooled down to 10 K and brought to an atomically smooth low-temperature end-form by pulsed field-evaporation. The specimen was then irradiated *in-situ* at a background pressure $\leq 2\text{x}10^{-9}$ Torr, in the absence of the electric field and imaging gas, with 30 keV W^+, Mo^+ or Cr^+ ions to a total dose of $(2\text{-}10)\text{x}10^{12}$ ion cm^{-2}. The flux of ions at the specimen was $\sim 10^{11}$ ion cm^{-2} sec^{-1}. In addition, one specimen was also irradiated with 18 keV Au^+ ions to a total dose of $5\text{x}10^{13}$ ion cm^{-2}; the flux of ions at this specimen was $\sim 2\text{x}10^{12}$ ion cm^{-2} sec^{-1}. The flux of ions was adjusted so that the time required to form an absorbed monolayer was always greater than the irradiation period. After the 10 K irradiation the specimen was re-imaged in the presence of helium imaging gas of $\sim 1\text{x}10^{-4}$ Torr. The specimen was then subjected to pulsed field-evaporation. Each FIM image was recorded photographically after a field-evaporation pulse had been initiated; the pulse height and duration were adjusted so that one atom, on the average, was removed per pulse on the (222) plane.

V.3. The Arrangement of Atoms in the Regions of the (222) and $(\bar{4}11)$ Poles

Only the regions of the (222) and (411) poles in the image of bcc tungsten specimens possessed sufficient atomic resolution for the atomic reconstruction of depleted zones and hence they were used for the present investigations. Two schematic diagram of two successive layers for the (222) and (411) poles are shown in figs. 15 and 16 respectively. There are sixteen planes in the region of the (222) pole; they are (222), (334), (233), (343), (332), (433), (323), (424), (244), (442), (543), (534), (435), (345), (354) and (453) planes. There are twelve planes in the region of the (411) pole; they are (411), (622), (521), (721), (732), (631), (842), (512), (712), (723), (613) and (824) planes. The atoms in the zeroth and first layers are indicated by the solid black circles and the open circles respectively. The Miller indices for each plane are shown in both figures. The vectors which lie along the intersection of two neighboring planes are also indicated. The vectors are in units of $a_o/2$ where a_o is the lattice constant†. The diagrams exhibited in figs. 15 and 16 were plotted by using the procedure and information given in Nicholas' Atlas.(78) The crystallography of the (433), (543), (875)*, (11 4 3)*, (765)*, (521), (631) and (831) planes were not given in Nicholas' Atlas; therefore they were determined and the results are

---

† The value of a_o for tungsten is 3.16 A.

* The (875), (765) and (11 4 3) planes were observed only when the tip radius of the specimen became sufficiently large. Hence, for clarity, they are not drawn in figs. 15 and 16 but their locations are indicated in fig. 17.

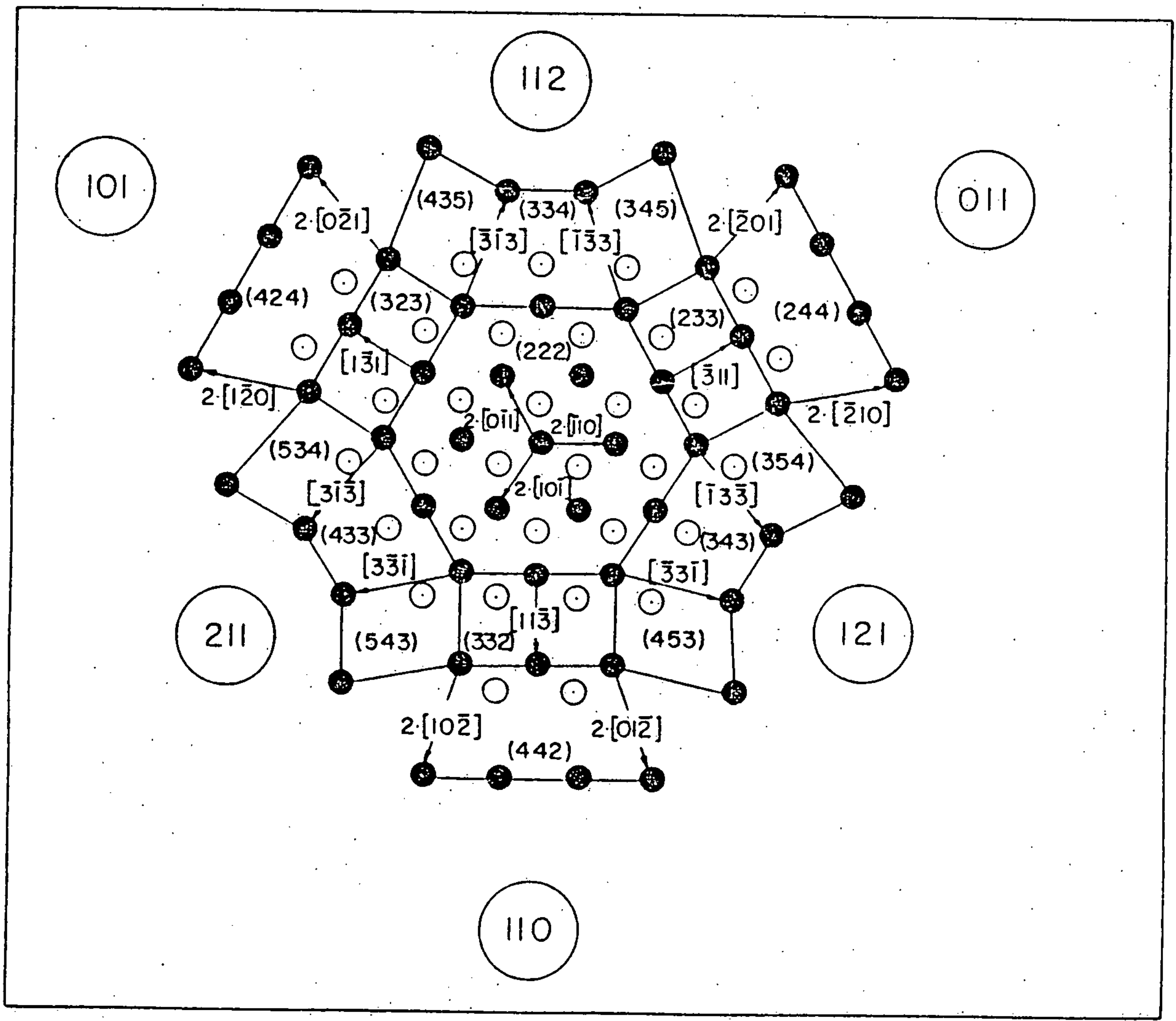

Figure 15: A schematic diagram showing the arrangement of atoms of various planes in and around the (222) pole. The solid black circles indicate the atoms in the zeroth layer and the open circles indicate the atoms in the first layer.

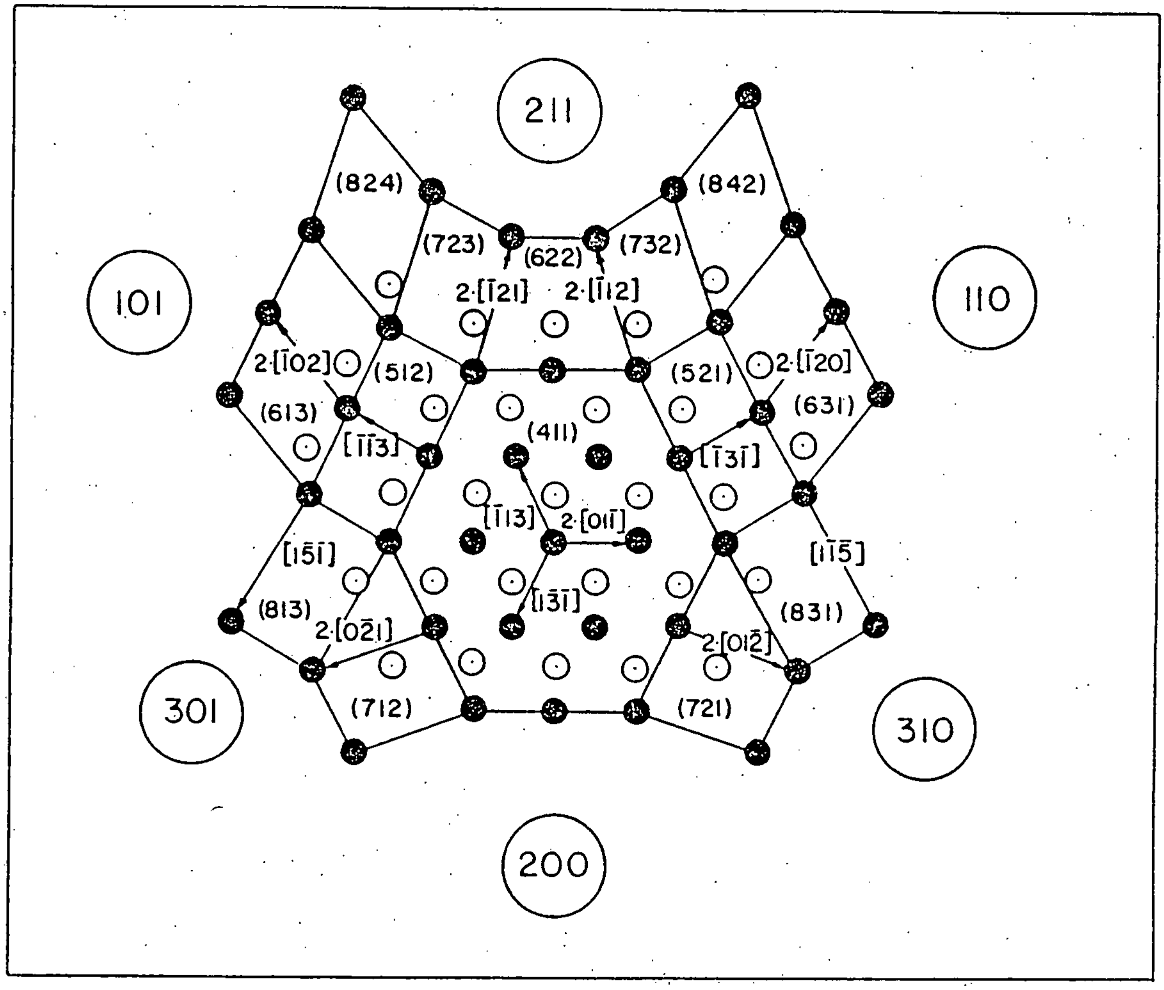

Figure 16: A schematic diagram showing the arrangement of atoms of various planes in and around the (411) pole. The solid black circles indicate the atoms in the zeroth layer and the open circles indicate the atoms in the first layer.

given in detail in Appendix B. Figure 17 is an FIM micrograph showing the location of each plane in the regions of the (222) and (411) poles.

V.4. Atomic Mapping Procedures

V.4.1. Calculation of the Coordinates of a VLS within a Depleted Zone

The construction of a depleted zone in three dimensions from two-dimensional FIM micrographs in a very time consuming and tedious process and one which is also prone to error; thus a procedure which allowed the computer to do most of the detailed computational work was found to be necessary. In the procedure that we now employ the position of each VLS was specified by a set of integers (p, u, v, Z) using a local coordinate system which is only characteristic of each layer of each {h k l} plane. The integer p was the identification number of the {h k l} plane in which a VLS was detected and (u, v, Z) were the local coordinates of this VLS. Computations which transformed the local coordinates (u, v, Z) of each VLS to the cubic coordinates (x', y', z') in a common cubic coordinate system were carried out by the computer. Details regarding the atomic mapping procedure and the BASIC program of the computations are given in Appendix C.

V.4.2. Calculation of the Coordinates of an SIA or a Depleted Zone within an FIM Specimen

The atomic mapping procedure and the computations given

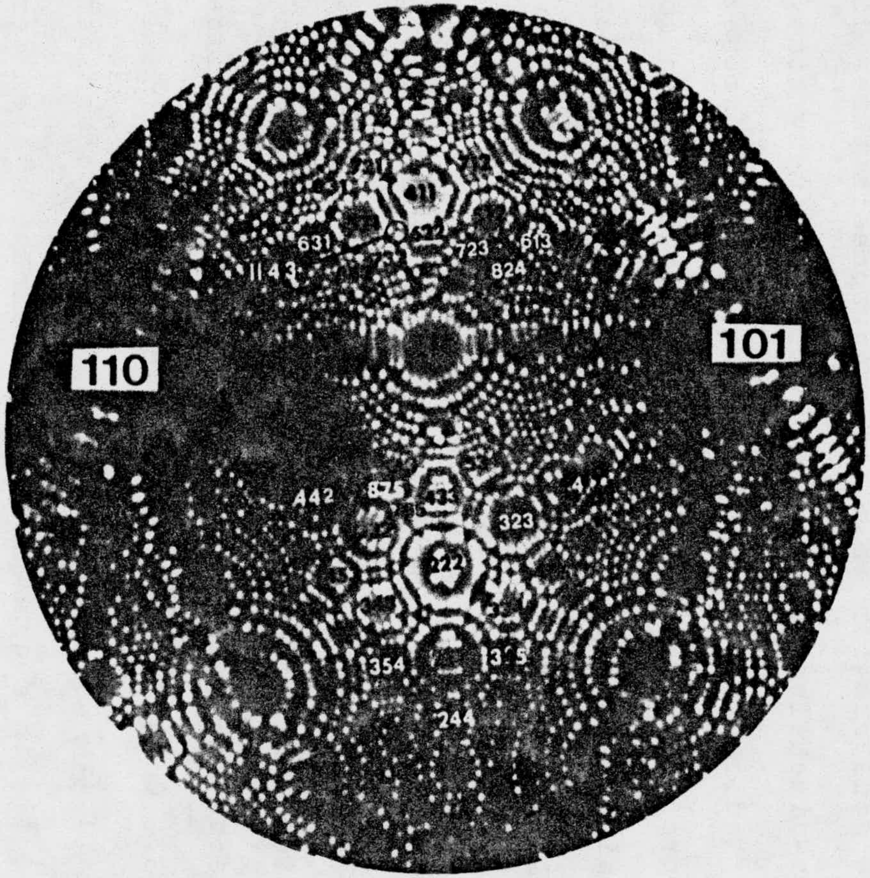

Figure 17: An FIM micrograph showing the location of planes in the regions of the (222) and (411) planes.

in Appendix C was used to obtain only the coordinates of VLSs (or SIAs) within a depleted zone which was located completely within a pole and its surrounding planes. The SIAs were found normally to locate in or around a pole different from which a depleted zone was located; for example, the depleted zone was found to be located in the (222), (332) and (433) planes around the (222) pole whereas the SIAs were found in the (411) and (521) planes around the (411) pole (see also fig. 17). The Correlation between the local coordinate system of the (411) plane and that of the (222) plane is normally impracticable as the atomic structure of the (211) plane can not be fully resolved. Thus, a procedure (see Appendix F) was developed for the construction of the positions of the SIAs as well as depleted zones* in an FIM tip specimen. In this procedure the position of an SIA (or a depleted zone) was specified by a set of integers (h_4, k_4, l_4, n) which was decoded so that the SIA (or the depleted zone) was located in the n^{th} layer of the $(h_4\ k_4\ l_4)$ plane measured from the initial surface of the specimen. The cubic coordinates (x, y, z) of the SIA (or the depleted zone) were then computed from this set of integers (h_4, k_4, l_4, n). Mathematical details and the BASIC program of the computations are given in Appendix F.

---

* It is noted that in this procedure we disregarded the detailed point-defect structure of a depleted zone and emphasized only the position of the center of the depleted zone relative to the positions of the SIAs.

V.5. Results

V.5.1. Pure Tungsten Control-Specimens

Control experiments were performed on unirradiated pure tungsten specimens to search for possible artifact VLSs and SIAs. The term artifact VLS or SIA implies the presence of an VLS or an SIA which was not the result of an irradiation. An VLS appears as a dark spot at the position of an atomic site. An SIA could produce a contrast pattern(49) consisting of: (a) a bright spot; (b) an extra bright-spot; and (c) a vacant lattice site (see also figs. 45 and 46).

The criteria which were employed for counting both atomic and vacant lattice sites are as follows:

(1) For smaller net planes (<20 atoms), we counted both atomic and vacant lattice sites within the first ring (see fig. 18) immediately after the last atomic site of the preceding plane was field-evaporated.

(2) For larger net planes (≥20 atoms), we counted both atomic and vacant lattice sites within the first ring when the first two outer rings of atoms became visible even though several atomic sites of the preceding plane still remained near the center.

Figure 18 shows a schematic diagram of an {h k l} net plane. The solid black-dots represent atomic sites and the open circles represent VLSs. The first ring was taken to be the solid line and only sites within the solid line were counted. In fig. 18, for example, there are two VLSs as

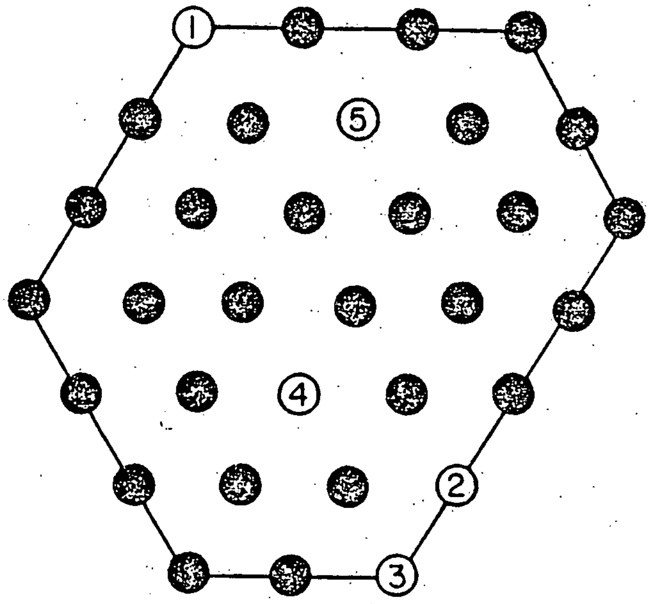

Figure 18: A schematic diagram of an $\{h\ k\ l\}$ net plane. The solid black circles indicate normal lattice atoms and the open circles indicate vacant lattice sites. The first ring of this net plane was taken to be the solid line.

indicated by the numbers 4 and 5 and the total number of atomic sites are 16. The VLSs denoted by the numbers 1 to 3 on the first ring were most likely created as the result of an irregular evaporation sequence at the edge of the plane. This artifact VLS concentration of the first ring is high and it is difficult to measure, therefore the artifact VLS concentration reported in this section do not include the VLSs which appeared on the first ring of a net plane.

Five families of planes around the (222) pole (i.e., the {222}, {332}, {433}, {442}, and {543} planes) and eight families of planes around the (411) pole (i.e., the {411}, {521}, {622}, {631}, {721}, {732}, {831} and {842} planes) were examined by the pulse field-evaporation technique. In a total number of 10^5 atoms counted in the five families of planes in the (222) pole we found no evidence of artifact VLSs and SIAs; the artifact VLS and SIA concentrations for these planes must be $\leq 1\times10^{-5}$ at.fr. More extensive control experiments on pure tungsten by the pulsed field-evaporation experiment have been performed by Park;(96) he found that for the planes around the (222) pole the artifact VLS concentration was $\leq 1\times10^{-5}$ at.fr.*

---

* In a total number of $\sim 1\times10^6$ atomic sites counted in the two well-annealed pure tungsten specimen Park found only one β dark-spot contrast effect; a β dark spot is a single dark-spot that suddenly appears within a well-resolved net plane during observation and remains there until all the atoms of that plane are field evaporated. This β dark-spot contrast, however, was not counted as a VLS in this thesis work.

No artifact VLS and SIA concentration measurements have been reported for the planes around the (411) pole and therefore they were examined extensively in this thesis work. The total number of atoms and artifact VLSs counted for each plane are listed in Table 1. In most cases the artifact VLSs concentration was between $1\text{x}10^{-4}$ and $1\text{x}10^{-3}$ at.fr. with the exception of the {622} planes. The total number of atoms among which the VLSs within a depleted zone were detected was typically $(1 \text{ to } 2)\text{x}10^3$; therefore less than one or two artifact VLSs may be included in the VLS count of a depleted zone even if the artifact VLS concentration was of the order of $1\text{x}10^{-3}$ at.fr. The artifact VLS concentration in the {622} plane was high; therefore this plane was used to observe a depleted zone only when: (1) a void-like VLS cluster in this plane could be identified clearly; and/or (2) a VLS cluster found in this plane was clearly a part of the depleted zone in an adjacent plane. In addition, no contrast patterns of SIAs were found in a total number of $\sim 7\text{x}10^5$ atomic sites counted in these studies; the artifact SIA concentration around the (411) pole must be $\leq 1.4\text{x}10^{-6}$ at.fr.

V.5.2. Depleted Zones Detected in Pure Tungsten Irradiated with 30 keV W^+, Mo^+ or Cr^+ Ions

V.5.2.1. Definition of the Quantities λ_1, λ_2, $\bar{\lambda}$, c_v, $R(i)$ and $\bar{N}(i)$

Before we report on the results of depleted zones obser-

Table 1: Artifact VLS concentratios detected in different planes in and around the (411) pole of unirradiated pure tungsten specimens

Plane	Number of atomic sites counted	Number of artifact VLSs counted	Artifact VLS concentration (at.fr.)
{411}	68,582	24	3.5×10^{-4}
{521}	109,655	3	2.7×10^{-5}
{622}	41,815	337	8.0×10^{-3}
{631}	88,084	8	9.1×10^{-5}
{721}	71,143	42	5.9×10^{-4}
{732}	62,497	120	1.9×10^{-3}
{831}	104,074	8	7.9×10^{-5}
{842}	108,793	171	1.6×10^{-3}

ved in pure tungsten irradiated with 30 keV W^+, Mo^+ or Cr^+ ions the quantities λ_1, λ_2, $\bar{\lambda}$, c_v, R(i) and $\bar{N}$(i) associated with the quantitative description of the depleted zones are described below.

(1) To first order the shape of a depleted zone was approximated by an ellipsoid*; the diameter parallel to the major axis was denoted by $\lambda_1$and the diameter parallel to the minor axis was called by λ_2. The computing procedure used to obtain the values of λ_1 and λ_2 for a depleted zone was as follows:

(1a) We determined the VLS distribution curves along the thirteen close-packed directions (i.e., the [100], [010], [001], [110], $[\bar{1}10]$, [011], $[0\bar{1}1]$, [101], $[\bar{1}01]$, [111], $[\bar{1}11]$, $[1\bar{1}1]$ and $[11\bar{1}]$ directions).

(1b) The standard deviation σ was calculated for each VLS distribution curve.

(1c) The largest value among the σs was denoted by σ_1. The quantity λ_1 was then given by $3\sigma_1$. The direction along which this λ_1 was measured was taken as the major axis of the ellipsoid.

(1d) The average of the σs measured along the directions which were perpendicular to the axis of the ellipsoid was denoted by σ_2. For example, if the axis of the ellipsoid determined in (1c) was the [011] direction, the

---

* This approximation was made so that we could calculate some geometrical properties of each depleted zone.

value of σ_2 was given by the average of the σs measured along the [100], $[0\bar{1}1]$ and $[1\bar{1}1]$ directions. The quantity λ_2 was then given by $3\sigma_2$.

(1e) The effective diameter $\bar{\lambda}$ of a depleted zone was given by $(\lambda_1\lambda_2^2)^{1/3}$. It is noted that the volume of a depleted zone thus defined contains ~87% of the total number of VLSs within the depleted zone if the VLS distribution curves are Gaussian or ~100% if the VLSs are uniformly distributed within the depleted zone.

(2) The standard procedure for estimating the average VLS concentration (c_v) within a depleted zone involved dividing the depleted zone into a series of rectangular slabs; each slab consisted of four successive (001) planes. The borders of each slab were determined by the four outermost VLSs in the four (001) planes. The VLS concentration was then calculated by dividing the total number of VLSs within the depleted zone by the total number of atomic sites contained in all the slabs. This procedure was repeated for the (100) and (010) planes. The VLS concentration of the depleted zone was obtained by averaging the three values of c_v described above.

(3) The radial distribution function R(i) was defined as the average number of VLSs at the i^{th} nearest-neighbor distance measured from any VLS. In fig. 19 the open circles represent VLSs within a depleted zone. The concentric circles were drawn around a j^{th} VLS. The radius of the i^{th}

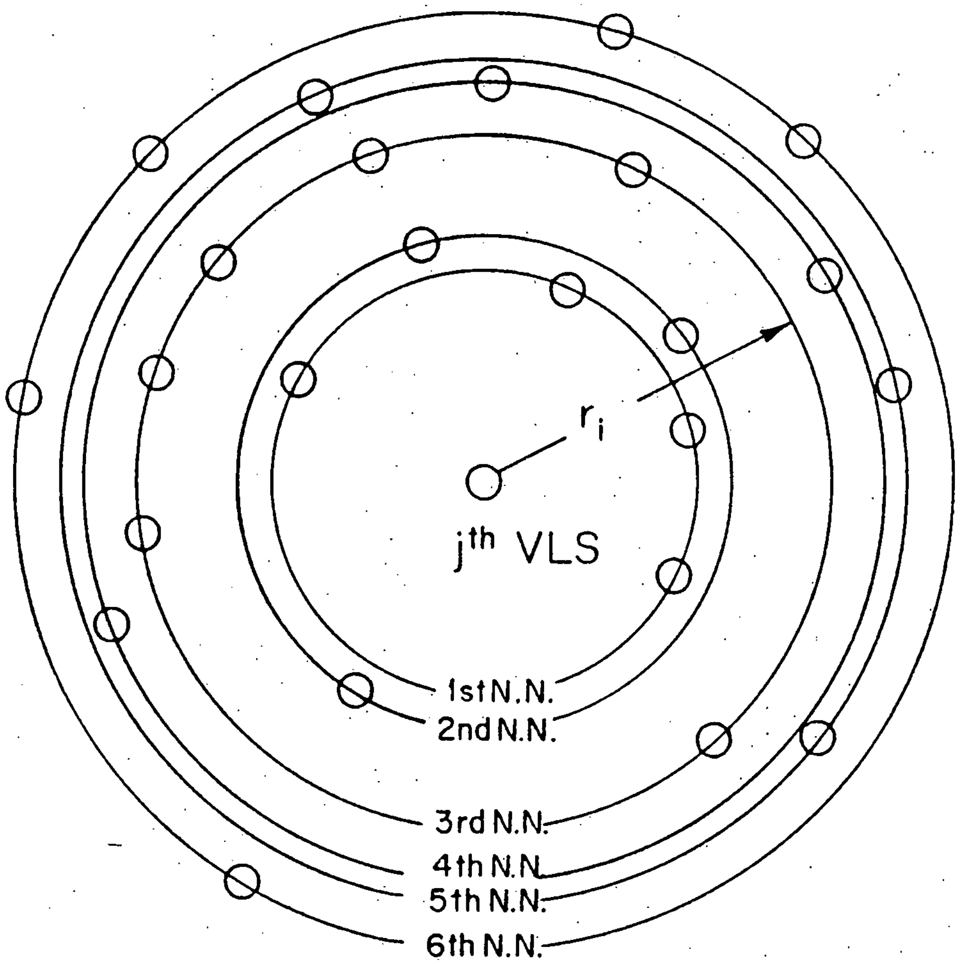

Figure 19: A schematic diagram showing the calculation of the radial distribution function R(i). The open circles represent vacant lattice sites. The radius of the i^{th} concentric circle (r_i) is equal to the i^{th} nearest-neighbor distance.

sphere (r_i) is equal to the i^{th} nearest-neighbor distance. The number of VLSs at r_i measured from the j^{th} VLS were counted and denoted by A(i,j). The quantity R(i) was then given by

$$R(i) = \frac{1}{N_t} \sum_{j=1}^{N_t} A(i,j), \qquad (7)$$

where N_t is the total number of VLSs within the depleted zone. The ratio of R(i)/Z(i) is therefore the probability of finding a VLS at the i^{th} nearest-neighbor distance. The quantity Z(i) is the coordination number at the i^{th} nearest-neighbor distance in an infinite crystal. In the limiting case that the VLSs are randomly distributed in an infinite crystal, the values of R(i)/Z(i) approach zero. Since the VLSs within a depleted zone are highly localized, only positive, none-zero R(i)/Z(i)s are expected. The values of R(i)/Z(i) were taken as ameasure of the degree of clustering for the VLSs within a depleted zone. The large values of the R(i)/Z(i)s indicate the high compactness of a depleted zone. In Practice, the values of R(i)/Z(i) were calculated out to the ninth nearest-neighbor distance.

(4) In order to display the distribution of VLSs within a depleted zone in another way a quantity $\bar{N}(i)$ was defined as the average number of VLSs in the i^{th} spherical shell around an VLS; this i^{th} shell was enclosed between the spheres of radii r_{i-1} and r_i. In fig. 20 the open circles represent VLSs within a depleted zone. Concentric

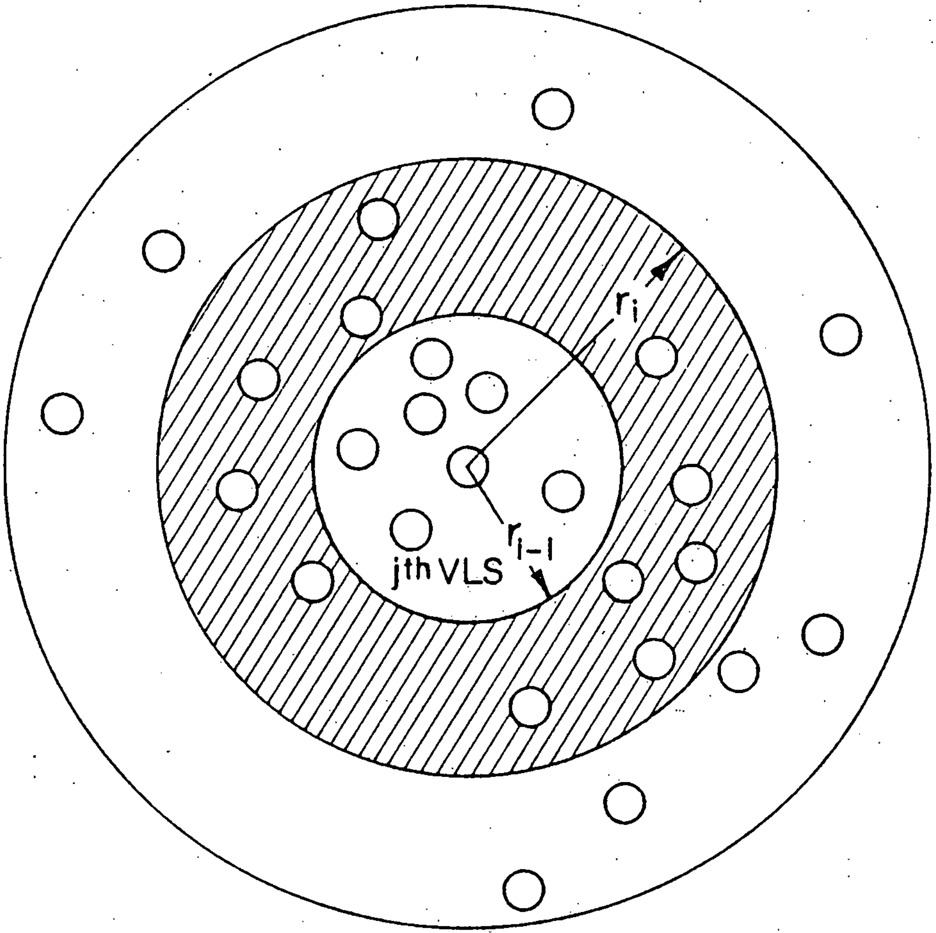

Figure 20: A schematic diagram showing the calculation of the quantity $\overline{N}(i)$. The open circles represent vacant lattice sites. The shadowed annular ring indicates the i^{th} shell.

circles representing concentric sphere are drawn from a j^{th} VLS. The number of VLSs within the i^{th} shadowed annular ring is denoted by B(i,j). The quantity $\bar{N}(i)$ was then given by

$$\bar{N}(i) = \frac{1}{N_t} \sum_{j=1}^{N_t} B(i,j). \qquad (9)$$

In practice, the thickness of each shell was made to equal to a_o.

The interpretation of the function $\bar{N}(i)$ is explained in fig. 21. Figure 21a shows $\bar{N}(i)$ for a cluster of 108 VLSs contained in a bcc volume of $4a_o x 4a_o x 4a_o$*; this cluster gives rise to only <u>one</u> peak at $3a_o$. Figure 21b shows $\bar{N}(i)$ for two clusters of 54 VLSs contained respectively in two bcc volumes of $3a_o x 3a_o x 3a_o$* separated by a distance of $10a_o$; these two clusters gave rise to a <u>second</u> peak at $12a_o$ at the expense of the first peak at $3a_o$. The separation between the first and the second peak was equal to the separation of the two clusters. Figure 21c shows $\bar{N}(i)$ for seven clusters of 16 VLSs contained respectively in seven bcc volumes of $2a_o x 2a_o x 2a_o$* separated by distances of 10, 15 or $20a_o$; these clusters result in a third broad peak between 15 and $27a_o$ at the expense of the first peak at $2a_o$ and the second peak at $12a_o$.

It was therefore clear that a depleted zone may contain only <u>one</u> jumbo cluster if $\bar{N}(i)$ showed only <u>one</u> peak at $\sim 3a_o$;

---

* The VLSs in this volume (or volumes) were close-packed.

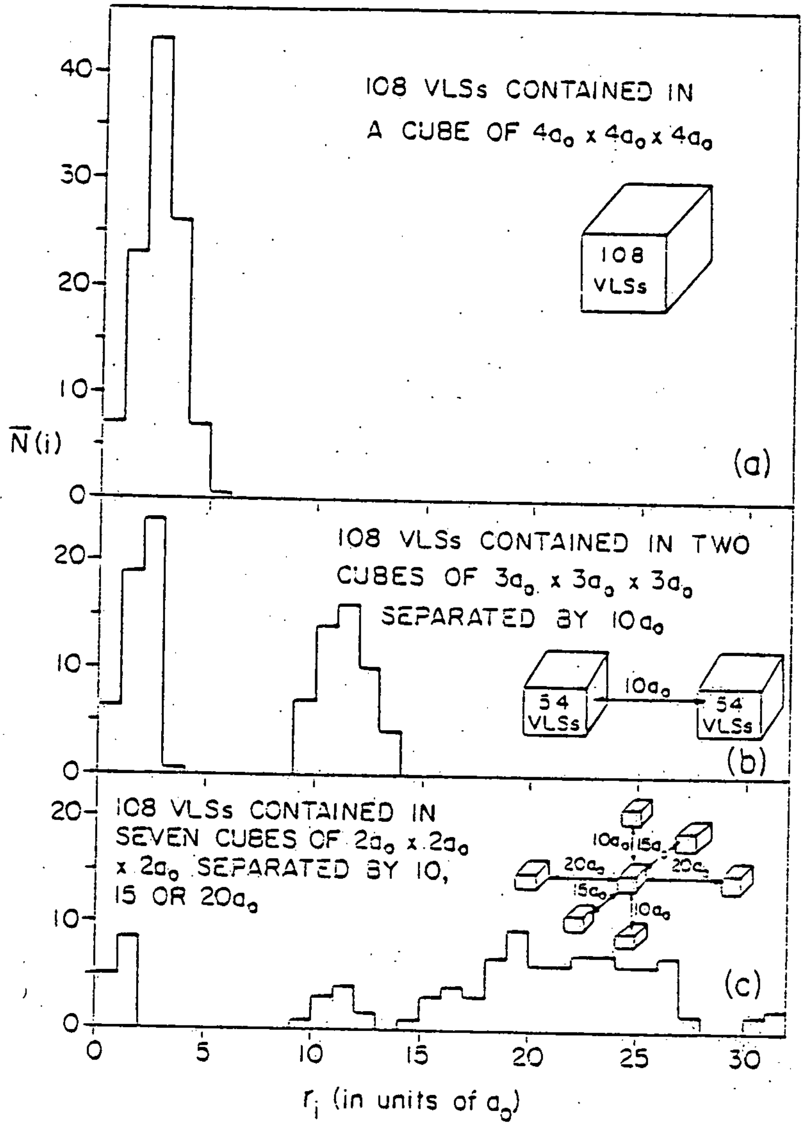

Figure 21: (a) This shows the values of the $\overline{N}(i)$s for a vacancy cluster; the cluster gives rise to one peak at $\sim 3a_o$.

(b) This shows the values of the $\overline{N}(i)$s for two vacancy clusters separated by $10a_o$; the two clusters give rise two peaks at $\sim 3a_o$ and 12 a_o respectively.

(c) This shows the vlues of the $\overline{N}(i)$s for seven vacancy clusters; these clusters give rise to an additional broad peak at $\sim 15a_o$. The quantity a_o is the lattice parameter of a standard non-primitive unit cell.

a depleted zone may have contained two jumbo clusters separated by a distance ε if $\bar{N}(i)$ showed a first peak at $\sim 3a_o$ and a second peak at $\sim(3+\varepsilon)a_o$; and a depleted zone may have contained more than two clusters if $\bar{N}(i)$ showed a very broad peak extended to a distance $>>3a_o$.

V.5.2.2. Depleted Zones in Pure Tungsten Produced by a Single 30 keV W^+ Ion

In three out of seven pure tungsten specimens irradiated with 30 keV W^+ ions we found five depleted zones out of eight isolated ones which were capable of being atomically mapped. They were denoted by DZ1a to DZ1c, DZ2a to DZ2c and DZ3a to DZ3b. Depleted zones DZ1a to DZ1c were found in a first specimen which had an average tip radius of ∿200 A; depleted zones DZ2a to DZ2c were detected in a second specimen which had an average tip radius of ∿160 A; and depleted zones DZ3a and DZ3b were found in a third specimen of an average tip radius of ∿240 A. All the three specimens had a [211] orientation. Figures 22a, 22c and 22e exhibit respectively three partial 211 standard stereographic projections which show the top view of each specimen. The plane (or planes) in which a depleted zone was detected is indicated; for example, in fig. 22c DZ1a was found within the (521) plane of the first specimen. The crosssectional sideviews of the tip specimen are shown in figs 22b, 22d and 22f. The separations between any two depleted zones are indicated by the letters a, b, c etc.; they ranged from 50 to 140 A.

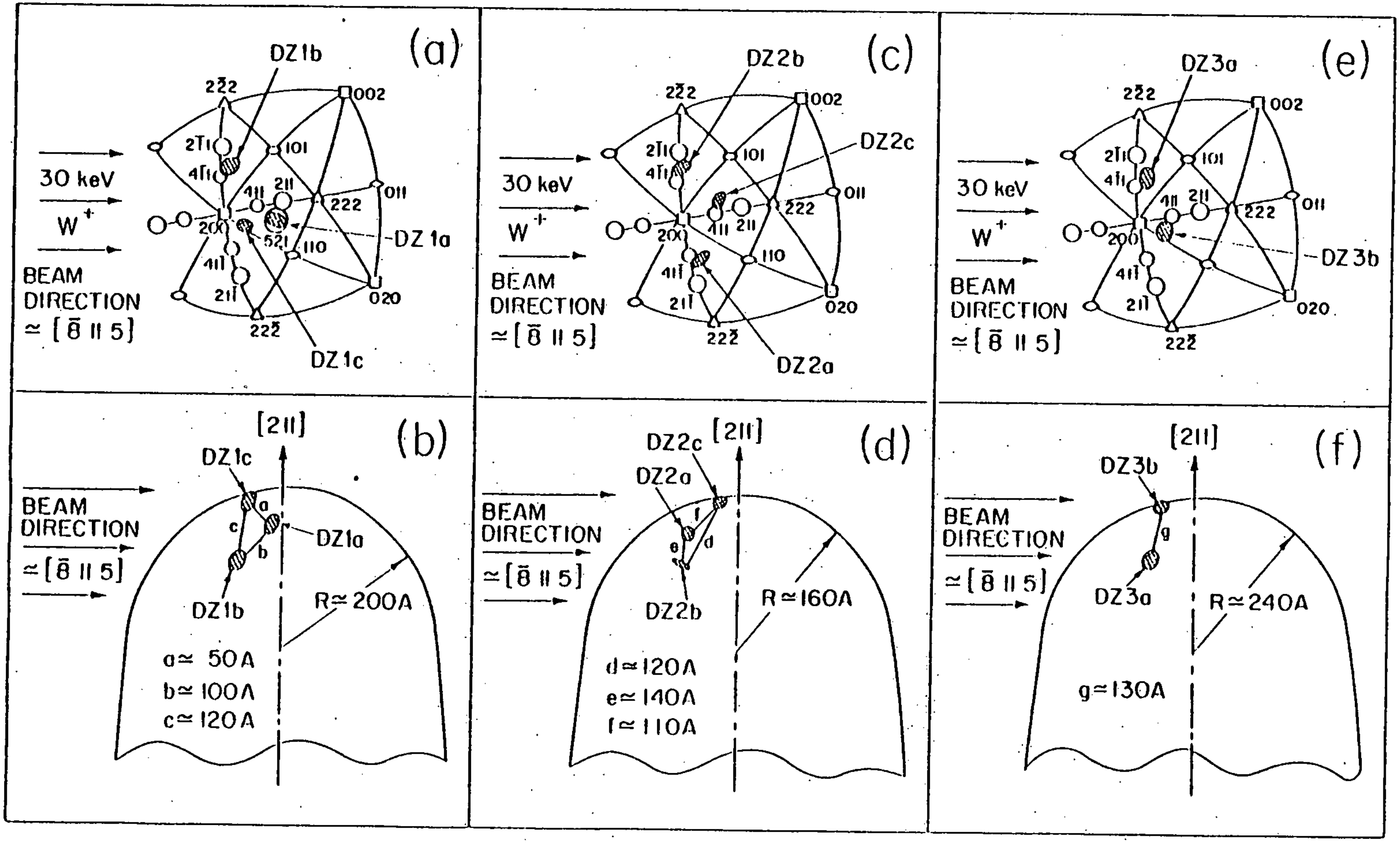

Figure 22: Three partial 211 stereographic projections in figs. 22a, 22c and 22e showing the location of depleted zones DZ1a to DZ3b. Figures 22b, 22d and 22f show three schematic cross-sectional views of the three FIM tip specimens which contain depleted zones DZ1a to DZ3b.

As an illustrative example of the contrast of a depleted zone produced by a single 30 keV W^+ ion fig. 23 shows a series of ten FIM micrographs of ten successive (521) planes; they were chosen from a total of 1.4×10^3 frames of 35 mm ciné film which were recorded and analyzed in the reconstruction of depleted zone DZ1a. The (521) and the surrounding planes are indexed in frame 1; the frame number of the ciné film is located in the lower right-hand corner below each micrograph and the layer number is preceeded by the letter n (e.g., n=1) in the upper left-hand corner above each micrograph. Frame 1 shows an atomically perfect plane in layer 1; the other frames exhibit (521) planes containing VLSs. The position of each atom in the (521) plane is indicated schematically below each micrograph by a solid black circle and a VLS is indicated by an open circle. Because of the small size of the (521) plane we have been forced to include ledge atoms in analyzing this depleted zone; a missing atom in the ledge was only counted as a VLS if <u>no</u> atom was detected in this site during the entire atom-by-atom dissection process of this plane.

Other detailed information obtained for each depleted zone is listed in Table 2 and is now described.

(1) Depleted zone DZ1a was found in the (521) plane of the first specimen. This depleted zone was ∿85 A from the irradiated surface. Figure 24 exhibits a computer-generated isometric drawing of the VLSs within DZ1a. The open circles represent the VLSs and the length of the connecting bonds

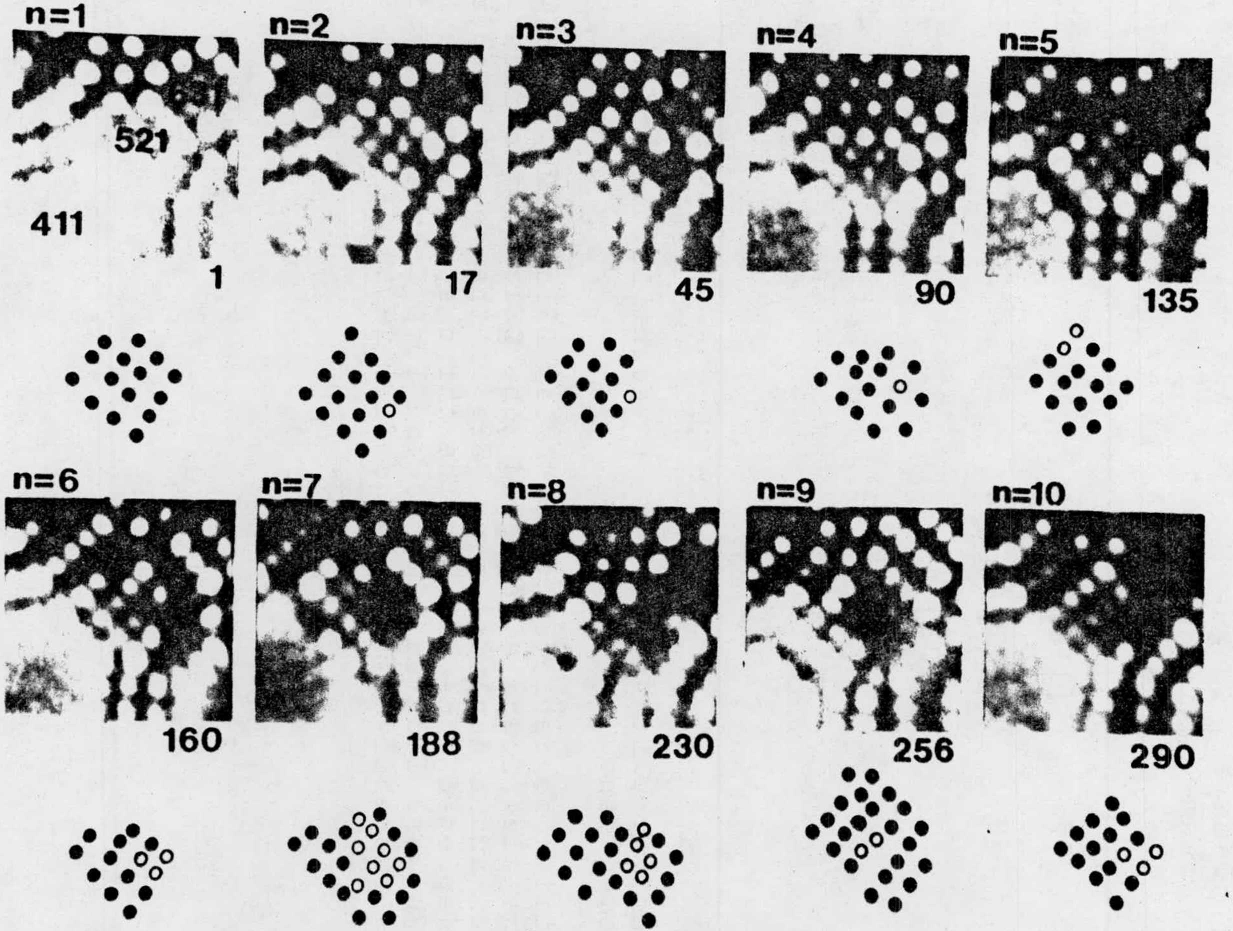

Figure 23: A series of ten FIM micrographs out of 290 recorded during the atom-by-atom dissection of depleted zone DZ1a. The solid black circles indicate normal lattice atoms and the open circles indicate vacant lattice sites.

Table 2: Data for depleted zones in pure tungsten produced by 30 keV W^+ ions

Depleted† zone No.	Damage range (A)	longation direction	λ_1 (A)	λ_2 (A)	$\bar{\lambda}$ (A)	ν*	c_v (at.%)
DZ1a	85	[110]	24	14	17	159	27
DZ1b	50	[111]	24	14	17	121	18
DZ2a	40	$[10\bar{1}]$	32	21	24	141	13
DZ2b	35	[001]	23	11	14	133	26
DZ3a	45	$[\bar{1}01]$	26	17	20	235	17

* The quantity ν is the number of vacant lattice sites within a depleted zone.

† In addition to depleted zones DZ1a, DZ1b, DZ2a, DZ2b and DZ3a, we also found a depleted zone DZ1c in the first specimen and a depleted zone DZ2c in the second specimen and a depleted zone DZ3b in the third specimen; DZ1c, DZ2c and DZ3b were located ∿20, 10 and 10 A from the irradiated surface respectively (see also fig. 22).

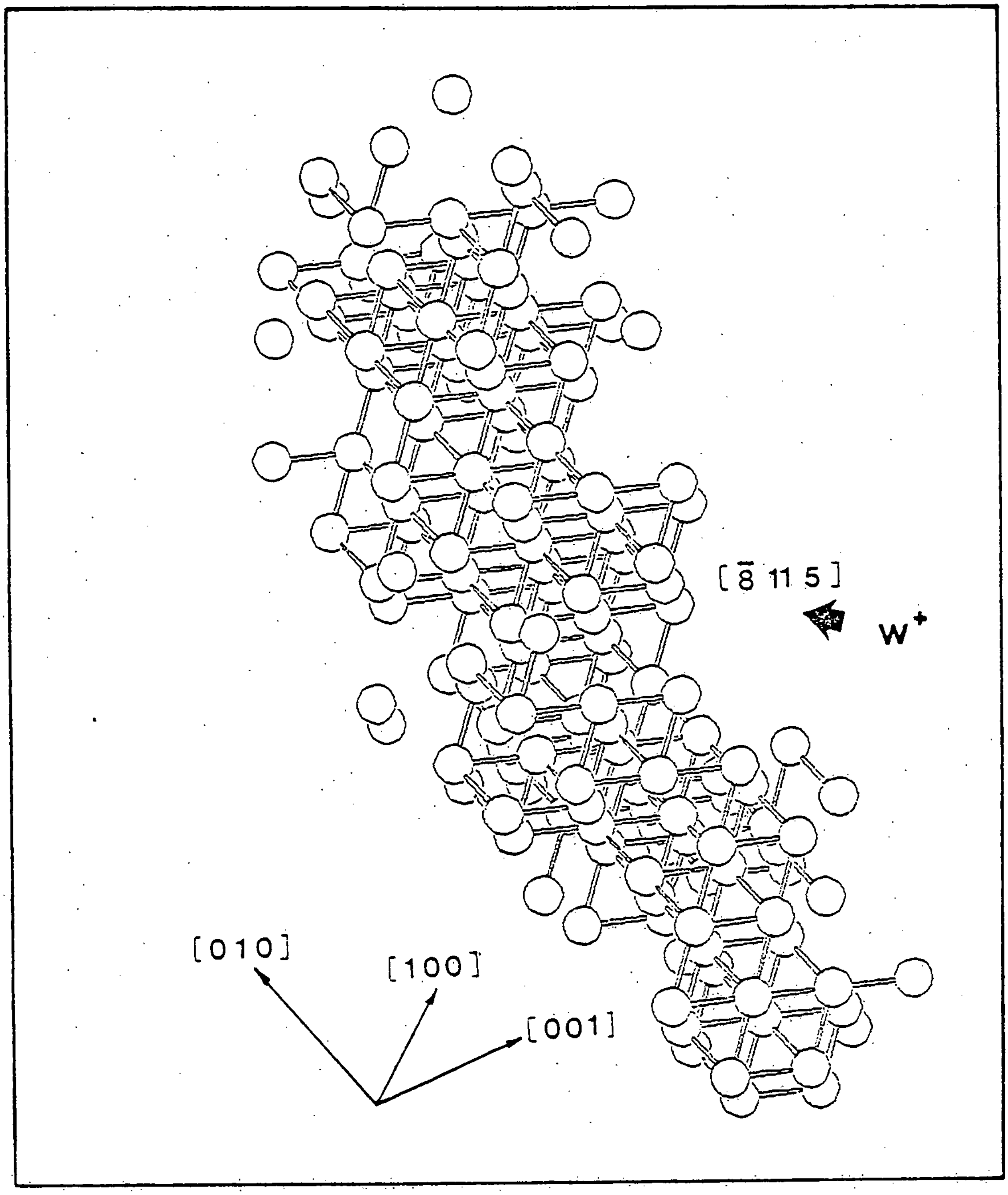

Figure 24: A computer-generated isometric drawing of depleted zone DZ1a. Each open circle represents a vacant lattice site and the bond length connecting any two vacant lattice sites is equal to the first nearest-neighbor distance ($a_o/\sqrt{2}$).

between VLSs is equal to the first nearest-neighbor distance ($a_o\sqrt{3}/2$) in the bcc lattice. The direction of the incident ion-beam is also indicated. DZ1a was found to consist of 159 VLSs. As already mentioned DZ1a was approximated by an ellipsoid ; the diameter λ_1 measured along the major axis was 24 A and the diameter λ_2 measured along the minor axis was 14 A. The major axis of this ellipsoid which indicates the elongation direction of DZ1a is also listed in Table 2. It is noted that this depleted zone was elongated along the [110] direction. The effective diameter $\bar{\lambda}$ of this depleted zone is 17 A. The VLS concentration associated with DZ1a is ∿27 at.%. The results of R(i)/Z(i) were calculated out to the ninth nearest-neighbor distance; the results are shown in fig. 25a. It is clear that the VLSs within DZ1a form clusters. The values of the $\bar{N}(i)$s for DZ1a were also calculated and are plotted in fig. 26a; this figure shows that DZ1a contained only one jumbo cluster. In addition, if only first nearest-neighbor VLSs are considered then the distribution of cluster sizes* was as follows: (1) four mono-VLSs; (2) one di-VLS; and (3) one jumbo cluster containing 153 VLSs.

(2) Depleted zone DZ1b was found in the $(4\bar{1}1)$ and $(5\bar{1}2)$ planes of the first specimen. This depleted zone was ∿50 A from the irradiated surface. Figure 27 exhibits a computer-

---

* The distribution of cluster sizes was computed with the aid of a computer (see also Appendix D).

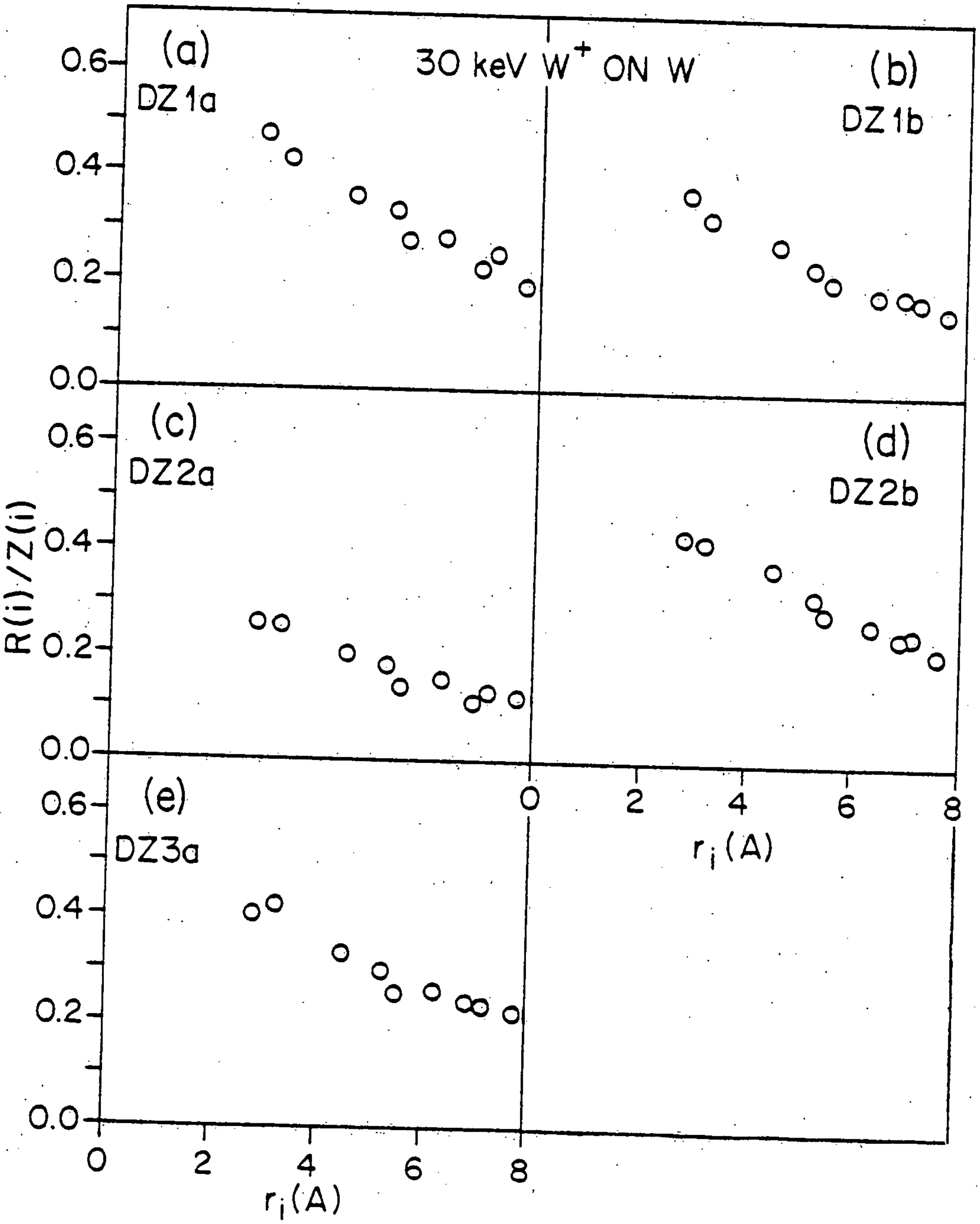

Figure 25: The normalized radial distribution function [R(i)/Z(i)] for depleted zones DZ1a, DZ1b, DZ2a, DZ2b and DZ3a.

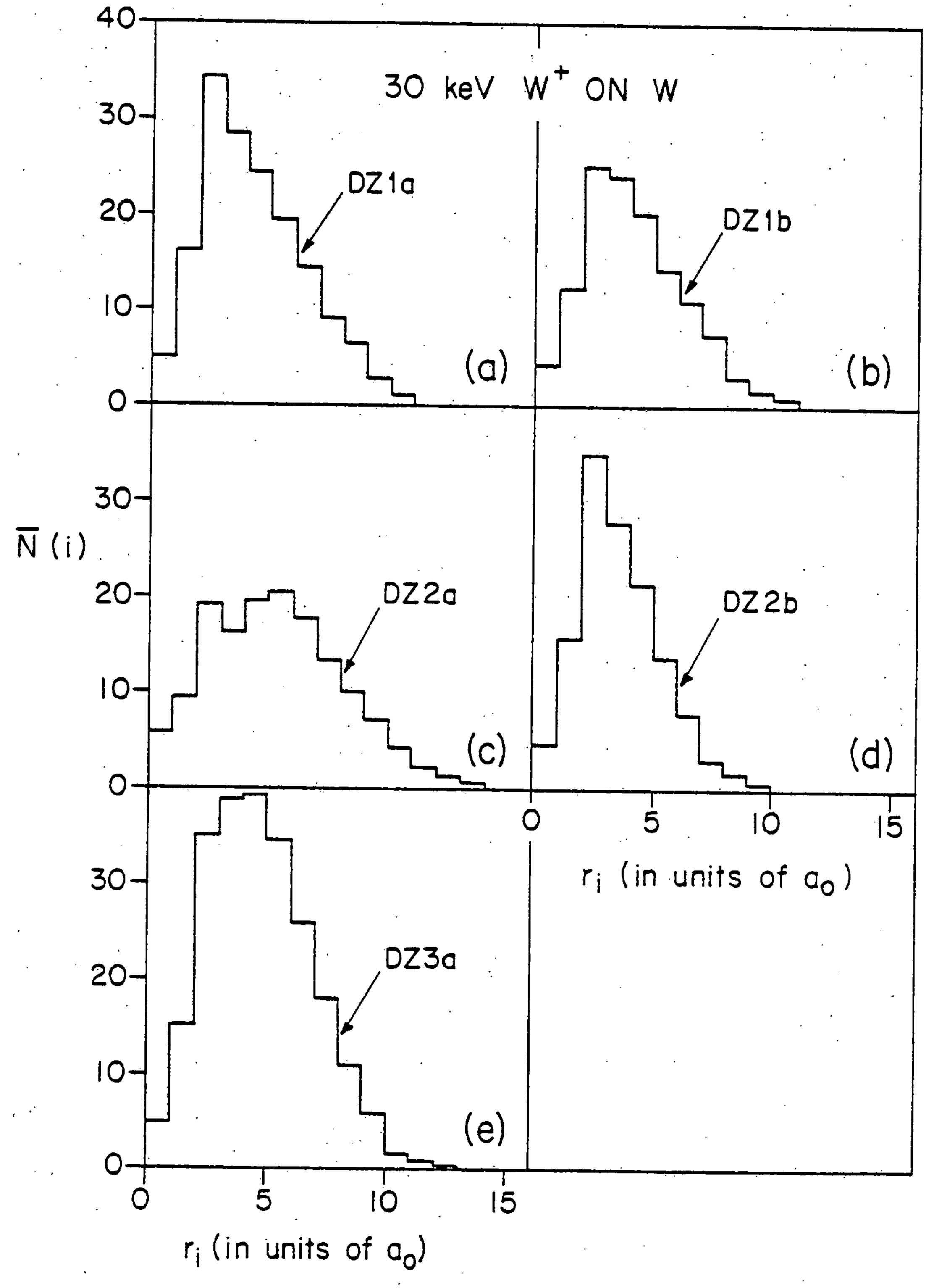

Figure 26: The spectra of the $\overline{N}(i)$s for depleted zones DZ1a, DZ1b, DZ2a, DZ2b and DZ3a.

generated isometric drawing of the VLSs within DZ1b. This depleted zone was found to consist of 121 VLSs. The measured values of λ_1 and λ_2 are 24 and 14 A respectively. This depleted zone was found to be elongated along the [111] direction. The effective diameter $\bar{\lambda}$ of DZ1b is 17 A. The VLS concentration associated with DZ1b was ∿18 at.%. The results of the R(i)/Z(i) are shown in fig. 25b; it is clear that the VLSs within this depleted zone form clusters. The values of the $\bar{N}$(i)s for this depleted zone were also calculated and are plotted in fig. 26b; this figure shows that DZ1b contains only one jumbo VLS cluster. In addition, if only first nearest-neighbor VLSs are considered then the distribution of cluster sizes was as follows: (1) 14 mono-VLSs; (2) one di-VLS; (3) one quadri-VLS; and (4) three jumbo clusters containing 7, 24 and 69 VLSs respectively. The fact that fig. 25b exhibits only one peak at ∿3a_o implies that these clusters must not be well separated.

(3) Depleted zone DZ2a was found in the $(62\bar{2})$, $(52\bar{1})$ and $(73\bar{2})$ planes of the second specimen. This depleted zone was ∿40 A from the irradiated surface. Figure 28 exhibits a computer-generated isometric drawing of the VLSs within DZ2a. DZ2a was found to consist of 141 VLSs. The measured values of λ_1 and λ_2 were 32 and 21 A respectively. This depleted zone was found to be elongated along the $[10\bar{1}]$ direction. The effective diameter $\bar{\lambda}$ of DZ2a is 24 A. The VLS concentration associated with this depleted zone was ∿13 at.%.

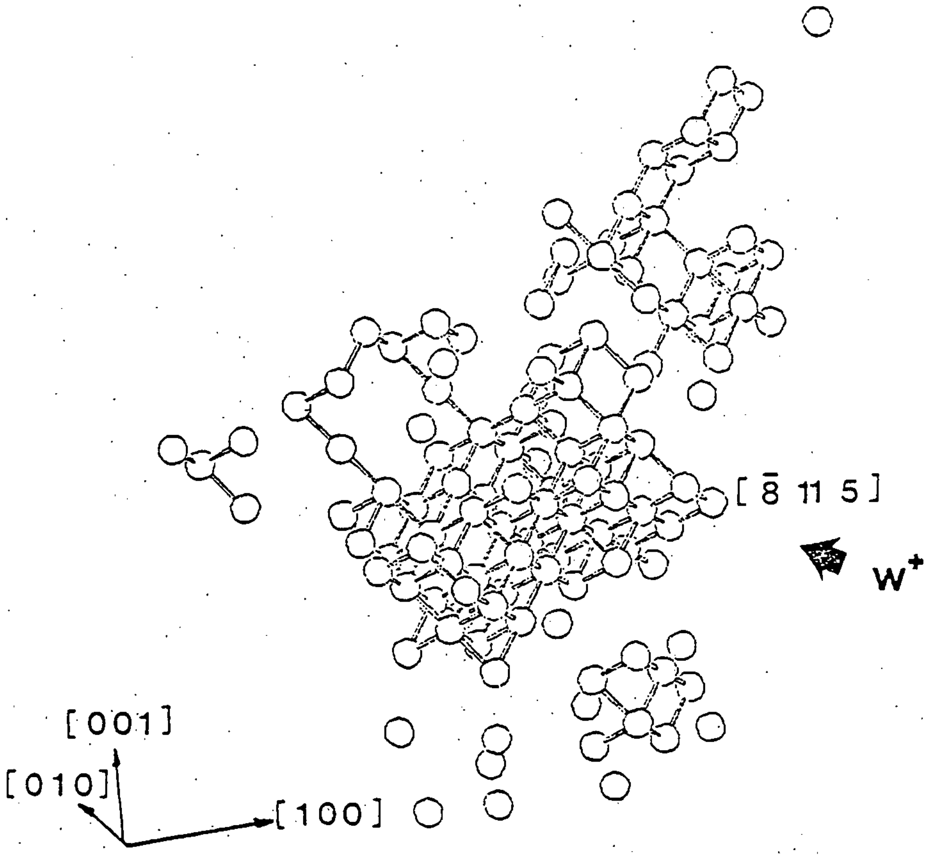

Figure 27: A computer-generated isometric drawing for depleted zone DZ1b.

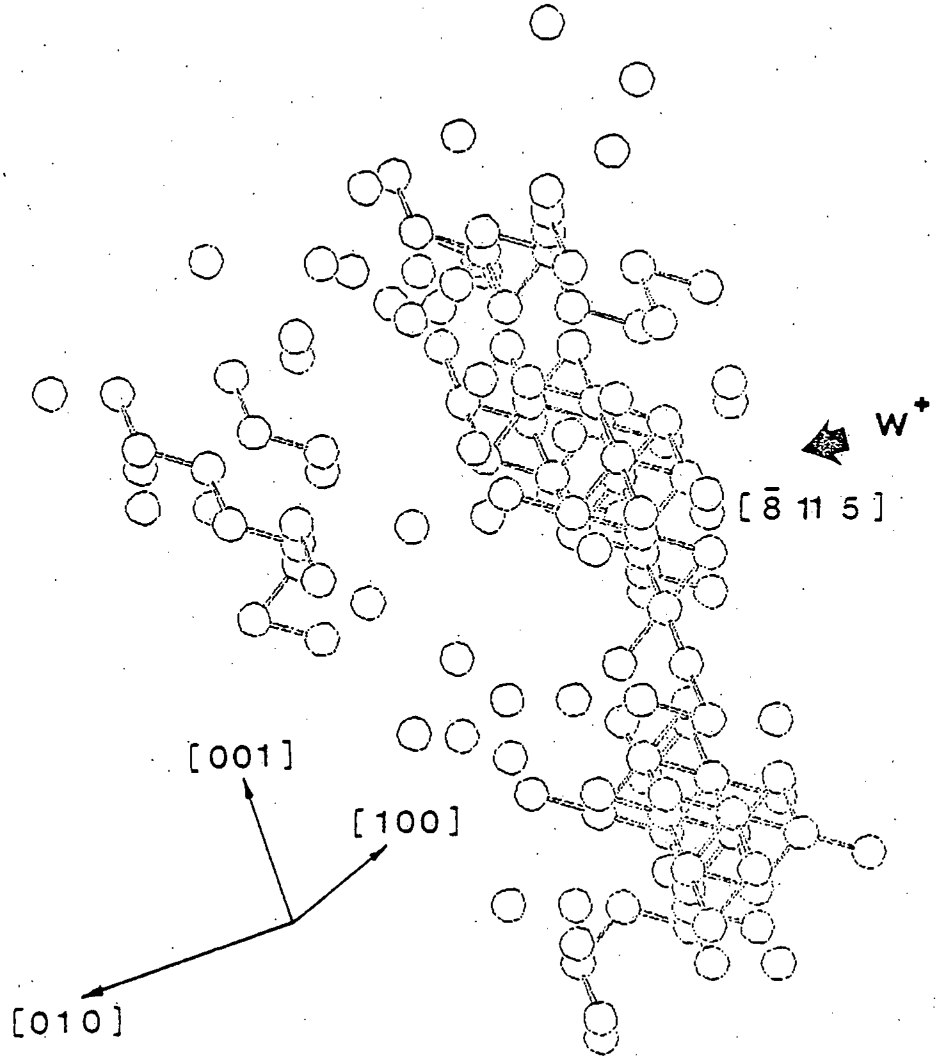

Figure 28: A computer-generated isometric drawing for depleted zone DZ2a.

The results of the R(i)/Z(i) are shown in fig. 25c; it is clear that the VLSs within DZ2a form clusters. The values of the $\bar{N}(i)$s for DZ2a were also calculated and are plotted in fig. 26c; this figure shows that DZ2a contained two or more jumbo VLS clusters. If only first nearest-neighbor VLSs were considered then the distribution of cluster sizes was as follows: (1) 34 mono-VLSs; (2) three di-VLSs; (3) one tri-VLS; (4) four jumbo clusters respectively containing 11, 15, 33 and 35 VLSs.

(4) Depleted zone DZ2b was found in the $(6\bar{2}2)$ and $(7\bar{2}3)$ planes of the second specimen. This depleted zone was ∿35 A from the irradiated surface. Figure 29 exhibits a computer-generated isometric drawing of the VLSs within DZ2b. DZ2b was found to consist of 133 VLSs. The measured values of λ_1 and λ_2 were 23 and 11 A respectively. It is noted that this depleted zone was elongated along the [001] direction. The effective diameter $\bar{\lambda}$ was found to be 14 A. The VLS concentration associated with this depleted zone was ∿26 at.%. The results of the R(i)/Z(i) measurements are shown in fig. 25d; it is clear that the VLSs within DZ2b formed clusters. The values of the $\bar{N}(i)$s for DZ2b were also calculated and are plotted in fig. 26d; this figure shows that DZ2b contains only one jumbo VLS cluster. If only first nearest-neighbor VLSs were considered then the distribution of cluster sizes was as follows: (1) eleven mono-VLSs; (2) one di-VLSs; and (3) one jumbo cluster containing 120 VLSs.

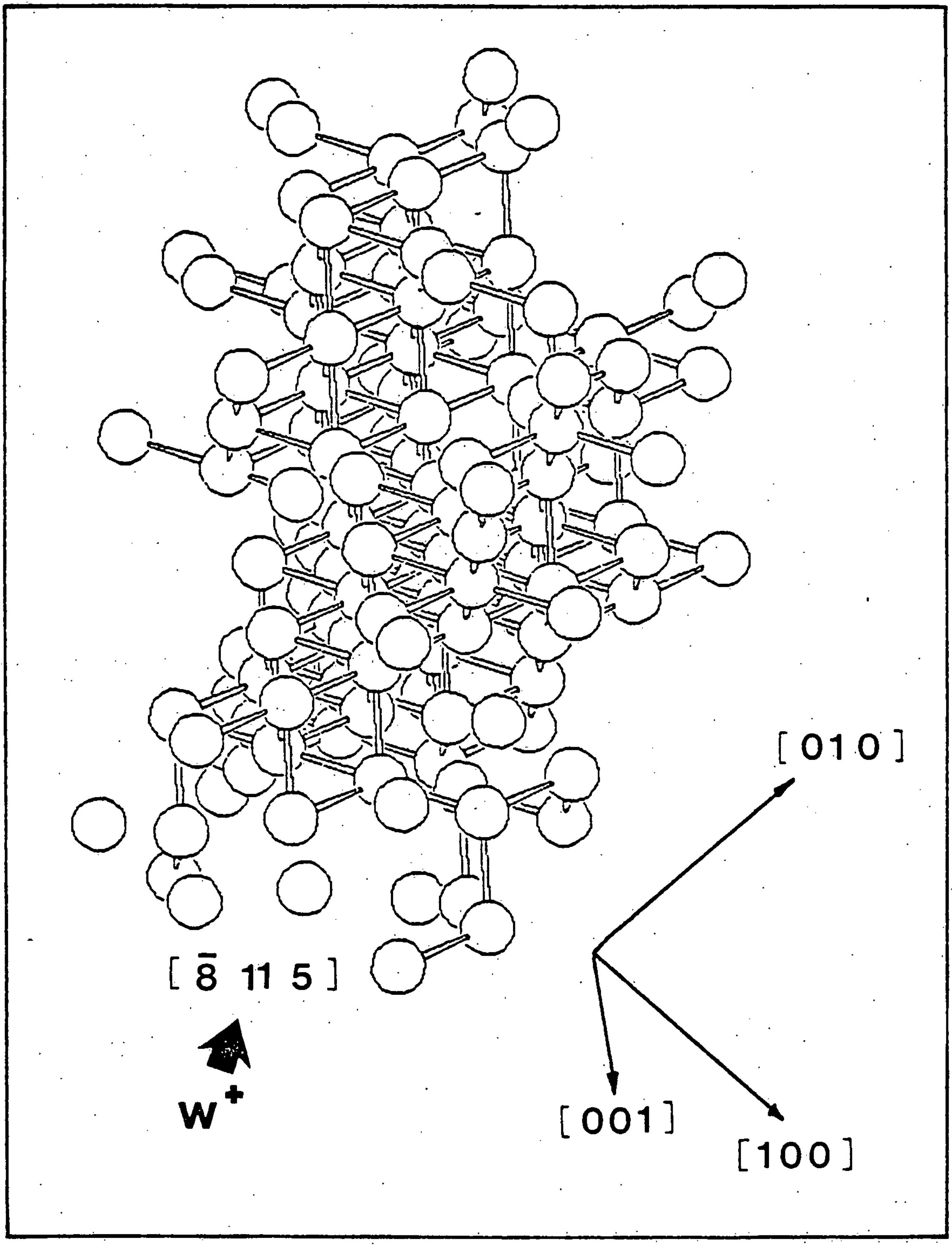

Figure 29: A computer-generated isometric drawing for depleted zone DZ2b.

(5) Depleted zone DZ3a was found in the $(7\bar{1}2)$ and $(8\bar{1}3)$ planes of the third specimen. This depleted zone was ∿45 A from the irradiated surface. Figure 30 exhibits a computer-generated isometric drawing of the VLSs within DZ3a. DZ3a was found to consist of 235 VLSs. The measured values of λ_1 and λ_2 were 26 and 17 A respectively. It is noted that DZ3a was elongated along the $[\bar{1}01]$ direction. The effective diameter $\bar{\lambda}$ of this depleted zone was ∿20 A. The VLS concentration associated with DZ3a was ∿17 at.%. The results of the R(i)/Z(i) measurements are shown in fig. 25e; it is clear that the VLSs within DZ3a formed clusters. The values of the $\bar{N}(i)$s for DZ3a were also calculated and are plotted in fig. 26e; this figure shows that DZ3a contains only one jumbo VLS cluster. If only first nearest-neighbor VLSs were considered then the distribution of cluster sizes was as follows: (1) 28 mono-VLSs; (2) two di-VLSs; (3) one quadri-VLS; and (4) one jumbo cluster containing 206 VLSs.

V.5.2.3. Depleted Zones in Pure Tungsten Produced by a Single 30 keV Mo^+ Ion

In only one out of the three pure tungsten specimens irradiated with 30 keV Mo^+ ions did we find depleted zones capable of being mapped; they were denoted as DZ4a to DZ4d. Depleted zones DZ4a to DZ4d were found in a specimen which had an average tip radius of ∿220 A; this specimen had a [211] orientation. Figure 31a exhibits a partial 211 standard stereographic projection which shows the top view of the

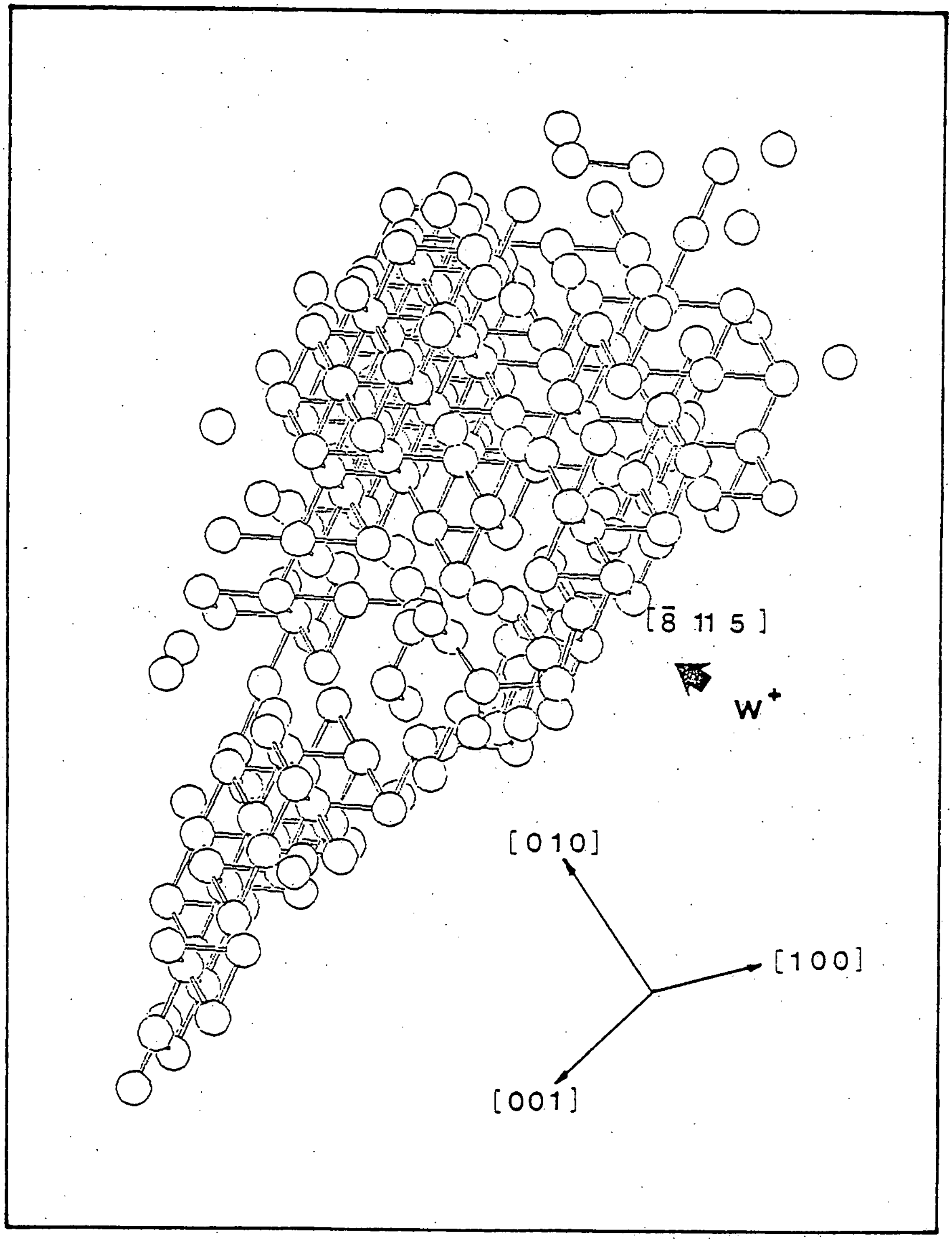

Figure 30: A computer-generated isometric drawing for depleted zone DZ3a.

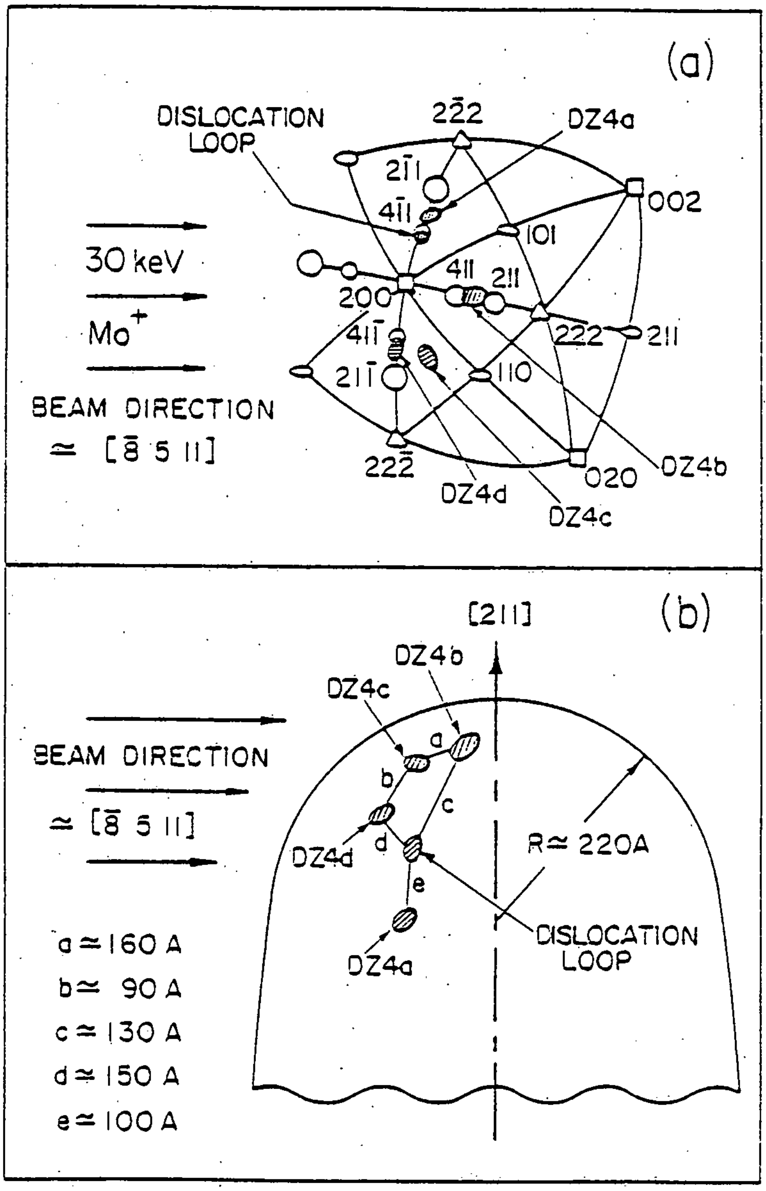

Figure 31: (a) A partial 211 stereographic projection showing the location of depleted zones DZ4a to DZ4d and the dislocation loop.
(b) A schematic cross-sectional view of the FIM tip specimen which contained depleted zones DZ4a to DZ4d.

specimen. The plane (or planes) in which a depleted zone was detected is indicated; for example, DZ4b was found near the (411) plane of the specimen. The cross-sectional side views of the specimen is shown in fig. 31b. The separation between any two depleted zones is indicated by letters a, b, c etc., they ranged from 90 to 160 A.

As an illustrative example of the contrast effects produced by a depleted zone created by a single 30 keV Mo^+ ion fig. 32 shows a series of ten FIM micrographs out of ten successive (622) planes; they were chosen from a total of $1.0x10^3$ frame of 35 mm ciné film which were recorded and analyzed in the construction of DZ4b. The (622) and the surrounding planes are indexed in frame 1. Frame 1 shows an atomically perfect plane in layer 1; the other frames exhibit (622) planes containing VLSs. Note that in frames 76 and 131 the (411) plane also shows vacancy damage as indicated by the arrows. It is also noted that void-like vacancy clusters appear in layers 6 to 10 which contain 20 VLSs out of the total number of 60 atomic sites; this corresponds to a local VLS concentration of ∿33 at.%. This high local VLS concentration allows us to state, with confidence, that DZ4b observed in the (622) plane could not have been due to artifact VLSs although the artifact VLSs in the (622) plane is high (∿0.8 at.%) as mentioned in sect.V.5.1.

Other detailed information obtained for each depleted zone is listed in Table 3 and is now described.

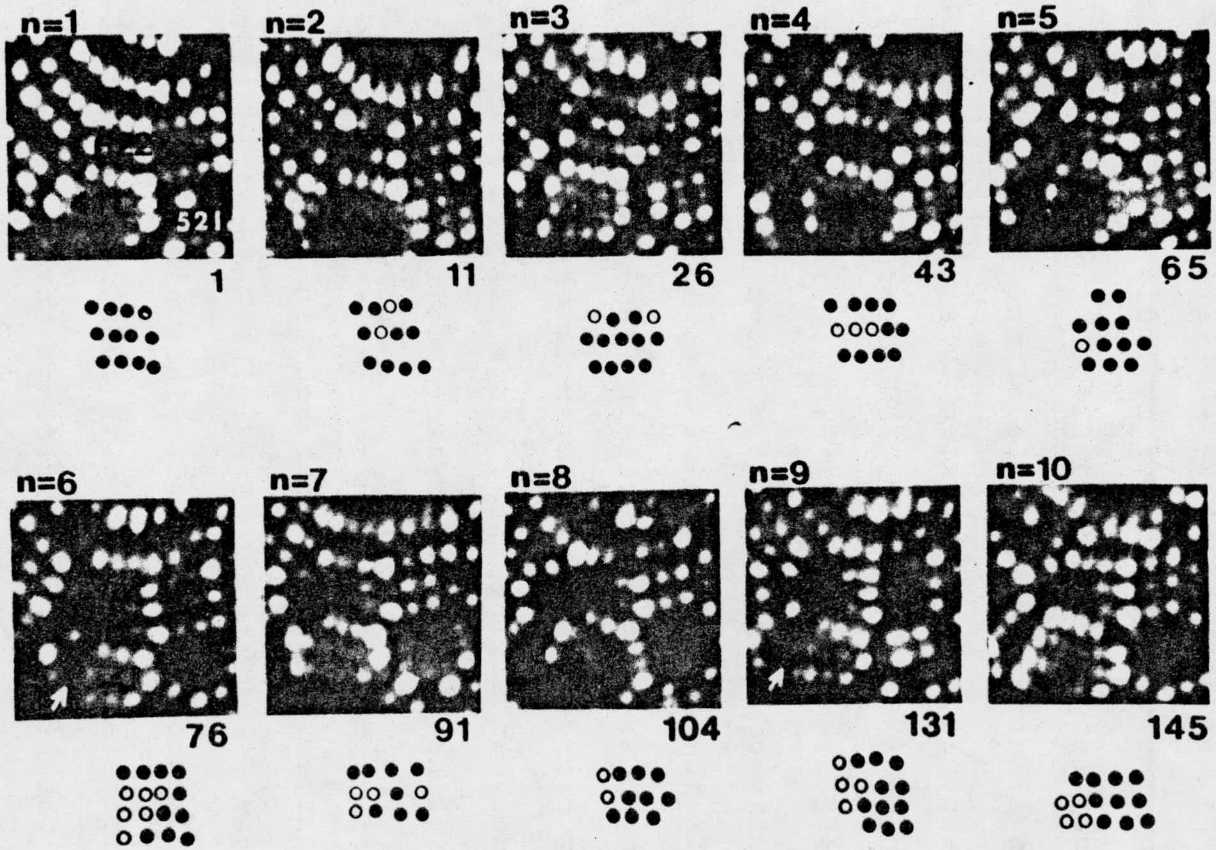

Figure 32: A series of ten FIM micrographs out of 145 recorded during atom-by-atom dissection of depleted zone DZ4b.

Table 3: Data for depleted zones in pure tungsten produced by 30 keV Mo$^+$ ions[†]

Depleted[*] zone No.	Damage range (A)	Elongation direction	λ_1 (A)	λ_2 (A)	$\bar{\lambda}$ (A)	ν	c_v (at.%)
DZ4a	50	[$\bar{1}$01]	30	20	23	216	10
DZ4b	40	[$\bar{1}$11]	40	17	23	160	10
DZ4c	25	[011]	38	24	28	156	11
DZ4d	35	[111]	45	17	24	168	9

[*] In addition to depleted zones DZ4a to DZ4d, we also found a dislocation loop in the (4$\bar{1}$1) plane of this specimen as indicated in fig. 31; this loop was located ∿60 A from the irradiated surface.

[†] See also footnotes in Table 2.

(1) Depleted zone DZ4a was found in the $(5\bar{2}1)$, $(7\bar{3}2)$ and $(6\bar{2}2)$ planes. This depleted zone was $\sim$50 A from the irradiated surface. Figure 33 exhibits a computer-generated isometric drawing of the VLSs within DZ4a. Dz4a was found to consist of 216 VLSs. The measured values of λ_1 and λ_2 were 30 and 20 A respectively. This depleted zone was found to be elongated along the $[\bar{1}01]$ direction. The effective diameter $\bar{\lambda}$ of DZ4a is 23 A. The VLS concentration associated with this depleted zone was $\sim$10 at.%. The results of the $R(i)/Z(i)$ are shown in fig. 34a; it is clear that the VLSs within DZ4a formed clusters. The values of the $\bar{N}(i)$s for DZ4a were also calculated and are plotted in fig. 35a; this figure shows that DZ4a contains two or more jumbo VLS clusters. If only first nearest-neighbor VLSs are considered then the distribution od cluster sizes is as follows: (1) 47 mono-VLSs; (2) five di-VLSs; (3) four tri-VLSs; (4) one quadri-VLS; (5) two penta-VLSs; (6) one hexa-VLS; and (7) two jumbo clusters containing 26 and 101 VLSs respectively.

(2) Depleted zone DZ4b was found in the (411) and (622) planes. This depleted zone was $\sim$40 A from the irradiated surface. Figure 36 exhibits a computer-generated isometric drawing of the VLSs within DZ4b. DZ4b was found to consist of 160 VLSs. The measured values of λ_1 and λ_2 were 40 and 17 A respectively. This depleted zone was elongated along the $[\bar{1}11]$ direction. The effective diameter $\bar{\lambda}$ of DZ4b was 23 A. The VLSs concentration associated with DZ4b was $\sim$10

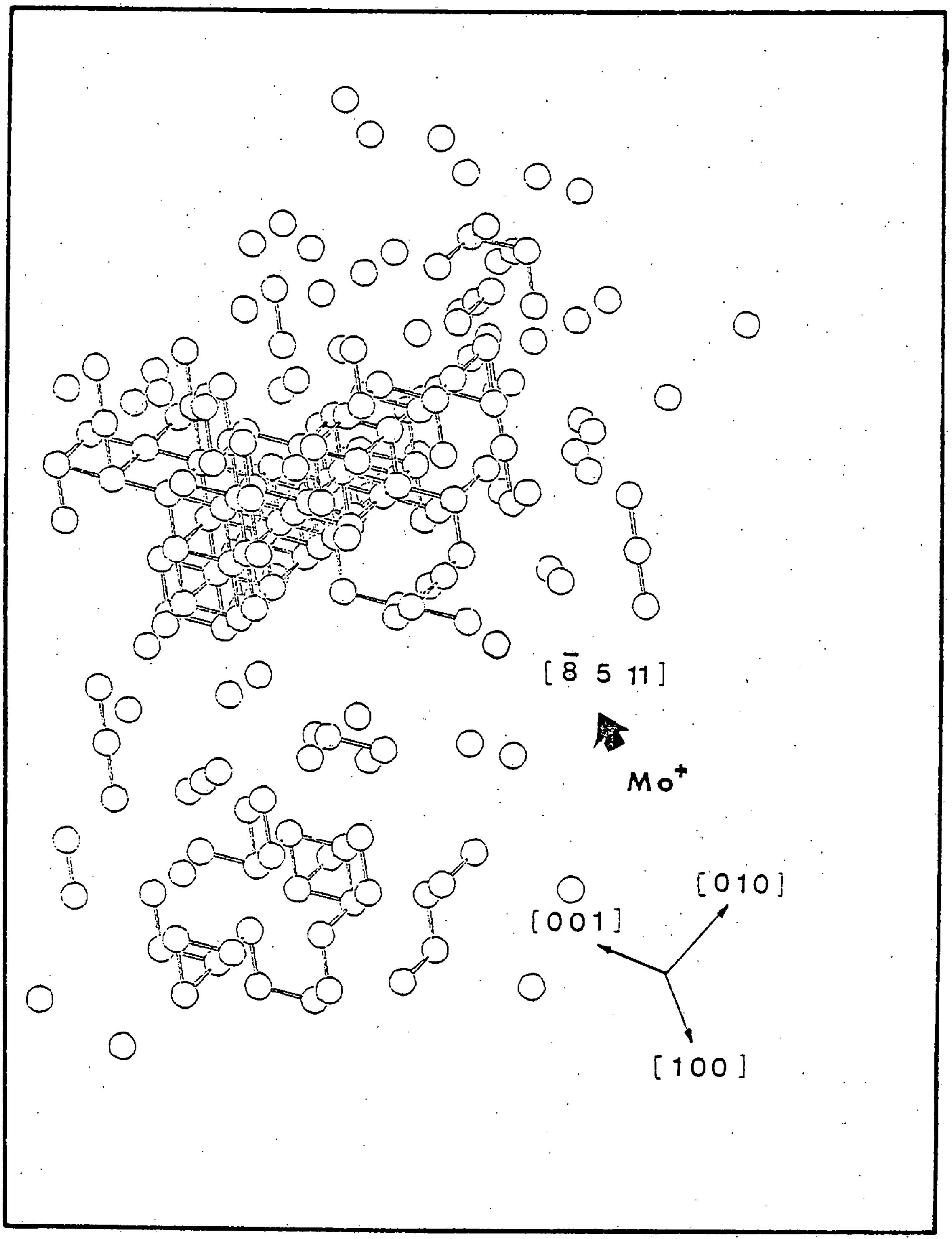

Figure 33: A computer-generated isometric drawing for depleted zone DZ4a.

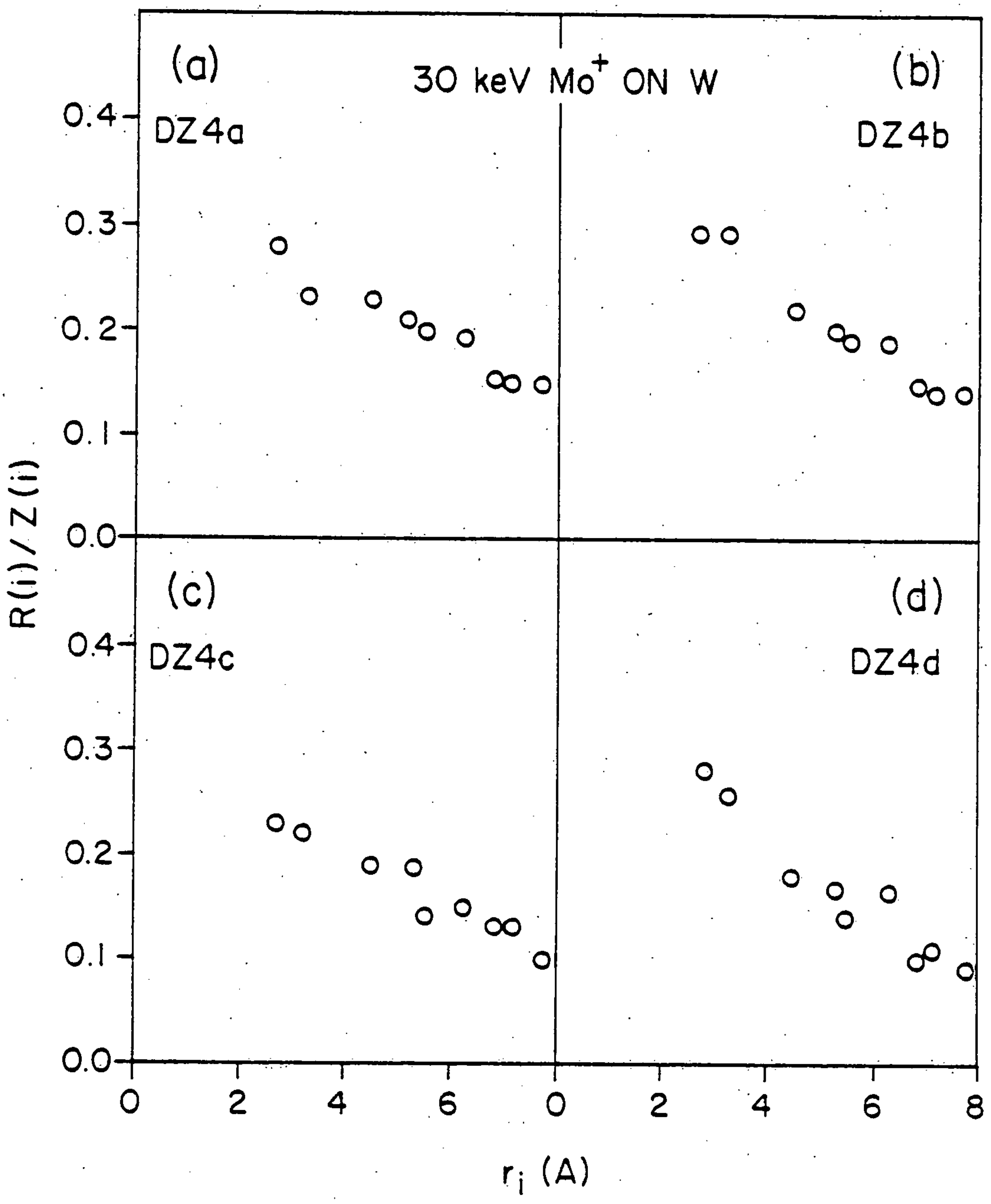

Figure 34: The normalized radial distribution function [R(i)/Z(i)] for depleted zones DZ4a to DZ4d.

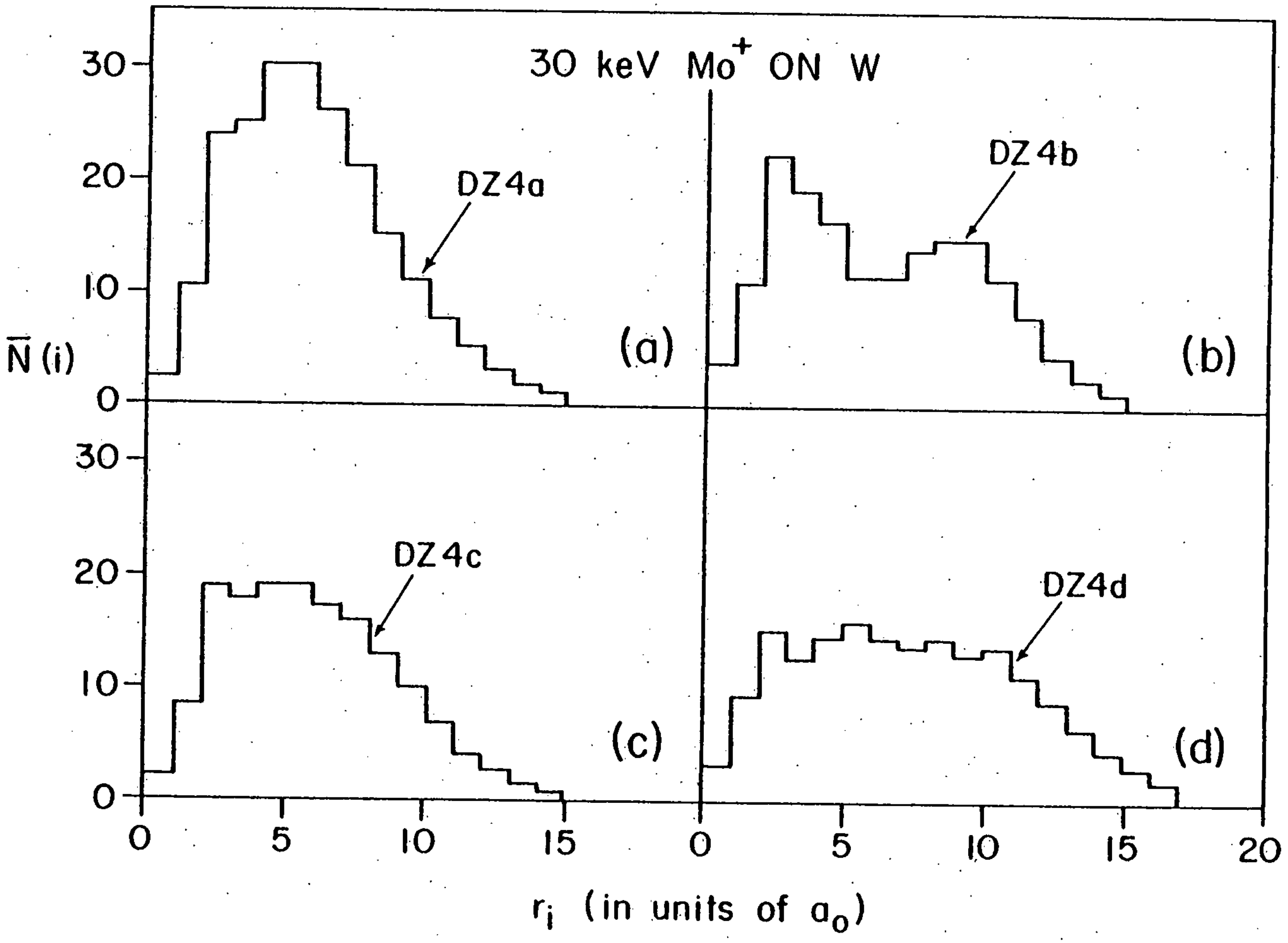

Figure 35: The spectra of the $\bar{N}(i)$s for depleted zones DZ4a to DZ4d.

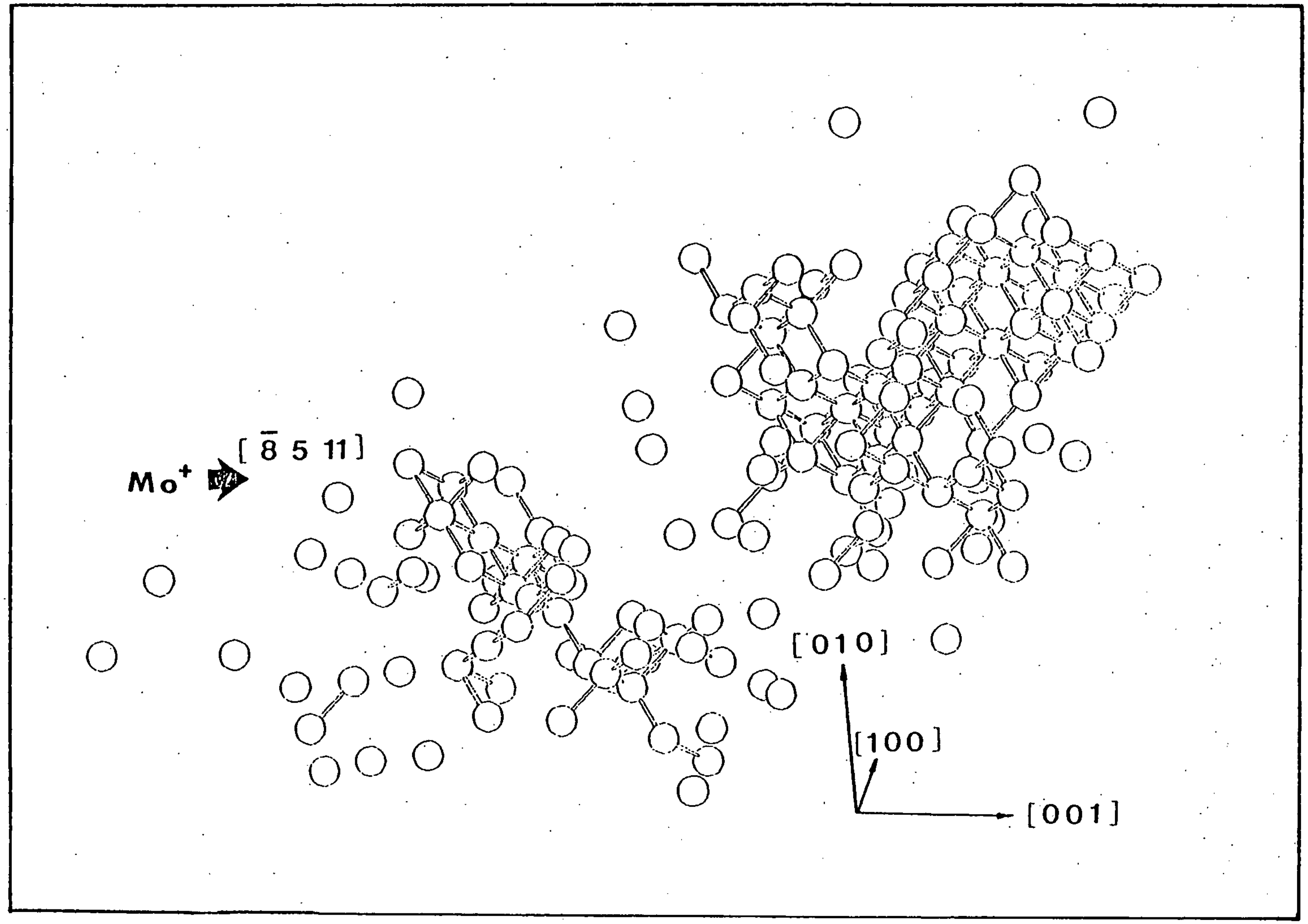

Figure 36: A computer-generated isometric drawing for depleted zone DZ4b.

at.%. The results of the R(i)/Z(i) are shown in fig. 34b; it is clear that the VLSs within DZ4b formed clusters. The values of the $\bar{N}(i)$s for this depleted zone were also calculated and are plotted in fig. 35b; this figure shows that DZ4b contains two or more jumbo VLS clusters separated by ∿20 A. If only first nearest-neighbor VLSs were considered then the distribution of cluster sizes was as follows: (1) 37 mono-VLSs; (2) four di-VLSs; (3) one quadri-VLS ; and (5) three jumbo clusters respectively containing 8, 27 and 76 VLSs.

(3) Depleted zone DZ4c was found in the $(52\bar{1})$ and $(63\bar{1})$ planes. This depleted zone was ∿25 A from the irradiated surface. Figure 37 exhibits a computer-generated isometric drawing of the VLSs and SIAs within DZ4c. DZ4c was found to consist of 156 VLSs. The measured values of λ_1 and λ_2 were 38 and 24 A respectively. DZ4c was found to be elongated along the [011] direction. The effective diameter $\bar{\lambda}$ of DZ4c was 28 A. The VLS concentration associated with this depleted zone was ∿11 at.%. The results of the R(i)/Z(i) measurements are shown in fig. 34c; it is clear that the VLSs within DZ4c formed clusters. The values of the $\bar{N}(i)$s for DZ4c were also calculated and are plotted in fig. 35c; this figure shows that DZ4c contained two or more jumbo VLS clusters. If only first nearest-neighbor VLSs were considered then the distribution of cluster sizes was as follows: (1) 28 mono-VLSs; (2) nine di-VLSs; (3) three tri-VLSs; and (4) five jumbo clusters respectively containing 6, 8, 9, 35, 43 VLSs.

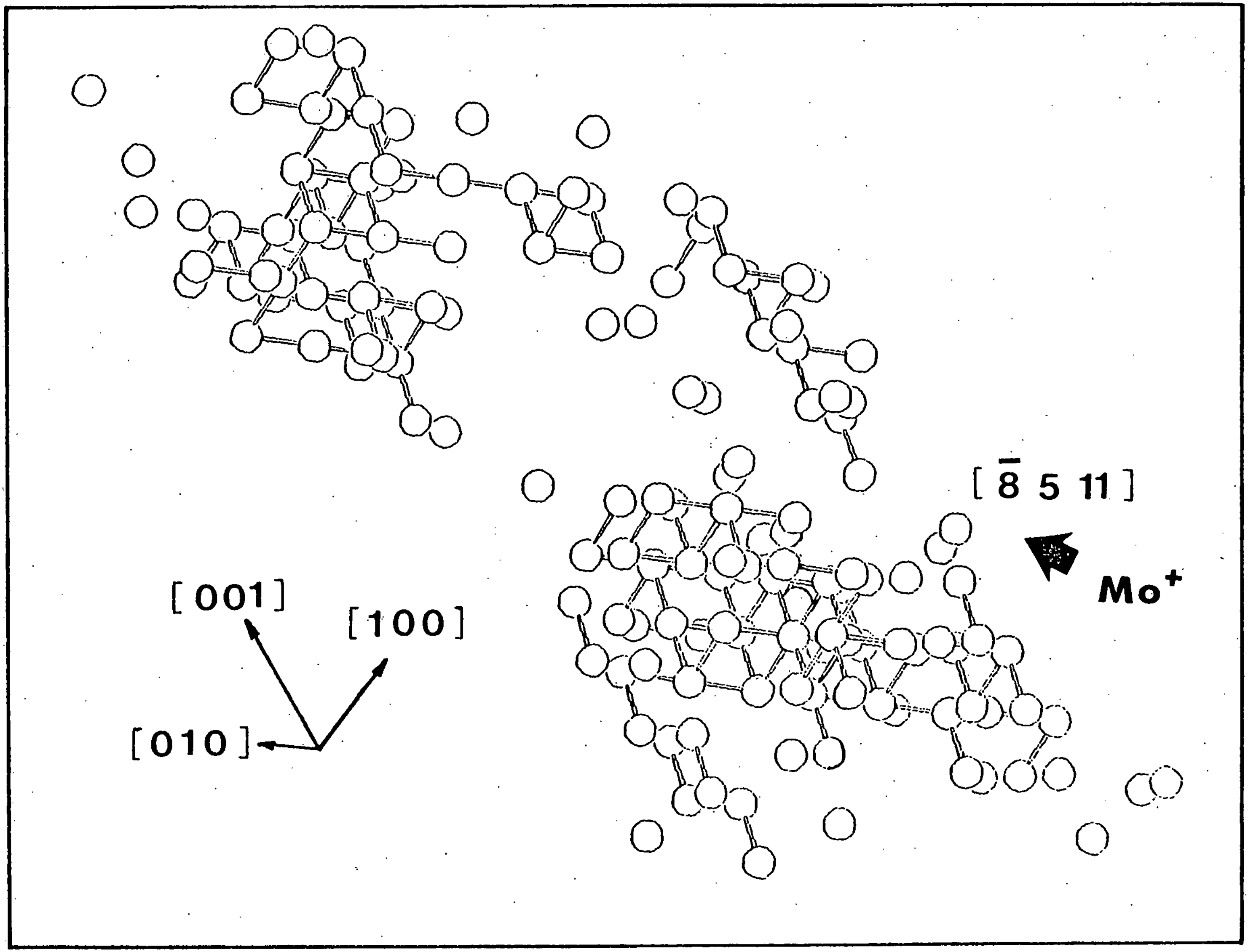

Figure 37: A computer-generated isometric drawing for depleted zone DZ4c.

(4) Depleted zone DZ4d was found in the $(41\bar{1})$, $(71\bar{2})$ and $(51\bar{2})$ planes. This depleted zone was ∿35 A from the irradiated surface. Figure 38 exhibits a computer-generated isometric drawing of the VLSs within DZ4d. DZ4d was found to consist of 168 VLSs. The measured values of λ_1 and λ_2 were 45 and 17 A respectively. DZ4d was found to be elongated along the [111] direction. The effective diameter $\bar{\lambda}$ of DZ4d was 24 A. The VLS concentration associated with this depleted zone was ∿9.1 at.%. The results of the R(i)/Z(i) are shown in fig. 34d; it is clear that the VLSs within DZ4d formed clusters. The values of the $\bar{N}(i)$s for DZ4d were also calculated and are plotted in fig. 35d; this figure shows that DZ4d contains more than two jumbo VLS clusters. If only first nearest-neighbor VLSs were considered then the distribution of cluster sizes was as follows: (1) 29 mono-VLSs; (2) six di-VLSs; (3) one tri-VLS; and (4) three clusters respectively containing 24, 28 and 72 VLSs.

V.5.2.4. Depleted Zones in Pure Tungsten Produced by a Single 30 keV Cr^+ Ion

In only one out of the four pure tungsten specimens irradiated with 30 keV Cr^+ ions did we find two depleted zones capable of being atomically mapped; they were denoted as DZ5a and DZ5b. Depleted zones DZ5a and DZ5b were found in a specimen which had an average tip radius of ∿400 A; this specimen had a [121] orientation. Figure 39a exhibits a partial 121 standard stereographic projection which shows the

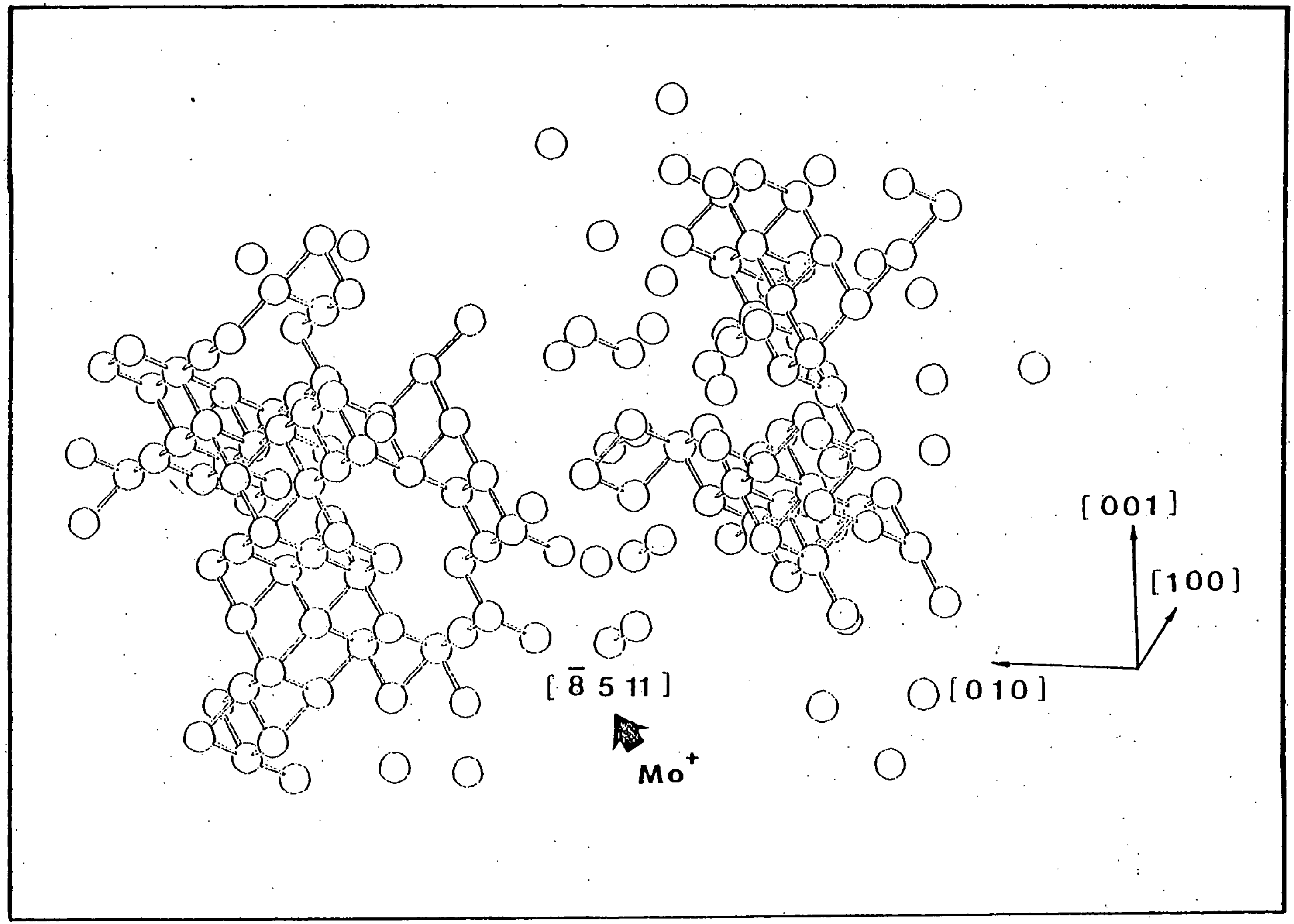

Figure 38: A computer-generated isometric drawing for depleted zone DZ4d.

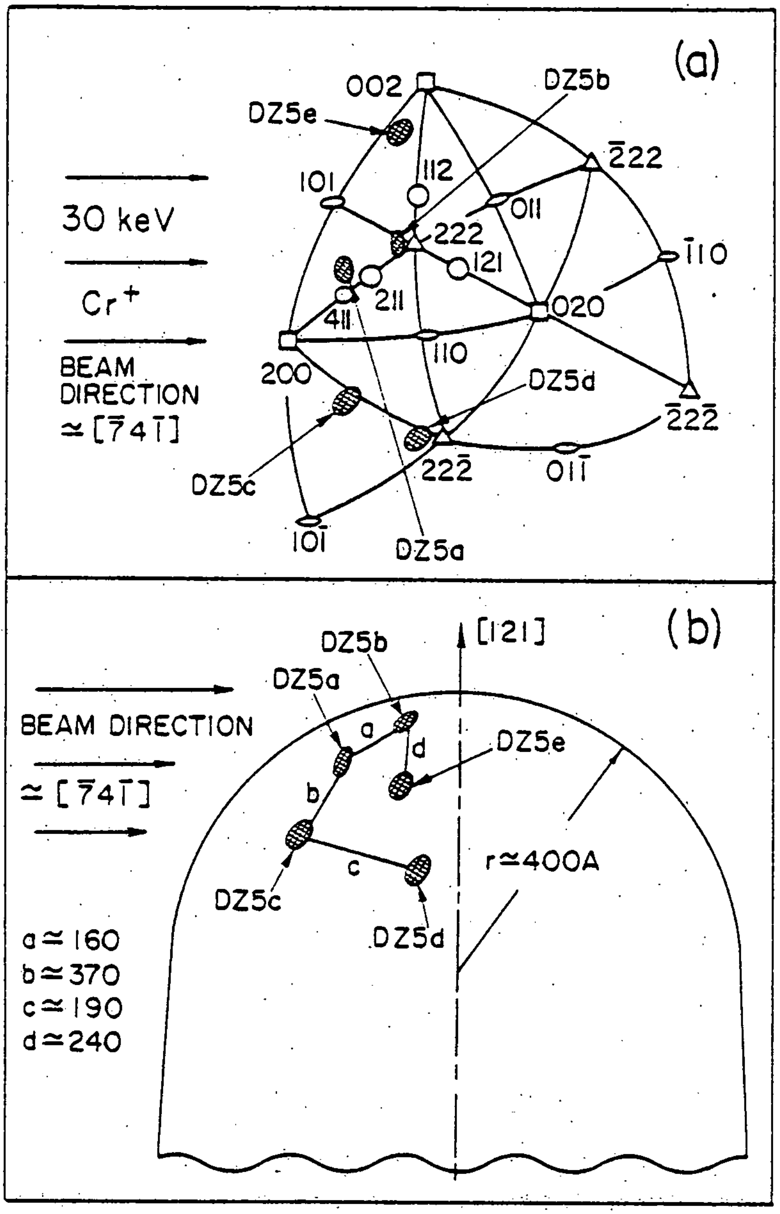

Figure 39: (a) A partial 121 stereographic projection showing the location of depleted zones DZ5a to DZ5e.
(b) A schematic cross-sectional view of the FIM tip specimen which contained depleted zones DZ5a to DZ5e.

top view of the specimen. The plane (or planes) in which a depleted zone was detected is indicated; for example, DZ5b was found near the (222) plane of the specimen. The cross-sectional side view of the tip specimen is shown in fig. 39b. The separations between any two depleted zones are indicated by the letters a, b, a etc.; they ranged from 160 to 370 A. Figure 40 shows a series of ten FIM micrographs of ten successive (824) planes; they were chosen from a total of $2x10^3$ frames of 35 mm ciné film which were recorded and analyzed in the reconstruction of DZ5a. The (824) and the surrounding planes are indexed in frame 1. Frames 1, 27 and 64 show atomically perfect planes in layers 1, 2 and 3; the other frames exhibit the (824) planes which contained VLSs. It is also noted that the void-like vacancy cluster which appeared in the (11 3 4) plane is indicated by the big open circles in each micrograph.

Other detailed information for each depleted zone is listed in Table 4 and is now described.

(1) Depleted zone DZ5a was found in the (512), (723), (824), (411) and (11 3 4) planes. This depleted zone was ∿40 A from the irradiated surface. Figure 41 exhibits a computer-generated isometric drawing of the VLSs within DZ5a. DZ5a was found to consist of 241 VLSs. The measured values of λ_1 and λ_2 were 75 and 36 A respectively. DZ5a was found to be elongated along the $[1\bar{1}0]$ direction. The effective diameter $\bar{\lambda}$ of DZ5a was 45 A. The VLS concentration associated

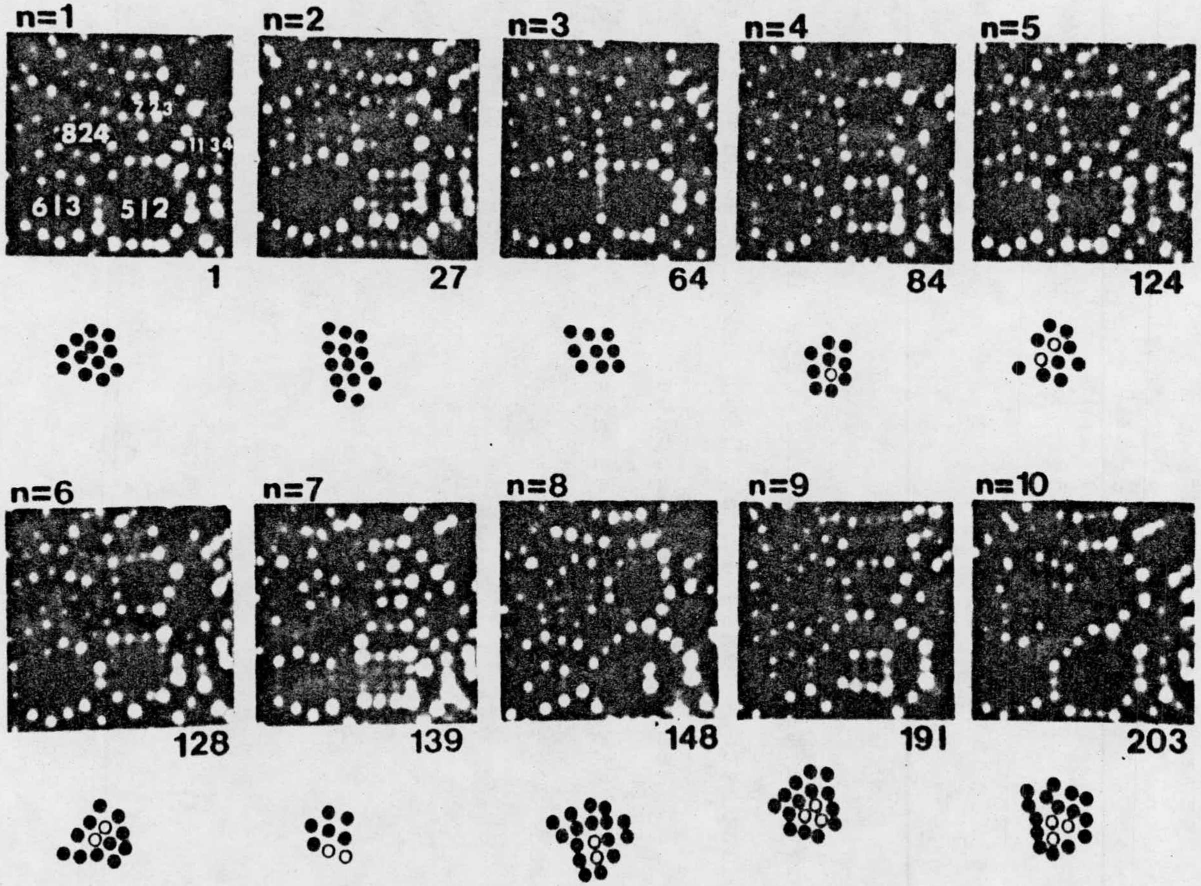

Figure 40: A series of ten FIM micrographs out of 203 recorded during atom-by-atom dissection of depleted zone DZ5b.

Table 4: Data for depleted zone in pure tungsten produced by 30 keV Cr$^+$ ions[†]

Depleted[*] zone No.	Damage range (A)	Elongation direction	λ_1 (A)	λ_2 (A)	$\bar{\lambda}$ (A)	ν	c_v (at.%)
DZ5a	40	$[1\bar{1}0]$	75	36	46	241	3.6
DZ5b	60	$[110]$	45	33	37	247	4.6

[*] In addition to depleted zones DZ5a and DZ5b we also found three depleted zones DZ5c, DZ5d and DZ5e in this specimen; DZ5c, DZ5b and DZ5e were located ∿10, 106 and 41 A from the irradiated surface (see also fig. 39).

[†] See also footnotes in Table 2.

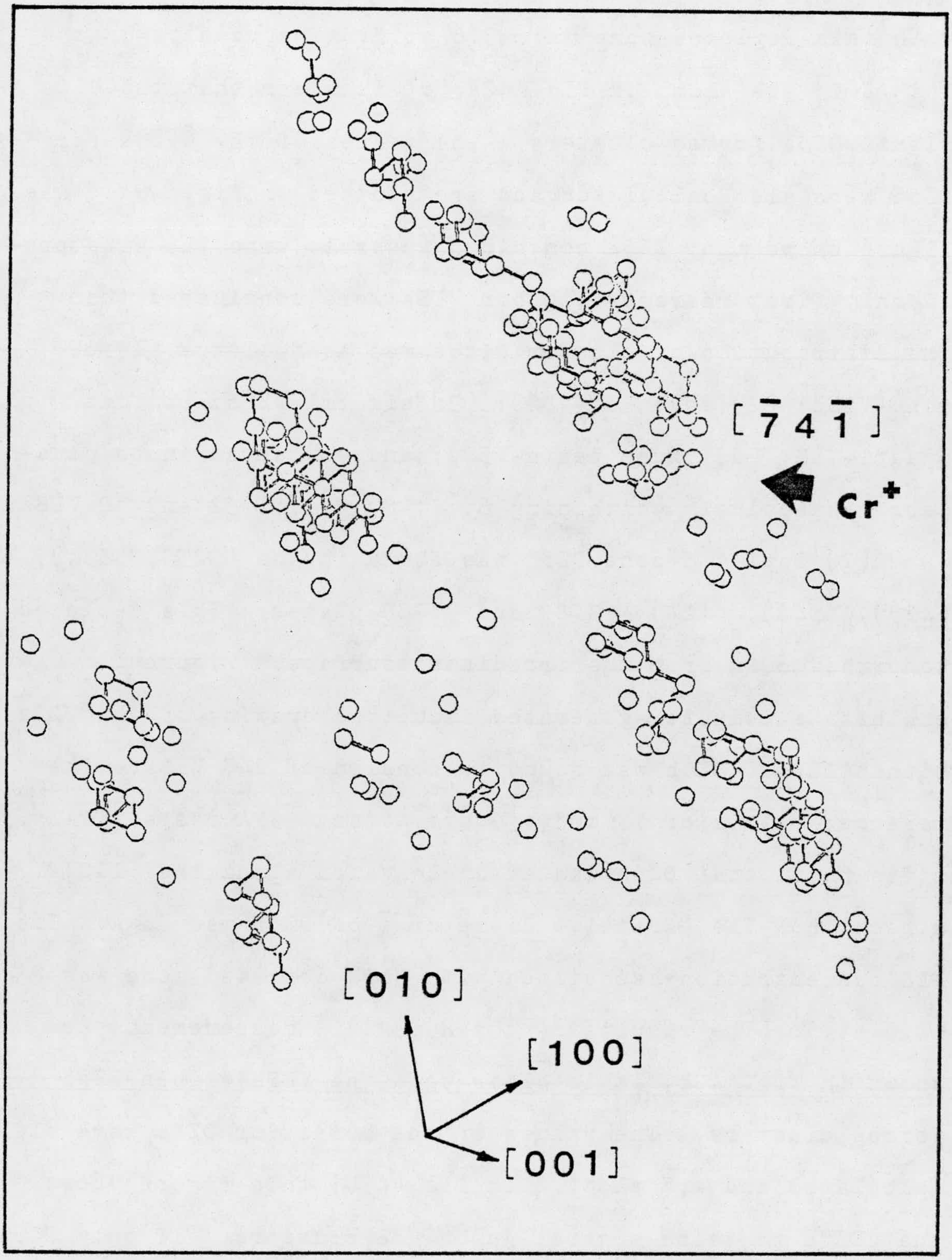

Figure 41: A computer-generated isometric drawing of depleted zone DZ5a.

with this depleted zone was ∿3.6 at.%. The results of the R(i)/Z(i) are shown in fig. 42a; it is clear that the VLSs within DZ5a formed clusters. The values of the $\bar{N}(i)$s for DZ5a were also calculated and are plotted in fig. 43a; this figure shows that DZ5a contained several jumbo VLS clusters. if only first nearest-neighbor VLSs were considered then the distribution of cluster sizes was as follows: (1) 69 mono-VLSs; (2) seven di-VLSs; (3) six tri-VLSs; (4) one quadri-VLS; (5) three penta-VLSs; and (6) seven jumbo clusters respectively containing 6, 7, 8, 9, 15, 32 and 50 VLSs.

(2) Depleted zone DZ5b was found in the (323), (534), (433), (543), (424), (758) and (576) planes. This depleted zone was ∿60 A from the irradiated surface. Figure 44 exhibits a computer-generated isometric drawing of the VLSs within DZ5b. DZ5b was found to consist of 247 VLSs. The measured values of λ_1 and λ_2 were 45 and 33 A respectively. It is noted that DZ5b was also elongated along the [110] direction. The effective diameter $\bar{\lambda}$ of DZ5b was 36 A. The VLS concentration associated with this depleted zone was ∿4.6 at.%. The results of the R(i)/Z(i) measurements are shown in fig. 42b; it is clear that the VLSs within DZ5b formed clusters. The values of the $\bar{N}(i)$s for DZ5b were also calculated and are plotted in fig. 43b; this figure shows that DZ5b contains several jumbo VLS clusters. If only first nearest-neighbor VLSs were considered then the distribution of cluster sizes was as follows: (1) 73 mono-VLSs; (2) nine

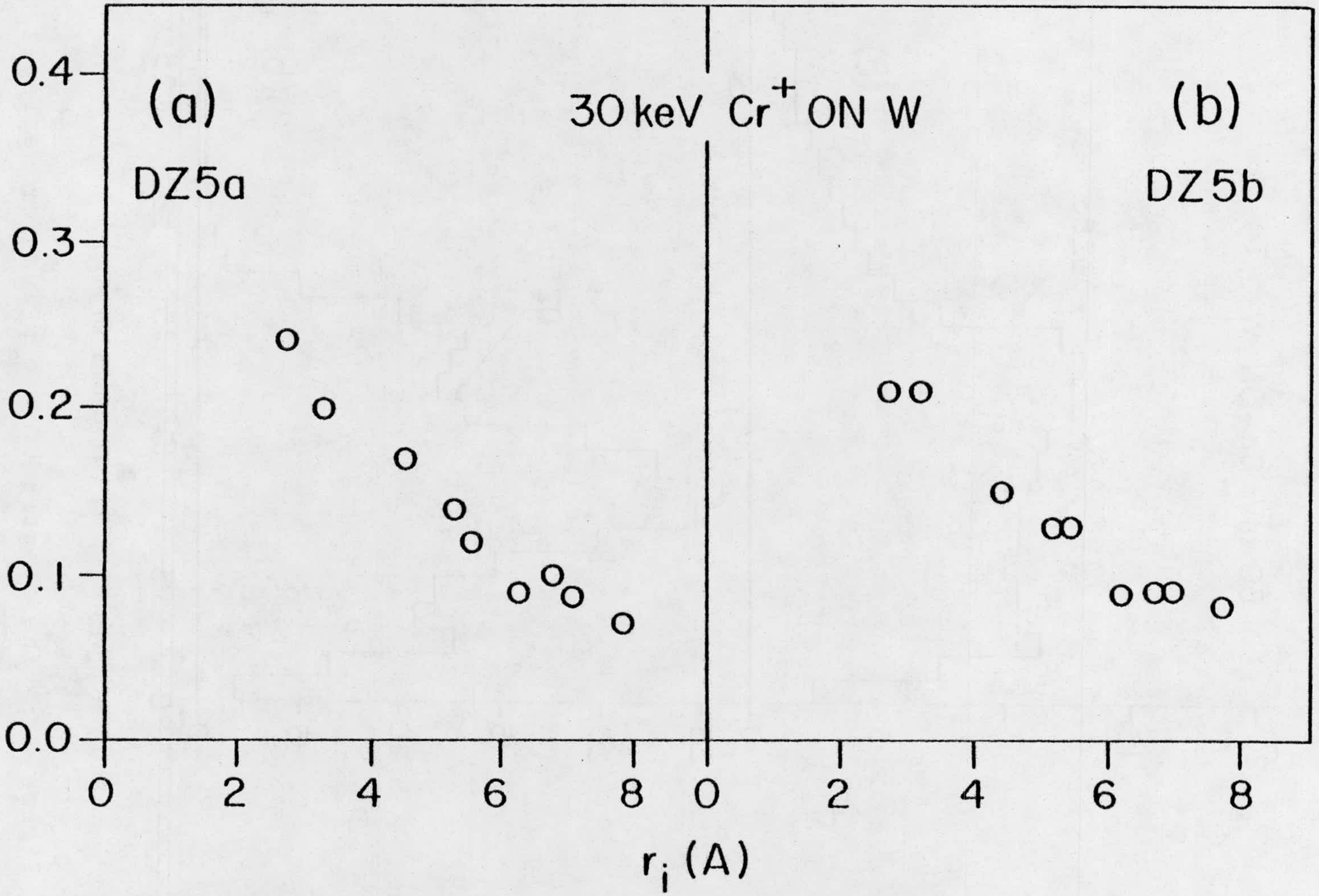

Figure 42: The normalized radial distribution function [R(i)/Z(i)] for depleted zones DZ5a and DZ5b.

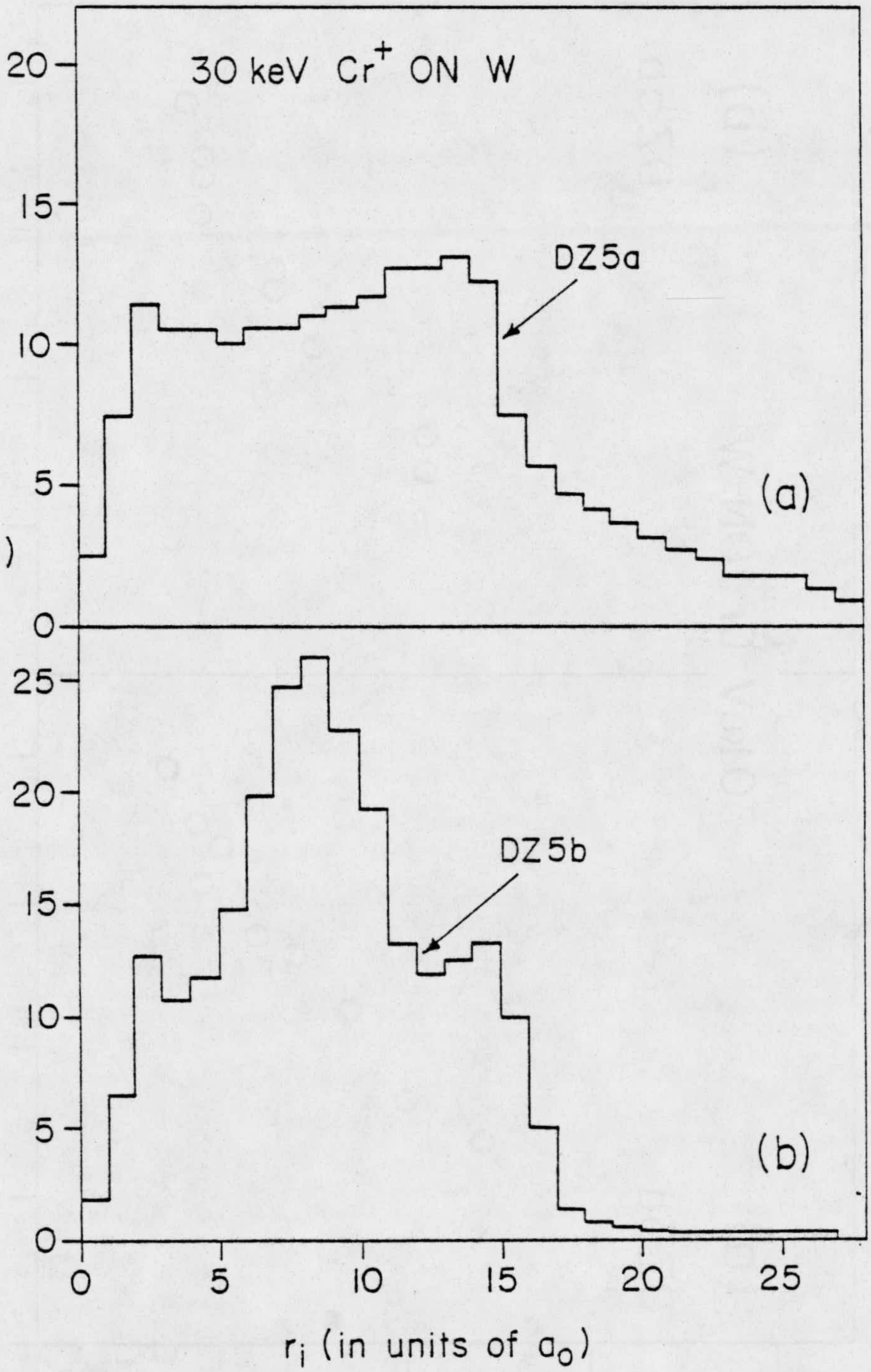

Figure 43: The spectra of the $\overline{N}(i)$s for depleted zones DZ5a and DZ5b.

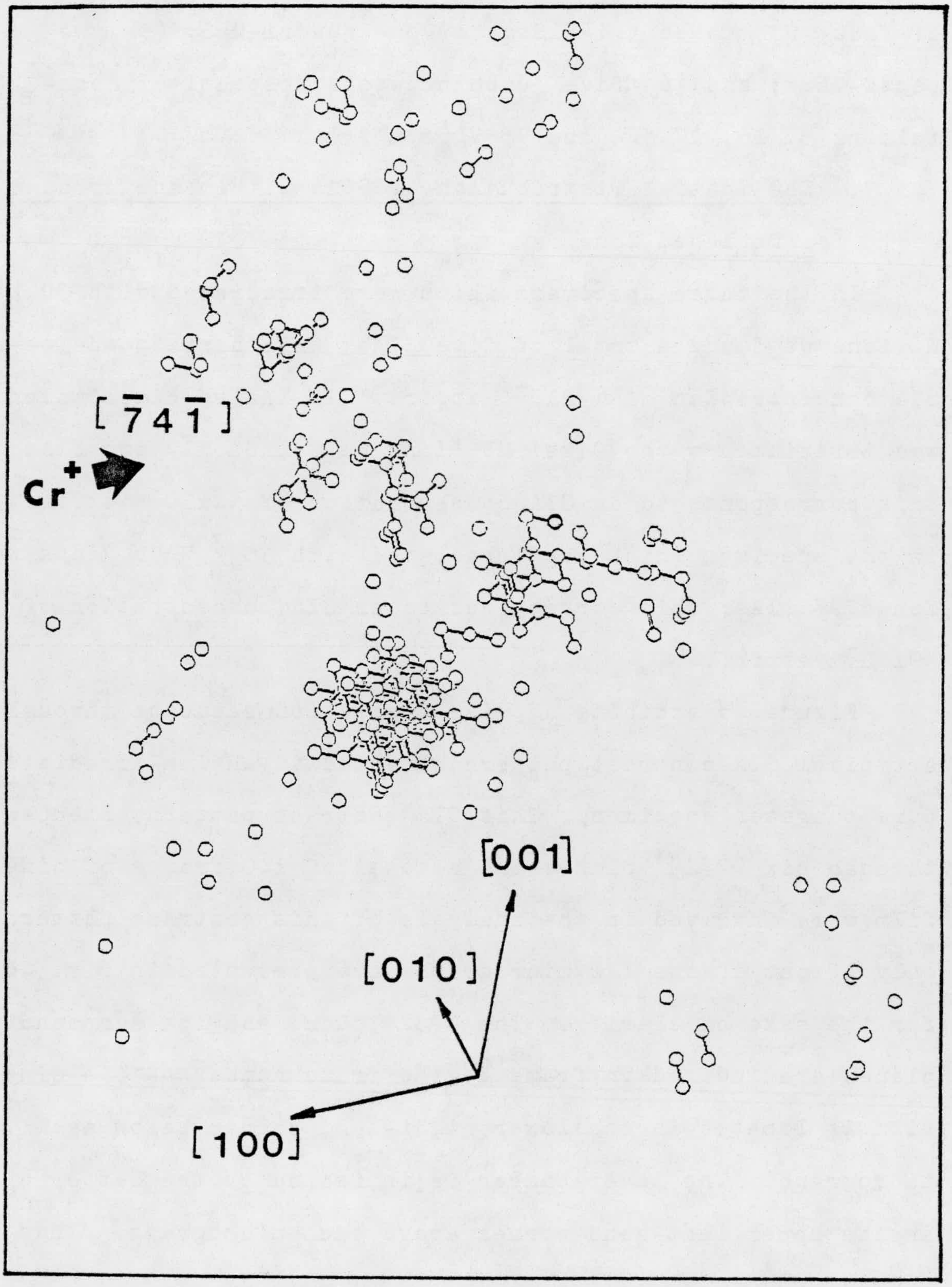

Figure 44: A computer-generated isometric drawing for depleted zone DZ5b.

di-VLSs; (3) three tri-VLSs; (4) one quadri-VLS; (5) two penta-VLSs; and (6) five jumbo clusters respectively containing 9, 16, 17, 24 and 75 VLSs.

V.5.3. The Spatial Distribution of SIAs within and arround a Depleted Zone

In the three specimens which were irradiated with 30 keV W^+ ions we found a total of five SIAs; this corresponds to an SIA concentration of $\sim 3\times10^{-5}$ at.fr.. In the specimen which was irradiated with 30 keV Mo^+ ions we found only two SIAs; this corresponds to an SIA concentration of $\sim 4\times10^{-5}$ at.fr.. In the specimen which was irradiated with 30 keV Cr^+ ions we found 97 SIAs; this corresponds to an SIA concentration of $\sim 9\times10^{-5}$ at.fr..

Figure 45 exhibits a pulse dissection sequence through a typical SIA contrast pattern detected in an ion-irradiated pure tungsten specimen. This SIA contrast pattern extended through six (732)* planes and a total of 140 frames of ciné film were involved in the analysis of this contrast pattern; only 12 out of the 122 micrographs are presented in fig. 46 for the sake of clarity. The (732) plane and the surrounding planes are indixed in frame 1; the frame number of the ciné film is located in the lower right-hand corner below each micrograph. The layer number is indicated by the letter n in the upper left-hand corner above each micrograph. Thus,

---

* This corresponds to a depth of 2.45 A.

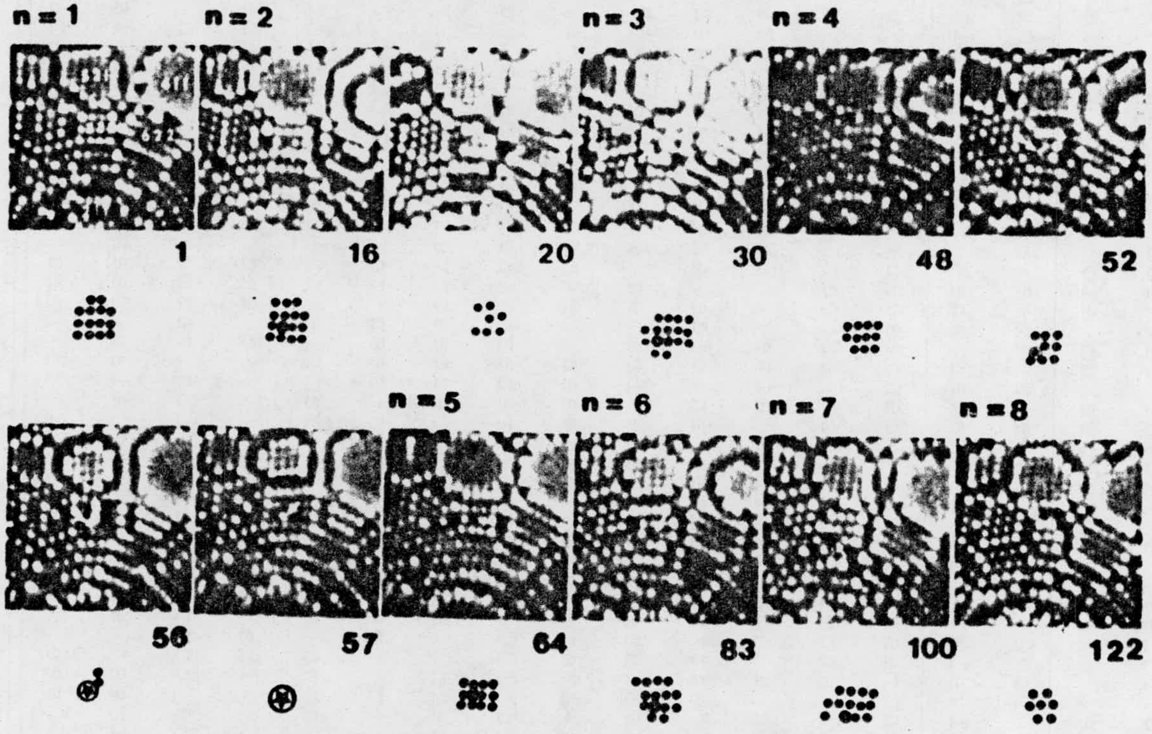

Figure 45: A series of twelve FIM micrographs out of 122 recorded during atom-by-atom dissection of an SIA.

for example, frame 1 corresponds to the n=1 layer and frame 16 to the n=2 layer. The positions of the atoms in the (732) plane are indicated schematically below each micrograph by the solid black circles; a vacant lattice site is indicated by an open circle. Frame 1 shows an atomically perfect plane in layer 1. Layers 2 and 3 (see frames 16 and 30) exhibit two VLSs respectively. It is noted that frame 30 also shows a bright-spot contrast effect (denoted by★). In layer 4 (frame 52) a weak atomic contrast effect (denoted by ⊛) is seen to appear in a non-lattice site. This extra bright-spot contrast effect increased in size and brightness as the n=4 layer was inssected (see frames 52, 56 and 57) and it finally field-evaporated between frames 57 and 64. Frames 64, 83 and 100 which represent the layers 5, 6 and 7 are seen to contain three VLSs respectively. Finally the n=8 layer shown in frame 122 was seen to be perfect.

Figure 46 shows one more example of the contrast pattern of an SIA. The layers 4, 5, 6 and 7 (see frames 239, 300, 358 and 403) contain six VLSs respectively. An extra bright-spot contrast effect was also seen in a non-lattice site in layer 5 (see frames 312, 337 and 345). Therefore, an SIA could produce a contrast pattern consisting of (1) a bright spot; (2) an extra bright-spot and (3) a vacant lattice site (see also Seidman and Lie(49)). This type of contrast pattern was observed only in the irradiated specimen and therefore could <u>not</u> have been caused by the artifacts

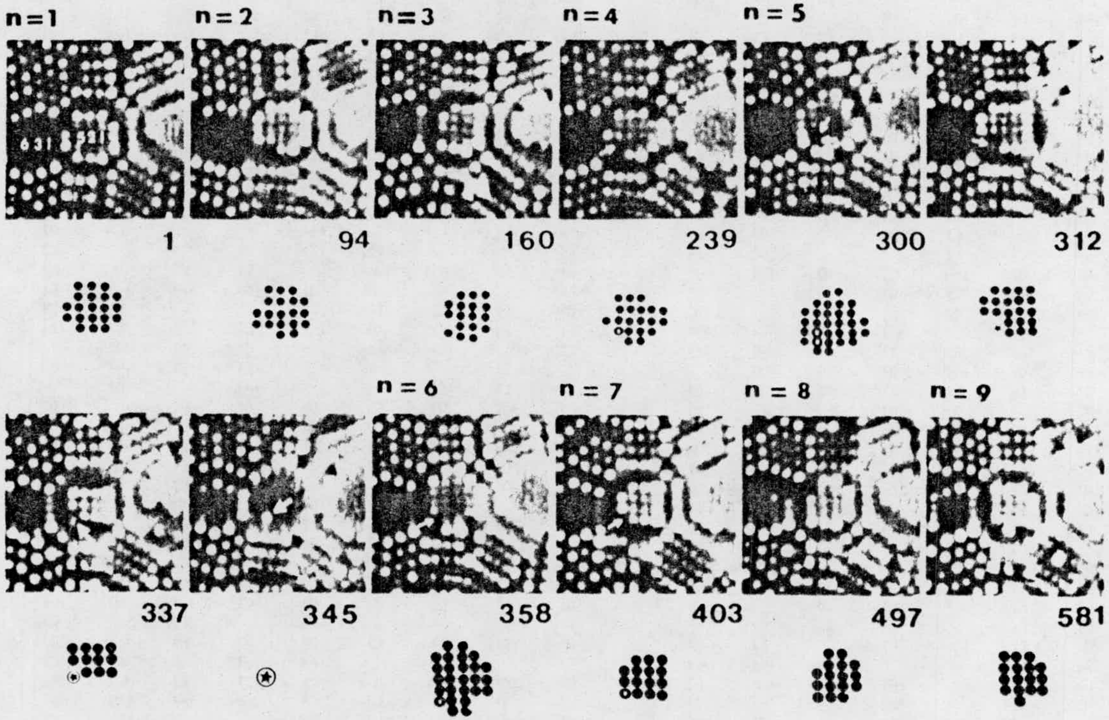

Figure 46: A series of twelve FIM micrographs out of 581 recorded showing the contrast pattern of an SIA.

(see also sect. V.5.1.).

A computer-generated isometric drawing of the 30 keV Cr^+-irradiated specimen is shown in fig. 47. The five open ellipses represent the depleted zones DZ5a to DZ5e and the solid black-dots represent the SIAs. The mathematical details of the mapping procedure is referred to Appendix F. It is noted in fig. 47 that the depleted zones were mainly on the incident-beam side of the specimen whereas a large fraction of the total number of SIAs were observed on the other side shielded from the ion beam. The clear separation between the depleted zones and SIAs is therefore evident in fig. 47.

A computer-generated isometric drawing of the specimen which was irradiated with 18 keV Au^+ ions is also shown in fig. 48. In this specimen depleted zones, which were denoted schematically by the open ellipses, were produced within ≤30 A* from the irradiated surfaces. The SIAs which were injected into the bulk of the specimen are indicated by the solid black dots; in this specimen we find a total of 33 SIAs. Figure 48, once again, shows very clearly that the SIAs are well separated from depleted zones. Further quantitative discussions are given in sect. V.6.7.

---

* This value was measured from the FIM micrographs.

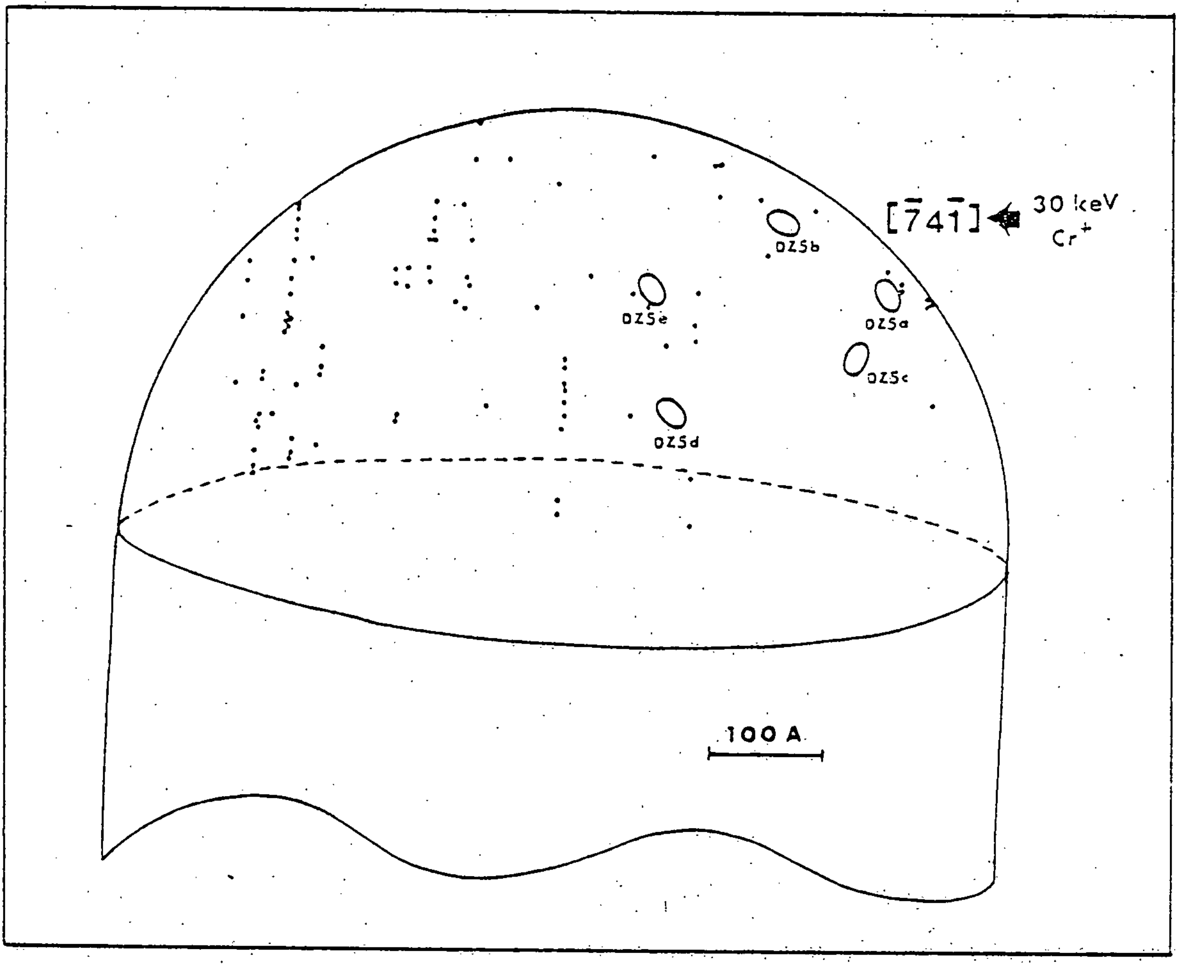

Figure 47: A computer-generated isometric drawing showing the location of the SIAs and depleted zones DZ5a to DZ5e in an FIM specimen which was irradiated with 30 keV Cr^+ ions at 10 K. The open ellipses indicate depleted zones and the solid black dots indicate the SIAs.

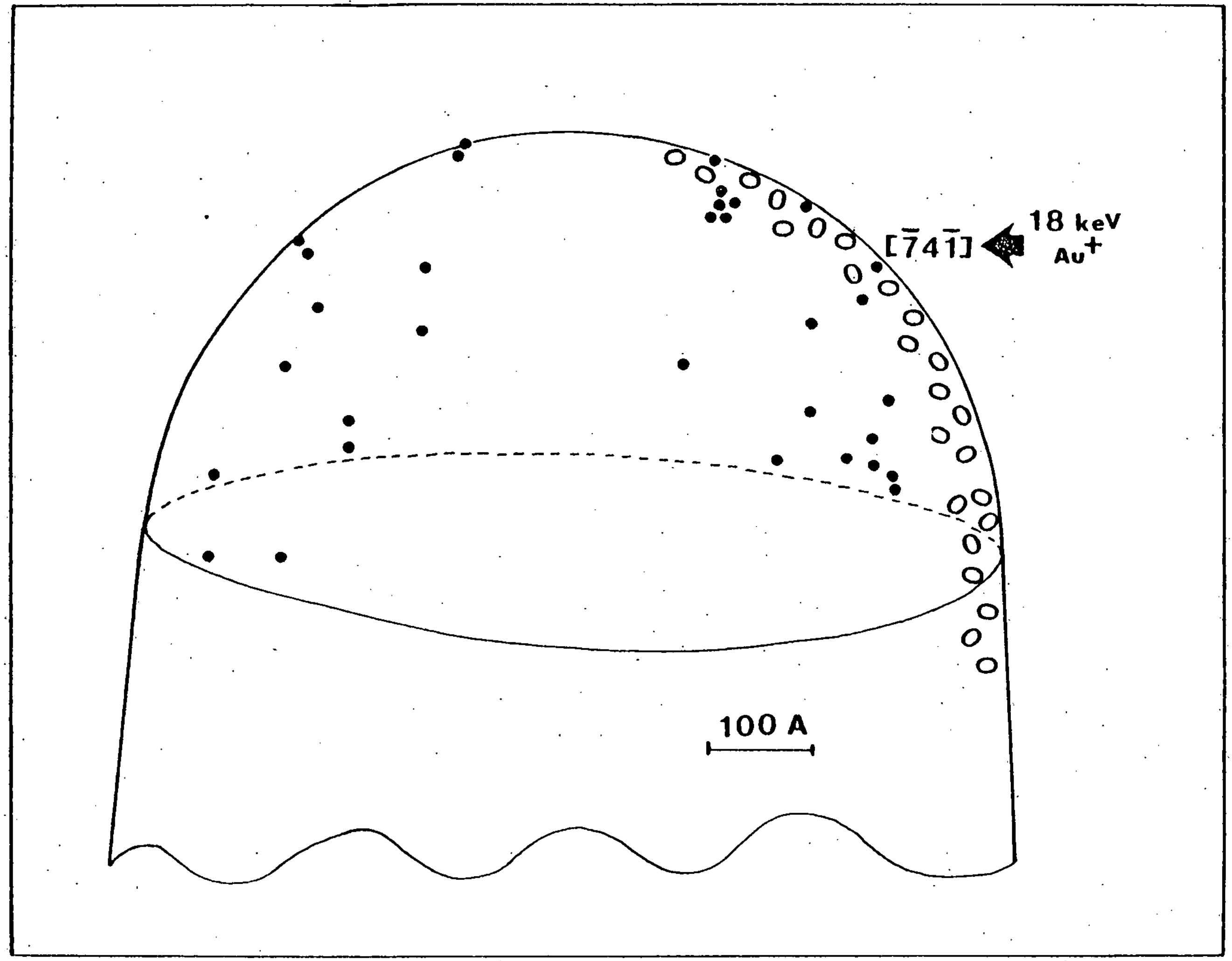

Figure 48: A computer-generated isometric drawing showing the location of the SIAs in an FIM tip specimen which was irradiated with 18 keV Au^+ ions at 10 K. The location of depleted zones are also indicated schematically by the open circles.

V.6. Discussion

V.6.1. Probability that Each Depleted Zone was Created by a Single Ion

The number of ions which may have hit the volume of each depleted zone was estimated employing a simple geometric argument. The cross-sectional area (A) of each depleted zone which had been exposed to the ion beam are listed in Table 5. In these calculations each depleted zone was approximated by an ellipsoid as defined in sect. V.5.2.1.; the quantity A* was given by

$$A = \frac{\pi}{4}\sqrt{\lambda_2\ \lambda_1{}^2\sin^2\alpha+\lambda_2{}^2\cos^2\alpha} \qquad (10)$$

where α is the angle between the direction of the incident ion beam and the major axis of the ellipsoid. The value of A was then multiplied by the total dose of ions to yield the number of ions which crossed this area. The number of ions thus obtained was most likely an upper bound because the calculation neglected the apread in the range of the incident ions. As listed in Table 5 the number of ions which hit each depleted zone was always less than 0.6. It was concluded that each depleted zone observed had most likely been created by only a single ion.

V.6.2. The Estimated Number of Artifact VLSs that May Have Been Included in Each Depleted Zone

In this section the number of artifact VLSs which may

---

* See Appendix E for the derivation of eq. (10).

Table 5: The estimated number of ions that traversed each depleted zone

Depleted zone No.	Irradiation* dose (10^{12} ion cm^{-2})	Cross-sectional area exposed to the ion beam (10^{-16} cm^2)	Estimated number of ions traversing this area
DZ1a	9 (W^+)	262	0.24
DZ1b	9 (W^+)	255	0.23
DZ2a	2 (W^+)	463	0.09
DZ2b	2 (W^+)	189	0.04
DZ3a	5 (W^+)	305	0.15
DZ4a	10 (Mo^+)	341	0.34
DZ4b	10 (Mo^+)	267	0.27
DZ4c	10 (Mo^+)	570	0.57
DZ4d	10 (Mo^+)	574	0.57
DZ5a	4 (Cr^+)	1150	0.46
DZ5b	4 (Cr^+)	1148	0.46

* The ion species is indicated in the parentheses.

have been included in each depleted zone was estimated. Basically, there are two types of artifact VLSs. The artifact VLS which appeared within the first ring of a net plane was denoted an artifact VLS of the first kind such as VLSs 4 and 5 in fig. 18. The artifact VLS which appeared in the first ring of a net plane was denoted by an artifact VLS of the second kind such as VLSs 1 to 3 in fig. 18. The artifact VLSs of the second kind could be avoided only by counting the atomic and vacant lattice sites contained within the first ring. Unfortunately, for a depleted zone which was located in a small plane or in more than two planes we have been forced to include ledge atoms (i.e., the atoms in the first ring) in analyzing this type of depleted zone; in this case we may have included artifact VLSs of second kind as well as artifact VLSs of first kind in our vacancy count of this depleted zone. The number of the artifact VLSs of first kind was estimated as follows: (1) in each plane the number of atomic sites which were used to search for the VLSs within the depleted zone was counted; (2) this number was multiplied by the artifact VLSs of the first kind concentration listed in Table 1 to yield the number of artifact VLSs of the first kind for that plane; and (3) the number of artifact VLSs of the first kind for each plane was then summed to yield the total number of artifact VLSs of the first kind which is then listed in Table 6. In most cases the number of the artifact VLSs of the first kind was $\leq 3\%$ of the total number of VLSs

Table 6: The estimated number of artifact VLSs of first kind that may have been included in each depleted zone

Depleted zone No.	Estimated number of artifact VLSs	Total number of VLSs within the depleted zone	Percentage of the total number of VLSs (%)
DZ1a	2	141	1.4
DZ1b	5	133	3.8
DZ2a	0	159	0
DZ2b	1	121	0.8
DZ3a	1	235	0.4
DZ5b	5	216	2.3
DZ5c	5	160	3.1
DZ5d	1	156	0.6
DZ5e	2	168	1.2
DZ6a	14	241	5.8
DZ6b	5	247	2.0

detected within a depleted zone. In no cases did artifact VLSs of the first kind ever exceed ∿6% of the total number of VLSs within the depleted zone. The number of artifact VLSs of the second kind was found difficult to estimate. However, since the number of ledge atoms was only a small fraction of the total number of atomic sites used to search for VLSs within a depleted zone, the number of artifact VLSs of the second kind should have been only a small fraction of the total number of the VLSs detected within the depleted zone. In addition, the contrast effects of a depleted zone as shown in figs 23, 32 and 40 have never been seen in unirradiated specimens. It was therefore concluded that the depleted zones we observed in irradiated specimens could not had been caused by artifact VLSs of the first and/or second kind.

V.6.3. The Number of VLSs Produced by a Single 30 keV W^+, Mo^+ or Cr^+ Ion

This thesis work provided a direct measurement of the number of Frenkel pairs produced by a single ion with a given amount of incident energy; we denote the value of this quantity ν. The observed values of ν_{exp} produced by a 30 keV W^+ ion is 158; this number is an average for five depleted zones (see Table 2). The value of ν_{exp} produced by a 30 keV Mo^+ ion is 175; this number is an average for four depleted zones (see Table 3). Finally the value of ν_{exp} produced by a 30 keV Cr^+ ion is 244; this number is an average for two depleted zones (see Table 4).

The theoretical estimate of the number of VLSs (and an equal number of SIAs) produced by a single ion with a given amount of incident energy was made according to the modified Kinchin-Pease amorphous solid model. The modified expression for ν is given by

$$\nu_{th} = \kappa \frac{\hat{E}}{2\,\bar{E}_d} \qquad (11)$$

where the quantity ν_{th} is the theoretical value of ν, $\hat{E}$ the damage energy, κ the displacement efficiency which is equal to 0.8 according to both the computer simulations(21) and the analytical calculations,(99) and $\bar{E}_d$ the average displacement threshold energy which was taken to be 42 eV in tungsten.(100) The quantity $\hat{E}$ is related to the incident ion energy E_o by the equation

$$\hat{E} = E_o - \hat{Q} \qquad (12)$$

where $\hat{Q}$ is the total energy lost from the incident ion through all inelastic processes. In the present situation the values of $\hat{Q}$ for 30 keV W^+, Mo^+ and Cr^+ ions were calculated for the Ta^+ on Ta, Ag^+ on Au and Al^+ on Zr situations employing the recent extensive tabulations given by Winterbon;(80) they were 6.9, 8.1 and 9.6 keV respectively. Thus employing eq. (11) the values of the quantity ν_{th} for a single 30 keV W^+, Mo^+ and Cr^+ ions are 220, 210 and 195 respectively; it is noted that the three values are not a strong function of the mass of the incident ion.

Figure 49 shows the experimental values of ν_{exp} and the calculated values of ν_{th} are also indicated by the dash line for comparison. Figure 49 seems to indicate that the value of ν_{exp} increases as decreasing the mass of the incident ion; we were, however, unable to conclude for certain this dependence of ν_{exp} on the mass of the incident ion because of the limited number of observations. Alternatively, to first order we may assume that the value of ν_{exp} is independent of the mass of the incident ion in this range of mass; we then obtained a value of $\langle\nu\rangle_{exp} = 180 \pm 44$ which represents an average of the total eleven depleted zones. It should be noted that the deviation between the values of $\langle\nu\rangle_{exp}$ and ν_{th} can not, at present, be over-emphasized since the value of ν_{th} is not well known.

Recently, Averback et al.(101) employed thin-film residual-resistivity measurements to determine point-defect production below 10 K in both copper and silver irradiated with ion masses between 1 and 209 amu in the energy range between 20 and 850 keV. The number of Frenkel pairs N_F produced by an incident ion was calculated from the expression(102-103)

$$N_F = \frac{N \cdot t}{\rho_F} \left(\frac{d\Delta\rho}{d\phi}\right)_o \qquad (13)$$

where N is the atomic density, t is the film thickness, ρ_F is the Frenkel-pair resistivity and $\left(\frac{d\Delta\rho}{d\phi}\right)_o$ is the size-effect-corrected initial damage rate.

They then defined a cascade efficiency ξ_a as

$$\xi_a = N_F/N_F^t \qquad (14)$$

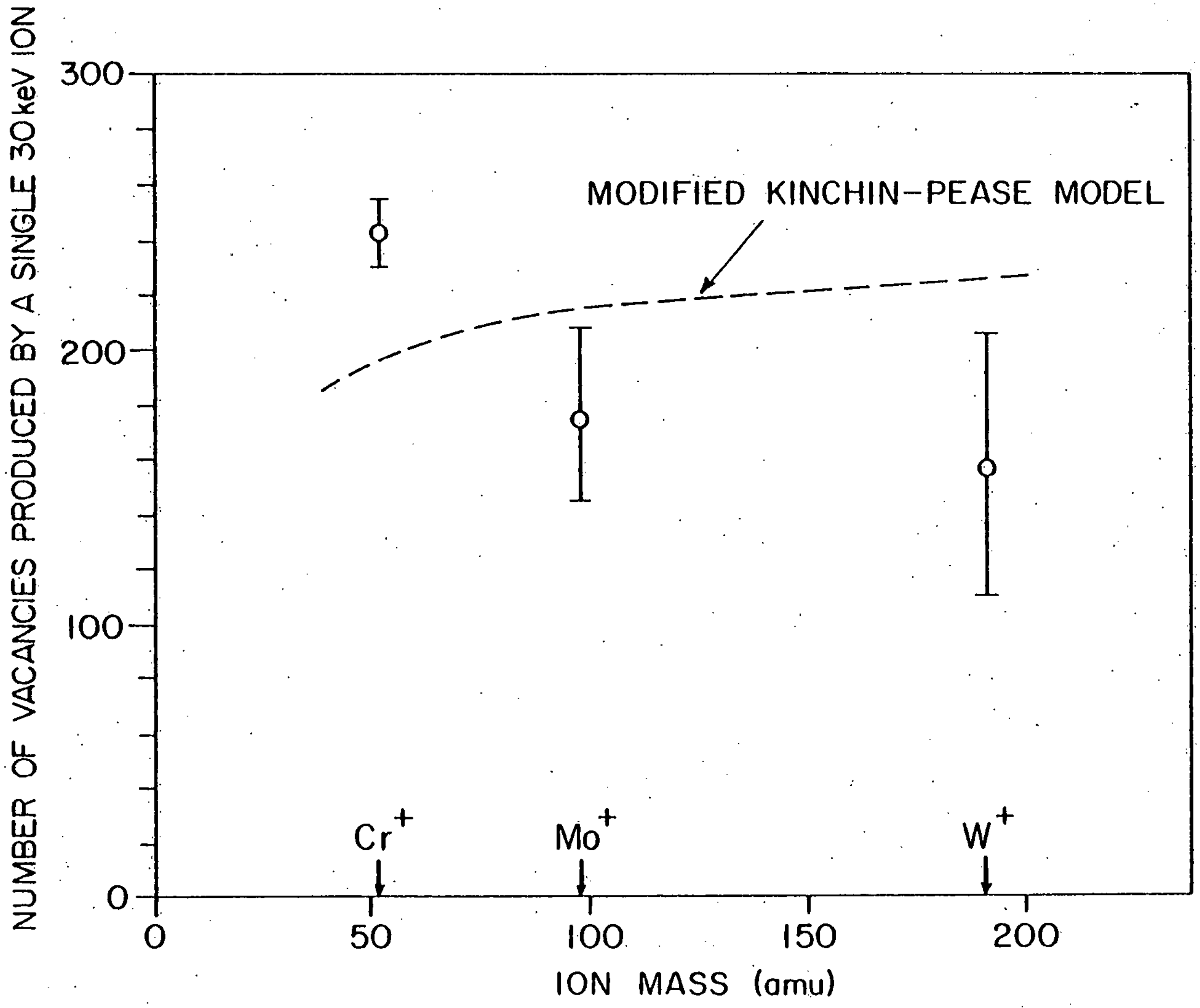

Figure 49: The experimental value of the number of vacant lattice sites produced by a single 30 keV W^+, Mo^+ or Cr^+ ion. The dash line indicates the theoretical curve estimated from the modified Kinchin-Pease model.

where the quantity N_F^t is the theoretical value(101) of the number of Frenkel-pairs; their values of N_F^t are almost the same as the values of ν_{th} calculated from the Winterbon's tabulations.(80) They found that the cascade efficiency decreased with ion mass for light projectiles, whereas at masses >20 the cascade efficiency remained rather constant and assumed a value of $\xi_a \approx 0.3$ for both Ag and Cu. This small cascade efficiency was explained, in part, as a result of the reduced resistivity contribution from VLS clusters within a depleted zone and, in part, by dynamic close-pair recombination effects.(104-106)

It has been shown(106) that residual resistivity measurement give a lower value of $\xi_a \approx 0.1$ above stage III* in Au and Ag, compared to $\xi_b \approx 0.4$ from TEM measurements; above stage III a considerable fraction of the defects survived in the form of clusters. A possible explanation for this low value of ξ_a in residual resistivity measurements is simply the low scattering probability per VLS for the VLS clusters.** Thus the residual resistivity measurements could have considerably underestimated the number of Frenkel pairs within a cascade.

On the other hand, Averback et al.(104) studied the isochronal recovery of electrical resistivity in silver

---

* Stage III starts at ∿500 K.

** A 50% reduction in resistivity seems reasonable for clusters containing several hundred VLSs.(109)

after 200 keV H^+, 225 keV Ne^+ and 720 keV Bi^{+++} irradiations. They found that the fraction of the total recovery in Stage I was 60, 29 and <5% for proton, neon and bismuth irradiations, respectively. In addition, they found no close-pair recovery below stage I_D ($T<23$ K) for bismuth irradiations; this compared with ∿7% close-pair recovery for proton irradiations. This result indicates that the cascade energy density* or the local defect concentration played an important role in determining the amount of recovery in stage I. They also studied the isochronal recovery in copper after proton, helium, argon and bismuth irradiation to two different dose levels. The fraction of the total recovery in stage I for the low dose case was 65, 62, 32 and 15% for proton, helium, argon and bismuth respectively. After high-dose irradiation, the fraction of the total recovery in stage I was reduced to 42, 29, 11 and 5% for proton, helium, argon and bismuth respectively. However, even after the high-dose proton irradiation with a radiation induced resistivity increment ($4.8\times10^{-7}\Omega$cm) that is close to the value reported for the saturation resistivity for fast neutron damage (4.7×10^{-7} Ωcm)(110) they found that the fraction of the total recovery in stage I (42%) was much greater then the recovery after the low-dose bismuth bombardment (15%). Therefore they con-

---

* The cascade energy density is defined as the mean energy deposited per target atom.(111)

cluded that, compared to the influence of the local defect concentration, the cascade energy density had a much greater effect on determining the fraction of the total recovery in stage I.

The observed decrease in the fraction of the total recovery in stage I as the cascade energy density increased, was believed to be caused, in part, by the instability of close-pairs in the vicinity of energetic displacement cascade. This dynamic close-pair recombination effect reduced the number of Frenkel pairs which could have had survived from recovery within a cascade even though the cascade was produced at a low temperature; i.e., a temperature at which no point defects were mobile. This dynamic close-pair recombination effect seem to be shown also in our FIM experiment if the observed dependence of ν_{exp} on the mass of ion was not a result of statistical fluctuation. It is, however, noted that no final decision can be made, at present, regarding the importance of the dynamic close-pair recombination effect in our FIM experiments because neither the theoretical value of ν_{th} nor the experimental value of ν_{exp} are known well enough to reach a firm conclusion.

V.6.4. The Point-Defect Structure of a Depleted Zone Produced by a Single 30 keV W^+, Mo^+ or Cr^+ Ion

Figures 50a to 50c show three computer-generated isometric drawings of DZ1a, DZ4b and DZ5b respectively; they are plotted approximately to scale for an easy comparison. Figure

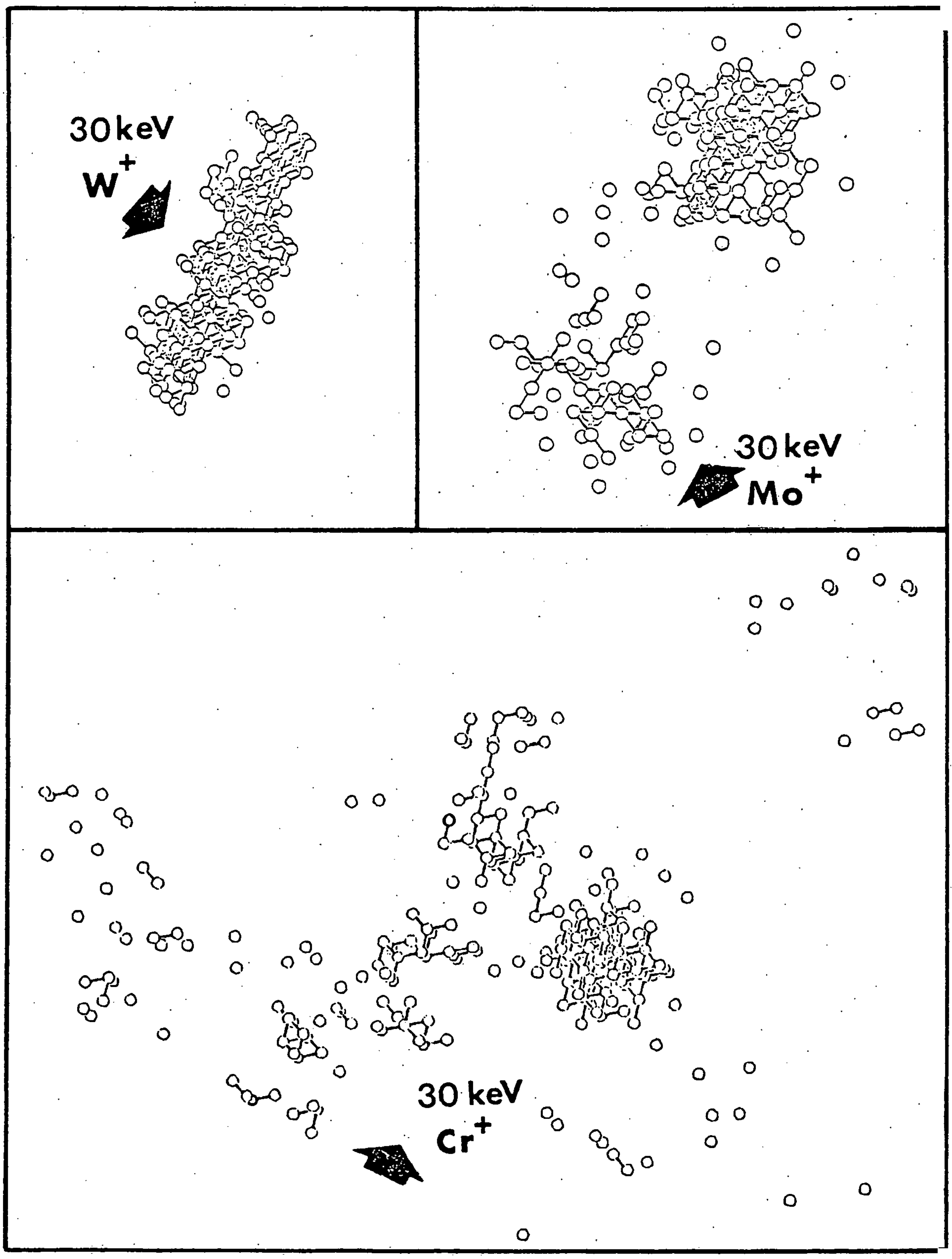

Figure 50: Three computer-generated isometric drawings of depleted zones DZ1a, DZ4b and DZ5b are plotted to scale.

50 shows very clearly that the depleted zone produced by a 30 keV W^+ ion consisted of mainly one jumbo vacancy cluster; that produced by a 30 keV Mo^+ ion splited into two subcascades; and that produced by a 30 keV Cr^+ ion exhibited the formation of several subcascades. The significant difference in the cascade structure is further explored in fig. 51 which shows the values of R(i)/Z(i) for each depleted zone. Figure 51 shows clearly that the distribution of VLSs within each depleted zone exhibited clustering and the degree of clustering decreased as the mass of incident ion was decreased; it is noted that the values of R(i)/Z(i) approach zero if the VLSs are distributed randomly in an infinite volume of crystal. In addition, fig. 52 shows the $\overline{N}(i)$s as a function of r_i for each depleted zone. As one can readily see for the case of the depleted zone produced by a W^+ ion that there is only one narrow peak at $r_i \approx 10$ A; for that produced by a Mo^+ ion a second peak at $r_i \approx 30$ A grows at the expense of the first peak; and for that produced by a Cr^+ ion the second peak dominates and a third peak shows up at $r_i \approx 45$ A. Figure 52 clearly indicates that the depleted zone becomes more extended as the mass of incident ion is decreased and the formation of subcascades became more evident for the lighter ion; these can be understood at least qualitatively by noting that between collisions the mean-energy transfer decreased while the mean free path increased as the mass of the incident ion became decreased, because of the greater mass mismatch between the incident

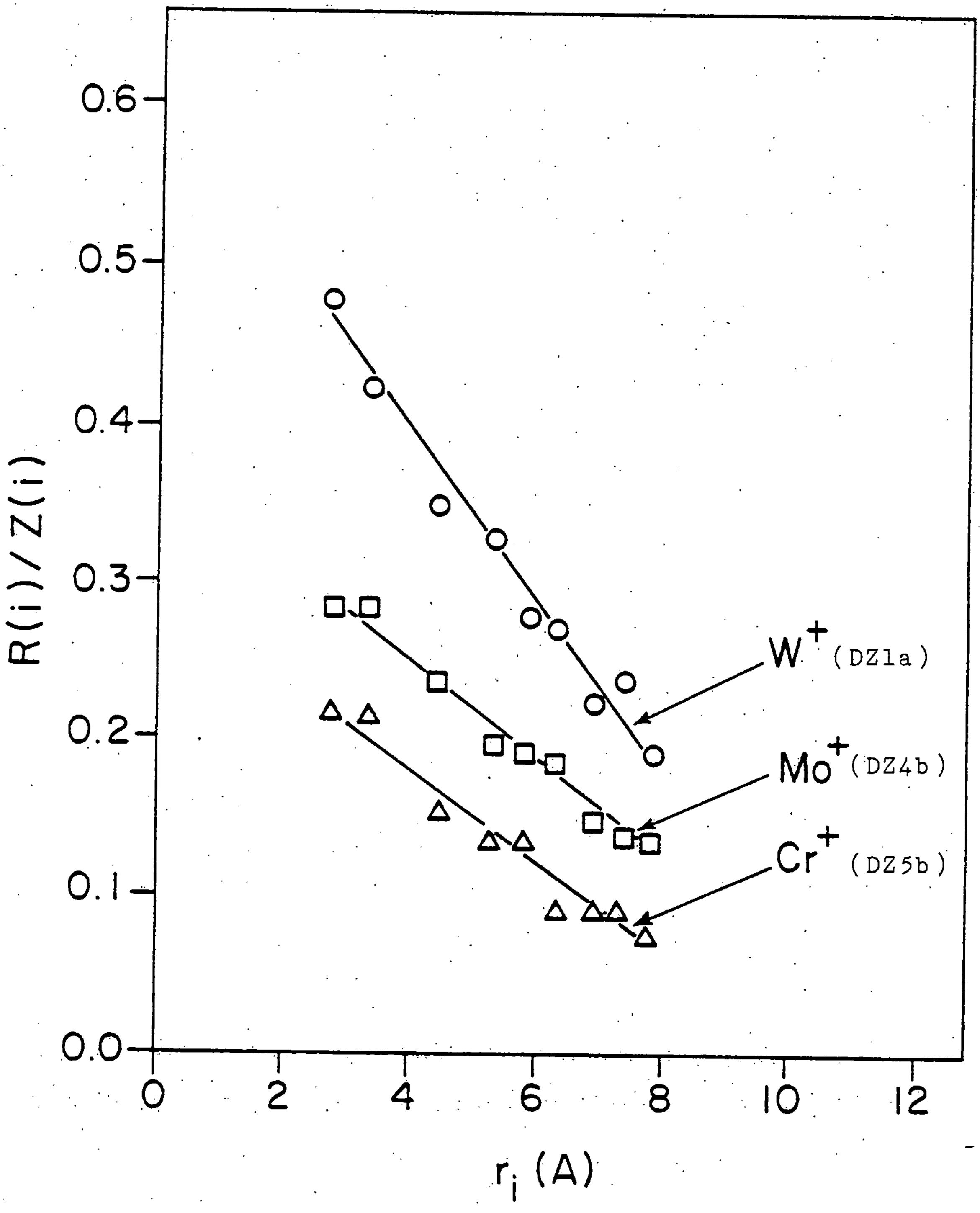

Figure 51: The normalized radial distribution function [R(i)/Z(i)] for depleted zones Dzla, DZ4b and DZ5b.

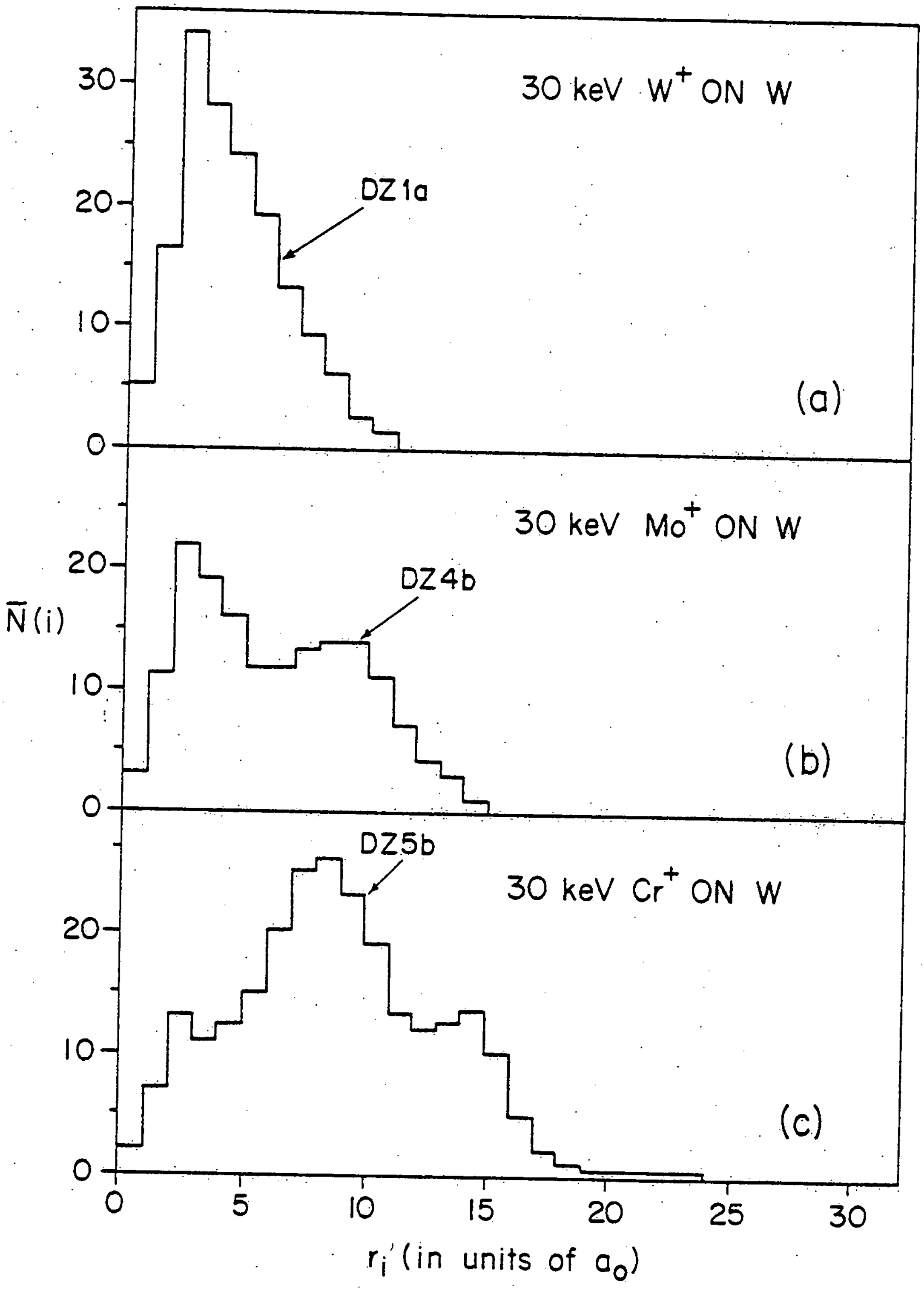

Figure 52: The spectra of the $\overline{N}(i)$s for depleted zones DZ1a, DZ4b and DZ5b.

ion and the target atom. This increased volume as the mass of the incident ion was decreased is consistent with the measured values of c_v as shown in fig. 53.

The only other technique which is comparable to the present results in regard to the detailed point-defect structure of the depleted zone is the computer simulation technique. The results of the point-defect structure of depleted zone for the bcc metal by the computer simulation technique have been obtained for α-iron(17) and tungsten(108) at 0 K; the primary knock-on atom (PKA) energy was in the range 0.5 to 20 keV. Although the energy range of the PKA was not the same as the one we used in the present studies, several significant qualitative comparisons can still be made. First, we observed for seven out of eleven depleted zones an elongation along a <110> type direction which was first observed by Beeler in the computer simulation and was atributed to the quasi-channeling* along a <110> type direction. Secondly, the present results also show clearly that the depleted zone consisted of a vacancy-rich core surrounded by a mantle of SIAs; the separation of SIAs from the vacancy-rich core was

---

* Quasi-channeling refers to channeling of shorter range than the channeling that may occur along the <100>, <110> and <111> tunnel-like cores in the bcc structure. Beeler(17) stated that quasi-channeling trajectories exhibit intermittent low-index channeling and are confined between two closely adjacent atom planes.

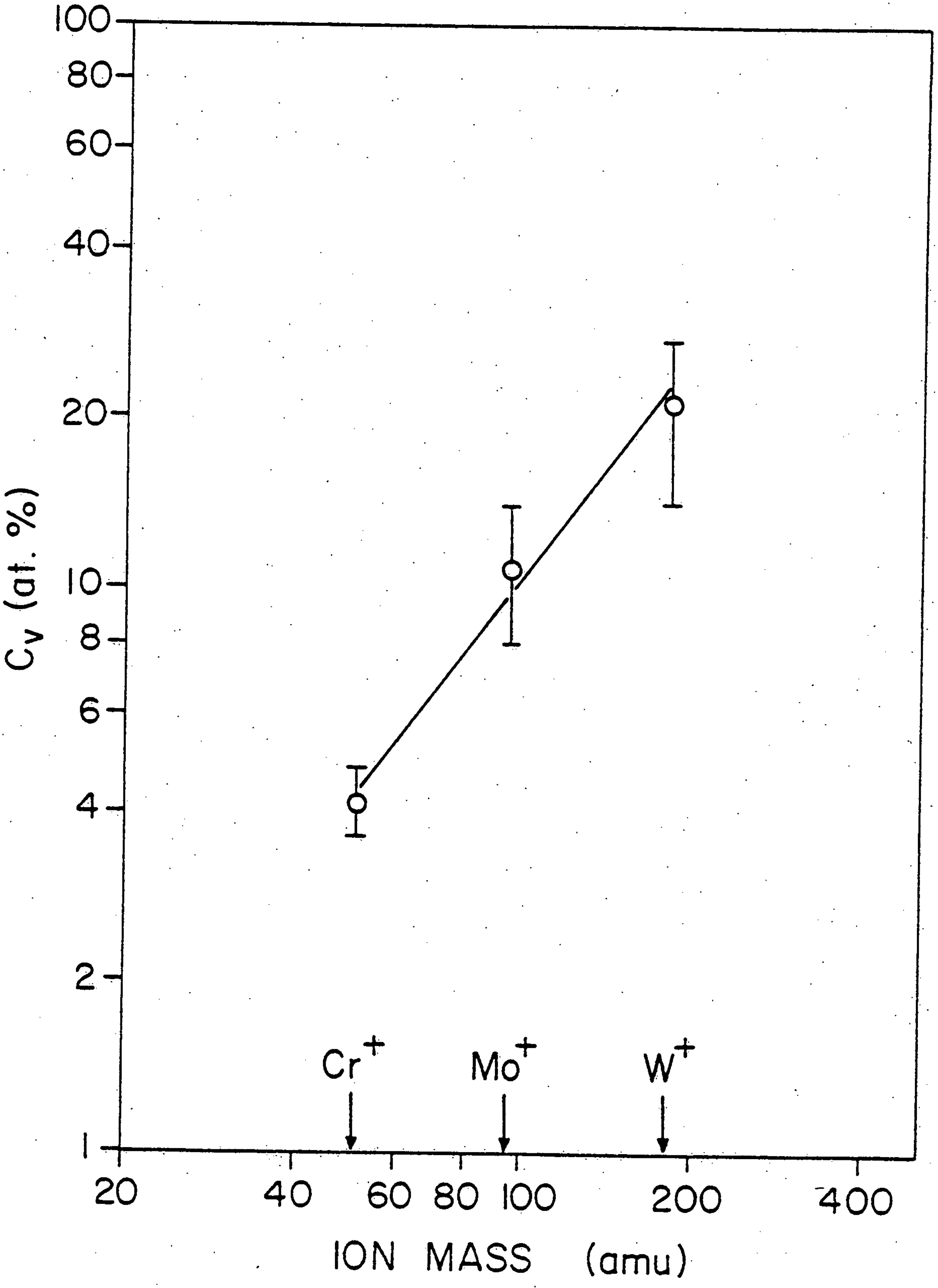

Figure 53: The average vacancy concentration c_v within a depleted zone as a function of the mass of the incident ion.

discussed in detail in sect. V.6.7. Thirdly, the major difference between the computer simulation results and the present work is the distribution of VLS cluster sizes; the computer simulation(108) showed that the majority of the VLSs within the depleted zone are in the form of mono-VLS or VLS cluster of size ≤ 5 whereas in Table 7 the FIM results show that most of VLSs within the depleted zone actually formed clusters of size >10. Torrens and Robinson(20) also showed, employing the computer simulation technique, that if N_i is the number of clusters of i vacant lattice sites in a depleted zone there exists a constant cluster factor f_c where

$$f_c = N_{i+1}/N_i . \qquad (15)$$

Thus if there are N_1 monovacancies there will be f_cN_1 divacancies, $f_c^2N_1$ trivacancies and so on. They performed their computer simulation experiments on copper, iron and gold, but did not perform it, unfortunately, for tungsten. In the case of gold they found that this empirical rule was less well obeyed than in the case of copper and iron, because of the formation of large clusters. In this sense our results on tungsten are similar to their computer results on gold.

It should be noted that the computer simulations are sensitive to the interatomic potential employed and therefore are model-dependent. Thus the present FIM studies present the only experimental technique which can reveal the point-defect structure of a depleted zone created by an energetic ion.

Table 7: Distribution of VLS cluster sizes for a depleted zone produced by a 30 keV W^+, Mo^+ or Cr^+ ion

Cluster size (n)	Fraction of the total number of VLSs		
	W^+	Mo^+	Cr^+
1	0.13	0.19	0.28
2	0.02	0.06	0.06
3	0.01	0.03	0.05
4	0.01	0.01	0.02
5	0.00	0.01	0.05
≥ 6	0.83	0.70	0.54

V.6.5. The Size of a Depleted Zone

In this section a comparison is made between the measured and the calculated size of a depleted zone in pure tungsten created by a single 30 keV W^+, Mo^+ or Cr^+ ion. The effective diameters of depleted zones produced by a W^+, Mo^+ and Cr^+ ion were respectively given by the average value of $\bar{\lambda}$ as listed in Table 2, 3 and 4. The expected diameter of a depleted zone was taken to be given by $2\langle y^2\rangle^{1/2}$(84) where $\langle y^2\rangle^{1/2}$ is the second moment of the elastic ion-energy distribution curve which is perpendicular to the direction of the incident ions. An estimate of the quantity $\langle y^2\rangle^{1/2}$ was made employing Winterbon's tabulations(80) which is based on the WSS theory(107) (see also sect. IV.6.3). Table 8 gives a comparison between the experimental values of $\bar{\lambda}_{exp}$ and the calculated values of $\bar{\lambda}_{th} = 2\langle y^2\rangle^{1/2}$. It is apparent that the calculated values of $\bar{\lambda}_{th}$ are consistently greater than the observed values of $\bar{\lambda}_{exp}$ by a factor of ~ 2; this disagreement is not too surprising because the WSS theory calculates the total distribution of the fraction of ion energy elastically deposited in atom motion which bears no simple direct relationship to the size of a single depleted zone. Jenkin and Wilkens(85) studied the displacement cascades in ordered Cu_3Au irradiated with 5-100 keV Cu^+ ions; they found that each incident ion of energy ≥ 10 keV created, at the core of the resulting displacement cascade, a zone of reduced long-range order which was imaged in the TEM. The diameter of the

Table 8: Comparison with the WSS theory

Irradiating ion	M_1/M_2*	$\bar{\lambda}_{th}$** (A)	$\bar{\lambda}_{exp}$ (A)	$\bar{\lambda}_{exp}/\bar{\lambda}_{th}$
W^+	1	32	18	0.56
Mo^+	0.52	50	25	0.5
Cr^+	0.28	84	42	0.5

* The quantities M_1 and M_2 are the mass of the incident ion and the target atom respectively.

** The value of the quantity λ_{th} is given by $2\langle y^2\rangle^{\frac{1}{2}}$ which was calculated according to the tabulations given by Winterbon(80); the tabulations were based on the WSS theory.(107)

disordered zones as a function of ion energy were measured and compared with the values of the quantity $2\langle y^2\rangle^{1/2}$ calculated from the WSS theory. The measured diameters agreed reasonably well with the theoretical calculations, except that at high energies (≥ 40 keV) the experimental values fell below the theoretical values. It was, however, felt that this agreement might be somewhat fortuitous as far as the absolute scale is concerned.(85) It should be noted that the disordered zone created as the result of replacements between Cu and Au atoms is different from the region of vacancy damage which we referred to as the depleted zone. Hence, their result should not be taken as an absolute measurement of the size of a depleted zone. It is therefore suggested that the quantity $\langle y^2\rangle^{1/2}$ is a better estimate of the size of a single depleted zone as opposed to the quantity $2\langle y^2\rangle^{1/2}$ originally suggested by Westmoreland and Sigmund.(84)

V.6.6. The Number of SIAs

The number of SIAs detected in all the specimens was always much less than the total number of VLSs observed. Possible physical reasons, in combination, for the SIAs uncounted for are: (1) only a small fraction ($\sim$0.1 to 0.2)* of the total tip volume was employed to search for SIAs; (2) the

---

* This value was extimated from the total number of atoms which was scanned and the total number of atoms within the tip volume. The tip volume (V_{tip}) was given by

$$V_{tip}=(\pi/3)(r_1^3-r_0^3)(1-\sin\omega)^2/\sin\omega \qquad (16)$$

where the quantities r_0 and r_1 are the initial and final tip radii and ω is the shank angle of the tip specimen.

SIAs were most likely not distributed randomly in the specimen and we did not search the volume in which the majority of SIAs were located; (3) if the average RCS chain length was greater than the tip's radius not all the RCSs would have been observed in the FIM image; and (4) the RCS produced on the incident beam side of the specimen were most likely shot out of the specimen, hence these RCSs would not have been detected in the FIM image. The fact that the low SIA concentration found in the W^+ or Mo^+-irradiated specimen of small tip radius (∿200 A) and the high SIA concentration observed in the Cr^+-irradiated specimen of large tip radius (∿400 A) is consistent of reason (3). Reason (4) is also evident in fig. 47 that only few SIAs were detected in the half of the specimen which has been exposed to the ion beam.

V.6.7. The Range of Replacement Collision Sequences

In this section the mean separation between the SIAs and depleted zones (see figs. 47 and 48) are discussed respectively in a quantitative manner.

In fig. 47 the distances between each SIA and depleted zones DZ5a to DZ5e were measured respectively. The close-packed directions (i.e., <100>, <110> and <111> directions) pointing from each SIA to the cross-sectional area of each depleted zone was also determined; the direction was measured simply from the SIA to the center of the depleted zone if no close-packed direction was found. The distances between each SIA and the specimen's surface on the beam side were also measured along all the possible <100> , <110> and

<111> directions.* We also included the specimen's surface on the beam side because a depleted zone might not be reconizable in the FIM image if this depleted zone located near the surface of the shank of the specimen; this depleted zone was most likely imaged near the edge of the total FIM image where a plane (or planes) might not be fully resolved. Since for all these measured distances we do not know which one was actually traversed by a given SIA, we were forced to take whichever distance was shortest as a lower bound of the propagation distance (denoted by R_{min}).† The results of the measured R_{min} for the total 97 SIAs are plotted in fig. 54; they ranged up to 400 A and the mean value is $<R>_{min} = 175 \pm 110$ A. It should be noted that the spectrum in fig. 54 is a result of the way of analyzing data and therefore may not represent the actual RCS range distribution curve. Figure 54, however, does indicate that the actual spectrum must be shifted to the right. The most striking result in fig. 54 is that almost 50% of the total number of SIAs must have propagated a distance of ≥200 A.

The long RCS chain length indicated in fig. 54 was also observed in a specimen irradiated with 18 keV Au^+ ions (see also fig. 48). In this specimen depleted zones were created

---

* The RCSs most likely propagated along the <100>, <110> and <111> directions.(7-9)

† A depleted zone was excluded occasionally if the direction pointing from this depleted zone to the SIA was not a close-packed direction.

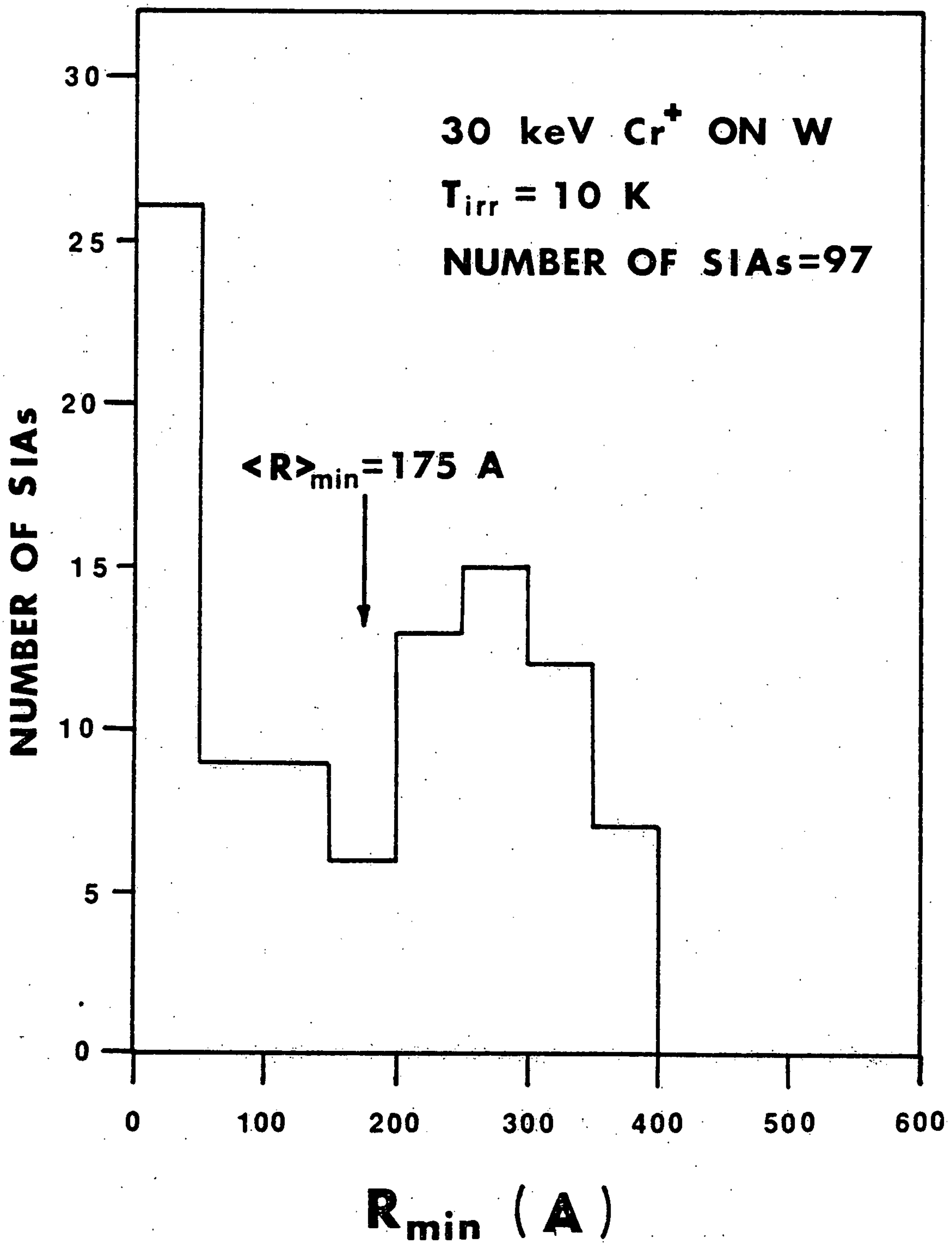

Figure 54: The spectrum of R_{min} in a specimen irradiated with 30 keV Cr$^+$ ions.

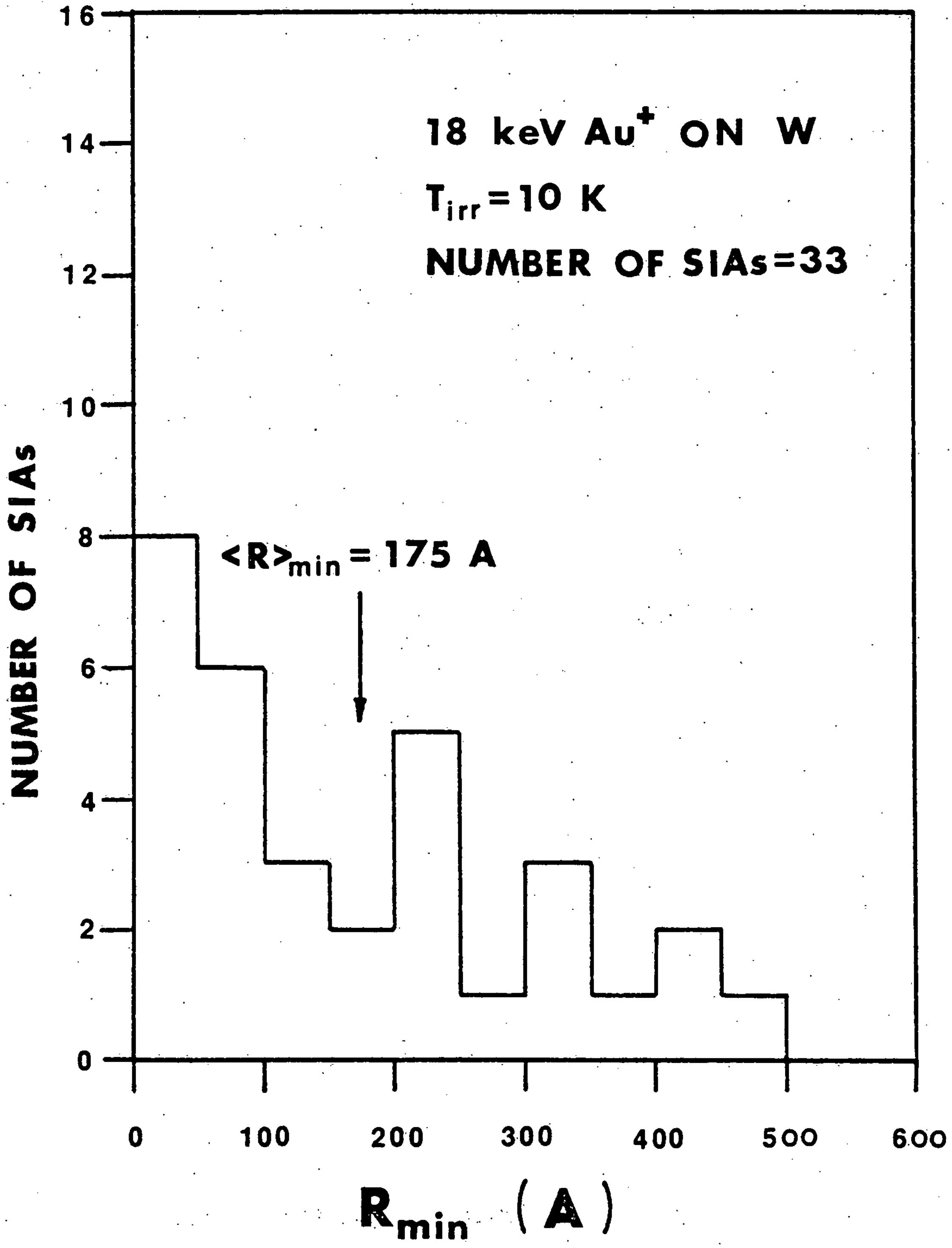

Figure 55: The spectrum of R_{min} in a specimen irradiated with 18 keV Au^+ ions.

within ≤ 30 A from the irradiated surface. Thus, the distances between each SIA and the specimen's surface on the beam side were measured along the possible [100], [110] and [111] types of crystallographic direction. Once again, we took whichever distance was shortest as the value of the quantity R_{min} for this SIA. The results for a total of 33 SIAs are plotted in fig. 55; they ranged up to 500 A. The value of $\langle R \rangle_{min}$ was 175 ±130 A. It is noted that ∿40% of the total number of SIAs propagated a distance of ≥200 A. It should be emphasized that in this experiment we employed a smaller kinetic energy and a bigger atomic mass of the incident ion to minimize the channeling of the incident ion. Thus, the possibility that the long RCS chain lengths (≥200 A) were caused by the dechanneled ions can be neglected. It was concluded on the basis of the results in figs. 54 and 55 that the lower bound for the average RCS chain length is ∿175± 85 A.

REFERENCE

1. J. A. Brinkman, J. Appl. Phys. 25, 961 (1954).
2. J. A. Brinkman, Am. J. Phys. 24, 246 (1956).
3. A. Seeger, in Proc. 2nd UN Int. Conf. Peaceful Uses of Atomic Energy (Geneva, 1958), Vol. 6, p. 250.
4. A. Seeger, in Radiation Damage in Solids (International Atomic Energy Agency, Vienna, 1962), Vol. 1, p. 101.
5. R. H. Silsbee, J. Appl. Phys. 28, 1246 (1957).
6. M. W. Thompson, Defects and Radiation Damage in Metals (Cambridge University Press, Cambridge, 1969), p. 196.
7. J. B. Gibson, A. N. Goland, M. Milgram and G. H. Vineyard, Phys. Rev. 120, 1229 (1960).
8. C. Erginsoy, G. H. Vineyard and A. Englert, Phys. Rev. 133, A595 (1964).
9. C. Erginsoy, G. H. Vineyard and A. Shimuzu, Phys. Rev. 139, A118 (1965).
10. M. Yoshida, J. Phys. Soc. Japan 16, 44 (1961).
11. M. T. Robinson and O. S. Oen., Phys. Rev. 132, 1385 (1963).
12. O. S. Oen., D. K. Holmes and M. T. Robinson, J. Appl. Phys. 34, 302 (1963).
13. J. R. Beeler, Jr. and D. G. Besco, J. Appl. Phys. 34, 2873 (1963).
14. J. R. Beeler, Jr., J. Appl. Phys. 35, 2226 (1964).
15. J. R. Beeler, Jr., J. Appl. Phys. 37, 3000 (1966).
16. J. R. Beeler, Jr., Phys. Rev. 150, 470 (1966).
17. D. G. Doran, Rad. Effects 2, 249 (1970).
18. D. G. Doran and R. A. Burnett, in Interatomic Potentials and Simulation of Lattice Defects, edited by P. C. Gehlen, J. R. Beeler, Jr., and R. I. Jaffee (Plenum, New York, 1972), p. 403.

19. I. M. Torrens and M. T. Robinson, in Interatomic Potentials and Simulation of Lattice Defects, edited by P. C. Gehlen, J. R. Beeler, Jr., and R. I. Jaffee (Plenum, New York, 1972), p. 423.

20. M. T. Robinson and I. M. Torrens, Phys. Rev. B. 9, 5008 (1974).

21. D. K. Holmes and M. T. Robinson in Atomic Collisions in solids edited by S. Datz, B. R. Appelton and C. D. Moak (Plenum, New York, 1974), Vol. 1, p. 225.

22. For reviews of the FIM technique and some of its applications see:
    (a) Field-Ion Microscopy, edited by J. J. Hren and S. Ranganathan (Plenum, New York, 1968);
    (b) E. W. Muller and T.-T. Tsong, Field-Ion Microscopy (American Elsevier, New York, 1969);
    (c) K. M. Bowkett and D. A. Smith, Field-Ion Microscopy (North-Holland, Amsterdam, 1970);
    (d) E. W. Müller and T.-T. Tsong, in Progress in Surface Science, edited by A. G. Davison (Pergamon Press, Oxford, 1973), Vol. 4, Part 1, pp. 1-139.

23. L. A. Beavan, R. M. Scanlan and D. N. Seidman, Acta Met. 19, 1339 (1971).

24. R. M. Scanlan, D. L. Styris and D. N. Seidman, Phil. Mag. 23, 1439 (1971).

25. R. M. Scanlan, D. L. Styris and D. N. Seidman, Phil. Mag. 23, 1459 (1971).

26. K. L. Wilson and D. N. Seidman in Nuclear Energy, Proc. Inter. Conf. on Defects and Defect Clusters in B.C.C. Metals and Their Alloys, edited by R. J. Arsenault (National Bureau of Standards, Gaithersburg, Maryland, 1973), Vol. 18, p. 216.

27. W. Hunz, Phys. Stat. Sol. (b), 48, 387 (1971).

28. M. J. Attardo and J. M. Galligan, Phys. Rev. Lett. 17, 191 (1966).

29. T. Inal and J. M. Galligan, Acta Met. 18, 557 (1970).

30. M. J. Attardo and J. M. Galligan, Phys. Stat. Sol. 16, 449 (1966).

31. J. T. Buswell, Phil. Mag. 21, 357 (1970).

32. J. T. Buswell, Phil. Mag. 23, 293, (1971).

33. P. Pétroff and J. Washburn, Phys. Stat. Sol. 32, 527 (1969).

34. M. A. Fortes and B. Ralph, Phil. Mag. 14, 188 (1966).

35. J. A. Hudson, R. S. Nelson and B. Ralph, Phil. Mag. 18, 839 (1968).

36. J. A. Hudson, B. L. Dury and B. Ralph, Phil. Mag. 21, 779 (1970).

37. J. A. Hudson and B. Ralph, Phil. Mag. 25, 265 (1972).

38. C. A. English, B. L. Eyre and J. Summers, Harwell Report AERE-R7960 (1975).

39. J. T. Buswell, Phil. Mag. 22, 787 (1970).

40. M. Wilkens, in Inter. Conf. on Fundamental Aspects of Radiation Damage in Metals, edited by M. T. Robinson and F. W. Young, Jr., (National Technical Information Service, Springfield, Virginia, 1975), p. 98.

41. M. Wilkens in Vacancies and Interstitials in Metals, edited by A. Seeger, D. Schumacher, W. Schilling and J. Diehl (North-Holland, Amsterdam, 1970), p. 485.

42. B. L. Eyre, in Defects in Refractory Metals, edited by R. de Batist, J. Nihoul and L. Stals (S.C.K./C.E.M., Mol, 1972), p. 311.

43. B. L. Eyre, J. Phys. F: Metal Phys. 3, 422 (1973).

44. B. L. Eyre, M. H. Loretto and R. E. Smallman, Harwell Report AERE-R8621 (1976).

45. C. A. English, B. L. Eyre and M. L. Jenkins, Nature 263, 400 (1976).

46. K. L. Merkle, in Radiation Damage in Metals, edited by N. L. Peterson and S. D. Harkness (American Society for Metals, Metals Park, Ohio, 1976), p. 58.

47. P. B. Hirsch, A. Howie, R. B. Nicholson, D. W. Pashley and M. J. Whelan, Electron Microscopy of Thin Crystals (Butterworths, Washington, D. C. , 1965).

48. M. W. Thompson, Defects and Radiation Damage in Metals (Cambridge University Press, Cambridge, 1969), p. 143.

49. D. N. Seidman and K. H. Lie, Acta Met. 20, 1045 (1972).

50. J. T. Robinson, K. L. Wilson and D. N. Seidman, Phil. Mag. 27, 1417 (1973).

51. P. Pétroff and D. N. Seidman, Appl. Phys. Lett. 18, 518 (1971).

52. P. Pétroff and D. N. Seidman, Acta Met. 21, 323 (1973).

53. D. N. Seidman, J. Phys. F: Metal Phys. 3, 393 (1973).

54. K. L. Wilson and D. N. Seidman, Rad. Effects 27, 67 (1975).

55. D. N. Seidman, K. L. Wilson and C. H. Nielsen, in Proc. of International Conference on Fundamental Aspects of Radiation Damage in Metals, edited by M. T. Robinson and F. W. Young, Jr. (National Technical Information Service, Springfield, VA, 1975), Vol. 1, p. 373.

56. D. N. Seidman, in Radiation Damage in Metals, edited by N. L. Peterson and S. D. Harkness (American Society for Metals, Metals Park, OH, 1976), p. 28-57.

57. C.-Y. Wei and D. N. Seidman, Rad. Effects 32, 229 (1977).

58. D. N. Seidman, R. M. Scanlan, D. L. Styris and J. W. Bohlen, J. Sci. Instrum. 2, 473 (1969).

59. D. G. Brandon, S. Ranganathan and D. S. Whitmell, Brit. J. Appl. Phys. 15, 55 (1964).

60. Only a very small fraction of total cross-sectional area of the ion beam actually hits the specimen to produce radiation damage; a typical value of the total cross-sectional area is 0.5 cm^2.

61. S. S. Brenner and J.T. McKinney, Surf. Sci. 23, 88 (1970).

62. The Sylvania No. 160 phosphor (p-1) is a Zn_2SiO_4:Mn material which has a fluorescent and phosphorescent color in the green; it is a medium peristence phosphor.

63. R. Gomer, Field-Emission and Field-Ionization (Harvard University Press, Cambridge, MA, 1961), p. 168-9.

64. F. Rosebury, Handbook of Electron Tube and Vacuum Techniques (Addison-Wesley, Reading, MA, 1965), p. 207.

65. For example, see Linear Applications (National Semiconduc-

tor Corp., Santa Clara, CA, 1973), p. AN31-1 for a description of the operation amplifier used in the dosimeter circuit.

66. D. N. Seidman, J. Phys. F: Metal Phys., **3**, 393 (1973).

67. D. N. Seidman, in *Radiation Damage in Metals*, edited by N. L. Peterson and S. D. Harkness (American Society for Metals, Metals Park, OH, 1976), p. 28.

68. M. J. Attardo and J. M. Galligan, Phys. Rev. **161**, 558 (1967).

69. W. Schilling, K. Sonnenberg and H. J. Dibbert, Rad. Effects, **16**, 57 (1972).

70. C. K. Johnson, Oak Ridge National Laboratory (USA) Report 3794 (1965) plus revisions (1970).

71. C. G. Chen and R. W. Balluffi, Acta Met.**23**, 931 (1976).

72. E. W. Müller and T.-T. Tsong, *Field-Ion Microscopy* (American Elsevier, New York, 1969), p. 119.

73. D. N. Seidman and R. M. Scanlan, Phil. Mag., **23**, 1429 (1971).

74. R. M. Scanlan, D. L. Styris, D. N. Seidman and D. G. Ast, Cornell Materials Science Center Report #1159 (1969).

75. A. J. W. Moore and J. F. Nicholas, J. Phys. Chem. Solids, **20**, 222 (1961).

76. W. B. Pearson, *A Handbook of Lattice Spacing Structure of Metals and Alloys* (Pergamon Press, 1958), Vol. 1, p. 821.

77. M. A. Jaswon and D. B. Dove, Acta Cryst., **8**, 88 (1955).

78. J. F. Nicholas, *An Atlas of Models of Crystals Surfaces* (Gordon and Breach, New York 1965).

79. G. H. Kinchin and R. S. Pease, Rep. Prog. Phys. **18**, 1 (1955).

80. K. B. Winterbon, *Ion Implantation Range and Energy Deposition Distributions: Low Incident Energies* (IFI/Plenum, New York, 1975).

81. P. Lucasson, in *Inter. Conf. on Fundamental Aspects*

of Radiation Damage in Metals, edited by M. T. Robinson and F. W. Young, Jr., (National Technical Information Service, Springfield, VA, 1975), p. 42.

82. P. Sigmund, Revue Roum. Phys., 17, 823 (1972).

83. M. T. Robinson, in Radiation Induced Voids in Metals, edited by J. W. Corbett and L. C. Lanniello, (U.S.Atomic Energy Commission, Washington, D. C., 1972), p. 397.

84. J. E. Westmoreland and P. Sigmund, Rad. Effects, 6, 187 (1970).

85. M. L. Jenkins and M. Wilkens, Phil. Mag., 34, 1155 (1976).

86. J. A. Sigler and D. Kuhlmann-Wilsdorf, in The Nature of Small Defect Clusters, edited by M. J. Makin (H. M. Stationary Office, London, 1966), p. 125.

87. R. A. Johnson, Phil. Mag. 16, 553 (1967).

88. M. J. Makin, in The Nature of Small Defect Clusters, edited by M. J. Makin (H. M. Stationary Office, London, 1966).

89. M. Rühle and M. Wilkins, Cryst. Lattice Defects, 6 129(1975).

90. R. Schindler, Dr. rer. nat. Thesis, University of Stuttgart, West Germany (1977).

91. E. J. Savino and R. C. Perrin, J. Phys. F: Metal Phys., 4, 1889 (1974).

92. E. Ruedl, P. Delavignette and S. Amelinckx, in Radiation Damage in Solids (IAEA, Vienna, 1962), Vol. 1, p. 363.

93. M. Rühle, F. Häusserman and M. Rapp, Phys. Stat. Sol., 39, 621 (1970).

94. J. Silcox and M. J. Whelan, Phil. Mag., 5, 1 (1960).

95. B. F. Addis, private communication.

96. J. Y. Park, Ph.D. Thesis, Cornell University (1975).

97. A. S. Burger, D. N. Seidman and R. W. Balluffi, Acta Met. 21, 123 (1973).

98. C. G. Chen and R. W. Balluffi, Acta Met. 23, 919 (1975).

99. P. Sigmund, Rad. Effects, 1,15 (1969).

100. J. A. DiCarlo and J. T. Stanley in Defects in Refractory Metals, edited by R. de Batist, J. Nihoul and L. Staals (Studiecentrum voor Kernenergiel Centre d'Etude de l'Energie Nuclearie, Mol, Belgium, 1972), p. 13.

101. R. S. Averback, R. Benedek and K. L. Merkle, in International Conference on the Properties of Atomic Defects in Metals, Argonne, Illinois (1976).

102. W. Kesternich and K. L. Merkle, in Applications of Ion Beams to Metals, edited by S. T. Picraux, E. P. EerNisse and F. L. Vook (Plenum Press, 1974), p. 441.

103. R. S. Averback and K. L. Merkle, in Proc. of International Conference on Fundamental Aspects of Radiation Damage in Metals, edited by M. T. Robinson and R. W. Young, Jr., (National Technical Information Service, Springfield, VA, 1975), Vol. 1, p. 127.

104. R. S. Averback, L. J. Thompson and K. L. Merkle, in International Conference on the Properties of Atomic Defects in Metals, Argonne, Illinois (1976).

105. M. Guinan, private communication.

106. K. L. Merkle and R. S. Averback, in Proc. of International Conference on the Properties of Atomic Defects in Metals, Argonne, Illinois (1976).

107. K. B. Winterbon, P. Sigmund and J. B. Sanders, Mat. Fys. Medd. Dan. Vid. Selesk., 37, 14 (1970).

108. J. R. Beeler, private communication.

Appendix A: The Crystallography of the $(75\bar{1})$ Plane of the FCC Lattice

The vectors $\overrightarrow{OR} = (a_o/2)\,[0\bar{1}\bar{1}]$, $\overrightarrow{OS} = (a_o/2)[0\bar{1}1]$ and $\vec{w} = \overrightarrow{O1} = (a_o/2)[\bar{1}10]$ define a primitive unit cell in the fcc lattice. The unit mesh exhibited in fig. 8 was shown from the model (fig. 7) to be determined by the vectors $\vec{u} = \overrightarrow{OR} - \overrightarrow{OS} + \overrightarrow{O1} = (a_o/2)[\bar{1}1\bar{2}]$ and $\vec{v} = \overrightarrow{OB} = \overrightarrow{OS} + \overrightarrow{O1} - 2\overrightarrow{OR} = (a_o/2)[\bar{1}23]$; the vectors $\vec{u}$, $\vec{v}$ and $\vec{w}$ also define a primitive unit cell. The shift vector $\vec{t}$ which is the projection of $\vec{w}$ onto the $(75\bar{1})$ plane is given by

$$\vec{t} = \vec{w} - \vec{d},$$

where the vector $\vec{d}$ is perpendicular to the $(75\bar{1})$ plane and has a magnitude equal to the spacing between $(75\bar{1})$ planes. For the $(75\bar{1})$ plane $\vec{d} = (a_o/75)[\bar{7}\bar{5}1]$ and $\vec{t} = (a_o/150)[\overline{61}\ 85\ \bar{2}]$. In fig. 8 $\vec{t}$ lies in the $(75\bar{1})$ plane and it connects 0 with the projection of 1 in the $(75\bar{1})$ plane; similarly the vector $2\vec{t}$ connects 0 with the projection of 2 in the $(75\bar{1})$ plane. The positions of atoms A and B and 1 to 5 relative to the cubic axes and also relative to 0 X Y Z were calculated following the approach developed by Nicholas (1965) and are listed in Table 9. This crystallographic information is given for completeness, it is not available elsewhere in the literature for the $(75\bar{1})$ plane.

Table 9: Table of atomic positions for the $(75\bar{1})$ plane of the fcc lattice

	Co-ordinates of Position*								
Atom	Relative to Cubic Axes			Relative to O X Y Z					
				$/\sqrt{6}$	$/\sqrt{450}$	$/\sqrt{75}$			
A	-1	1	-2	6	0	0	2.4495	0	0
B	-1	2	3	-3	75	0	-1.2247	2.5355	0
1	-1	1	0	2	24	-2	0.8165	1.1314	-0.2309
2	-2	2	0	4	48	-4	1.6330	2.2627	-0.4619
3	-2	2	2	0	72	-6	0	3.3941	-0.6928
4	-2	1	-1	5	21	-8	2.0412	0.9899	-0.9238
5	-2	1	1	1	45	-10	0.4082	2.1213	-1.1547

* The coordinates are given in terms of the length $a_o/2$, where a_o is the lattice parameter of the standard non-primitive unit cell. The coordinates relative to O X Y Z are given both in exact form and also numerically to four significant figures. The axes OX and OY are indicated in fig. 8 and OZ is the unit vector normal to the $(75\bar{1})$ plane.

Appendix B: The Crystallography of Various Planes of the BCC Lattice

The crystallography of the (521), (433), (543), (875), (765), (631), (831) and (11 4 3) planes in the bcc lattice were not given in Nicholas' Atlas(78); therefore we first constructed a ball model for each plane according to the procedure developed by Moore and Nicholas.(75) Figures 56, 58, 60, 62, 64, 66, 68 and 70 respectively show photographs of ball models for these planes which are built on a (200) plane. The dark balls indicate the atoms in the outmost (zeroth) layer and the visible atoms, within the primitive mesh defined by the dark balls O, A, B and C, from different layers are indicated by the numbers 1, 2, 3, 4 etc. The ball model for each plane was used to determine the unit mesh and the stacking sequence of layers zero to at least four. In the example of the (521) plane, the vectors $\overrightarrow{OR} = (a_o/2)[0\bar{2}0]$, $\overrightarrow{OS} = (a_o/2)[\bar{1}11]$, and $\vec{w} = \overrightarrow{O1} = (a_o/2)[00\bar{2}]$ define a primitive unit cell. The unit mesh exhibited in fig. 57 was shown from the ball model (see fig. 56) to be determined by the vectors $\vec{u} = \overrightarrow{OA} = \overrightarrow{O1} - \overrightarrow{OS} = a_o[1\bar{1}\bar{3}]$ and $\vec{v} = \overrightarrow{OB} = \overrightarrow{O1} + \overrightarrow{OS} - \overrightarrow{OR} = (a_o/2)[\bar{1}3\bar{1}]$; the vectors $\vec{u}$, $\vec{v}$ and $\vec{w}$ also define a primitive unit cell. The shift vector $\vec{t}$ which is the projection of $\vec{w}$ onto the zeroth layer of the (521) plane is given by $\vec{t} = \vec{w} - \vec{d}$, where the vector $\vec{t}$ is perpendicular to the (521) plane and has a magnitude equal to the spacing between (521) planes; for the (521) plane $\vec{d} = (a_o/3)[\bar{5}\bar{2}\bar{1}]$ and $\vec{t} = (a_o/30)[5\ 2\ 29]$. In fig. 57 $\vec{t}$ lies in the (521) plane; it connects the atom 0 with the projection of the atom 1 onto the zeroth layer of the (521) plane. The positions of atoms A, B and 1 to 4 relative to the cubic axes and 0 X Y Z were calculated following the approach developed by Nicholas(78) and are listed in Table 10 which is given for completeness. Results for the (433), (543), (875), (765), (631), (831) and (11 4 3) are obtained in a similar manner and are shown in figs. 59, 61, 63, 65, 67, 69 and 71 and Table 11 to 17.

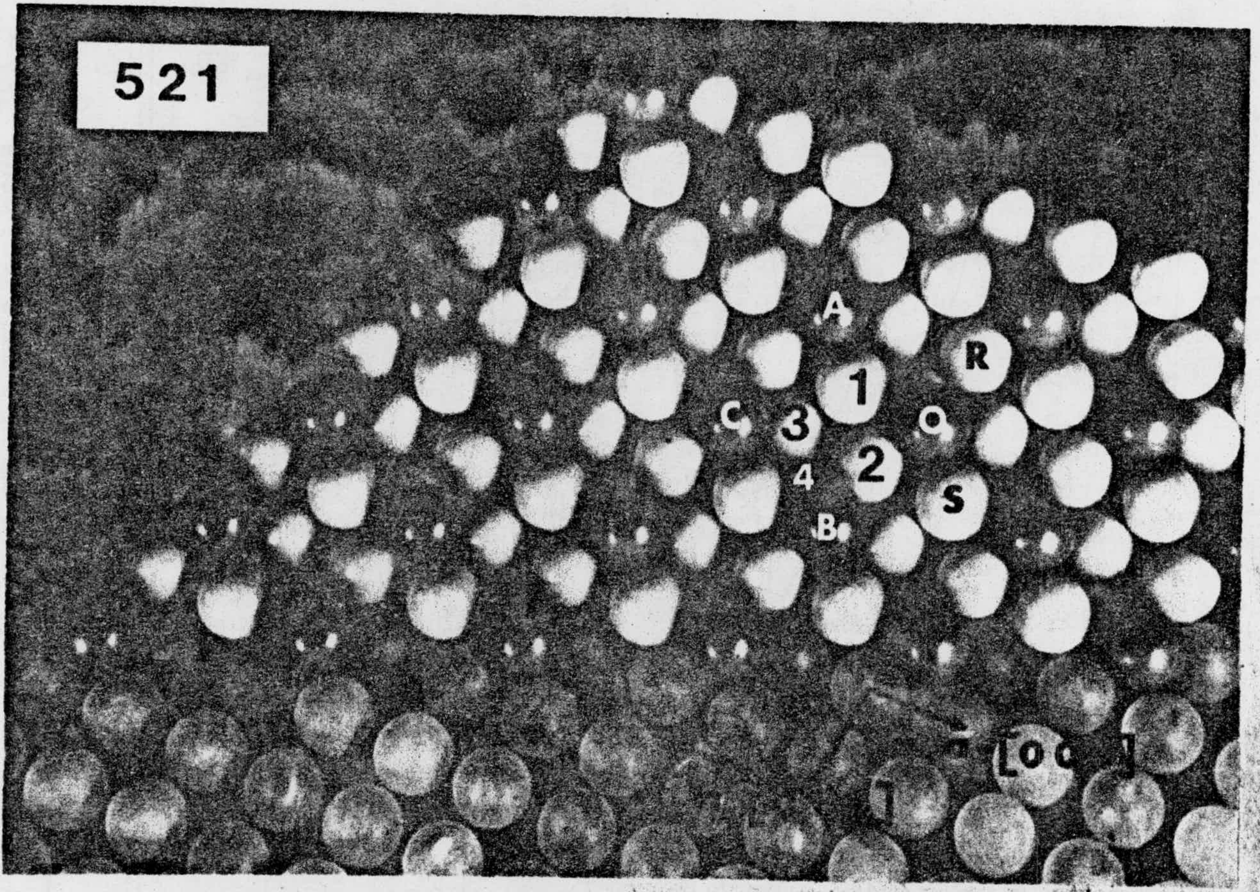

Figure 56: A photograph of a ball model of the (521) plane built on a (200) plane.

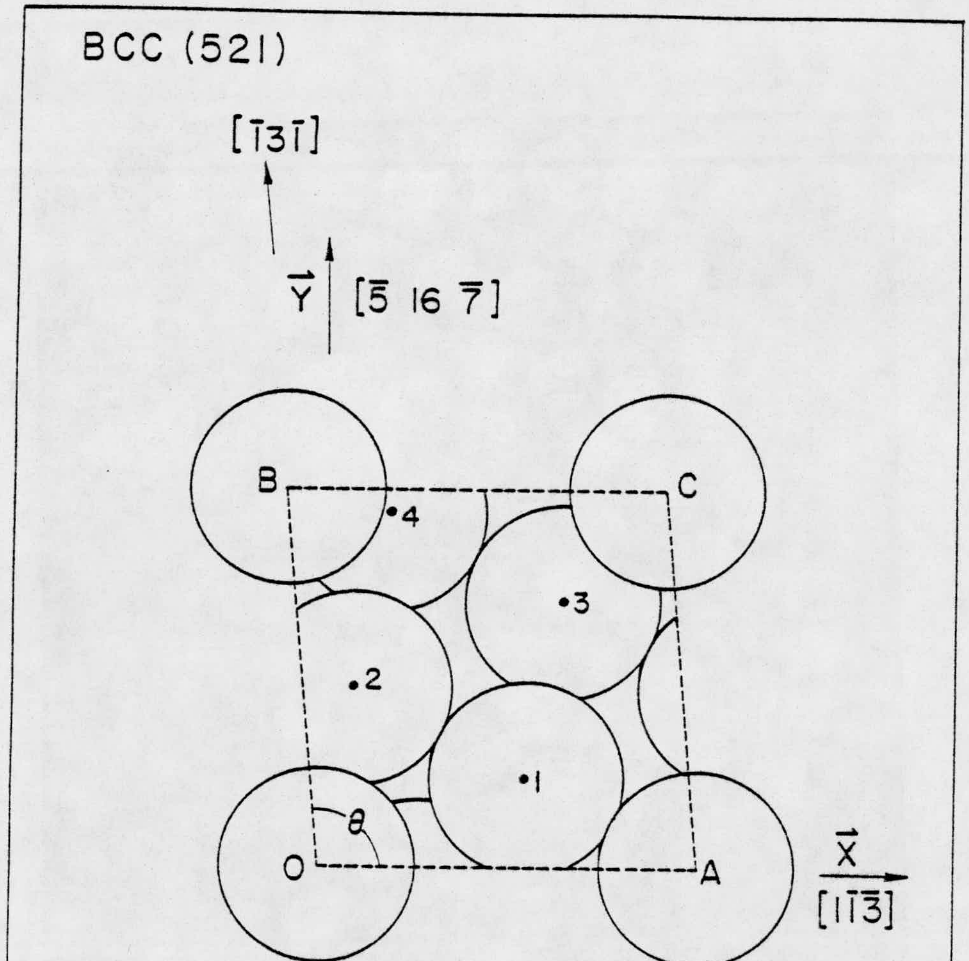

Figure 57: The primitive mesh (OABC) of the (521) plane and the projection of the atoms that lie within the primitive mesh for layers 1 to 4.

Table 10: Table of atomic positions for the (521) plane of the bcc lattice

	Co-ordinates of Position*, **								
Atom	Relative to Cubic Axes			Relative to O X Y Z					
				$/\sqrt{11}$	$/\sqrt{330}$	$/\sqrt{30}$			
A	1	-1	-3	11	0	0	3.3166	0	0
B	-1	3	-1	-1	60	0	-0.3015	3.3029	0
1	0	0	-2	6	14	-2	1.8091	0.7707	-0.3651
2	-1	1	-1	1	28	-4	0.3015	1.5413	-0.7303
3	-1	1	-3	7	42	-6	2.1106	2.3120	-1.0954
4	-2	2	-2	2	56	-8	0.6030	3.0827	-1.4606

* The coordinates are given in terms of the length $a_o/2$, where a_o is the lattice parameter of the standard non-primitive unit cell. The coordinates relative to O X Y Z are given both in exact form and also numerically to four significant figures.

** The axes OX and OY are indicated in fig. 57 and OZ is the unit vector normal to the (521) plane.

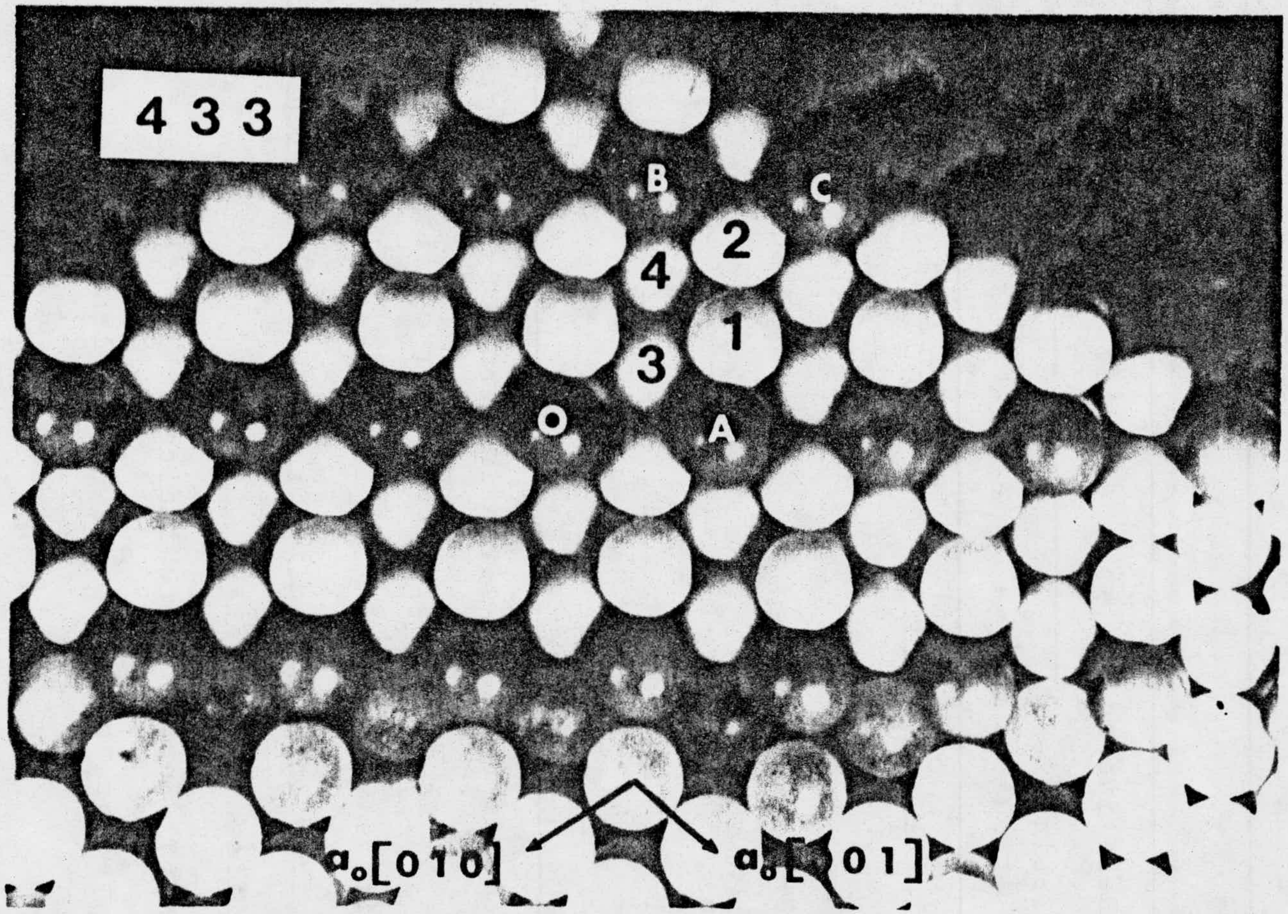

Figure 58: A photograph of a ball model of the (433) plane.

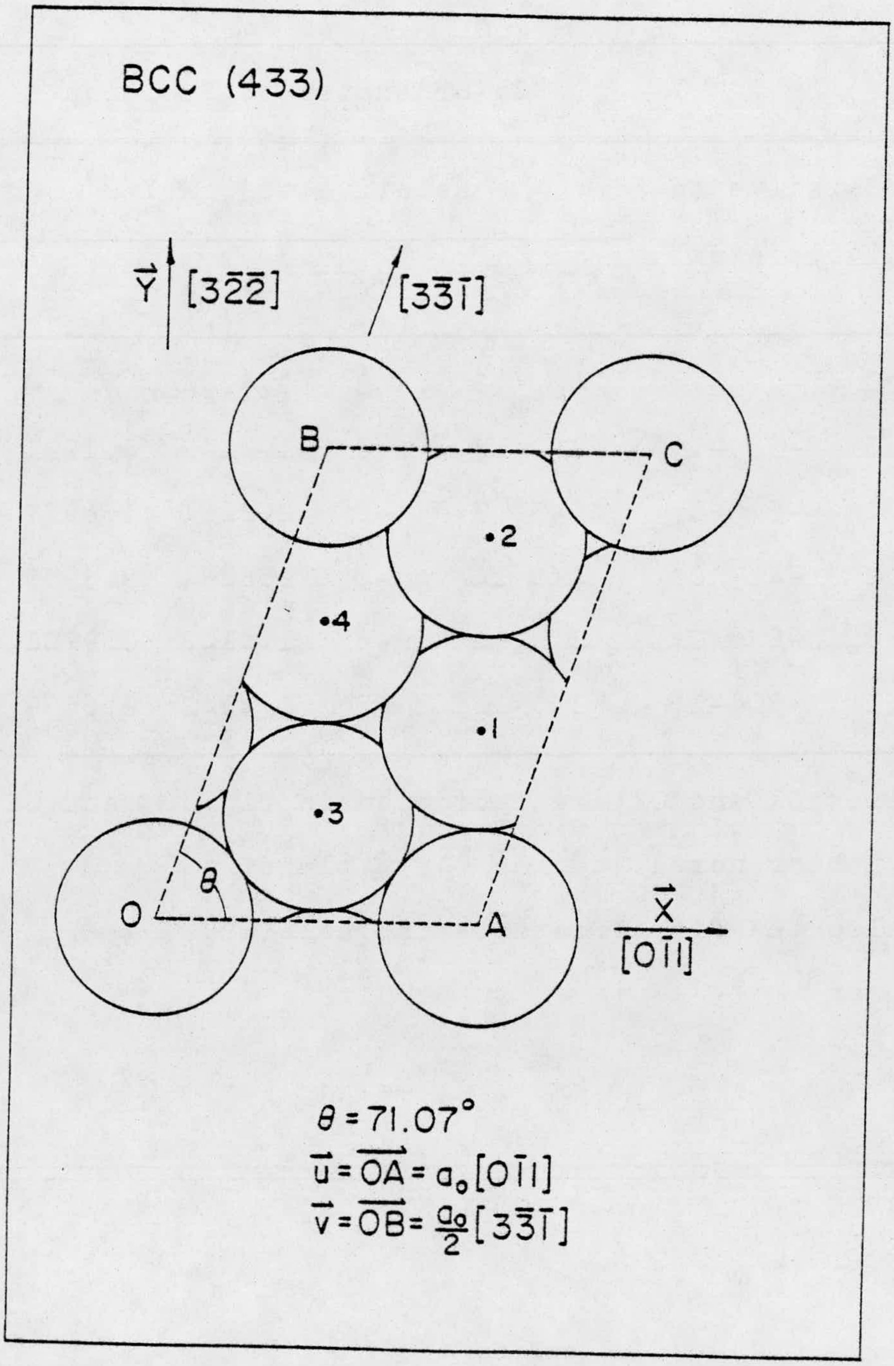

Figure 59: The primitive mesh (OABC) of the (433) plane and the projection of the atoms that lie within this primitive mesh for layers 1 to 4.

Table 11: Table of atomic positions for the (433) plane of the bcc lattice

	Co-ordinates of Position[*], [**]								
Atom	Relative to Cubic Axes			Relative to O X Y Z					
				$/\sqrt{2}$	$/\sqrt{17}$	$/\sqrt{34}$			
A	0	-2	2	4	0	0	2.8284	0	0
B	3	-3	-1	2	17	0	1.4142	4.1231	0
1	1	-3	1	4	7	-2	2.8284	1.6977	-0.3430
2	2	-4	0	4	14	-4	2.8284	3.3955	-0.6860
3	0	-2	0	2	4	-6	1.4142	0.9701	-1.0290
4	1	-3	-1	2	11	-8	1.4142	2.6679	-1.3720

[*] The axes OX and OY are indicated in fig. 59 and OZ is the unit vector normal to the (433) plane.

[**] See also the first footnote in Table 10.

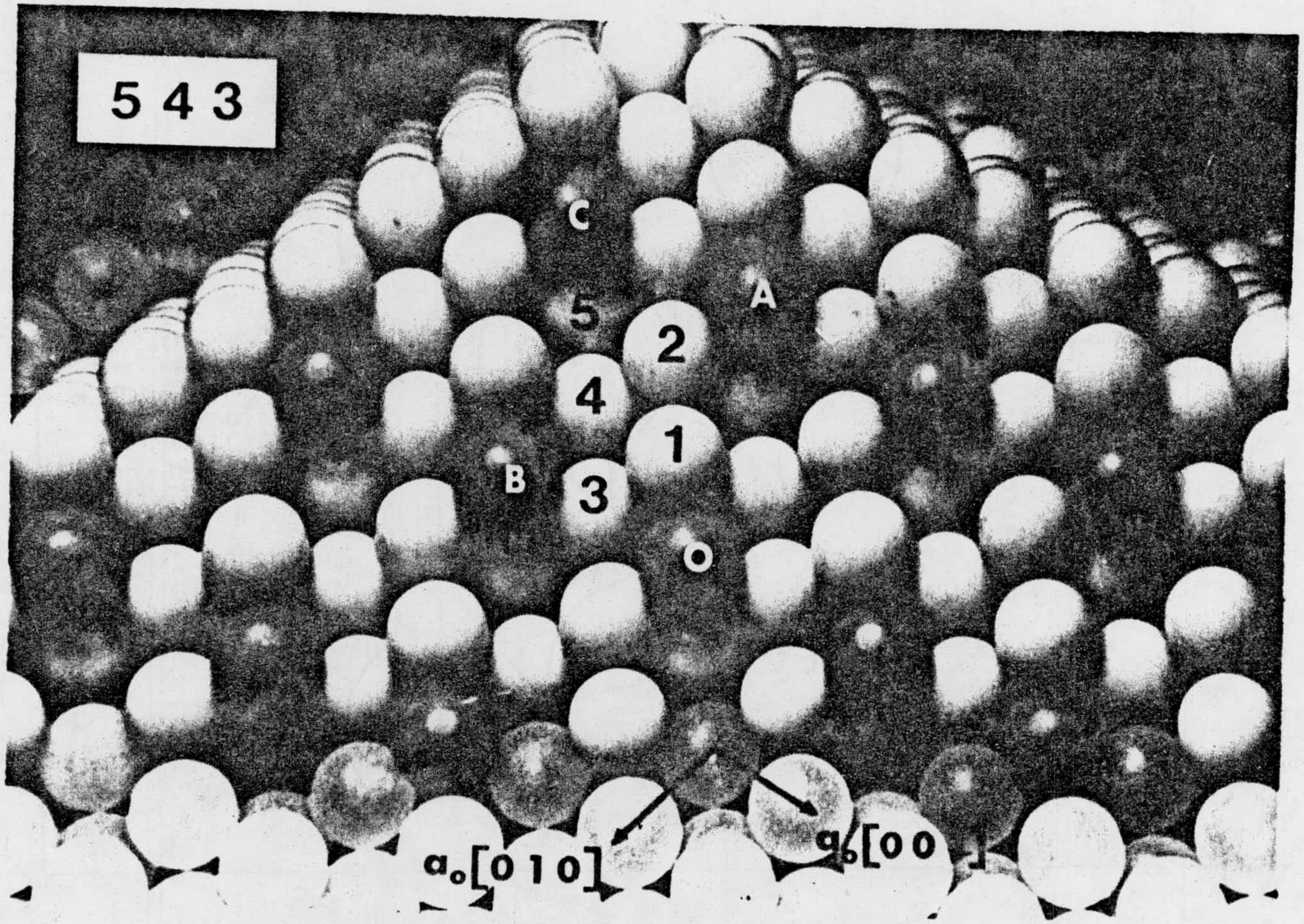

Figure 60: A photograph of a ball model of the (543) plane.

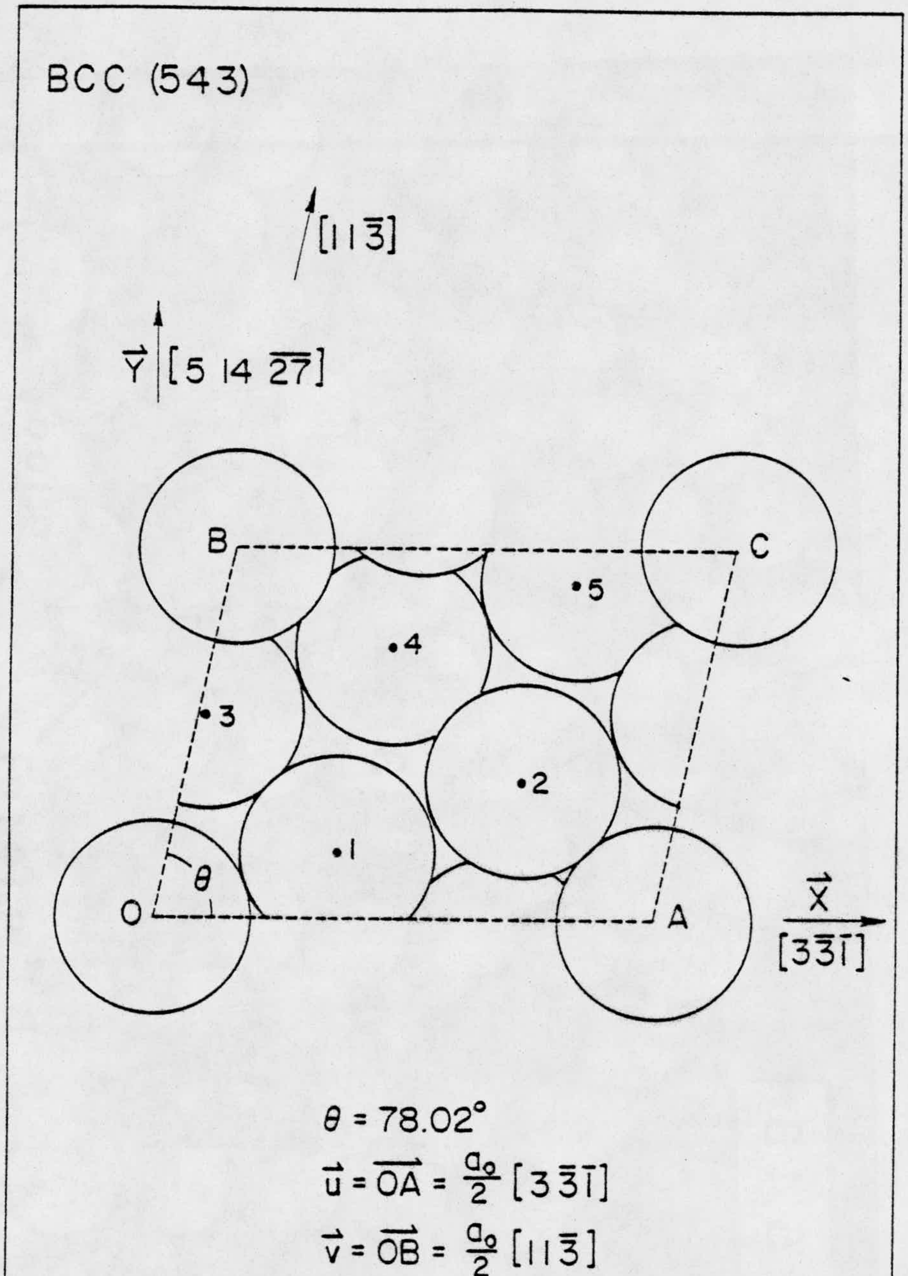

Figure 61: The primitive mesh (OABC) of the (543) plane and the projection of the atoms that lie within this primitive mesh for layers 1 to 5.

Table 12: Table of atomic positions for the (543) plane of the bcc lattice

Atom	Co-ordinates of Position*, **								
	Relative to Cubic Axes			Relative to O X Y Z					
				$/\sqrt{19}$	$/\sqrt{950}$	$/\sqrt{50}$			
A	3	-3	-1	19	0	0	4.3589	0	0
B	1	1	-3	3	100	0	0.6882	3.2444	0
1	1	-1	-1	7	18	-2	1.6059	0.5840	-0.2828
2	2	-2	-2	14	36	-4	3.2118	1.1680	-0.5657
3	0	0	-2	2	54	-6	0.4588	1.7520	-0.8485
4	1	-1	-3	9	72	-8	2.0647	2.3360	-1.1314
5	2	-2	-4	16	90	-10	3.6707	2.9200	-1.4142

* The axes OX and OY are indicated in fig. 61 and OZ is the unit vector normal to the (543) plane.

** See also the first footnote in Table 10.

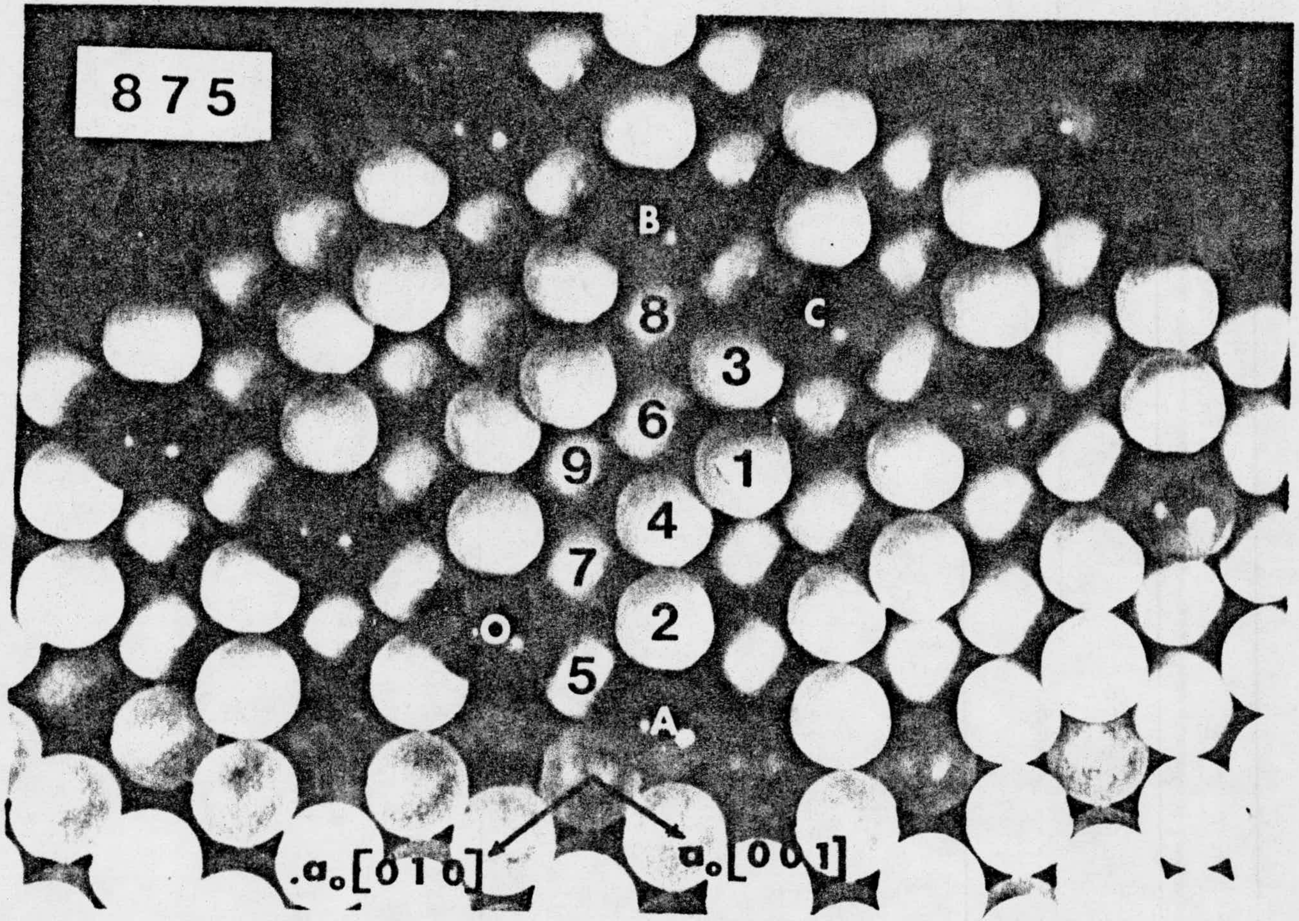

Figure 62: A photograph of a ball model of the (875) plane.

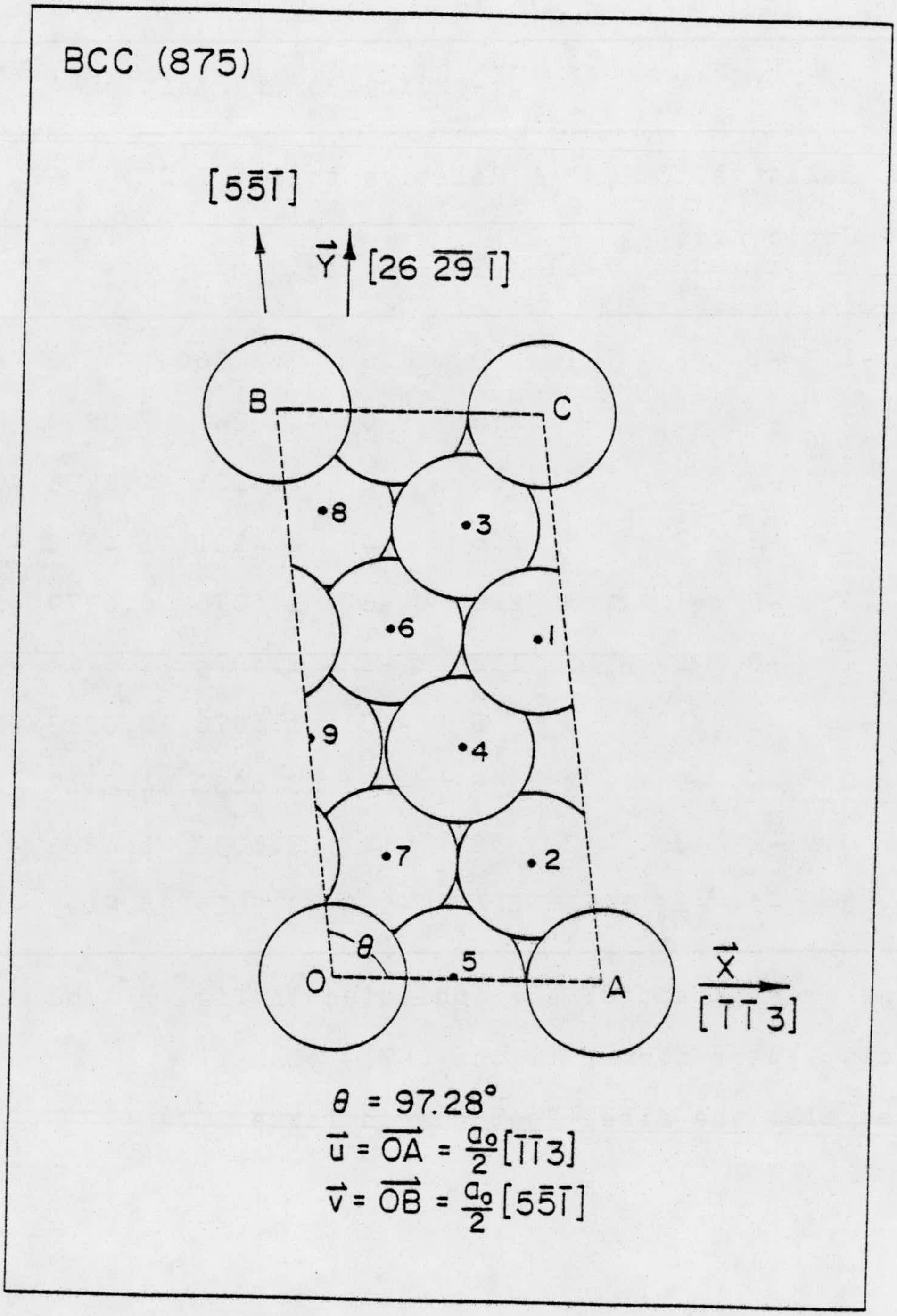

Figure 63: The primitive mesh (OABC) of the (875) plane and the projection of the atoms that lie within this primitive mesh for layers 1 to 9.

Table 13: Table of atomic positions for the (875) plane of the bcc lattice

	Co-ordinates of Position*, **								
Atom	Relative to Cubic Axes			Relative to O X Y Z					
				$/\sqrt{11}$	$/\sqrt{1518}$	$/\sqrt{138}$			
A	-1	-1	3	11	0	0	3.3166	0	0
B	5	-5	-1	-3	276	0	-0.9045	7.0839	0
1	2	-4	2	8	166	-2	2.4121	4.2606	-0.1703
2	0	-2	2	8	56	-4	2.4121	1.4373	-0.3405
3	3	-5	1	5	222	-6	1.5076	5.6979	-0.5108
4	1	-3	1	5	112	-8	1.5076	2.8746	-0.6810
5	-1	-1	1	5	2	-10	1.5076	0.0513	-0.8513
6	2	-4	0	2	168	-12	0.6030	4.3119	-1.0215
7	0	-2	0	2	58	-14	0.6030	1.4886	-1.1918
8	3	-5	-1	-1	224	-16	-0.3015	5.7493	-1.3620

* The axes OX and OY are indicated in fig. 63 and OZ is the unit vector normal to the (875) plane.

** See also the first footnote in Table 10.

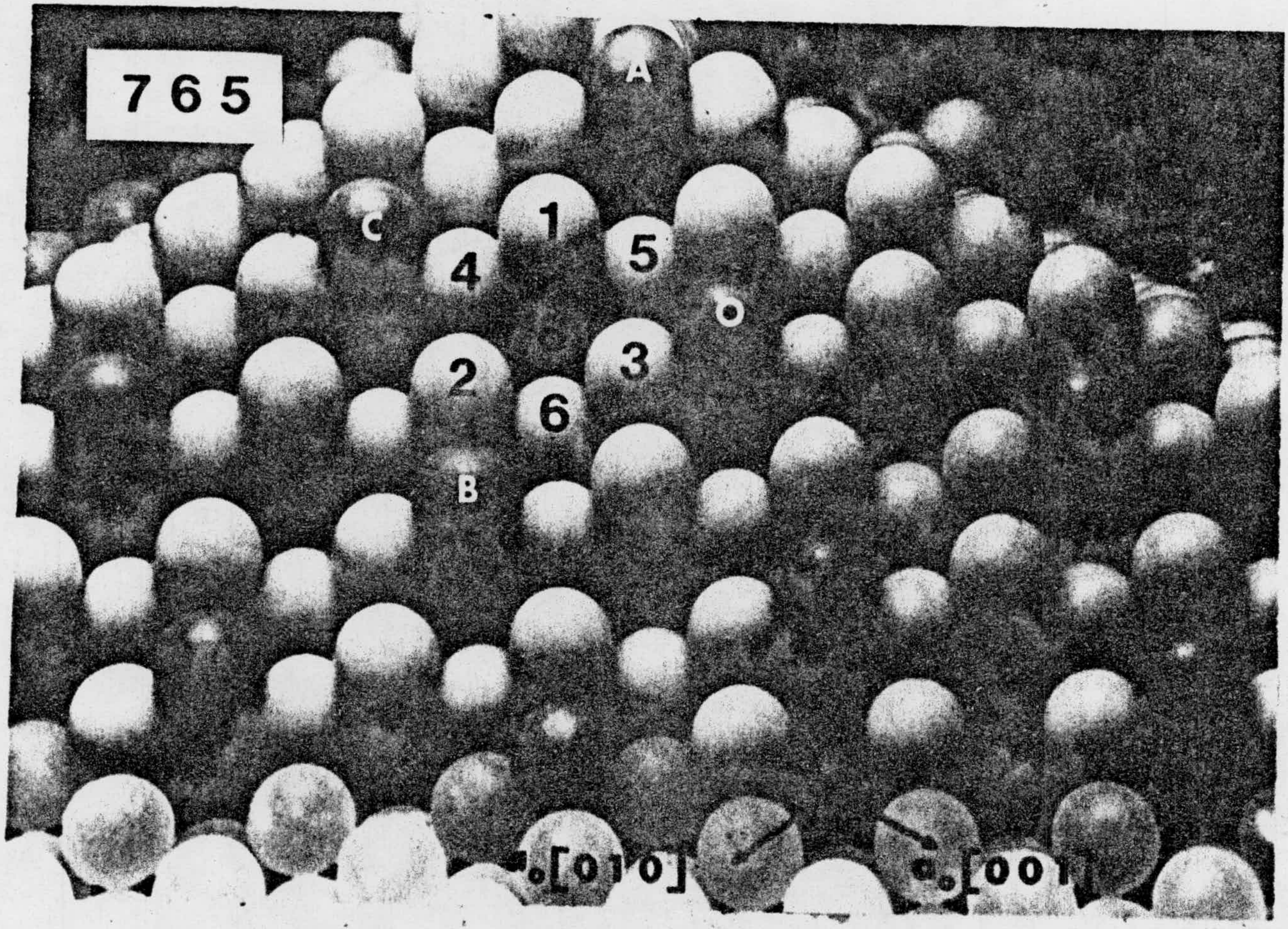

Figure 64: A photograph of a ball model of the (765) plane.

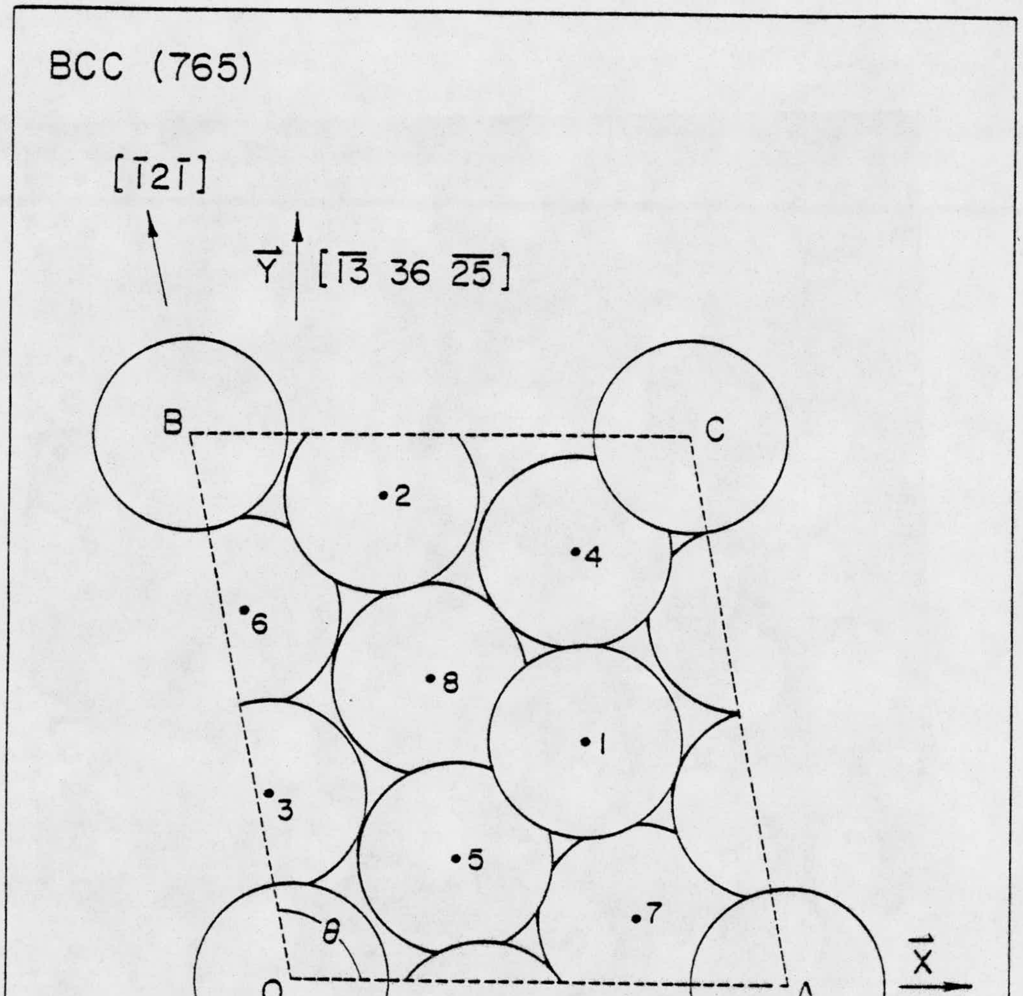

Figure 65: The primitive mesh (OABC) of the (765) plane and the projection of the atoms that lie within this primitive mesh for layers 1 to 8.

Table 14: Table of Atomic Positions for the (765) plane of the bcc lattice

				Co-ordinates of Position*,**					
Atom	Relative to Cubic Axes			Relative to O X Y Z					
				$/\sqrt{19}$	$/\sqrt{2090}$	$/\sqrt{110}$			
A	3	-1	-3	19	0	0	4.3589	0	0
B	-2	4	-2	-4	220	0	-0.9177	4.8123	0
1	1	1	-3	11	98	-2	2.5236	2.1436	-0.1907
2	-1	3	-3	3	196	-4	0.6882	4.2873	-0.3814
3	-1	1	-1	-1	74	-6	-0.2294	1.6187	-0.5721
4	0	2	-4	10	172	-8	2.2942	3.7623	-0.7628
5	0	0	-2	6	50	-10	1.3765	1.0937	-0.9535
6	-2	2	-2	-2	148	-12	-0.4588	3.2373	-1.1442
7	1	-1	-3	13	26	-14	2.9824	0.5687	-1.3348
8	-1	1	-3	5	124	-16	1.1471	2.7124	-1.5255

* The axes OX and OY are indicated in fig. 65 and OZ is the unit vector normal to the (765) plane.

** See also the first footnote in Table 10.

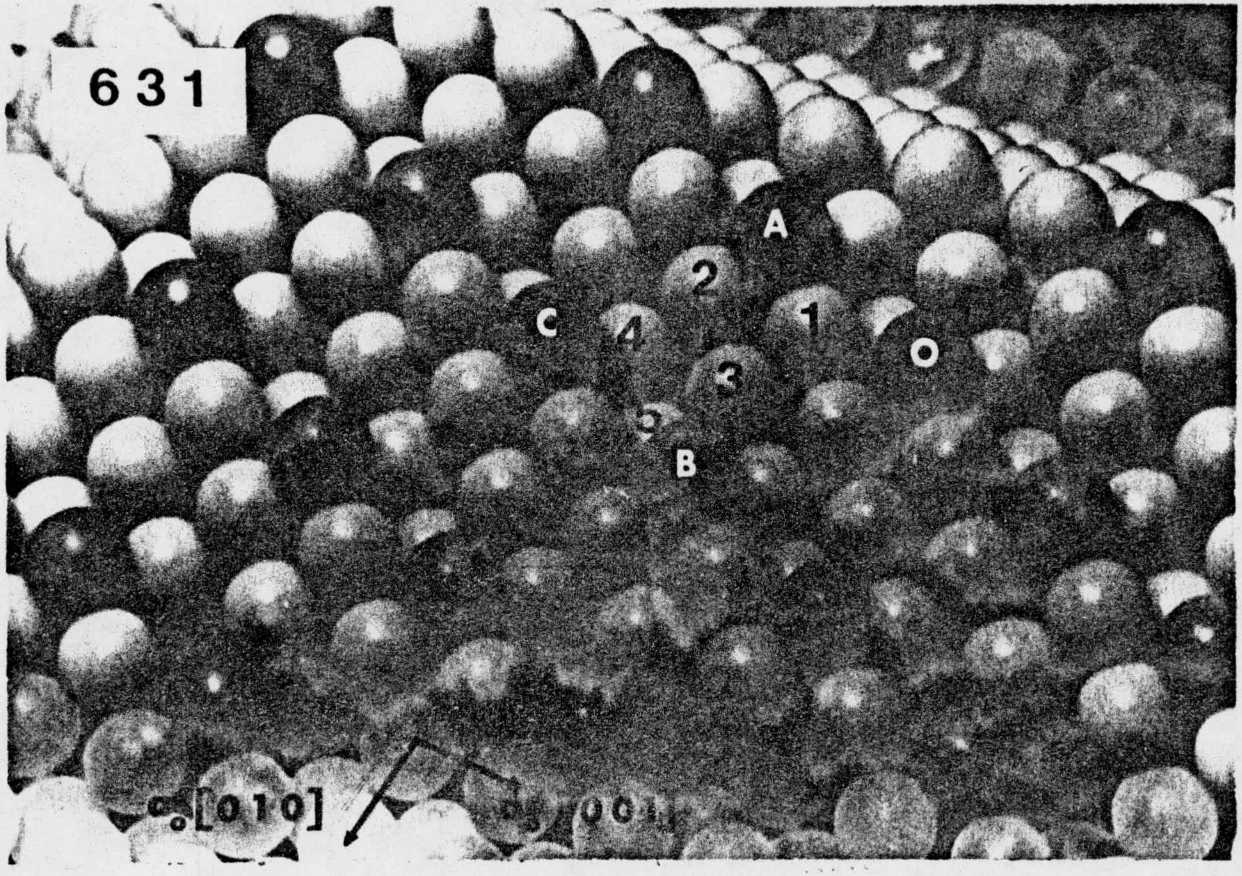

Figure 66: A photograph of a ball model of the (631) plane.

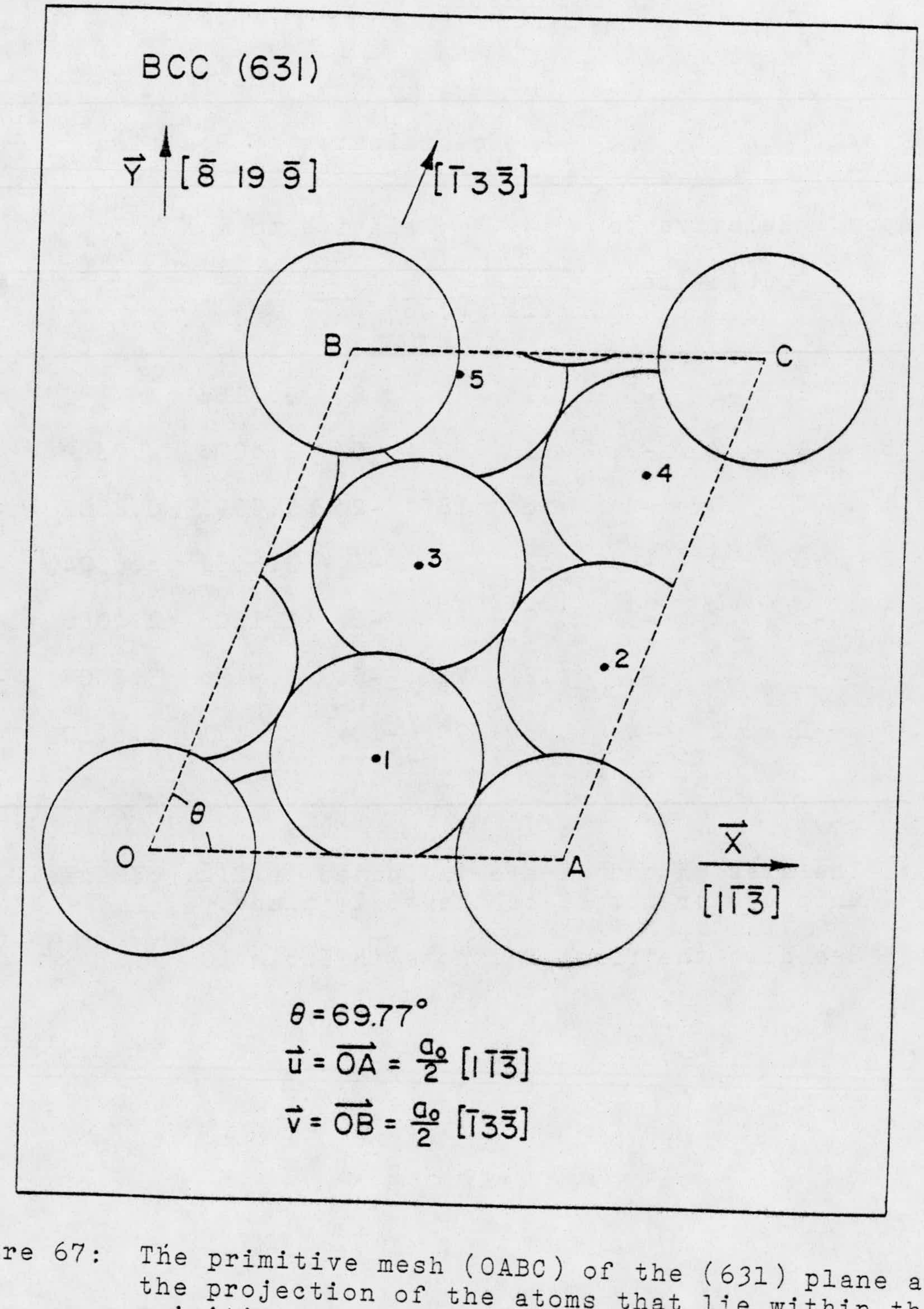

Figure 67: The primitive mesh (OABC) of the (631) plane and the projection of the atoms that lie within this primitive mesh for layers 1 to 5.

Table 15: Table of Atomic Positions for the (631) Plane of the bcc Lattice

	Co-ordinates of Position$^{*,\ **}$								
Atom	Relative to Cubic Axes			Relative to O X Y Z					
				$/\sqrt{11}$	$/\sqrt{506}$	$/\sqrt{46}$			
A	1	-1	-3	11	0	0	3.3166	0	0
B	-1	3	-3	5	92	0	1.5076	4.0899	0
1	0	0	-2	6	18	-2	1.8091	0.8002	-0.2949
2	0	0	-4	12	36	-4	3.6181	1.6004	-0.5898
3	-1	1	-3	7	54	-6	2.1106	2.4006	-0.8847
4	-1	1	-5	13	72	-8	3.9196	3.2008	-1.1795
5	-2	2	-4	8	90	-10	2.4121	4.0010	-1.4744

* The axes OX and OY are indicated in fig. 67 and OZ is the unit vector normal to the (631) plane.

** See also the first footnote in Table 10.

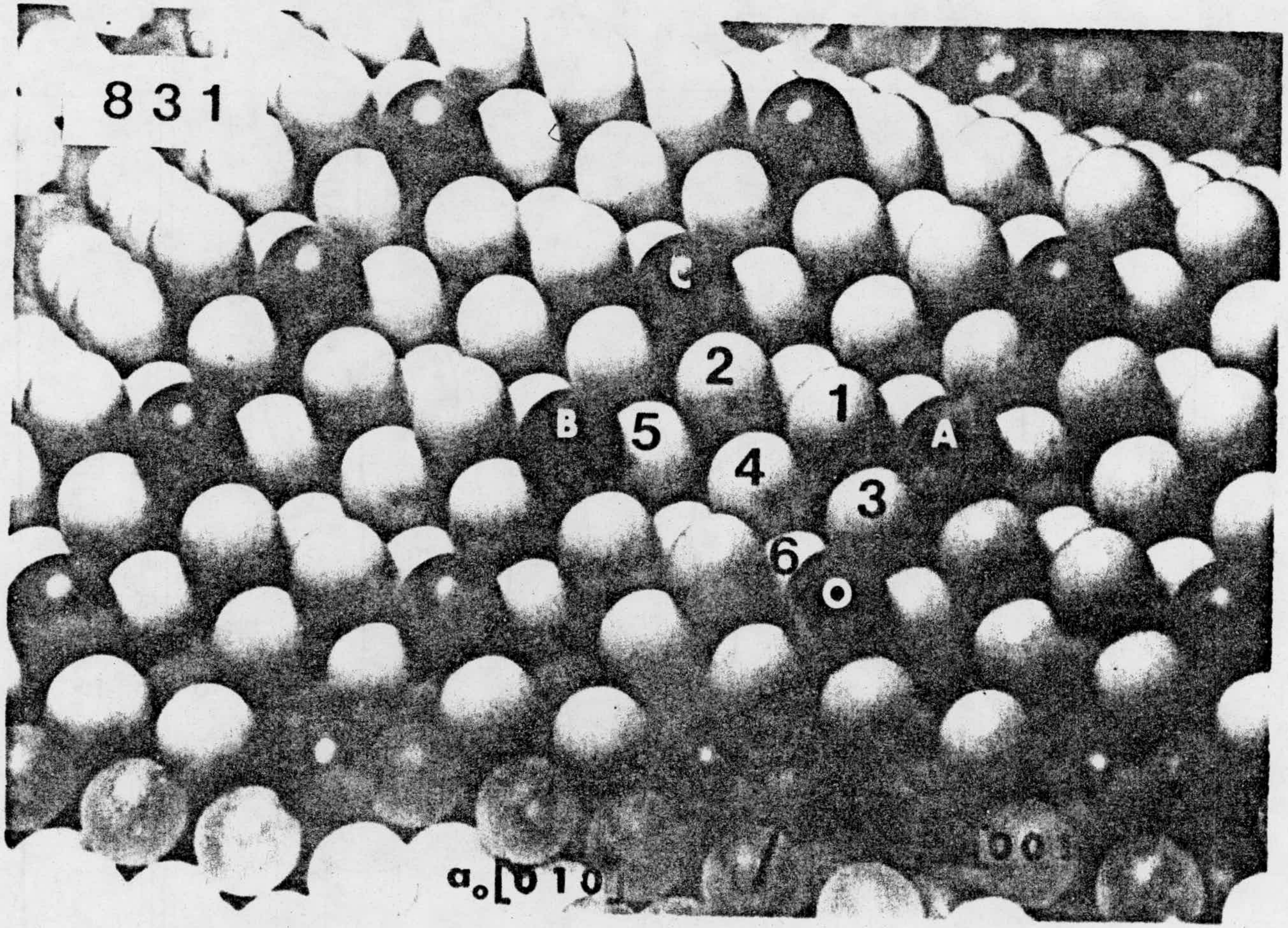

Figure 68: A photograph of a ball model of the (831) plane.

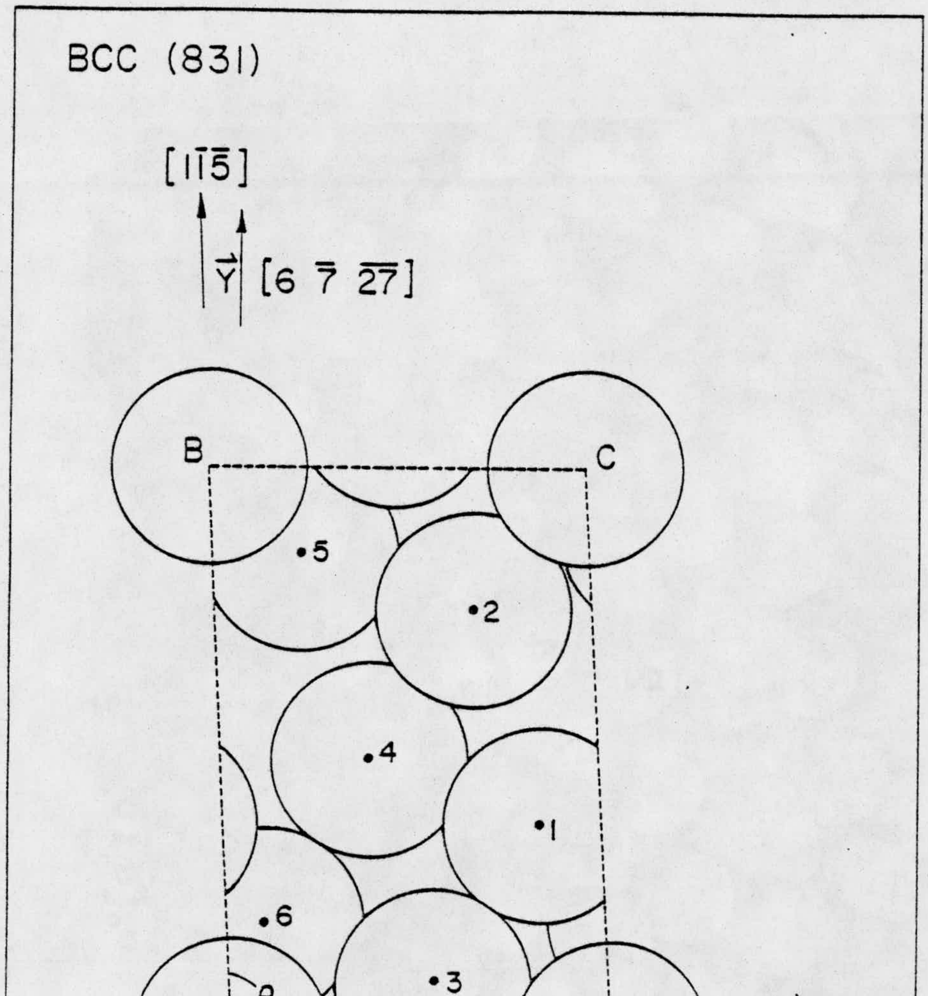

Figure 69: The primitive mesh (OABC) of the (831) plane and the projection of the atoms that lie within this primitive mesh for layers 1 to 6.

Table 16: Table of atomic positions for the (831) plane of the bcc lattice

	Co-ordinates of Position*, **								
Atom	Relative to Cubic Axes			Relative to O X Y Z					
				$/\sqrt{11}$	$/\sqrt{450}$	$/\sqrt{75}$			
A	1	-3	1	11	0	0	3.3166	0	0
B	1	-1	-5	-1	148	0	-0.3015	5.1874	0
1	1	-3	-1	9	54	-2	2.7136	1.8927	-0.2325
2	1	-3	-3	7	108	-4	2.1106	3.7854	-0.4650
3	0	-2	0	6	14	-6	1.8091	0.4907	-0.6975
4	0	-2	-2	4	68	-8	1.2060	2.3894	-0.9300
5	0	-2	-4	2	122	-10	0.6030	4.2761	-1.1625
6	-1	-1	-1	1	28	-12	0.3015	0.9814	-1.3950

* The axes OX and OY are indicated in fig. 69 and OZ is the unit vector normal to the (831) plane.

** See also the first footnote in Table 10 .

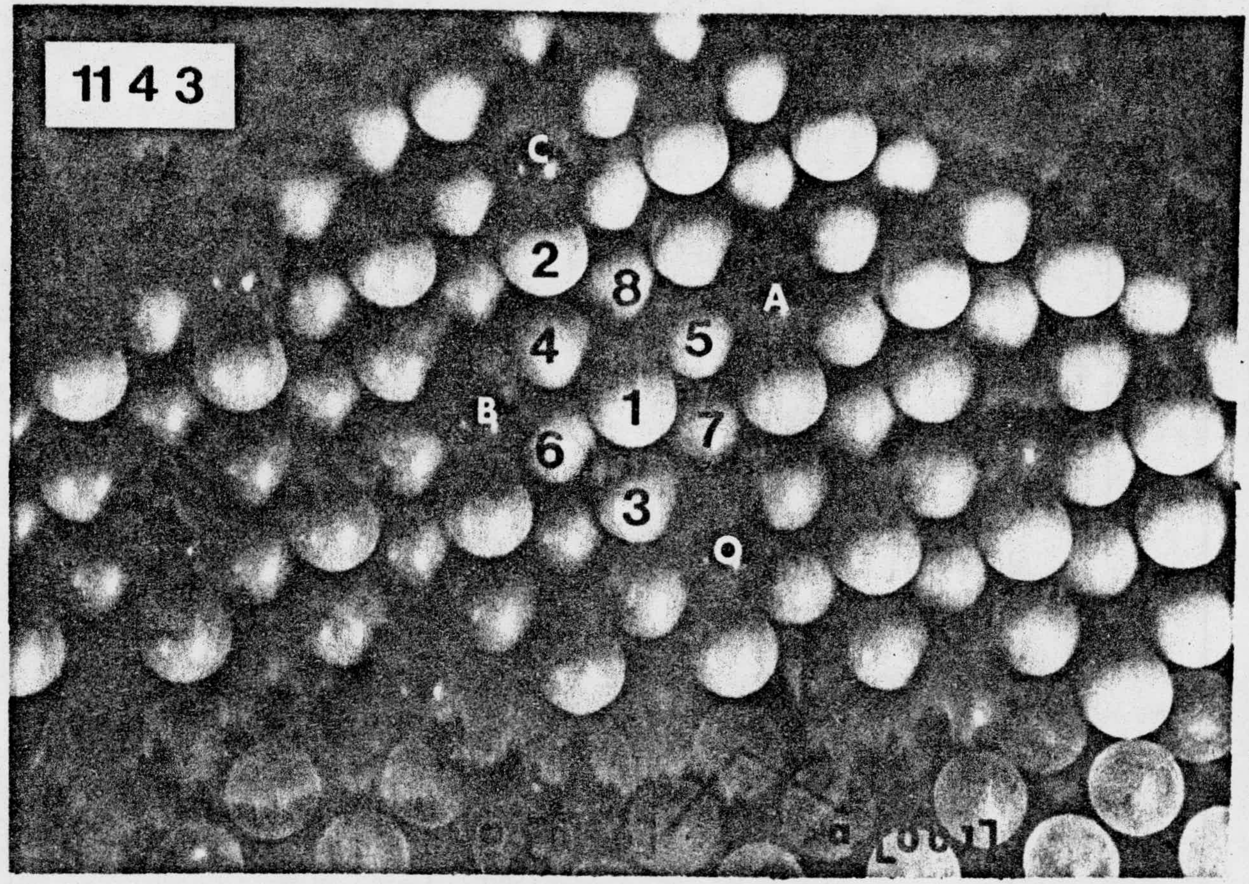

Figure 70: A photograph of a ball model of the (11 4 3) plane.

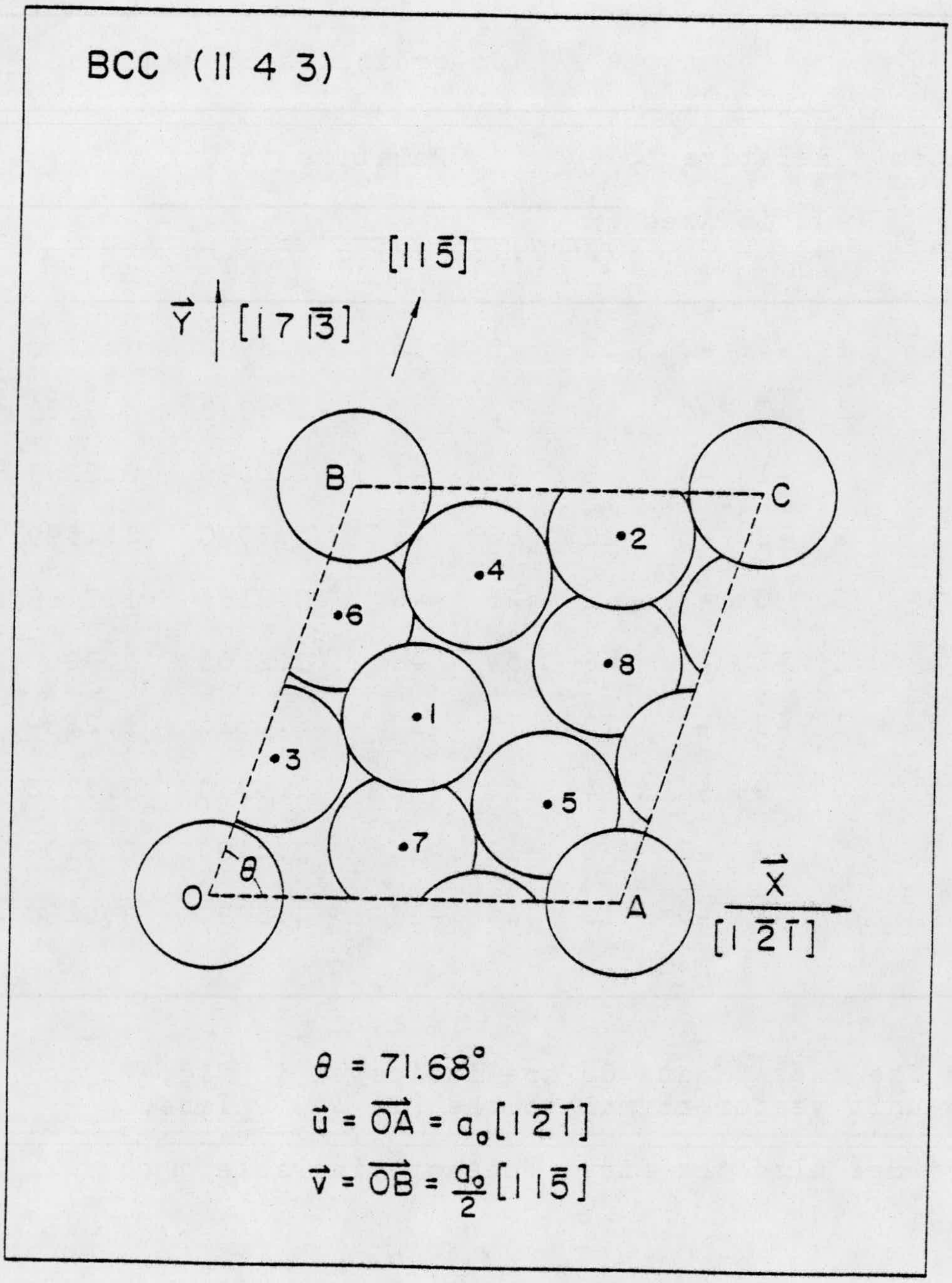

$\theta = 71.68^\circ$

$\vec{u} = \overrightarrow{OA} = a_o[1\bar{2}\bar{1}]$

$\vec{v} = \overrightarrow{OB} = \frac{a_o}{2}[11\bar{5}]$

Figure 71: The primitive mesh (OABC) of the (11 4 3) plane and the projection of the atoms that lie within this primitive mesh for layers 1 to 8.

Table 17: Table of atomic positions for the (11 4 3) plane of the bcc lattice

	Co-ordinates of Position*, **								
Atom	Relative to Cubic Axes			Relative to O X Y Z					
				$/\sqrt{6}$	$/\sqrt{219}$	$/\sqrt{146}$			
A	2	-4	-2	12	0	0	4.8990	0	0
B	1	1	-5	4	73	0	1.6330	4.9329	0
1	1	-1	-3	6	33	-2	2.4495	2.2299	-0.1655
2	2	-2	-6	12	66	-4	4.8990	4.4599	-0.3310
3	0	0	-2	2	26	-6	0.8165	1.7569	-0.4966
4	1	-1	-5	8	59	-8	3.2660	3.9869	-0.6621
5	1	-3	-3	10	19	-10	4.0825	1.2839	-0.8276
6	0	0	-4	4	52	-12	1.6330	3.5138	-0.9931
7	0	-2	-2	6	12	-14	2.4495	0.8109	-1.1586
8	1	-3	-5	12	45	-16	4.8990	3.0408	-1.3242

* The axes OX and OY are indicated in fig. 71 and OZ is the unit vector normal to the (11 4 3) plane.

** See also the first footnote in Table 10.

Appendix C: Procedure for the Construction of a Depleted Zone Which Occupied More Than One {h k l} Plane

C.1. Mathematical Details of the Mapping Procedure

In this appendix the procedure employed to construct a depleted zone in three dimensions from the FIM micrographs is described.

(1) The FIM micrograph was first indexed for those {h k l} planes in which a depleted zone was found. The Miller indices of the vectors which lay along the intersection of any two neighboring {h k l} planes were also calculated. The Miller indices of the planes and the vectors determined on the micrograph were then compared with the schematic diagrams in fig. 15 or 16 for consistency.

(2) The positions of all atomic and vacant lattice sites (VLSs) in each layer of each {h k l} plane were transferred to a sheet of graph paper with the aid of the x-y cross-hairs on the motion analyzer in conjunction with the x-y recorder. The positions of atoms and VLSs were plotted with respect to one of the common fiducial marks which had been engraved in the phosphor screen portion of the internal image-intensification system. The choice of the common reference point*

---

* It generally requires two reference points to correct errors in the positions of the atoms caused by the two-dimensional slippage of film. In practice, it was found that only one reference point is required in order to correct the errors in the position of the atoms; this implies that the slippage of film was essentially one-dimensional.

eliminated all errors in the positions of atoms caused by the slippage of film in either the ciné camera or the motion analyzer.

(3) A procedure was then defined to determine the coordinates of any atomic sites or VLSs. As a demonstration we first consider the upper portion of the disgram in fig. 72 which shows the positions of the atoms in two successive layers of the (222) plane. The atomic sites in the zeroth and the first layers are once again represented by solid black circles and open circles respectively. The atomic site 0 was chosen arbitrarily as the origin for the zeroth layer. The vector $a_o[\bar{1}10]$ which lies along the intersection of the (222) and (332) planes and the vector $a_o[0\bar{1}1]$ which lies along the intersection of the (222) and (233) planes as determined in step (1) (see also fig. 15) were taken as the u- and v- axes respectively. The vector $(a_o/6)[111]$ which is normal to the (222) plane was taken as the Z-axis. This local coordinate system consisting of the u-, v-, Z-axes and point 0 as the origin was then used to specify the positions of any atomic sites in the zeroth layer of the (222) plane in terms of the integers; for example, the sites 0, A and B have coordinates (0,0,0), (1,0,0) and (0,1,0) respectively.

The atomic site in the first layer which is projected within the primitive unit cell of the zeroth layer is denoted by 0'. The point $0'_p$ denotes the projection of 0' onto the zeroth layer. The coordinates of any atomic site in the fir

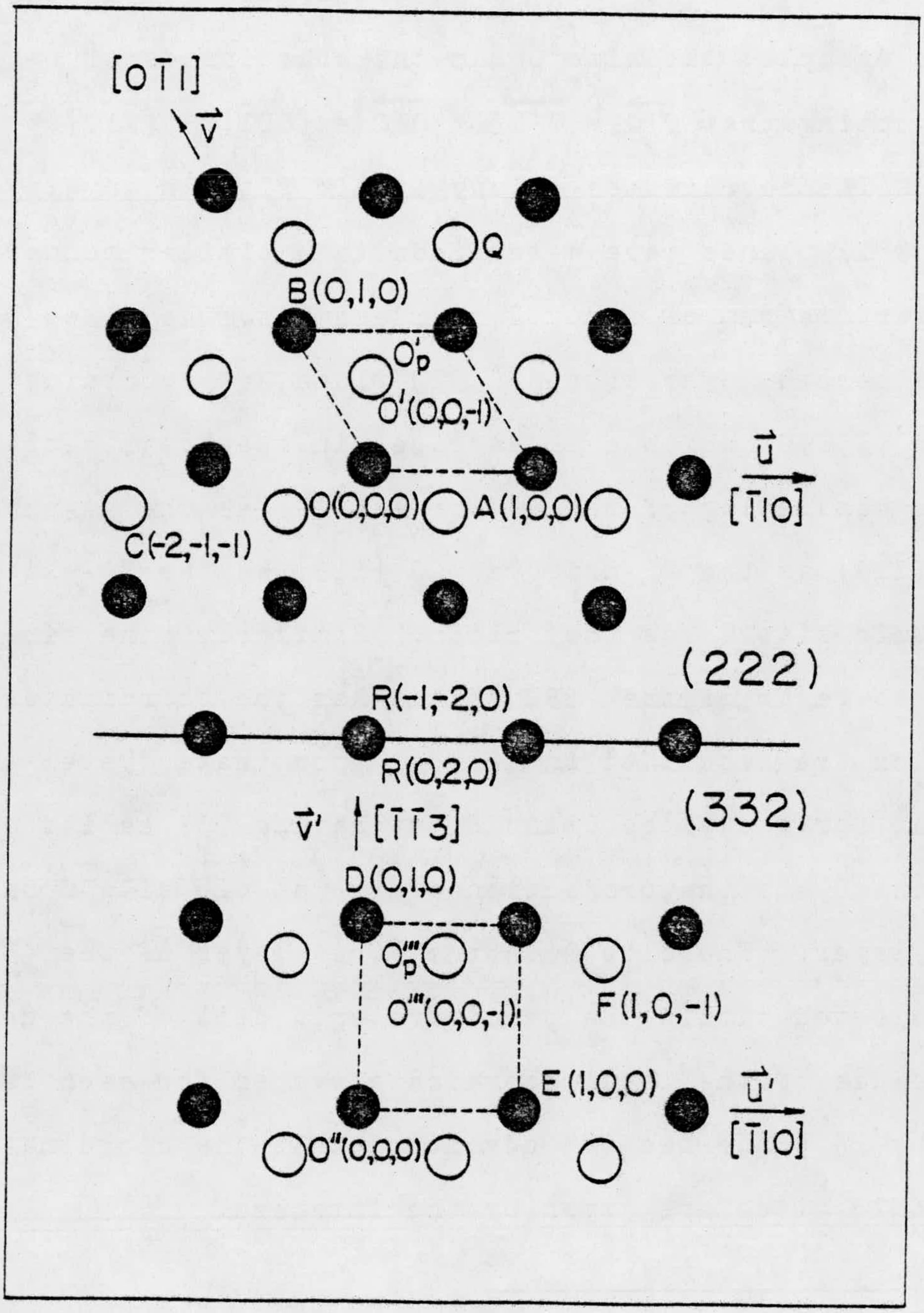

Figure 72: A schematic diagram showing the zeroth and the first layers of the (222) and (332) planes. This figure is used to explain how a depleted zone was reconstructed from the FIM image; see sect. C.1 for the details.

layer determined by using the local coordinate system which consists of the u-, v-, Z-axes and point O'_p as the origin*. For example, the site C has the coordinates of (-2,-1,-1) by noting that $\overrightarrow{O'_pC} = \overrightarrow{O'_pO'} + \overrightarrow{O'C} = [00\bar{1}] + [\bar{2}\bar{1}0] = [\bar{2}\bar{1}\bar{1}]$.

The coordinates of any atomic site in any layer of other {h k 1} planes were determined in a similar manner. In the lower diagram of fig. 72, for example, the sites D and E in the zeroth layer of the (332) plane have coordinates of (0,1,0) and (1,0,0) which are described in the local coordinate system consisting of the vector $a_o[\bar{1}10]$ as the u'-axis, the vector $a_o[\bar{1}\bar{1}3]$ as the v'-axis $(a_o/22)[113]$ as the Z'-axis and the atomic site O" as the origin. Similarly, the site F in the first layer of the (332) plane has the coordinates of (1,0,-1) which are described in a local coordinate system the same as that for the sites D and E but having O'''_p as its origin. The point O_p is the projection of the atomic site O onto the zeroth layer. The site O in the first layer of the (332) plane is projected within the primitive unit cell of the zeroth layer. The use of the local coordinate system for each layer of each (h k 1) plane has the advantage that the coordinates of all atomic sites are given by the integers.

---

* The choice of the point O'_p instead of any atomic site Q as the origin for the first layer of the (222) plane eliminates the accurate measurement of $\overrightarrow{OQ}$ as required in the approach used by Chen and Balluffi(98); the benifit of this choice is obvious if one notes that $|\overrightarrow{OO'_p}|$ is equal to the magnitude o the shift vector as defined in step (4).

In the following the transformation from the local coordinate systems to a common cubic coordinate system is described. In practice, the transformation was programmed in BASIC language and computed with the aid of Nova 1220 minicomputer.

(4) The coordinate of the atomic site C relative to the origin O was obtained by adding the shift vector $\overrightarrow{OO'_p} \equiv \vec{t} = [t_u\ t_v\ 0]$ to $\overrightarrow{O'_pC}$. That is, $\overrightarrow{OC} = \overrightarrow{OO'_p} + \overrightarrow{O'_pC} = [t_u\ t_v\ 0] + [\bar{2}\bar{1}\bar{1}] = [t_u-2\ t_v-1\ -1]$. The shift vector $\vec{t}$ is the projection of $\overrightarrow{OO'}$ onto the (222) plane and is given by [.333333 .666667 0] (see Table 18). Hence, the site C has the coordinates of (-1.66667, -0.333333, -1) relative to the origin O. In a similar manner the site F has the coordinates of (1.5, 0.727272, -1) relative to the origin O" by noting that $\overrightarrow{O''F} = \overrightarrow{O''O''_p} + \overrightarrow{O''_pF} = [0.5\ 0.727272\ 0] + [1\ 0\ \bar{1}] = [1.5\ 0.727272\ \bar{1}]$. The vector $\overrightarrow{O''O''_p}$ given by [0.5 0.727272 0] (see Table 18) is the shift vector of the (332) plane. The coordinates of any other atomic sites in other layers of plane were determined in the same manner described in the above.

(5) The coordinates of the atomic sites observed in the (222) plane were then transformed to a local cubic coordinate system with O as its origin while these observed in the (332) plane were transformed to another local cubic coordinate system with O" as its origin. It is noted that the two local cubic coordinate systems are related only by a translation vector.

Table 18: Table of the local coordinate system for an {h k l} plane of the bcc lattice

Plane	$\vec{u}$*	$\vec{v}$*	$\vec{Z}$*	t_u**	t_v**
(222)	$[\bar{2}20]$	$[0\bar{2}2]$	[111]	0.333333	0.666667
(332)	$[\bar{2}20]$	$[\bar{1}\bar{1}3]$	[664]	0.500000	0.727272
(433)	$[0\bar{2}2]$	$[3\bar{1}\bar{3}]$	[866]	0.794118	0.411765
(442)	$[\bar{2}20]$	$[0\bar{2}4]$	[442]	0.388888	0.777777
(543)	$[3\bar{3}\bar{1}]$	$[11\bar{3}]$	[10 8 6]	0.340000	0.180000
(875)	$[\bar{1}\bar{1}3]$	$[5\bar{5}\bar{1}]$	[16 14 10]	0.891304	0.601449
(765)	$[3\bar{1}\bar{3}]$	$[\bar{2}4\bar{2}]$	[14 12 10]	0.672727	0.445455
(411)	$[\bar{1}31]$	[022]	[822]	0.555556	0.277778
(521)	$[1\bar{1}\bar{3}]$	$[\bar{1}3\bar{1}]$	[10 4 2]	0.566666	0.233333
(622)	$[02\bar{2}]$	$[\bar{2}24]$	[311]	0.181818	0.363636
(732)	$[\bar{1}3\bar{1}]$	$[\bar{2}24]$	[14 6 4]	0.161290	0.306452
(721)	$[1\bar{3}\bar{1}]$	$[02\bar{4}]$	[14 4 2]	0.259259	0.425926
(631)	$[1\bar{1}\bar{3}]$	$[\bar{1}3\bar{3}]$	[12 6 2]	0.456522	0.195652
(824)	$[2\bar{4}\bar{2}]$	$[04\bar{2}]$	[824]	0.595238	0.857143
(831)	$[1\bar{3}1]$	$[1\bar{1}\bar{5}]$	[16 6 2]	0.851351	0.364865
(11 4 3)	$[2\bar{4}\bar{2}]$	$[11\bar{5}]$	[22 8 6]	0.349316	0.452054

* The Miller indices for the $\vec{u}$-, $\vec{v}$- and $\vec{Z}$-axes are given such that the magnitudes of the vectors $\vec{u}$, $\vec{v}$ and $\vec{Z}$ are in units of $a_o/2$, where a_o is the lattice parameter of the standard non-primitive unit cell.

** The values of the quantities t_u and t_v are given in the fraction of the magnitudes of the vectors $\vec{u}$ and $\vec{v}$ respectively.

(6) Finally, we have to interlink the two local cubic coordinate systems. In order to transform the coordinates of an atomic site in the local cubic coordinate system of the (332) plane to the local cubic coordinate system of the (222) plane the coordinates of one[*] atomic site R which lies at the intersection of the (222) and (332) planes were determined according to steps (3), (4) and (5). The coordinates of the atomic site R in the local cubic coordinate system of the (222) plane is denoted by (ξ', ζ', η') and that in the (332) plane is given by (ξ,ζ,η). The coordinates (x,y,z) of an atomic site in the local coordinate system of the (332) plane were finally transformed to the coordinates (x,y,z) in the local cubic coordinate system of the (222) plane according to the equations.

$$x' = x - \xi + \xi' \tag{C1}$$

$$y' = y - \zeta + \zeta' \tag{C2}$$

$$z' = z - \eta + \eta' \tag{C3}$$

Extending this procedure all atomic sites observed in all {h k l} planes can be transformed to a common cubic coordinate system. In practice, the computations in steps (4) to (6) were programmed in BASIC language and excuted with the aid of a NOVA 1220 minicomputer in conjunction with a Tetronix 4010 graphic display terminal, a three cassette tape-transport and

---

[*] Since the two local cubic coordinate systems are related only by a translation vector, only one atomic site is needed in determining the transformation equations of the two coordinate systems. In practice, two atomic sites were used; the first atomic site was used to solve the eqs. (C1) to (C3) and the second atomic site was used to check the solutions.

an ASR 33 teletype; this program is denoted by Subprogram A. The flow chart of Subprogram A is shown in sect. C.3. The detail of Subprogram A is given in sect. C.4. An example of the input statements is also given in sect. C.2.

C.2. Input Statements for Subprogram A

In this section typical input statements are given as an example to demonstrate how to enter the data for Subprogram A. Comments are given after each data statement. In this demonstrative example it was assumed that a depleted zone consisting of five VLSs and three SIAs in the (622), (512) and (723) planes (see also figs. 16 and 17); two VLSs were found in the (622) plane, one VLS and one SIA in the (512) plane and two VLSs and two SIAs in the (723) plane. Each VLS (or SIA) was specified by an integer p and the local coordinates (u, v, Z); the integer p is the identification number of the (h k l) plane in which the VLS (or SIA) was detected. The values of p are equal to 1, 2 and 3 for the (622), (512) and (723) planes respectively. For example, the fourth VLS which was found in the (512) plane had coordinates (2, -1, -2, -7) which can be decoded as p=2 and (u, v, Z)=(-1, -2, -7). The details of the input statements are described in the following:

```
8000 DATA 2
```

Enter Y6=1 for a fcc lattice or Y6=2 for a bcc lattice.

```
8010 DATA 3
```

Enter Iϕ=3 for the total number of the {h k l} planes in which the VLSs and SIAs within a depleted zone were detected.

```
8020 DATA 0.181818, 0.363636, 0, 1, -1, -1, 2, 6, 2, 2
```

Enter sequentially the values of t_u and t_v and the Miller indices of the u-, v- and Z-axes of the (622) plane (see Table) for variables A(I1), B(I1) and B1 to B9.

```
8030 DATA 0.767676, 0.433333, 1, 1, -3, -1, 3, 1, 5, 1, 2
```

See comment in statement 8020 except that this is for the (512) plane.

```
8040 DATA 0.838709, 0.306451, 1, 1, -3, -1, 2, 1, 7, 2, 3
```

See comment in statement 8020 except that this is for the (723) plane.

```
8050 DATA 5
```

Enter I1=5 for the total number of the VLSs.

```
8060 DATA 3
```

Enter I2=3 for the total number of the SIAs.

In the following each set of coordinates will be stored in variables V, V1, V2 and V3.

```
8070 DATA 1, 0, 1, -1, 1, 2, -1, -3
```

Enter the coordinates of the two VLSs detected in the (622) plane.

```
8080 DATA 2, -1, -2, -7
```

Enter the coordinates of the VLS detected in the (512) plane.

```
8090 DATA 3, 0, -2, -43, 3, 1, 1, -56
```

Enter the coordinates of the two VLSs detected in the (723) plane.

```
8100 DATA 2, 0.6, -0.2, -3.8
```

Enter the coordinates of the SIA detected in the (512) plane.

```
8110 DATA 3, -3.2, 2.6, -20.5, 3, 4.7, -0.8, -31.5
```

Enter the coordinates of the two SIAs detected in the (723) plane.

```
8120 DATA 1, -2, -2, -9, 2, 1, 1, -1
```

Enter the two sets of coordinates of the first selected atomic sites which lies at the intersection of the (622) (512) planes. This atomic site had coordinates (1, -2, -2, -9) as specified in the local coordinate system of the (622) plane and coordinates (2, 1, 1, -1) in the local coordinate system of the (512) plane. The two sets of coordinates of the first selected atomic site were used to solve the transformation equations between the (512) and the (622) planes.

```
8130 DATA 1, -2, -2, -9, 2, 1, 1, -1
```

Similarly, enter the two sets of coordinates of the second selected atomic site which lies at the intersection of the (622) and the (512) planes. These two sets of coordinates were used to check the transformation equations determined by statement 8120.

```
8140 DATA 2, -2, -1, -4, 3, -3, -3, -14
```

See comment in statement 8120 except that this is for determining the transformation equations between the (723) and the (512) planes.

```
8150 DATA 2, -1, -1, -4, 3, -2, -3, -14
```

See comment in statement 8130 except that this is used to check the transformation equations determined by statement 8140.

```
8160 DATA 99, 0, 0, 0
```

This is a signal to stop reading the coordinates. Enter "999, 0, 0, 0" if there is only one (h k l) planes, otherwise enter "99, 0, 0, 0".

```
8170 DATA 3, 3, 6, 6
```

Since the coordinates of the VLSs and SIAs were entered in sequence as shown in statements 8070 to 8110, we assigned any VLS (or SIA) a serial number according to the sequence in which the VLS (or SIA) was entered. For example, atomic site No. 3 is a VLS in the (512) plane and had coordinates (2, -1, -2, -7) and the atomic site No. 6 is an SIA in the (512) plane and had coordinates (2, 6, -0.2, -3.8). Statement 8170 was used to command the computer to transform the coordinates of atomic sites No. 3 and 6 in the (512) plane to the coordinate system of the (622) plane according to the transformation equations determined by statements 8120 and 8130.

```
8180 DATA 4, 5, 7, 8
```

See comment in statement 8170 except that this is for the VLSs and SIAs in the (723) plane.

C.3. Flow Chart for Subprogram A

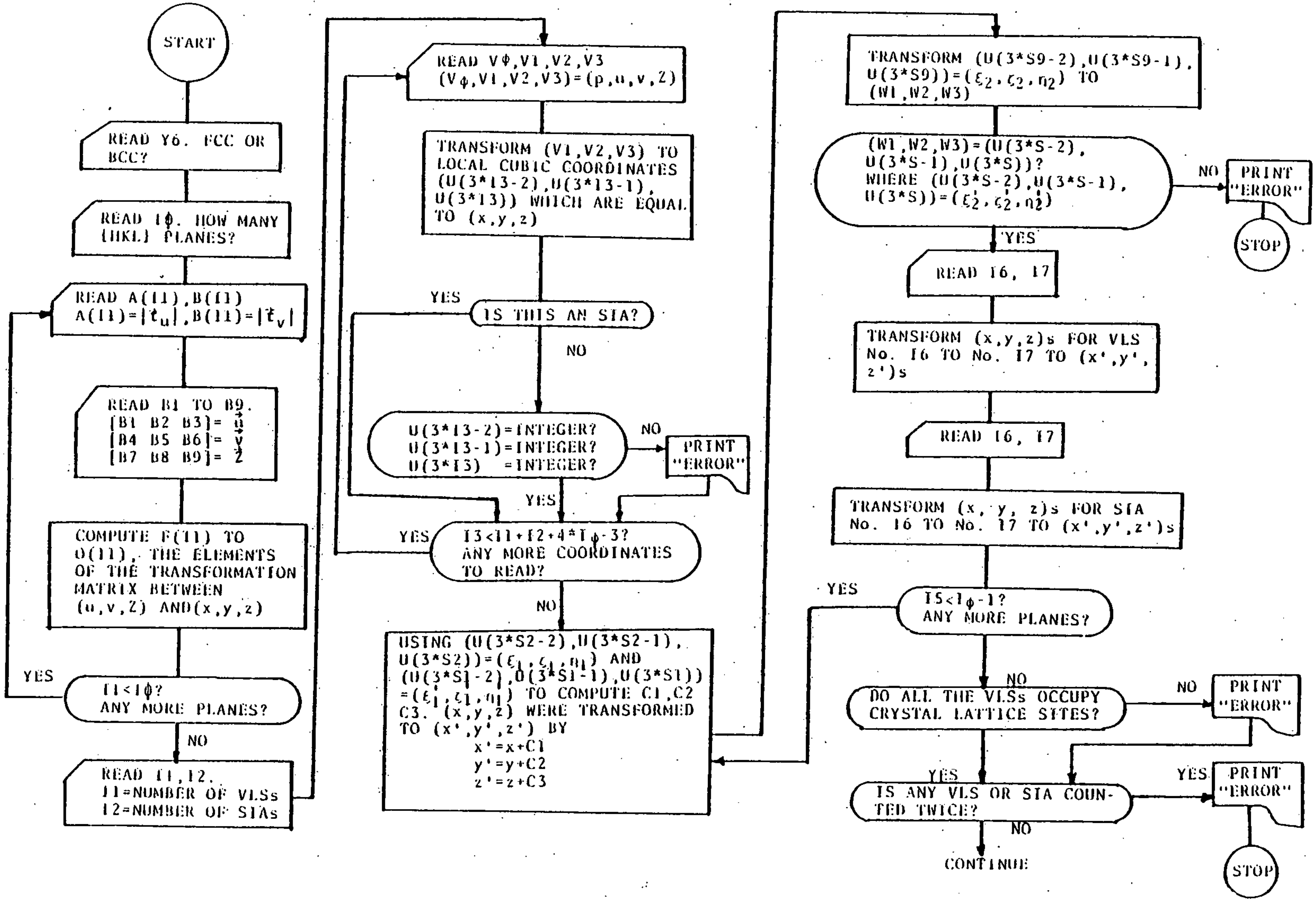

C.4. Subprogram A

```
0032 REM
0034 REM SUBPROGRAM A
0036 REM
0040 REM MAXIMUM NUMBER OF ATOMS = 300
0050 REM MAXIMUM SIZE OF CLUSTER = 200
0060 REM
0070 DIM F[16],G[16],H[16],J[16],K[16],L[16],M[16],N[16],O[16]
0080 DIM U[1000],A[300],B[200]
0090 DIM E[3,3]
0100 DIM P[16]
0110 INPUT "HOW MANY DEPLETED ZONES, ONE(1) OR MORE THAN ONE(2)?",K3
0120 INPUT "DO YOU WANT TO PRINT COORDINATES, YES(1) OR NO(2)?",Y4
0130 READ Y6
0140 READ I0
0150 FOR I1=1 TO I0
0160   READ A[I1],B[I1]
0170   READ B1,B2,B3,B4,B5,B6,B7,B8,B9
0180   LET C1=SQR(B1*B1+B2*B2+B3*B3)
0190   LET C2=SQR(B4*B4+B5*B5+B6*B6)
0200   LET C3=SQR(B7*B7+B8*B8+B9*B9)
0210   ON Y6 THEN GOTO 0220, 0390
0220   IF B1+B2+B3=2*INT((B1+B2+B3)/2+.001) THEN GOTO 0250
0230   LET X0=2*C1
0240   GOTO 0260
0250   LET X0=C1
0260   IF B4+B5+B6=2*INT((B4+B5+B6)/2+.001) THEN GOTO 0290
0270   LET Y0=2*C2
0280   GOTO 0300
0290   LET Y0=C2
0300   IF B7/2=INT(B7/2+.001) THEN GOTO 0340
0310   IF B8/2><INT(B8/2+.001) THEN IF B9/2><INT(B9/2+.001) THEN GOTO 03
70
0320   LET Z0=1/C3
0330   GOTO 0380
0340   IF B8/2=INT(B8/2+.001) THEN IF B9/2=INT(B9/2+.001) THEN GOTO 0370
0350   LET Z0=1/C3
0360   GOTO 0380
0370   LET Z0=2/C3
0380   GOTO 0600
0390   IF B1/2=INT(B1/2+.001) THEN GOTO 0430
0400   IF B2/2><INT(B2/2+.001) THEN IF B3/2><INT(B3/2+.001) THEN GOTO 04
60
0410   LET X0=2*C1
0420   GOTO 0470
0430   IF B2/2=INT(B2/2+.001) THEN IF B3/2=INT(B3/2+.001) THEN GOTO 0460
0440   LET X0=2*C1
0450   GOTO 0470
0460   LET X0=C1
0470   GOTO 0480
0480   IF B4/2=INT(B4/2+.001) THEN GOTO 0520
0490   IF B5/2><INT(B5/2+.001) THEN IF B6/2><INT(B6/2+.001) THEN GOTO 05
50
0500   LET Y0=2*C2
```

```
0510 GOTO 0560
0520 IF B5/2=INT(B5/2+.001) THEN IF B6/2=INT(B6/2+.001) THEN GOTO 0550
0530 LET Y0=2*C2
0540 GOTO 0560
0550 LET Y0=C2
0560 IF B7+B8+B9=2*INT((B7+B8+B9)/2+.001) THEN GOTO 0590
0570 LET Z0=1/C3
0580 GOTO 0600
0590 LET Z0=2/C3
0600 LET F[I1]=X0*B1/C1
0610 LET G[I1]=Y0*B4/C2
0620 LET H[I1]=Z0*B7/C3
0630 LET J[I1]=X0*B2/C1
0640 LET K[I1]=Y0*B5/C2
0650 LET L[I1]=Z0*B8/C3
0660 LET M[I1]=X0*B3/C1
0670 LET N[I1]=Y0*B6/C2
0680 LET O[I1]=Z0*B9/C3
0690 NEXT I1
0700 PRINT
0710 PRINT
0720 READ I1
0730 ON Y4 THEN GOTO 0740, 0800
0740 PRINT "(U,V,W)S ARE COORDINATES BASED ON TWO COPLANAR AXES AND THE"
;
0750 PRINT "AXIS PERPENDICULAR TO THE PLANE."
0760 PRINT
0770 PRINT
0780 PRINT "DEFECT NO.","(HKL) PLANE","U","V","W"
0790 PRINT
0800 FOR Y2=1 TO I0
0810   LET P[Y2]=-9999
0820 NEXT Y2
0830 READ I2
0840 FOR I3=1 TO (I1+I2+4*(I0-1)+1)
0850   READ V0,V1,V2,V3
0860   IF V0=999 THEN GOTO 1530
0870   IF V0=99 THEN GOTO 1180
0880   ON Y4 THEN GOTO 0890, 0960
0890   IF I3=<I2+I1 THEN GOTO 0920
0900   PRINT I3;"(R)",V0,V1,V2,V3
0910   GOTO 0960
0920   IF I3=<I2 THEN GOTO 0950
0930   PRINT I3;"(I)",V0,V1,V2,V3
0940   GOTO 0960
0950   PRINT I3;"(V)",V0,V1,V2,V3
0960   IF V3>P[V0] THEN LET P[V0]=V3
0970   LET V3=V3-P[V0]
0980   LET W4=A[V0]*ABS(V3)
0990   LET W5=B[V0]*ABS(V3)
1000   LET W4=W4-INT(W4+.001)
```

```
1010 LET W5=W5-INT(W5+.001)
1020 LET U[3*I3-2]=F[V0]*(V1+W4)+G[V0]*(V2+W5)+H[V0]*V3
1030 LET U[3*I3-1]=J[V0]*(V1+W4)+K[V0]*(V2+W5)+L[V0]*V3
1040 LET U[3*I3]=M[V0]*(V1+W4)+N[V0]*(V2+W5)+O[V0]*V3
1050 IF I3>I2 THEN IF I3=<I1+I2 THEN GOTO 1090
1060 IF ABS(U[3*I3-2]-INT(U[3*I3-2]+.99))>.01 THEN GOTO 1100
1070 IF ABS(U[3*I3-1]-INT(U[3*I3-1]+.99))>.01 THEN GOTO 1100
1080 IF ABS(U[3*I3]-INT(U[3*I3]+.99))>.01 THEN GOTO 1100
1090 GOTO 1110
1100 PRINT I3;"ERROR",U[3*I3-2],U[3*I3-1],U[3*I3-2]
1110 IF I3=<I2 THEN GOTO 1140
1120 IF I3>I1+I2 THEN GOTO 1140
1130 GOTO 1170
1140 LET U[3*I3-2]=INT(U[3*I3-2]+.05)
1150 LET U[3*I3-1]=INT(U[3*I3-1]+.05)
1160 LET U[3*I3]=INT(U[3*I3]+.05)
1170 NEXT I3
1180 FOR I5=1 TO (I0-1)
1190   LET S1=(I1+I2)+4*(I5-1)+1
1200   LET S2=(I1+I2)+4*(I5-1)+2
1210   LET S=(I1+I2)+4*(I5-1)+3
1220   LET S9=(I1+I2)+4*(I5-1)+4
1230   LET C1=U[3*S1-2]-U[3*S2-2]
1240   LET C2=U[3*S1-1]-U[3*S2-1]
1250   LET C3=U[3*S1]-U[3*S2]
1260   LET W1=U[3*S9-2]+C1
1270   LET W2=U[3*S9-1]+C2
1280   LET W3=U[3*S9]+C3
1290   IF INT(W1+.001)=INT(U[3*S-2]+.001) THEN IF INT(W2+.001)=INT(U[3*S
-1]+.001) THEN GOTO 1310
1300   GOTO 1320
1310   IF INT(W3+.001)=INT(U[3*S]+.001) THEN GOTO 1350
1320   PRINT "ERROR--- SECOND REFERENCE SITE IS NOT CORRECTLY TRANSFORME
D";
1330   PRINT "-------- CHECK DATA FOR NO.";I5;"(HKL) PLANE"
1340   STOP
1350   READ I6,I7
                 1360   IF I6=0 THEN IF I7=0 THEN GOTO 1450
1370   FOR I8=I6 TO I7
1380     LET W1=U[3*I8-2]+C1
1390     LET W2=U[3*I8-1]+C2
1400     LET W3=U[3*I8]+C3
1410     LET U[3*I8-2]=INT(W1+.1)
1420     LET U[3*I8-1]=INT(W2+.1)
1430     LET U[3*I8]=INT(W3+.1)
1440   NEXT I8
1450   READ I6,I7
1460   IF I6=0 THEN IF I7=0 THEN GOTO 1520
1470   FOR I8=I6 TO I7
1480     LET W1=U[3*I8-2]+C1
1490     LET W2=U[3*I8-1]+C2
1500     LET W3=U[3*I8]+C3
```

```
1510 NEXT I8
1520 NEXT I5
1530 ON Y4 THEN GOTO 1540, 1600
1540 PRINT
1550 PRINT "(X,Y,Z)S ARE COORDINATES BASED ON AXES (1 0 0), (0 1 0), AND
 (0 0 1)"
1560 PRINT
1570 PRINT
1580 PRINT "DEFECT NO.","**","X","Y","Z"
1590 PRINT
1600 FOR Y2=1 TO I1+I2
1610   ON Y4 THEN GOTO 1620, 1630
1620   IF Y2>I2 THEN GOTO 1740
1630   ON Y6 THEN GOTO 1640, 1660
1640   IF (U[3*Y2-2]+U[3*Y2-1]+U[3*Y2])/2=INT((U[3*Y2-2]+U[3*Y2-1]+U[3*Y
2]+1)/2) THEN GOTO 1720
1650   GOTO 1700
1660   IF U[3*Y2-2]/2=INT((U[3*Y2-2]+1)/2) THEN GOTO 1690
1670   IF U[3*Y2-1]/2<INT((U[3*Y2-1]+1)/2) THEN IF U[3*Y2]/2<INT((U[3*Y2
]+1)/2) THEN GOTO 1720
1680   GOTO 1700
1690   IF U[3*Y2-1]/2=INT((U[3*Y2-1]+1)/2) THEN IF U[3*Y2]/2=INT((U[3*Y2
]+1)/2) THEN GOTO 1720
1700   PRINT Y2,"ERR0R",U[3*Y2-2],U[3*Y2-1],U[3*Y2]
1710   GOTO 1770
1720   ON Y4 THEN GOTO 1730, 1770
1730   IF Y2=<I2 THEN GOTO 1760
1740   PRINT Y2;"(I)","**",U[3*Y2-2],U[3*Y2-1],U[3*Y2]
1750   GOTO 1770
1760   PRINT Y2;"(V)","**",U[3*Y2-2],U[3*Y2-1],U[3*Y2]
1770 NEXT Y2
1780 PRINT "DELETE THE COORDINATE OF THE VACANCY WHICH HAS BEEN DOUBLY "
;
1790 PRINT "COUNTED IN THE DATA LISTING"
1800 FOR Y1=1 TO I2-1
1810   FOR Y2=Y1+1 TO I2
1820     IF U[3*Y1]><U[3*Y2] THEN GOTO 1860
1830     IF U[3*Y1-1]><U[3*Y2-1] THEN GOTO 1860
1840     IF U[3*Y1-2]><U[3*Y2-2] THEN GOTO 1860
1850     PRINT "V(";Y1;") = V(";Y2;")"
1860   NEXT Y2
1870 NEXT Y1
1880 PRINT "CHECK INPUT DATA IF THE ABOVE RESULTS SHOW ERROR MESSAGES!"
```

Appendix D: Programs for the OR TEP Plots and the Computations of Quantities c_v, $R(i)/Z(i)$, $\bar{N}(i)$, λ_1, λ_2

D.1. Introduction

In this appendix the three programs denoted by DZP1, DZP2 and DZP3 are described:

DZP1 was used to arrange the coordinates of VLSs and SIAs in a format acceptable for the OR TEP program which was written in FORTRAN language and stored in a PRIME computer in the Materials Science Center at Cornell University. The OR TEP program at Cornell University is capable of plotting a maximum of only 168 atomic sites at one time. Therefore, any depleted zone which consisted of more than 168 VLSs (and SIAs) had to be divided and plotted in two or more separate plots; these separated plots were then put together to make one single plot.

DZP2 was used to calculate: (1) the average VLS concentration (c_v) within a depleted zone; (2) the values of $R(i)/Z(i)$s out to the 9th nearest-neighbor distance; (3) the values of $\bar{N}(i)$s; and (4) the distribution of VLS cluster sizes of a depleted zone.

DZP3 was used to compute the VLS distribution curves along the [100], [010], [001], [110], $[\bar{1}10]$, [011], $[0\bar{1}1]$, [101], $[\bar{1}01]$, [111], $[\bar{1}11]$, and $[1\bar{1}1]$ directions and to calculate the standard deviation σ for each curve. The values of the quantities λ_1 and λ_2 were then determined from the values of σs.

A flow chart for programs DZP1, DZP2 and DZP3 is shown in sect.D.2. The details of the programs are listed in sects.D.3. to D.5. The input statements for these three programs are the same as those for Subprogram A described in sect.C.3 of Appendix C.

D.2. Flow Chart for Programs DZP1, DZP2 and DZP3

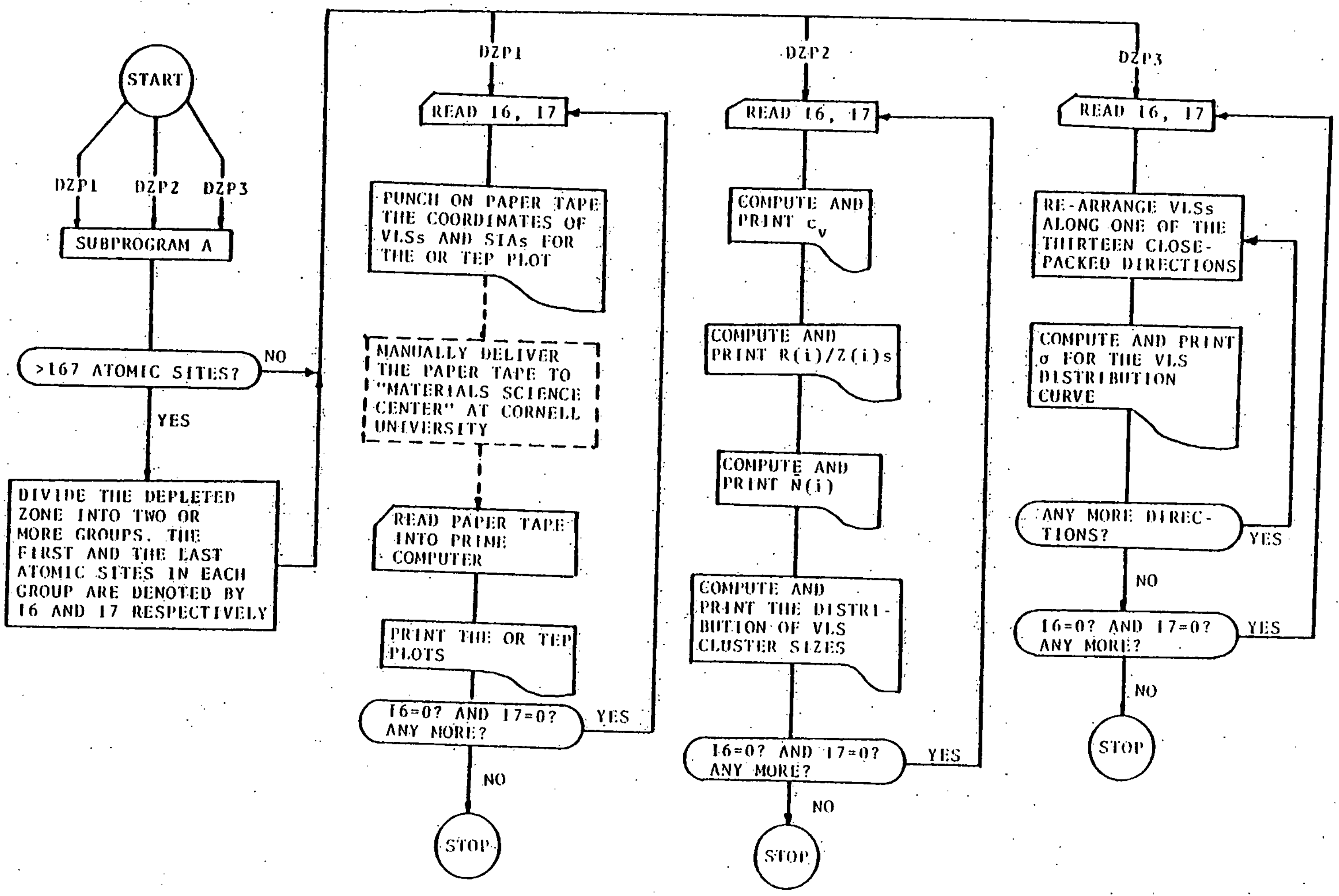

D.3. Program DZP1

```
0010 REM
0020 REM DZP1
0030 REM INSERT SUBPROGRAM A
0031 REM
1890 INPUT "ARE YOU READY TO PUNCH DATA ON PAPER TAPE, YES(1) OR NO(2)?"
,K5
1900 INPUT "WHAT IS THE LATTICE CONSTANT IN ANGSTROM?",D8
1910 ON K5 THEN GOTO 1920, 1960
1920 INPUT "WHAT COOR. SYSM. DO YOU WANT TO TRANSFORM TO, A1 TO A9?",A1,
A2,A3,A4,A5,A6,A7,A8,A9
1930 LET I6=1
1940 LET I7=I1+I2
1950 GOTO 2060
1960 INPUT "DO YOU NEED THE FIRST DRAFT OF THIS DEPLETED ZONE, YES(1) OR
 NO(2)?",Y4
1970 LET I6=1
1980 LET I7=I2+I1
1990 ON Y4 THEN GOTO 2000, 2040
2000 GOSUB 5610
2010 GOSUB 5770
2020 GOSUB 4880
2030 GOTO 1960
2040 INPUT "WHAT COOR. SYSM. DO YOU WANT TO TRANSFORM TO, A1 TO A9?",A1,
A2,A3,A4,A5,A6,A7,A8,A9
2050 INPUT "FROM WHICH TO WHICH VACANCY DO YOU WANT TO TRANSFORM,FROM I6
 TO I7 ?",I6,I7
2060 GOSUB 3940
2070 GOSUB 4080
2080 FOR Y2=I6 TO I7
2090   GOSUB 4290
2100 NEXT Y2
2110 LET B7=2*INT((A7+1.2)/2)
2120 LET B8=2*INT((A8+1.2)/2)
2130 LET B9=2*INT((A9+1.2)/2)
2140 LET B6=2*INT((A7+A8+A9+1.2)/2)
2150 LET B5=SQR(A7*A7+A8*A8+A9*A9)
2160 ON Y6 THEN GOTO 2170, 2200
2170 IF A7=B7 THEN IF A8=B8 THEN IF A9=B9 THEN GOTO 2220
2180 IF A7=B7-1 THEN IF A8=B8-1 THEN IF A9=B9-1 THEN GOTO 2220
2190 GOTO 2240
2200 IF A7+A8+A9=B6 THEN GOTO 2220
2210 GOTO 2240
2220 LET S=2/B5
2230 GOTO 2250
2240 LET S=1/B5
2250 FOR Y2=I6 TO I7
2260   LET U[3*Y2]=INT(U[3*Y2]/S+.1)
2270 NEXT Y2
2280 LET Z0=U[3*I6]
2290 LET Z9=U[3*I6]
2300 FOR Y2=I6+1 TO I7
2310   IF U[3*Y2]<Z0 THEN LET Z0=U[3*Y2]
2320   IF U[3*Y2]>Z9 THEN LET Z9=U[3*Y2]
2330 NEXT Y2
2340 LET Z0=INT(Z0)
2350 LET Z9=INT(Z9+.9)
```

```
2360 FOR Y2=I6 TO I7
2370   LET U[3*Y2]=U[3*Y2]-Z0+1
2380 NEXT Y2
2390 FOR Y2=1 TO 200
2400   LET A[Y2]=0
2410 NEXT Y2
2420 LET C3=SQR(A7↑2+A8↑2+A9↑2)
2430 ON Y6 THEN GOTO 2440, 2530
2440 IF A7/2=INT(A7/2+.001) THEN GOTO 2480
2450 IF A8/2><INT(A8/2+.001) THEN IF A9/2><INT(A9/2+.001) THEN GOTO 2510
2460 LET I5=1/C3
2470 GOTO 2520
2480 IF A8/2=INT(A8/2+.001) THEN IF A9/2=INT(A9/2+.001) THEN GOTO 2510
2490 LET I5=1/C3
2500 GOTO 2520
2510 LET I5=2/C3
2520 GOTO 2570
2530 IF A7+A8+A9=2*INT((A7+A8+A9)/2+.001) THEN GOTO 2560
2540 LET I5=1/C3
2550 GOTO 2570
2560 LET I5=2/C3
2570 LET K2=1
2580 ON K2 THEN GOTO 2590, 2720
2590 LET I4=INT(2.82842/I5+.5)
2600 FOR Y2=I6 TO I7
2610   LET B4=INT(U[3*Y2]/I4-.1)+1
2620   LET A[B4]=A[B4]+1
2630 NEXT Y2
2640 LET S9=0
2650 PRINT "THE THICKNESS OF THE SLAB IS";I4*I5*D8/2;" A "
2660 PRINT "SLAB NO.","VAC. NO.","SUM"
2670 FOR Y2=1 TO INT((Z9-Z0+1)/I4-.1)+1
2680   LET S9=S9+A[Y2]
2690   PRINT Y2,A[Y2],S9
2700 NEXT Y2
2710 GOTO 2870
2720 FOR Y2=I6 TO I7
2730   LET B4=U[3*Y2]
2740   LET A[B4]=A[B4]+1
2750 NEXT Y2
2760 LET S8=0
2770 LET S9=0
2780 FOR Y2=1 TO INT(Z9-Z0+1+.1)
2790   LET S8=S8+Y2*A[Y2]
2800   LET S9=S9+Y2↑2*A[Y2]
2810 NEXT Y2
2820 LET S8=(S8/(I7-I6+1))↑2
2830 LET S9=S9/(I7-I6+1)
2840 LET S9=SQR(S9-S8)
2850 LET S9=S9*I5*D8/2
```

```
2860 PRINT "THE DAMAGE WIDTH ALONG [";A7;A8;A9;"] = ";S9;" A "
2870 GOSUB 3770
2880 FOR Y2=I6 TO I7
2890   LET U[3*Y2]=U[3*Y2]+Z0-1
2900   LET U[3*Y2]=S*U[3*Y2]
2910 NEXT Y2
2920 GOSUB 4080
2930 FOR Y2=I6 TO I7
2940   GOSUB 4290
2950   LET Y4=ABS(U[3*Y2-2]-INT(U[3*Y2-2]+.01))
2960   LET Y5=ABS(U[3*Y2-1]-INT(U[3*Y2-1]+.01))
2970   LET Y7=ABS(U[3*Y2]-INT(U[3*Y2]+.01))
2980   IF Y4<.001 THEN IF Y5<.001 THEN IF Y7<.001 THEN GOTO 3000
2990   GOTO 3030
3000   LET U[3*Y2-2]=INT(U[3*Y2-2]+.1)
3010   LET U[3*Y2-1]=INT(U[3*Y2-1]+.1)
3020   LET U[3*Y2]=INT(U[3*Y2]+.1)
3030 NEXT Y2
3040 REM
3050 REM DETERMINATION OF I6 AND I7
3060 REM
3070 GOSUB 5610
3080 GOSUB 5770
3090 INPUT "WHAT ARE YOU GOING TO DO NOW? OLD PLOT(1), NEW PLOT(2), OR P
UNCH PTR(3)?",Y4
3100 ON Y4 THEN GOTO 3110, 2040, 3130
3110 GOSUB 4880
3120 GOTO 3090
3130 GOTO 3170
3140 REM
3150 REM ARRANGE AND PUNCH DATA ON PTR FOR ORTEP PROGRAM IN MSC CENTER
3160 REM
3170 FOR Y1=I6 TO I7
3180   LET Y4=ABS(U[3*Y1-2]-INT(U[3*Y1-2]+.01))
3190   LET Y5=ABS(U[3*Y1-1]-INT(U[3*Y1-1]+.01))
3200   LET Y7=ABS(U[3*Y1]-INT(U[3*Y1]+.01))
3210   IF Y4<.01 THEN IF Y5<.01 THEN IF Y7<.01 THEN GOTO 3230
3220   GOTO 3300
3230   FOR Y2=0 TO 2
3240     LET V1=U[3*Y1-Y2]
3250     IF V1=0 THEN LET U[3*Y1-Y2]=.222222
3260     IF V1/10=>.099 THEN IF V1/10=<.95 THEN LET U[3*Y1-Y2]=V1+.22222
3270     IF V1/100=>.095 THEN IF V1/100=<.995 THEN LET U[3*Y1-Y2]=V1+.22
22
3280     IF V1/1000=>.0995 THEN IF V1/1000=<.9995 THEN LET U[3*Y1-Y2]=V1
+.222
3290   NEXT Y2
3300 NEXT Y1
3310 INPUT "FROM WHICH TO WHICH VACANCY DO YOU WANT TO PUNCH ON PTR,I6 T
O I7?",I6,I7
3320 FOR Y1=1 TO 1000
3330   GOTO 3340
3340 NEXT Y1
3350 PRINT "DEPLETED ZONE - ";I2;"(";I7-I6+2;")"
```

```
3360 GOSUB 4490
3370 GOSUB 4790
3380 GOSUB 4530
3390 GOSUB 4730
3400 FOR Y1=I6 TO I7
3410   GOSUB 4580
3420   IF Y1=<I7-1 THEN GOTO 3440
3430   PRINT "1";
3440   GOSUB 4620
3450 NEXT Y1
3460 LET K1=101
3470 GOSUB 4370
3480 LET K1=201
3490 GOSUB 4370
3500 PRINT  TAB(6);"301"; TAB(12);"16.000"; TAB(21);"11.000"; TAB(30);"5
00.00";
3510 PRINT  TAB(39);"0.5000"; TAB(48);"0.0000"; TAB(57);"0.0000"; TAB(66
);"0.0000"
3520 LET K1=303
3530 GOSUB 4370
3540 LET K1=401
3550 GOSUB 4660
3560 LET K1=501
3570 GOSUB 4840
3580 PRINT  TAB(6);"502"; TAB(17);"1"; TAB(24);"30."; TAB(35);"2"; TAB(4
2);"30.";
3590 PRINT  TAB(53);"3"; TAB(60);"30."
3600 PRINT  TAB(6);"604"; TAB(12);"0.0000"; TAB(21);"0.0000"; TAB(30);"0
.0000";
3610 PRINT  TAB(39);"5.0000"; TAB(48);"0.0000"; TAB(57);"0.0000"; TAB(66
);"0.0000"
3620 PRINT  TAB(6);"611"; TAB(12);"0.0000"; TAB(21);"0.0000"; TAB(30);"0
.8000";
3630 PRINT  TAB(39);"0.0000"; TAB(48);"0.0000"; TAB(57);"0.0000"; TAB(66
);"0.0000"
3640 PRINT  TAB(6);"704"; TAB(12);"0.0000"; TAB(21);"0.0000"; TAB(30);"0
.0000";
3650 PRINT  TAB(39);"0.0000"; TAB(48);"0.1000"; TAB(57);"0.0500"; TAB(66
);"0.0500"
3660 LET K1=802
3670 GOSUB 4410
3680 GOSUB 4450
3690 LET K1=202
3700 GOSUB 4370
3710 LET K1=202
3720 GOSUB 4370
3730 LET K1=-1
3740 GOSUB 4690
3750 END
3760 STOP
3770 FOR Y1=I7 TO I6 STEP -1
3780   FOR Y2=I6 TO Y1-1
3790     IF U[3*Y2]>U[3*Y1] THEN GOTO 3810
3800     GOTO 3900
3810     LET W1=U[3*Y2-2]
3820     LET W2=U[3*Y2-1]
3830     LET W3=U[3*Y2]
3840     LET U[3*Y2-2]=U[3*Y1-2]
3850     LET U[3*Y2-1]=U[3*Y1-1]
```

```
3860 LET U[3*Y2]=U[3*Y1]
3870 LET U[3*Y1-2]=W1
3880 LET U[3*Y1-1]=W2
3890 LET U[3*Y1]=W3
3900 NEXT Y2
3910 NEXT Y1
3920 RETURN
3930 STOP
3940 LET C1=SQR(A1*A1+A2*A2+A3*A3)
3950 LET C2=SQR(A4*A4+A5*A5+A6*A6)
3960 LET C3=SQR(A7*A7+A8*A8+A9*A9)
3970 LET E[1,1]=A1/C1
3980 LET E[2,1]=A2/C1
3990 LET E[3,1]=A3/C1
4000 LET E[1,2]=A4/C2
4010 LET E[2,2]=A5/C2
4020 LET E[3,2]=A6/C2
4030 LET E[1,3]=A7/C3
4040 LET E[2,3]=A8/C3
4050 LET E[3,3]=A9/C3
4060 RETURN
4070 STOP
4080 LET B1=E[2,2]*E[3,3]-E[2,3]*E[3,2]
4090 LET B2=E[2,3]*E[3,1]-E[2,1]*E[3,3]
4100 LET B3=E[2,1]*E[3,2]-E[2,2]*E[3,1]
4110 LET B4=E[1,3]*E[3,2]-E[1,2]*E[3,3]
4120 LET B5=E[1,1]*E[3,3]-E[1,3]*E[3,1]
4130 LET B6=E[1,2]*E[3,1]-E[1,1]*E[3,2]
4140 LET B7=E[1,2]*E[2,3]-E[1,3]*E[2,2]
4150 LET B8=E[1,3]*E[2,1]-E[1,1]*E[2,3]
4160 LET B9=E[1,1]*E[2,2]-E[1,2]*E[2,1]
4170 LET C4=E[1,1]*B1+E[1,2]*B2+E[1,3]*B3
4180 LET E[1,1]=B1/C4
4190 LET E[1,2]=B4/C4
4200 LET E[1,3]=B7/C4
4210 LET E[2,1]=B2/C4
4220 LET E[2,2]=B5/C4
4230 LET E[2,3]=B8/C4
4240 LET E[3,1]=B3/C4
4250 LET E[3,2]=B6/C4
4260 LET E[3,3]=B9/C4
4270 RETURN
4280 STOP
4290 LET W1=E[1,1]*U[3*Y2-2]+E[1,2]*U[3*Y2-1]+E[1,3]*U[3*Y2]
4300 LET W2=E[2,1]*U[3*Y2-2]+E[2,2]*U[3*Y2-1]+E[2,3]*U[3*Y2]
4310 LET W3=E[3,1]*U[3*Y2-2]+E[3,2]*U[3*Y2-1]+E[3,3]*U[3*Y2]
4320 LET U[3*Y2-2]=W1
4330 LET U[3*Y2-1]=W2
4340 LET U[3*Y2]=W3
4350 RETURN
```

```
4360 STOP
4370 PRINT  TAB(5);K1; TAB(12);"0.0000"; TAB(21);"0.0000"; TAB(30);"0.00
00";
4380 PRINT  TAB(39);"0.0000"; TAB(48);"0.0000"; TAB(57);"0.0000"; TAB(66
);"0.0000"
4390 RETURN
4400 STOP
4410 PRINT  TAB(2);"2"; TAB(5);K1; TAB(11);"0.00000"; TAB(20);"0.00000";
 TAB(29);"0.00000";
4420 PRINT  TAB(38);"0.00000"; TAB(47);"0.00000"; TAB(56);"0.00000"; TAB
(65);"0.00000"
4430 RETURN
4440 STOP
4450 PRINT  TAB(2);"0"; TAB(11);"2"; TAB(13);"00"; TAB(17);"2"; TAB(19);
"00"; TAB(23);"1";
4460 PRINT  TAB(25);"1.500"; TAB(31);"1.900"; TAB(37);"0.040"
4470 RETURN
4480 STOP
4490 PRINT  TAB(2);"2.00000"; TAB(11);"2.00000"; TAB(20);"2.00000";
4500 PRINT  TAB(29);"0.00000"; TAB(38);"0.00000"; TAB(47);"0.00000"
4510 RETURN
4520 STOP
4530 PRINT "1"; TAB(6);"0.0000000"; TAB(17);"1"; TAB(20);"0"; TAB(23);"0
"; TAB(30);"0.0000000";
4540 PRINT  TAB(41);"0"; TAB(44);"1"; TAB(47);"0"; TAB(54);"0.0000000";
4550 PRINT  TAB(65);"0"; TAB(68);"0"; TAB(71);"1"
4560 RETURN
4570 STOP
4580 PRINT  TAB(11);"0.00000"; TAB(20);"0.00000"; TAB(28);U[3*Y1-2];
4590 PRINT  TAB(37);U[3*Y1-1]; TAB(46);U[3*Y1]; TAB(61);"2."
4600 RETURN
4610 STOP
4620 PRINT  TAB(2);"0.50000"; TAB(11);"0.00000"; TAB(20);"0.00000"; TAB(
29);"0.00000";
4630 PRINT  TAB(38);"0.00000"; TAB(47);"0.00000"; TAB(61);"6."
4640 RETURN
4650 STOP
4660 PRINT  TAB(5);K1; TAB(12);"255502"; TAB(18);"-    55502"
4670 RETURN
4680 STOP
4690 PRINT  TAB(7);K1; TAB(12);"0.0000"; TAB(21);"0.0000"; TAB(30);"0.00
00";
4700 PRINT  TAB(39);"0.0000"; TAB(48);"0.0000"; TAB(57);"0.0000"; TAB(66
);"0.0000"
4710 RETURN
4720 STOP
4730 PRINT  TAB(11);"0.00000"; TAB(20);"0.00000"; TAB(29);"0.00000";
4740 PRINT  TAB(38);"0.00000"; TAB(47);"0.00000"; TAB(61);"2."
4750 PRINT  TAB(2);"0.50000"; TAB(11);"0.00000"; TAB(20);"0.00000"; TAB(
29);"0.00000";
4760 PRINT  TAB(38);"0.00000"; TAB(47);"0.00000"; TAB(61);"6."
4770 RETURN
4780 STOP
4790 PRINT  TAB(6);"0.0000000"; TAB(17);"1"; TAB(20);"0"; TAB(23);"0"; T
AB(30);"0.0000000";
4800 PRINT  TAB(41);"0"; TAB(44);"1"; TAB(47);"0"; TAB(54);"0.0000000";
TAB(65);"0";
4810 PRINT  TAB(68);"0"; TAB(71);"1"
4820 RETURN
4830 STOP
4840 PRINT  TAB(5);K1; TAB(12);"155502"; TAB(21);"155500"; TAB(30);"1655
00"; TAB(39);"155500";
4850 PRINT  TAB(48);"156500"; TAB(57);"0.0000"; TAB(71);"1"
```

```
4860 RETURN
4870 STOP
4880 INPUT "WHAT IS THE VIEW DIRECTION , (1) OR (2) ?",K7
4890 INPUT "FRONT(1), R-H SIDE(2), OR TOP VIEW(3) ?",V0
4900 INPUT "WHICH VACANCIES DO YOU LIKE TO LABEL , H(1) TO H(4)?",H[1],H
[2],H[3],H[4]
4910 ON K7 THEN GOTO 4950, 4920
4920 LET S1=0
4930 LET S2=0
4940 GOTO 4970
4950 LET S1=2/3
4960 LET S2=1/3
4970 LET V4=150
4980 LET V5=80
4990 IF Y6=1 THEN LET V6=2
5000 IF Y6=2 THEN LET V6=3
5010 ON V0 THEN GOTO 5120, 5020, 5070
5020 IF 975/(Y9+S1*X9)>780/(Z9+S2*X9) THEN GOTO 5050
5030 LET W6=950/(Y9+S1*X9)
5040 GOTO 5160
5050 LET W6=700/(Z9+S2*X9)
5060 GOTO 5160
5070 IF 975/(X9+S1*Z9)>780/(Y9+S2*Z9) THEN GOTO 5100
5080 LET W6=950/(X9+S1*Z9)
5090 GOTO 5160
5100 LET W6=700/(Y9+S2*Z9)
5110 GOTO 5160
5120 IF 975/(X9+S1*Y9)>780/(Z9+S2*Y9) THEN GOTO 5150
5130 LET W6=950/(X9+S1*Y9)
5140 GOTO 5160
5150 LET W6=700/(Z9+S2*Y9)
5160 LET W6=.8*W6
5170 PRINT "<27><12>"
5180 ON K7 THEN GOTO 5240, 5190
5190 CALL 20,45,0,1020,0
5200 CALL 20,1020,0,1020,780
5210 CALL 20,1020,780,45,780
5220 CALL 20,45,780,45,0
5230 GOTO 5400
5240 CALL 20,45,0,630,0
5250 CALL 20,630,0,630,585
5260 CALL 20,630,585,45,585
5270 CALL 20,45,585,45,0
5280 CALL 20,630,0,1020,195
5290 CALL 20,1020,195,1020,780
5300 CALL 20,1020,780,435,780
5310 CALL 20,1020,780,630,585
5320 CALL 20,435,780,45,585
5330 FOR Y1=0 TO 38 STEP 2
5340   CALL 20,45+390*Y1/39,195*Y1/39,45+390*(Y1+1)/39,195*(Y1+1)/39
5350 NEXT Y1
```

```
5360 FOR Y1=0 TO 44 STEP 2
5370   CALL 20,435+Y1*585/45,195,435+(Y1+1)*585/45,195
5380   CALL 20,435,195+Y1*585/45,435,195+(Y1+1)*585/45
5390 NEXT Y1
5400 FOR Y2=I6 TO I7
5410   ON V0 THEN GOTO 5480, 5420, 5450
5420   LET W1=W6*U[3*Y2-1]+V4+W6*S1*(U[3*I2-2]+1-U[3*Y2-2])
5430   LET W2=W6*U[3*Y2]+V5+W6*S2*(U[3*I2-2]+1-U[3*Y2-2])
5440   GOTO 5500
5450   LET W1=W6*U[3*Y2-2]+V4+W6*S1*(U[3*I2]+1-U[3*Y2])
5460   LET W2=W6*U[3*Y2-1]+V5+W6*S2*(U[3*I2]+1-U[3*Y2])
5470   GOTO 5500
5480   LET W1=W6*U[3*Y2-2]+V4+W6*S1*U[3*Y2-1]
5490   LET W2=W6*U[3*Y2]+V5+W6*S2*U[3*Y2-1]
5500   GOTO 5510
5510   CALL 20,W1,W2,W1,W2
5520   FOR Y3=1 TO 4
5530     IF Y2=H[Y3] THEN PRINT Y2
5540   NEXT Y3
5550 NEXT Y2
5560 FOR Y1=1 TO 40
5570   PRINT
5580 NEXT Y1
5590 RETURN
5600 STOP
5610 LET X0=U[3*I6-2]
5620 LET X9=U[3*I6-2]
5630 LET Y0=U[3*I6-1]
5640 LET Y9=U[3*I6-1]
5650 LET Z0=U[3*I6]
5660 LET Z9=U[3*I6]
5670 FOR Y2=I6 TO I7
5680   IF U[3*Y2-2]<X0 THEN LET X0=U[3*Y2-2]
5690   IF U[3*Y2-2]>X9 THEN LET X9=U[3*Y2-2]
5700   IF U[3*Y2-1]<Y0 THEN LET Y0=U[3*Y2-1]
5710   IF U[3*Y2-1]>Y9 THEN LET Y9=U[3*Y2-1]
5720   IF U[3*Y2]<Z0 THEN LET Z0=U[3*Y2]
5730   IF U[3*Y2]>Z9 THEN LET Z9=U[3*Y2]
5740 NEXT Y2
5750 RETURN
5760 STOP
5770 IF X0/2><INT(X0/2) THEN LET X0=X0-1
5780 IF Y0/2><INT(Y0/2) THEN LET Y0=Y0-1
5790 IF Z0/2><INT(Z0/2) THEN LET Z0=Z0-1
5800 FOR Y1=I6 TO I7
5810   LET U[3*Y1-2]=U[3*Y1-2]-X0
5820   LET U[3*Y1-1]=U[3*Y1-1]-Y0
5830   LET U[3*Y1]=U[3*Y1]-Z0
5840 NEXT Y1
5850 LET X9=X9-X0
```

```
5860 LET Y9=Y9-Y0
5870 LET Z9=Z9-Z0
5880 LET X0=0
5890 LET Y0=0
5900 LET Z0=0
5910 RETURN
```

D.4. Program DZP2

```
0010 REM
0020 REM DZP2
0030 REM
1890 ON K3 THEN GOTO 1900, 1930
1900 LET I6=1
1910 LET I7=I2
1920 GOTO 2770
1930 READ A1,A2,A3,A4,A5,A6,A7,A8,A9
1940 GOSUB 5160
1950 GOSUB 5300
1960 FOR Y2=1 TO I1+I2
1970   GOSUB 5510
1980 NEXT Y2
1990 LET B7=2*INT((A7+1.2)/2)
2000 LET B8=2*INT((A8+1.2)/2)
2010 LET B9=2*INT((A9+1.2)/2)
2020 LET B6=2*INT((A7+A8+A9+1.2)/2)
2030 LET B5=SQR(A7*A7+A8*A8+A9*A9)
2040 ON Y6 THEN GOTO 2050, 2080
2050 IF A7=B7 THEN IF A8=B8 THEN IF A9=B9 THEN GOTO 2100
2060 IF A7=B7-1 THEN IF A8=B8-1 THEN IF A9=B9-1 THEN GOTO 2100
2070 GOTO 2120
2080 IF A7+A8+A9=B6 THEN GOTO 2100
2090 GOTO 2120
2100 LET S=2/B5
2110 GOTO 2130
2120 LET S=1/B5
2130 FOR Y2=1 TO I1+I2
2140   LET U[3*Y2]=INT(U[3*Y2]/S+.1)
2150 NEXT Y2
2160 LET Z0=U[3]
2170 LET Z9=U[3]
2180 FOR Y2=2 TO I1+I2
2190   IF U[3*Y2]<Z0 THEN LET Z0=U[3*Y2]
2200   IF U[3*Y2]>Z9 THEN LET Z9=U[3*Y2]
2210 NEXT Y2
2220 FOR Y2=1 TO I1+I2
2230   LET U[3*Y2]=U[3*Y2]-Z0+1
2240 NEXT Y2
2250 FOR Y2=1 TO 200
2260   LET A(Y2]=0
2270 NEXT Y2
2280 LET C3=SQR(A7↑2+A8↑2+A9↑2)
2290 ON Y6 THEN GOTO 2300, 2390
2300 IF A7/2=INT(A7/2+.001) THEN GOTO 2340
2310 IF A8/2><INT(A8/2+.001) THEN IF A9/2><INT(A9/2+.001) THEN GOTO 2370
2320 LET I5=1/C3
2330 GOTO 2380
2340 IF A8/2=INT(A8/2+.001) THEN IF A9/2=INT(A9/2+.001) THEN GOTO 2370
2350 LET I5=1/C3
2360 GOTO 2380
2370 LET I5=2/C3
2380 GOTO 2430
2390 IF A7+A8+A9=2*INT((A7+A8+A9)/2+.001) THEN GOTO 2420
2400 LET I5=1/C3
2410 GOTO 2430
2420 LET I5=2/C3
2430 LET I4=INT(2.82842/I5+.5)
2440 FOR Y2=1 TO I1+I2
2450   LET B4=INT(U[3*Y2]/I4-.1)+1
2460   LET A[B4]=A[B4]+1
2470 NEXT Y2
2480 LET S9=0
2490 PRINT "SLAB NO.","VAC. NO.","SUM"
2500 FOR Y2=1 TO INT((Z9-Z0+1)/I4-.1)+1
```

```
2510 LET S9=S9+A[Y2]
2520 PRINT Y2,A[Y2],S9
2530 NEXT Y2
2540 LET I6=1
2550 LET I7=I1+I2
2560 GOSUB 4830
2570 FOR Y2=1 TO I1+I2
2580   LET U[3*Y2]=U[3*Y2]+Z0-1
2590   LET U[3*Y2]=S*U[3*Y2]
2600 NEXT Y2
2610 GOSUB 5300
2620 FOR Y2=1 TO I1+I2
2630   GOSUB 5510
2640   LET Y4=ABS(U[3*Y2-2]-INT(U[3*Y2-2]+.01))
2650   LET Y5=ABS(U[3*Y2-1]-INT(U[3*Y2-1]+.01))
2660   LET Y7=ABS(U[3*Y2]-INT(U[3*Y2]+.01))
2670   IF Y4<.001 THEN IF Y5<.001 THEN IF Y7<.001 THEN GOTO 2690
2680   GOTO 2720
2690   LET U[3*Y2-2]=INT(U[3*Y2-2]+.1)
2700   LET U[3*Y2-1]=INT(U[3*Y2-1]+.1)
2710   LET U[3*Y2]=INT(U[3*Y2]+.1)
2720 NEXT Y2
2730 REM
2740 REM VACANCY CONCENTRATION
2750 REM
2760 READ I6,I7
2770 IF I6=0 THEN IF I7=0 THEN GOTO 4630
2780 GOSUB 4650
2790 GOSUB 5000
2800 LET S0=4
2810 FOR Y3=1 TO 3
2820   IF Y3=1 THEN LET A1=X0
2830   IF Y3=1 THEN LET A2=X9+1
2840   IF Y3=2 THEN LET A1=Y0
2850   IF Y3=2 THEN LET A2=Y9+1
2860   IF Y3=3 THEN LET A1=Z0
2870   IF Y3=3 THEN LET A2=Z9+1
2880   LET S9=0
2890   FOR Y1=A1 TO A2 STEP S0
2900     FOR Y2=I6 TO I7
2910       GOSUB 5590
2920       IF U[A3]=>Y1 THEN IF U[A3]=<Y1+S0-1 THEN GOTO 2950
2930     NEXT Y2
2940     GOTO 3230
2950     LET B1=U[A4]
2960     LET B2=U[A4]
2970     LET B3=U[A5]
2980     LET B4=U[A5]
2990     FOR Y2=I6 TO I7
3000       GOSUB 5590
```

```
3010 IF U[A3]=>Y1 THEN IF U[A3]=<Y1+S0-1 THEN GOTO 3030
3020 GOTO 3070
3030 IF U[A4]<B1 THEN LET B1=U[A4]
3040 IF U[A4]>B2 THEN LET B2=U[A4]
3050 IF U[A5]<B3 THEN LET B3=U[A5]
3060 IF U[A5]>B4 THEN LET B4=U[A5]
3070 NEXT Y2
3080 LET B8=B2-B1
3090 LET B9=B4-B3
3100 IF B8=0 THEN LET B8=2
3110 IF B9=0 THEN LET B9=2
3120 ON Y6 THEN GOTO 3130, 3190
3130 IF B8=2*INT((B8+1)/2) THEN IF B9=2*INT((B9+1)/2) THEN GOTO 3160
3140 LET Y4=0
3150 GOTO 3170
3160 LET Y4=1
3170 LET S=INT(((B8+1)*(B9+1)+1)/2)*S0-INT(S0/2)*Y4
3180 GOTO 3220
3190 LET A8=INT(B8/2+1)
3200 LET A9=INT(B9/2+1)
3210 LET S=A8*A9*S0-INT(S0/2)*(A8*A9-(A8-B8/2+A8-1)*(A9-B9/2+A9-1))
3220 LET S9=S9+S
3230 NEXT Y1
3240 LET B5=.1*INT(1000*(I7-I6+1)/S9)
3250 LET G[Y3]=B5
3260 PRINT "C(";Y3;")=";B5;" %"
3270 NEXT Y3
3280 LET G[4]=(G[1]+G[2]+G[3])/300
3290 PRINT "THE AVERAGE VACANCY CONCENTRATION IS ";G[4]*100;" %"
3300 REM
3310 REM R(I)/RAN(I)
3320 REM
3330 FOR Y1=1 TO 9
3340   LET J[Y1]=0
3350 NEXT Y1
3360 FOR Y1=I6 TO I7
3370   FOR Y2=I6 TO I7
3380     IF Y2=Y1 THEN GOTO 3500
3390     LET R=(U[3*Y1-2]-U[3*Y2-2])↑2+(U[3*Y1-1]-U[3*Y2-1])↑2+(U[3*Y1]-
U[3*Y2])↑2
3400     ON Y6 THEN GOTO 3410, 3430
3410     IF R=<19 THEN LET J[INT(R/2+.1)]=J[INT(R/2+.1)]+1
3420     GOTO 3500
3430     IF R=<25 THEN GOTO 3450
3440     GOTO 3500
3450     LET Y3=INT((R/8-INT(R/8-.1))*8+.1)
3460     LET Y4=3*INT(R/8-.1)
3470     IF Y3=3 THEN LET J[Y4+1]=J[Y4+1]+1
3480     IF Y3=4 THEN LET J[Y4+2]=J[Y4+2]+1
3490     IF Y3=8 THEN LET J[Y4+3]=J[Y4+3]+1
3500   NEXT Y2
```

```
3510 NEXT Y1
3520 ON Y6 THEN GOTO 3530, 3630
3530 LET F[1]=12
3540 LET F[2]=6
3550 LET F[3]=24
3560 LET F[4]=12
3570 LET F[5]=24
3580 LET F[6]=8
3590 LET F[7]=48
3600 LET F[8]=6
3610 LET F[9]=36
3620 GOTO 3720
3630 LET F[1]=8
3640 LET F[2]=6
3650 LET F[3]=12
3660 LET F[4]=24
3670 LET F[5]=8
3680 LET F[6]=6
3690 LET F[7]=24
3700 LET F[8]=24
3710 LET F[9]=24
3720 FOR Y1=1 TO 9
3730   PRINT "R(";Y1;")","R(";Y1;")/RAN(";Y1;")"
3740   PRINT J[Y1]/(I7-I6+1),J[Y1]/(I7-I6+1)/F[Y1]/G[4]
3750 NEXT Y1
3760 REM
3770 REM RADIAL DISTRIBUTION FUNCTION OF FIRST KIND
3780 REM
3790 FOR Y1=1 TO 50
3800   LET A[Y1]=0
3810   LET B[Y1]=0
3820 NEXT Y1
3830 FOR Y1=I6 TO I7
3840   FOR Y2=I6 TO I7
3850     IF Y2=Y1 THEN GOTO 3940
3860     LET R=(U[3*Y1-2]-U[3*Y2-2])↑2+(U[3*Y1-1]-U[3*Y2-1])↑2+(U[3*Y1]-
U[3*Y2])↑2
3870     LET R=SQR(R)
3880     IF ABS(R/2-INT(R/2+.0001))<.0001 THEN GOTO 3910
3890     LET A[INT(R/2)+1]=A[INT(R/2)+1]+1
3900     GOTO 3940
3910     LET B1=INT(R/2+.0001)
3920     LET A[B1]=A[B1]+.5
3930     LET A[B1+1]=A[B1+1]+.5
3940   NEXT Y2
3950 NEXT Y1
3960 PRINT "THE RADIAL DISTRIBUTION FUNCTIONS OF FIRST KIND ARE :"
3970 FOR Y1=1 TO 50
3980   LET A1=2*Y1
3990   LET V1=4*3.14159*(A1↑3-(A1-2)↑3)/3
4000   IF Y6=1 THEN LET A2=V1/2
```

```
4010 IF Y6=2 THEN LET A2=V1/4
4020 IF A[Y1]=0 THEN GOTO 4040
4030 PRINT "C(";Y1;") = ";A[Y1]/(I7-I6+1)/A2
4040 NEXT Y1
4050 GOSUB 4650
4060 GOSUB 4830
4070 GOSUB 5000
4080 GOSUB 5730
4090 REM
4100 REM SIZE DISTRIBUTION OF CLUSTERS
4110 REM
4120 FOR Y1=I6 TO I7
4130   LET A[Y1]=0
4140 NEXT Y1
4150 FOR Y1=I6 TO I7
4160   LET Y5=1
4170   LET A1=Y1
4180   GOSUB 5960
4190   IF ABS(A[Y1]-.01)<.00001 THEN GOTO 4220
4200   LET A[Y1]=1
4210   GOTO 4230
4220   LET A[Y1]=0
4230 NEXT Y1
4240 FOR Y1=I6 TO I7
4250   LET Y5=2
4260   IF A[Y1]>.0001 THEN GOTO 4300
4270   LET A1=Y1
4280   GOSUB 5960
4290   GOTO 4320
4300 NEXT Y1
4310 GOTO 4510
4320 FOR Y3=1 TO 200
4330   FOR Y1=I6 TO I7
4340     IF A[Y1]=>1 THEN GOTO 4380
4350     IF ABS(A[Y1]-.01)>.00001 THEN GOTO 4380
4360     LET A1=Y1
4370     GOSUB 5960
4380   NEXT Y1
4390   LET B[Y3]=0
4400   FOR Y1=I6 TO I7
4410     IF ABS(A[Y1]-.01)>.00001 THEN GOTO 4430
4420     LET B[Y3]=B[Y3]+1
4430   NEXT Y1
4440   IF B[Y3]=B[Y3-1] THEN GOTO 4460
4450   GOTO 4500
4460   FOR Y1=I6 TO I7
4470     IF ABS(A[Y1]-.01)<.00001 THEN LET A[Y1]=B[Y3]
4480   NEXT Y1
4490   GOTO 4240
4500 NEXT Y3
```

```
4510 LET S9=0
4520 FOR Y1=0 TO 200
4530   LET S=0
4540   FOR Y2=I6 TO I7
4550     IF A[Y2]=Y1 THEN LET S=S+1
4560   NEXT Y2
4570   IF S=0 THEN GOTO 4620
4580   PRINT "NO. OF VACANCY CLUSTER OF SIZE ";Y1;"=";S/Y1;"(";S/(I7-I6+
1);")"
4590   LET S9=S9+S
4600   IF S9=I7-I6+1 THEN IF I7=I2 THEN GOTO 4630
4610   IF S9=I7-I6+1 THEN GOTO 2760
4620 NEXT Y1
4630 END
4640 STOP
4650 LET X0=U[3*I6-2]
4660 LET Y0=U[3*I6-1]
4670 LET Z0=U[3*I6]
4680 FOR Y2=I6+1 TO I7
4690   IF X0>U[3*Y2-2] THEN LET X0=U[3*Y2-2]
4700   IF Y0>U[3*Y2-1] THEN LET Y0=U[3*Y2-1]
4710   IF Z0>U[3*Y2] THEN LET Z0=U[3*Y2]
4720 NEXT Y2
4730 LET X9=U[3*I6-2]
4740 LET Y9=U[3*I6-1]
4750 LET Z9=U[3*I6]
4760 FOR Y2=I6+1 TO I7
4770   IF X9<U[3*Y2-2] THEN LET X9=U[3*Y2-2]
4780   IF Y9<U[3*Y2-1] THEN LET Y9=U[3*Y2-1]
4790   IF Z9<U[3*Y2] THEN LET Z9=U[3*Y2]
4800 NEXT Y2
4810 RETURN
4820 STOP
4830 FOR Y1=I7 TO I6 STEP -1
4840   FOR Y2=I6 TO Y1-1
4850     IF U[3*Y2]>U[3*Y1] THEN GOTO 4870
4860     GOTO 4960
4870     LET W1=U[3*Y2-2]
4880     LET W2=U[3*Y2-1]
4890     LET W3=U[3*Y2]
4900     LET U[3*Y2-2]=U[3*Y1-2]
4910     LET U[3*Y2-1]=U[3*Y1-1]
4920     LET U[3*Y2]=U[3*Y1]
4930     LET U[3*Y1-2]=W1
4940     LET U[3*Y1-1]=W2
4950     LET U[3*Y1]=W3
4960   NEXT Y2
4970 NEXT Y1
4980 RETURN
4990 STOP
5000 IF X0/2><INT(X0/2) THEN LET X0=X0-1
```

```
5010 IF Y0/2><INT(Y0/2) THEN LET Y0=Y0-1
5020 IF Z0/2><INT(Z0/2) THEN LET Z0=Z0-1
5030 FOR Y1=I6 TO I7
5040   LET U[3*Y1-2]=U[3*Y1-2]-X0
5050   LET U[3*Y1-1]=U[3*Y1-1]-Y0
5060   LET U[3*Y1]=U[3*Y1]-Z0
5070 NEXT Y1
5080 LET X9=X9-X0
5090 LET Y9=Y9-Y0
5100 LET Z9=Z9-Z0
5110 LET X0=0
5120 LET Y0=0
5130 LET Z0=0
5140 RETURN
5150 STOP
5160 LET C1=SQR(A1*A1+A2*A2+A3*A3)
5170 LET C2=SQR(A4*A4+A5*A5+A6*A6)
5180 LET C3=SQR(A7*A7+A8*A8+A9*A9)
5190 LET E[1,1]=A1/C1
5200 LET E[2,1]=A2/C1
5210 LET E[3,1]=A3/C1
5220 LET E[1,2]=A4/C2
5230 LET E[2,2]=A5/C2
5240 LET E[3,2]=A6/C2
5250 LET E[1,3]=A7/C3
5260 LET E[2,3]=A8/C3
5270 LET E[3,3]=A9/C3
5280 RETURN
5290 STOP
5300 LET B1=E[2,2]*E[3,3]-E[2,3]*E[3,2]
5310 LET B2=E[2,3]*E[3,1]-E[2,1]*E[3,3]
5320 LET B3=E[2,1]*E[3,2]-E[2,2]*E[3,1]
5330 LET B4=E[1,3]*E[3,2]-E[1,2]*E[3,3]
5340 LET B5=E[1,1]*E[3,3]-E[1,3]*E[3,1]
5350 LET B6=E[1,2]*E[3,1]-E[1,1]*E[3,2]
5360 LET B7=E[1,2]*E[2,3]-E[1,3]*E[2,2]
5370 LET B8=E[1,3]*E[2,1]-E[1,1]*E[2,3]
5380 LET B9=E[1,1]*E[2,2]-E[1,2]*E[2,1]
5390 LET C4=E[1,1]*B1+E[1,2]*B2+E[1,3]*B3
5400 LET E[1,1]=B1/C4
5410 LET E[1,2]=B4/C4
5420 LET E[1,3]=B7/C4
5430 LET E[2,1]=B2/C4
5440 LET E[2,2]=B5/C4
5450 LET E[2,3]=B8/C4
5460 LET E[3,1]=B3/C4
5470 LET E[3,2]=B6/C4
5480 LET E[3,3]=B9/C4
5490 RETURN
5500 STOP
```

```
5510 LET W1=E[1,1]*U[3*Y2-2]+E[1,2]*U[3*Y2-1]+E[1,3]*U[3*Y2]
5520 LET W2=E[2,1]*U[3*Y2-2]+E[2,2]*U[3*Y2-1]+E[2,3]*U[3*Y2]
5530 LET W3=E[3,1]*U[3*Y2-2]+E[3,2]*U[3*Y2-1]+E[3,3]*U[3*Y2]
5540 LET U[3*Y2-2]=W1
5550 LET U[3*Y2-1]=W2
5560 LET U[3*Y2]=W3
5570 RETURN
5580 STOP
5590 ON Y3 THEN GOTO 5600, 5640, 5680
5600 LET A3=3*Y2-2
5610 LET A4=3*Y2-1
5620 LET A5=3*Y2
5630 GOTO 5710
5640 LET A3=3*Y2-1
5650 LET A4=3*Y2
5660 LET A5=3*Y2-2
5670 GOTO 5710
5680 LET A3=3*Y2
5690 LET A4=3*Y2-2
5700 LET A5=3*Y2-1
5710 RETURN
5720 STOP
5730 LET S=0
5740 FOR Y1=Z0 TO Z9
5750   LET A[Y1]=0
5760   FOR Y2=S+1 TO I7
5770     IF U[3*Y2]>C1+.4 THEN GOTO 5810
5780     IF U[3*Y2]<Y1-.5 THEN GOTO 5810
5790     LET A[Y1]=A[Y1]+1
5800     GOTO 5830
5810     LET S=S+A[Y1]
5820     GOTO 5840
5830   NEXT Y2
5840 NEXT Y1
5850 LET A[Z9+1]=0
5860 LET A[Z9+2]=0
5870 LET A[Z9+3]=0
5880 LET I3=A[Z0]+A[Z0+1]+A[Z0+2]
5890 FOR Y1=Z0 TO Z9
5900   IF I3>A[Y1+1]+A[Y1+2]+A[Y1+3] THEN GOTO 5920
5910   LET I3=A[Y1+1]+A[Y1+2]+A[Y1+3]
5920 NEXT Y1
5930 RETURN
5940 STOP
5950 STOP
5960 IF A1-I3<1 THEN GOTO 5990
5970 LET I5=A1-I3
5980 GOTO 6000
5990 LET I5=1
6000 IF A1+I3>I7 THEN GOTO 6030
```

```
6010 LET I8=A1+I3
6020 GOTO 6040
6030 LET I8=I7
6040 FOR Y2=I5 TO I8
6050   LET R=(U[3*A1-2]-U[3*Y2-2])*(U[3*A1-2]-U[3*Y2-2])
6060   LET R=R+(U[3*A1-1]-U[3*Y2-1])*(U[3*A1-1]-U[3*Y2-1])
6070   LET R=R+(U[3*A1]-U[3*Y2])*(U[3*A1]-U[3*Y2])
6080   IF Y6=1 THEN IF ABS(R-2)>.0001 THEN GOTO 6130
6090   IF Y6=2 THEN IF ABS(R-3)>.0001 THEN GOTO 6130
6100   LET A[A1]=.01
6110   IF Y5=1 THEN LET A[Y2]=0
6120   IF Y5=2 THEN LET A[Y2]=.01
6130 NEXT Y2
6140 RETURN
```

D.5. Program DZP3

```
0010 REM
0020 REM DZP3
0030 REM
0040 REM INSERT SUBPROGRAM A
1890 LET K6=0
1900 INPUT " WHAT IS THE LATTICE CONSTANT IN ANGSTROM?",D8
1910 FOR KS=1 TO 14
1920   IF KS=1 THEN IF K6=1 THEN GOTO 4300
1930   ON KS THEN GOTO 1950, 2000, 2150, 2250, 2350, 2450, 2550
1940   ON KS-7 THEN GOTO 2650, 2750, 2850, 2950, 3050, 3150, 3250
1950   LET I6=1
1960   LET I7=I2
1970   READ A1,A2,A3,A4,A5,A6,A7,A8,A9
1980   IF K3=1 THEN GOTO 4300
1990   GOTO 3340
2000   READ I6,I7
2010   IF I6=0 THEN IF I7=0 THEN GOTO 4330
2020   PRINT
2030   PRINT "THE FOLLOWING RESULTS ARE FOR VACANCIES NO.";I6;" TO ";I7
2040   PRINT
2050   LET A1=0
2060   LET A2=1
2070   LET A3=0
2080   LET A4=0
2090   LET A5=0
2100   LET A6=1
2110   LET A7=1
2120   LET A8=0
2130   LET A9=0
2140   GOTO 3340
2150   LET A1=1
2160   LET A2=0
2170   LET A3=0
2180   LET A4=0
2190   LET A5=0
2200   LET A6=-1
2210   LET A7=0
2220   LET A8=1
2230   LET A9=0
2240   GOTO 3340
2250   LET A1=1
2260   LET A2=0
2270   LET A3=0
2280   LET A4=0
2290   LET A5=1
2300   LET A6=0
2310   LET A7=0
2320   LET A8=0
2330   LET A9=1
2340   GOTO 3340
2350   LET A1=0
```

```
2360 LET A2=0
2370 LET A3=1
2380 LET A4=1
2390 LET A5=-1
2400 LET A6=0
2410 LET A7=1
2420 LET A8=1
2430 LET A9=0
2440 GOTO 3340
2450 LET A1=0
2460 LET A2=0
2470 LET A3=-1
2480 LET A4=1
2490 LET A5=1
2500 LET A6=0
2510 LET A7=1
2520 LET A8=-1
2530 LET A9=0
2540 GOTO 3340
2550 LET A1=0
2560 LET A2=1
2570 LET A3=0
2580 LET A4=-1
2590 LET A5=0
2600 LET A6=1
2610 LET A7=1
2620 LET A8=0
2630 LET A9=1
2640 GOTO 3340
2650 LET A1=0
2660 LET A2=1
2670 LET A3=0
2680 LET A4=1
2690 LET A5=0
2700 LET A6=1
2710 LET A7=1
2720 LET A8=0
2730 LET A9=-1
2740 GOTO 3340
2750 LET A1=1
2760 LET A2=0
2770 LET A3=0
2780 LET A4=0
2790 LET A5=1
2800 LET A6=-1
2810 LET A7=0
2820 LET A8=1
2830 LET A9=1
2840 GOTO 3340
2850 LET A1=-1
```

```
2860 LET A2=0
2870 LET A3=0
2880 LET A4=0
2890 LET A5=1
2900 LET A6=1
2910 LET A7=0
2920 LET A8=1
2930 LET A9=-1
2940 GOTO 3340
2950 LET A1=1
2960 LET A2=-1
2970 LET A3=0
2980 LET A4=1
2990 LET A5=0
3000 LET A6=-1
3010 LET A7=1
3020 LET A8=1
3030 LET A9=1
3040 GOTO 3340
3050 LET A1=0
3060 LET A2=1
3070 LET A3=1
3080 LET A4=1
3090 LET A5=0
3100 LET A6=1
3110 LET A7=1
3120 LET A8=1
3130 LET A9=-1
3140 GOTO 3340
3150 LET A1=1
3160 LET A2=1
3170 LET A3=0
3180 LET A4=0
3190 LET A5=1
3200 LET A6=1
3210 LET A7=1
3220 LET A8=-1
3230 LET A9=1
3240 GOTO 3340
3250 LET A1=1
3260 LET A2=1
3270 LET A3=0
3280 LET A4=-1
3290 LET A5=0
3300 LET A6=-1
3310 LET A7=-1
3320 LET A8=1
3330 LET A9=1
3340 GOSUB 4520
3350 GOSUB 4660
```

```
3360 FOR Y2=I6 TO I7
3370   GOSUB 4870
3380 NEXT Y2
3390 LET B7=2*INT((A7+1.2)/2)
3400 LET B8=2*INT((A8+1.2)/2)
3410 LET B9=2*INT((A9+1.2)/2)
3420 LET B6=2*INT((A7+A8+A9+1.2)/2)
3430 LET B5=SQR(A7*A7+A8*A8+A9*A9)
3440 ON Y6 THEN GOTO 3450, 3480
3450 IF A7=B7 THEN IF A8=B8 THEN IF A9=B9 THEN GOTO 3500
3460 IF A7=B7-1 THEN IF A8=B8-1 THEN IF A9=B9-1 THEN GOTO 3500
3470 GOTO 3520
3480 IF A7+A8+A9=B6 THEN GOTO 3500
3490 GOTO 3520
3500 LET S=2/B5
3510 GOTO 3530
3520 LET S=1/B5
3530 FOR Y2=I6 TO I7
3540   LET U[3*Y2]=INT(U[3*Y2]/S+.1)
3550 NEXT Y2
3560 LET Z0=U[3*I6]
3570 LET Z9=U[3*I6]
3580 FOR Y2=I6+1 TO I7
                       3590   IF U[3*Y2]<Z0 THEN LET Z0=U[3*Y2]
3600   IF U[3*Y2]>Z9 THEN LET Z9=U[3*Y2]
3610 NEXT Y2
3620 FOR Y2=I6 TO I7
3630   LET U[3*Y2]=U[3*Y2]-Z0+1
3640 NEXT Y2
3650 FOR Y2=1 TO 200
3660   LET A[Y2]=0
3670 NEXT Y2
3680 LET C3=SQR(A7↑2+A8↑2+A9↑2)
3690 ON Y6 THEN GOTO 3700, 3790
3700 IF A7/2=INT(A7/2+.001) THEN GOTO 3740
3710 IF A8/2><INT(A8/2+.001) THEN IF A9/2><INT(A9/2+.001) THEN GOTO 3770
3720 LET I5=1/C3
3730 GOTO 3780
3740 IF A8/2=INT(A8/2+.001) THEN IF A9/2=INT(A9/2+.001) THEN GOTO 3770
3750 LET I5=1/C3
3760 GOTO 3780
3770 LET I5=2/C3
3780 GOTO 3830
3790 IF A7+A8+A9=2*INT((A7+A8+A9)/2+.001) THEN GOTO 3820
3800 LET I5=1/C3
3810 GOTO 3830
3820 LET I5=2/C3
3830 IF K5=1 THEN GOTO 3850
3840 GOTO 3990
3850 LET I4=INT(2.82842/I5+.5)
```

```
3860 FOR Y2=I6 TO I7
3870   LET B4=INT(U[3*Y2]/I4-.1)+1
3880   LET A[B4]=A[B4]+1
3890 NEXT Y2
3900 LET S9=0
3910 PRINT "THE THICKNESS OF EACH SLAB IS ";I4*I5*D8/2;" A "
3920 PRINT "SLAB NO.","VAC. NO.","SUM"
3930 FOR Y2=1 TO INT((Z9-Z0+1)/I4-.1)+1
3940   LET S9=S9+A[Y2]
3950   PRINT Y2,A[Y2],S9
3960 NEXT Y2
3970 GOSUB 4350
3980 GOTO 4140
3990 FOR Y2=I6 TO I7
4000   LET B4=U[3*Y2]
4010   LET A[B4]=A[B4]+1
4020 NEXT Y2
4030 LET S8=0
4040 LET S9=0
4050 FOR Y2=1 TO INT(Z9-Z0+1+.1)
4060   LET S8=S8+Y2*A[Y2]
4070   LET S9=S9+Y2↑2*A[Y2]
4080 NEXT Y2
4090 LET S8=(S8/(I7-I6+1))↑2
4100 LET S9=S9/(I7-I6+1)
4110 LET S9=SQR(S9-S8)
4120 LET S9=S9*I5*D8/2
4130 PRINT " THE DAMAGE WIDTH ALONG [";A7;A8;A9;"] = ";S9;" A "
4140 FOR Y2=I6 TO I7
4150   LET U[3*Y2]=U[3*Y2]+Z0-1
4160   LET U[3*Y2]=S*U[3*Y2]
4170 NEXT Y2
4180 GOSUB 4660
4190 FOR Y2=I6 TO I7
4200   GOSUB 4870
4210   LET Y4=ABS(U[3*Y2-2]-INT(U[3*Y2-2]+.01))
4220   LET Y5=ABS(U[3*Y2-1]-INT(U[3*Y2-1]+.01))
4230   LET Y7=ABS(U[3*Y2]-INT(U[3*Y2]+.01))
4240   IF Y4<.001 THEN IF Y5<.001 THEN IF Y7<.001 THEN GOTO 4260
4250   GOTO 4290
4260   LET U[3*Y2-2]=INT(U[3*Y2-2]+.1)
4270   LET U[3*Y2-1]=INT(U[3*Y2-1]+.1)
4280   LET U[3*Y2]=INT(U[3*Y2]+.1)
4290 NEXT Y2
4300 NEXT K5
4310 LET K6=1
4320 GOTO 1910
4330 END
4340 STOP
4350 FOR Y1=I7 TO I6 STEP -1
```

```
4360 FOR Y2=I6 TO Y1-1
4370   IF U[3*Y2]>U[3*Y1] THEN GOTO 4390
4380   GOTO 4480
4390   LET W1=U[3*Y2-2]
4400   LET W2=U[3*Y2-1]
4410   LET W3=U[3*Y2]
4420   LET U[3*Y2-2]=U[3*Y1-2]
4430   LET U[3*Y2-1]=U[3*Y1-1]
4440   LET U[3*Y2]=U[3*Y1]
4450   LET U[3*Y1-2]=W1
4460   LET U[3*Y1-1]=W2
4470   LET U[3*Y1]=W3
4480 NEXT Y2
4490 NEXT Y1
4500 RETURN
4510 STOP
4520 LET C1=SQR(A1*A1+A2*A2+A3*A3)
4530 LET C2=SQR(A4*A4+A5*A5+A6*A6)
4540 LET C3=SQR(A7*A7+A8*A8+A9*A9)
4550 LET E[1,1]=A1/C1
4560 LET E[2,1]=A2/C1
4570 LET E[3,1]=A3/C1
4580 LET E[1,2]=A4/C2
4590 LET E[2,2]=A5/C2
4600 LET E[3,2]=A6/C2
4610 LET E[1,3]=A7/C3
4620 LET E[2,3]=A8/C3
4630 LET E[3,3]=A9/C3
4640 RETURN
4650 STOP
4660 LET B1=E[2,2]*E[3,3]-E[2,3]*E[3,2]
4670 LET B2=E[2,3]*E[3,1]-E[2,1]*E[3,3]
4680 LET B3=E[2,1]*E[3,2]-E[2,2]*E[3,1]
4690 LET B4=E[1,3]*E[3,2]-E[1,2]*E[3,3]
4700 LET B5=E[1,1]*E[3,3]-E[1,3]*E[3,1]
4710 LET B6=E[1,2]*E[3,1]-E[1,1]*E[3,2]
4720 LET B7=E[1,2]*E[2,3]-E[1,3]*E[2,2]
4730 LET B8=E[1,3]*E[2,1]-E[1,1]*E[2,3]
4740 LET B9=E[1,1]*E[2,2]-E[1,2]*E[2,1]
4750 LET C4=E[1,1]*B1+E[1,2]*B2+E[1,3]*B3
4760 LET E[1,1]=B1/C4
4770 LET E[1,2]=B4/C4
4780 LET E[1,3]=B7/C4
4790 LET E[2,1]=B2/C4
4800 LET E[2,2]=B5/C4
4810 LET E[2,3]=B8/C4
4820 LET E[3,1]=B3/C4
4830 LET E[3,2]=B6/C4
4840 LET E[3,3]=B9/C4
4850 RETURN
```

```
4860 STOP
4870 LET W1=E[1,1]*U[3*Y2-2]+E[1,2]*U[3*Y2-1]+E[1,3]*U[3*Y2]
4880 LET W2=E[2,1]*U[3*Y2-2]+E[2,2]*U[3*Y2-1]+E[2,3]*U[3*Y2]
4890 LET W3=E[3,1]*U[3*Y2-2]+E[3,2]*U[3*Y2-1]+E[3,3]*U[3*Y2]
4900 LET U[3*Y2-2]=W1
4910 LET U[3*Y2-1]=W2
4920 LET U[3*Y2]=W3
4930 RETURN
```

Appendix E: The Derivation of the Cross-sectional Area A

In this appendix the derivation of the cross-sectional area A is described. In fig. 73 the ellipsoid represents a depleted zone; the diameter along the major axis is λ_1 and the diameter along the minor axis is λ_2. The direction of the incident ions is indicated by an arrow. The angle between the major axis of the ellipsoid and the direction of the incident ions is denoted by α.

An orthogonal coordinate system was first chosen so that the z-axis was parallel to the major axis of the ellipsoid and the x-z plane contained the vector which was parallel to the direction of the incident ions. The equation governing the surface of the ellipsoid was therefore given by

$$\frac{x^2 + y^2}{\left(\frac{\lambda_2}{2}\right)^2} + \frac{z^2}{\left(\frac{\lambda_1}{2}\right)^2} = 1 \qquad \text{(E1)}$$

It was found to be more convenient to describe the surface of the ellipsoid in a new orthogonal coordinate system which was obtained by rotating the z-axis through an angle equal to α. The z'-axis of the new coordinate system was therefore parallel to the direction of the incident ion-beam. The transformation equations between the old and the new coordinate systems were given by

$$x = x'\cos\alpha + z'\sin\alpha \qquad \text{(E2)}$$

$$y = y' \qquad \text{(E3)}$$

$$z = -x'\sin\alpha + z'\cos\alpha \qquad \text{(E4)}$$

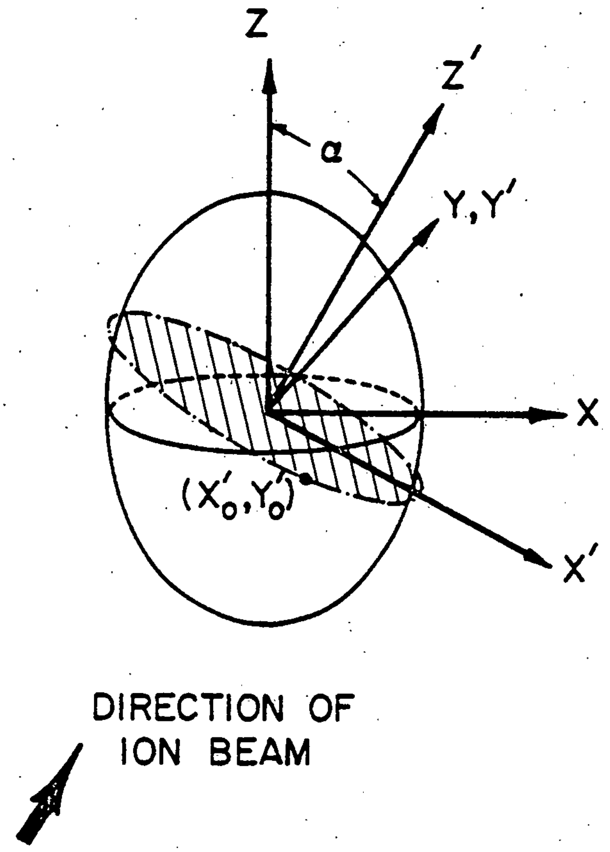

Figure 73: A drawing showing the derivation of the shadowed area (A). The ellipsoid represents a depleted zone.

The substitution of eqs. (E2) to (E4) into eq. (E1) yielded

$$\frac{(x'\cos\alpha + z'\sin\alpha)^2 + y'^2}{(\frac{\lambda_2}{2})^2} + \frac{(-x'\sin\alpha + z'\cos\alpha)^2}{(\frac{\lambda_1}{2})^2} = 1 \qquad (E5)$$

Equation (5) was then re-written as

$$x'^2(\lambda_1^2\cos^2\alpha+\lambda_2^2\sin^2\alpha) + 2x'z'(\lambda_1^2-\lambda_2^2)\sin\alpha\cos\alpha + z'^2(\lambda_1^2\sin^2\alpha+\lambda_2^2\cos^2\alpha) + \lambda_1^2 y'^2 = \frac{\lambda_1^2\lambda_2^2}{4} \qquad (E6)$$

In this new coordinate system the cross-sectional area A lay in the x'-y' plane. It is noted that the projections of any point on the surface of the ellipsoid onto the x'-y' plane is confined within the cross-sectional area A. The contour of this area A was obtained by noting that any point (x_o' y_o' z_o') which was on the surface of the ellipsoid and was projected onto the outermost boundary of this area A satisfied the equation

$$\frac{\partial x'}{\partial z'})_{x'=x_o',\ y'=y_o'} = 0 \qquad (E7)$$

or

$$\frac{\partial y'}{\partial z'})_{x'=x_o',\ y'=y_o'} = 0 \qquad (E8)$$

Solving eq. (E7) or (E8) we obtained

$$z_o' = -\frac{(\lambda_1^2 - \lambda_2^2)\sin\alpha\cos\alpha}{\lambda_1^2\sin^2\alpha+\lambda_2^2\cos^2\alpha}\, x_o' \qquad (E9)$$

The substitution of eq. (E9) into eq. (E6) yielded

$$\frac{x_o'^2}{(\lambda_1/2)^2\sin^2\alpha+(\lambda_2/2)^2\cos^2\alpha} + \frac{y_o'^2}{(\lambda_2/2)^2} = 1 \qquad \text{(E10)}$$

Equation (E10) is an equation for an ellipse. Thus the area A is an ellipse; the length (a) of the semi-major axis is given by

$$a = \frac{1}{2}\sqrt{\lambda_1^2\sin^2\alpha + \lambda_2^2\cos^2\alpha} \qquad \text{(E11)}$$

and the length (b) of the semi-minor axis is given by

$$b = \frac{\lambda_2}{2} \qquad \text{(E12)}$$

The quantity $A = \pi ab$ was therefore given by

$$A = \frac{\pi}{4}\lambda_2\sqrt{\lambda_1^2\sin^2\alpha + \lambda_2^2\cos^2\alpha} \qquad \text{(E13)}$$

As a check on the validity of eq. (E13) note that eq. (E13) reduces to

$$A = (\pi/4)\,\lambda_2^2 \qquad \text{for } \alpha=0 \qquad \text{(E14)}$$

$$A = (\pi/4)\,\lambda_1\lambda_2 \qquad \text{for } \alpha=\pi/2 \qquad \text{(E15)}$$

as it is obvious in fig. 73.

Appendix F: Procedure for the Mapping of the Positions of the SIAs and Depleted Zones in an FIM Specimen

F.1. Mathematical Details of the Mapping Procedure

In this appendix the details of the procedure for mapping the positions of the SIAs with respect to depleted zones in an FIM tip specimen is described. It was assumed that the end form of the FIM specimen could be approximated by a hemisphere. Figure 74 shows a schematic diagram of a specimen which has an average tip radius r_o initially. As the specimen was successively field-evaporated layer-by-layer, a final end-form of an average radius of curvature r_1 was obtained. Points 0 and 0' are respectively the centers of the initial and the final hemispheres of the tip.

From the FIM micrographs we knew the (h k l) plane and the number of layers n in which a given SIA was found; the number of layers was measured from the initial surface. For example, an SIA at C was found in the n^{th} layer of the $(h_4\ k_4\ l_4)$ plane measured from the initial surface at B. It was then a problem to determine the coordinates of point C if one knows the quantities h_4, k_4, l_4 and n.

In fig.74 we first chose the beam direction as the u-axis, the orientation of the specimen $[h_3\ k_3\ l_3]$ as the w-axis and the vector $[h_2\ k_2\ l_2]$ as the v-axis; the vector $[h_2\ k_2\ l_2]$ was determined from the cross-product,

$$[h_2\ k_2\ l_2] = [h_3\ k_3\ l_3] \times [h_1\ k_1\ l_1] \qquad (F1)$$

The u-, v-, w- axes and the origin 0 therefore constituted a rectangular coordinate system. The coordinates of point C were given by (u, v, w) in this rectangular coordinate system. However, it was found easier to employ a spherical coordinate system. The spherical coordinates (ρ, θ, ϕ) of point C are shown in fig. 74.

Initially, the center of the $(h_4\ k_4\ l_4)$ plane was at B. As the specimen was field-evaporated layer-by-layer to the final end-form the final location of the $(h_4\ k_4\ l_4)$ plane was at point D. In general, the vector $\overrightarrow{BD}$ is tilted from the w-axis by an angle $\Delta\theta$. The angle $\Delta\theta$ was determined by noting the triangle BDF; point F defined by the expression $|\overrightarrow{O'F}| = r_o$. The length $|\overrightarrow{AE}|$ was estimated by counting the number of layers (m) of the $(h_3\ k_3\ l_3)$ plane which had been field-evaporated as the specimen reached its final end-form; that is

$$g \equiv |\overrightarrow{AE}| = md_{h_3k_3l_3} \tag{F2}$$

where the quantity $d_{h_3k_3l_3}$ is the interplanar spacing of the $(h_3\ k_3\ l_3)$ plane.

In the triangle BDF we have

$$|\overrightarrow{BF}| = |\overrightarrow{OO'}| = g + r_1 - r_o, \tag{F3}$$

$$|\overrightarrow{DF}| = r_1 - r_o, \tag{F4}$$

and

$$\measuredangle\, BFD = \theta_o, \tag{F5}$$

hence the quantity $\Delta\theta$ was given by

$$\Delta\theta = \cos^{-1}\left(\frac{q^2 + (g + r_1 - r_o)^2 - (r_1 - r_o)^2}{2q\,(g + r_1 - r_o)}\right) \tag{F6}$$

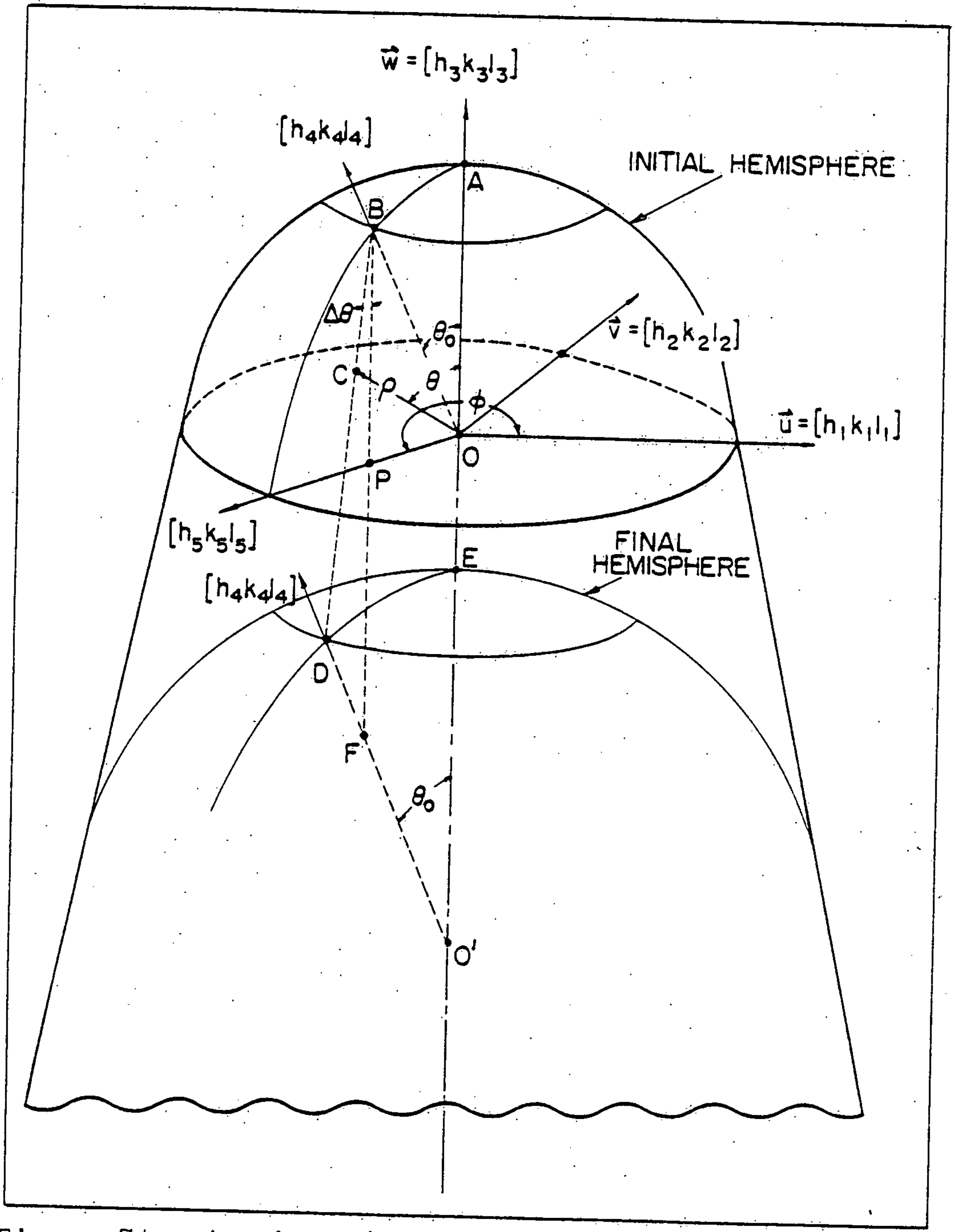

Figure 74: A schematic drawing of an FIM tip specimen illustrating how the coordinates of an SIA (or a depleted zone) at point C within the tip specimen was determined.

where the quantity q was given by

$$q \equiv |\overrightarrow{BD}| = \sqrt{(r_1-r_o)^2+(g+r_1-r_o)^2-2(r_1-r_o)(g+r_1-r_o)\cos\theta_o} \qquad (F7)$$

The quantity θ_o, the angle between the normal vector $[h_4\ k_4\ l_4]$ of the $(h_4\ k_4\ l_4)$ plane and the w-axis, was given by

$$\theta_o = \cos^{-1}\left(\frac{h_3h_4+k_3k_4+l_3l_4}{\sqrt{h_3^2+k_3^2+l_3^2}\sqrt{h_4^2+k_4^2+l_4^2}}\right) \qquad (F8)$$

In the triangle BCO we have

$$|\overrightarrow{BO}| = r_o, \qquad (F9)$$

$$\measuredangle CBO = \theta_o + \Delta\theta, \qquad (F10)$$

and
$$s \equiv |\overrightarrow{BC}| = \frac{n\, d_{h_4k_4l_4}}{\cos(\theta_o+\Delta\theta)}, \qquad (F11)$$

where the quantity $d_{h_4k_4l_4}$ is the interplanar spacing of the $(h_4\ k_4\ l_4)$ plane. Therefore, the quantity ρ was given by

$$\rho \equiv |\overrightarrow{OC}| = \sqrt{s^2+r_o^2-2sr_o\cos(\theta_o+\Delta\theta)} \qquad (F12)$$

and
$$\measuredangle COB = \cos^{-1}\left(\frac{r_o^2+\rho^2-s^2}{2r_o\rho}\right) \qquad (F13)$$

The angle θ was given by

$$\theta = \theta_o + \measuredangle COB = \theta_o + \cos^{-1}\left(\frac{r_o^2+\rho^2-s^2}{2r_o\rho}\right) \qquad (F14)$$

The projection of point B onto the u-v plane is denoted by point P. The vector $[h_5\ k_5\ l_5] \equiv \overrightarrow{OP}$ was therefore given by

$$\overrightarrow{OP} = \overrightarrow{OB} + \overrightarrow{BP} \qquad (F15)$$

or

$$[h_5\ k_5\ l_5] = \frac{r_o}{\sqrt{h_4^2+k_4^2+l_4^2}}\ [h_4\ k_4\ l_4] - \frac{r_o\cos\theta_o}{\sqrt{h_3^2+k_3^2+l_3^2}}\ [h_3\ k_3\ l_3] \qquad \text{(F16)}$$

Since the projection of the vector $\overrightarrow{OC}$ onto the u-v plane is parallel to the vector $[h_5\ k_5\ l_5]$, we obtained

$$\phi = \cos^{-1}\left(\frac{h_4h_5+\ k_4k_5\ +\ l_4l_5}{\sqrt{h_4^2+k_4^2+l_4^2}\ \sqrt{h_5^2+k_5^2+l_5^2}}\right) \qquad \text{(F17)}$$

The spherical coordinates (ρ,θ,ϕ) of point C determined by eqs. (F12), (F14) and (F17) were then transformed to the rectangular coordinates (u, v, w) according to the relationship

$$u = \rho\sin\theta\cos\phi, \qquad \text{(F18)}$$

$$v = \rho\sin\theta\sin\phi, \qquad \text{(F19)}$$

and

$$w = \rho\cos\theta. \qquad \text{(F20)}$$

The rectangular coordinates (u, v, w) were finally transformed to the standard cubic coordinates (x, y, z). Thus, in eqs. (F1) to (F20) we could calculate the cubic coordinates (x, y, z) for any SIA by knowing the values of the quantities r_o, r_1, h_1, k_1, l_1, h_3, k_3, l_3, h_4, k_4, l_4, m and n which were measured from the micrographs. In practice, the above computations were carried out with the aid of the NOVA 1220 minicomputer; the program for these computations is denoted by DZP4. An example of input statements, the flow chart and the BASIC program for DZP4 are given in sect. F2, F3 and F4 respectively.

F.2. Input Statement for Program DZP4

In this section typical input statements are given as an example to demonstrate how to enter the data for program DZP4. Comments are given after each data statement. In this demonstrative example it was assumed that a depleted zone was found to locate in the 45th layer of the (323) plane and two SIAs were detected respectively in the 47th layer of the (222) plane and the 142nd layer of the (433) plane. The FIM tip specimen had a [121] orientation. The initial and the final tip radii were 375 and 420 A respectively. The number of layers of the (121) planes which were field-evaporated was 200. The direction of the incident ions is [$\bar{7}4\bar{1}$]. Only the region around the (222) pole was used in the search for SIAs. The details of the input statements is described as follows:

```
9000 DATA 2
```

Enter Y6=1 for a fcc lattice or Y6=2 for a bcc lattice.

```
9010 DATA 3.16
```

Enter D8=3.16 A for the lattice constant of tungsten.

```
9020 DATA -7, 4, -1, -1, -1, -1, 3, 1, 2, 1
```

Enter the Miller indices of the u-, v- and w-axes for variables H2, K2, L2, H3, K3, L3, H1, K1 and L1.

```
9030 DATA 375, 420, 200
```

Enter the initial tip radius, the final tip radius and the number of layers of the (121) plane which have been field-evaporated for variables S, S0 and I4.

```
9040 DATA 1
```

Enter V4=1 for the number of poles which have been used to search for the SIAs.

9050 DATA 2, 2, 2

Enter the Miller indices of the poles which have been used to search for the SIAs.

9060 DATA 1

Enter I1=1 for the number of the depleted zones detected.

9070 DATA 2

Enter I3=2 for the number of the SIAs detected. In the following the coordinates are stored in variable H4, K4, L4 and I2.

9080 DATA 3, 2, 3, 45

Enter the coordinates of the depleted zone.

9090 DATA 2, 2, 2, 47, 4, 3, 3, 147

Enter the coordinates of the two SIAs.

9100 DATA 25

Enter H(Y1)=25 A for the effective radius of the depleted zone.

F.3. Flow Chat for Program DZP4

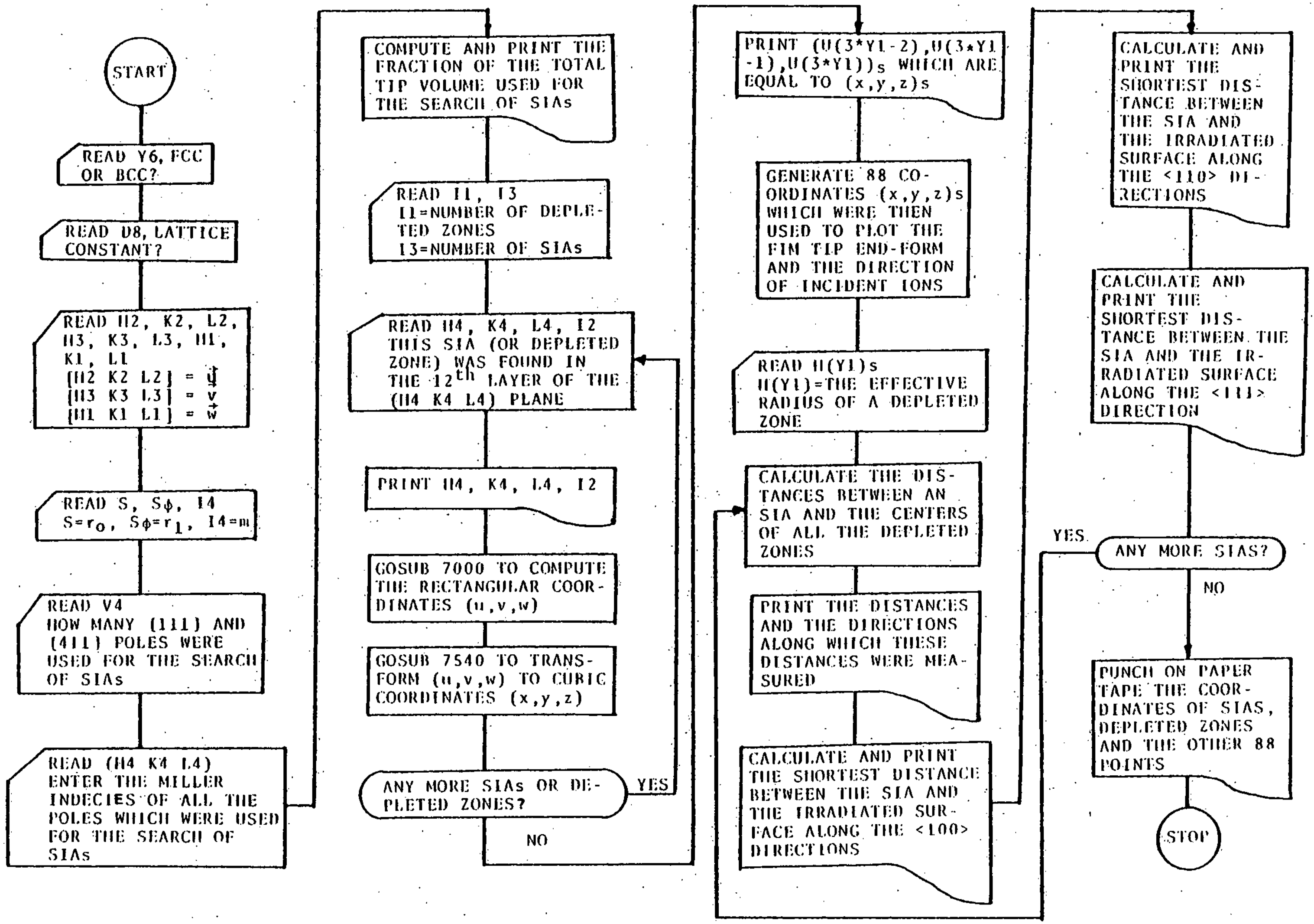

F.4. Program DZP4

```
0010 REM
0020 REM DZP-4
0030 REM
0040 DIM U[900],E[3,3],H[10],F[10],A[200]
0050 DIM C[30],G[10],Q[30]
0060 READ Y6
0070 READ D8
0080 READ H2,K2,L2,H3,K3,L3,H1,K1,L1
0090 LET G[1]=H2
0100 LET G[2]=K2
0110 LET G[3]=L2
0120 LET G[4]=H3
0130 LET G[5]=K3
0140 LET G[6]=L3
0150 LET G[7]=H1
0160 LET G[8]=K1
0170 LET G[9]=L1
0180 READ S,S0,I4
0190 LET S1=SQR(H1↑2+K1↑2+L1↑2)
0200 LET S2=SQR(H2↑2+K2↑2+L2↑2)
0210 LET S3=SQR(H3↑2+K3↑2+L3↑2)
0220 ON Y6 THEN GOTO 0230, 0320
0230 IF H1/2=INT(H1/2+.001) THEN GOTO 0270
0240 IF K1/2><INT(K1/2+.001) THEN IF L1/2><INT(L1/2+.001) THEN GOTO 0300
0250 LET Y0=1/S1
0260 GOTO 0310
0270 IF K1/2=INT(K1/2+.001) THEN IF L1/2=INT(L1/2+.001) THEN GOTO 0300
0280 LET Y0=1/S1
0290 GOTO 0310
0300 LET Y0=2/S1
0310 GOTO 0360
0320 IF H1+K1+L1=2*INT((H1+K1+L1)/2+.001) THEN GOTO 0350
0330 LET Y0=1/S1
0340 GOTO 0360
0350 LET Y0=2/S1
0360 LET V1=0
0370 LET V9=Y0
0380 READ V4
0390 FOR Y1=1 TO V4
0400   READ H4,K4,L4
0410   LET V2=(H4*H1+K4*K1+L4*L1)/SQR(H4↑2+K4↑2+L4↑2)/S1
0412   ON Y6 THEN GOTO 0414, 0420
0414   LET Y2=.059855
0416   GOTO 0460
0420   IF ABS(H4)=ABS(K4) THEN IF ABS(K4)=ABS(L4) THEN GOTO 0450
0430   LET Y2=.216435
0440   GOTO 0460
0450   LET Y2=.303916
0460   LET V2=3.14159*S↑2*.25*I4*Y0*D8*.5*Y2*V2
0470   LET V1=V1+V2
0480 NEXT Y1
0490 IF S=S0 THEN GOTO 0530
0500 LET V0=(I4*Y0*D8/2+S0-S)/(S0-S)
0505 LET V0=(1-V0)↑2/V0
```

```
0510 LET V0=3.14159*(S0↑3-S↑3)*.333333*V0
0520 GOTO 0540
0530 LET V0=3.14159*S↑2*I4*Y0*DR/2
0540 PRINT "THE PERCENTAGE OF THE TOTAL TIP VOLUME EXAMINED IS";INT(V1/V
0*1000)/10;"%"
0550 READ I1,I3
0560 PRINT
0570 PRINT "DEFECT NO.","PLANE (HKL)","LAYER NO."
0580 PRINT
0590 FOR Y1=1 TO I1+I3
0600   READ H4,K4,L4,I2
0610   GOSUB 7000
0620   GOSUB 7540
0630   FOR T2=1 TO I1
0640     IF Y1=<I1 THEN GOTO 0690
0650     LET W1=U[3*Y1-2]-U[3*T2-2]
0660     LET W2=U[3*Y1-1]-U[3*T2-1]
0670     LET W3=U[3*Y1]-U[3*T2]
0680     LET A[(Y1-1)*I1+T2]=(H4*W1+K4*W2+L4*W3)/SQR(H4↑2+K4↑2+L4↑2)/SQR
(W1↑2+W2↑2+W3↑2)
0690   NEXT T2
0700 NEXT Y1
0710 LET I9=10
0720 FOR Y3=1 TO 2
0730   FOR Y1=1 TO I9
0740     LET H4=H1+(-1)↑Y3*H2*(Y1-1)/I9
0750     LET K4=K1+(-1)↑Y3*K2*(Y1-1)/I9
0760     LET L4=L1+(-1)↑Y3*L2*(Y1-1)/I9
0770     LET I2=0
0780     IF Y3=1 THEN LET Y1=I1+I3+Y1
0790     IF Y3=2 THEN LET Y1=I1+I3+I9+Y1
0800     GOSUB 7000
0810     GOSUB 7540
0820     IF Y3=1 THEN LET Y1=Y1-I1-I3
0830     IF Y3=2 THEN LET Y1=Y1-I1-I3-I9
0840   NEXT Y1
0850 NEXT Y3
0860 FOR Y3=1 TO 2
0870   FOR Y1=1 TO I9
0880     LET H4=(-1)↑Y3*H2+H1*(Y1-1)/I9
0890     LET K4=(-1)↑Y3*K2+K1*(Y1-1)/I9
0900     LET L4=(-1)↑Y3*L2+L1*(Y1-1)/I9
0910     LET I2=0
0920     IF Y3=1 THEN LET Y1=Y1+I1+I3+2*I9
0930     IF Y3=2 THEN LET Y1=Y1+I1+I3+3*I9
0940     GOSUB 7000
0950     GOSUB 7540
0960     IF Y3=1 THEN LET Y1=Y1-I1-I3-2*I9
0970     IF Y3=2 THEN LET Y1=Y1-I1-I3-3*I9
0980   NEXT Y1
0990 NEXT Y3
1000 LET I8=5
```

```
1010 FOR Y3=1 TO 4
1020   FOR Y1=1 TO I8
1030     LET H4=(-1)↑(INT(Y3/2-.2))*H3+(-1)↑(Y3+1)*H2*(Y1-1)/I8
1040     LET K4=(-1)↑(INT(Y3/2-.2))*K3+(-1)↑(Y3+1)*K2*(Y1-1)/I8
1050     LET L4=(-L)↑INT(Y3/2-.2)*L3+(-1)↑(Y3+1)*L2*(Y1-1)/I8
1060     LET I2=0
1070     LET Y1=Y1+I1+I3+4*I9+(Y3-1)*I8
1080     GOSUB 7000
1090     GOSUB 7540
1100     LET Y1=Y1-(I1+I3+4*I9+(Y3-1)*I8)
1110   NEXT Y1
1120 NEXT Y3
1130 FOR Y3=1 TO 4
1140   FOR Y1=1 TO I8
1150     LET H4=(-1)↑(INT(Y3/2-.2))*H2+(-1)↑(Y3+1)*H3*(Y1-1)/I8
1160     LET K4=(-1)↑(INT(Y3/2-.2))*K2+(-1)↑(Y3+1)+K3*(Y1-1)/I8
1170     LET L4=(-1)↑(INT(Y3/2-.2))*L2+(-1)↑(Y3+1)*L3*(Y1-1)/I8
1180     LET I2=0
1190     LET Y1=Y1+I1+I3+4*I9+(4+Y3-1)*I8
1200     GOSUB 7000
1210     GOSUB 7540
1220     LET Y1=Y1-(I1+I3+4*I9+(3+Y3)*I8)
1230   NEXT Y1
1240 NEXT Y3
1250 LET Y3=I1+I3+4*I9+8*I8
1260 LET V4=S*2/D8
1270 FOR Y2=Y3+1 TO Y3+5
1280   LET U[3*Y2-2]=V4*(-1)*(.9+(Y2-Y3-1)*.06)
1290   LET U[3*Y2-1]=0
1300   LET U[3*Y2]=V4*.8
1305   LET Y1=Y2
1310   GOSUB 7540
1320 NEXT Y2
1330 FOR Y2=Y3+6 TO Y3+11
1340   LET U[3*Y2-2]=V4*(-1)*(.93+.03*INT((Y2-Y3-6)/2+.1))
1350   LET U[3*Y2-1]=0
1360   LET U[3*Y2]=.8*V4+(-1)↑(Y2-Y3-6)*.015*V4*(INT((Y2-Y3-6)/2+.1)+1)
1365   LET Y1=Y2
1370   GOSUB 7540
1380 NEXT Y2
1390 PRINT
1400 PRINT "(X, Y, Z)S ARE COORDINATES BASED ON AXES [1 0 0], [0 1 0] AN
D ";
1410 PRINT "[0 0 1]"
1420 PRINT
1430 PRINT
1440 PRINT "DEFECT NO."," X"," Y"," Z"
1450 PRINT
1460 FOR Y1=1 TO I1+I3
1470   IF Y1=<I1 THEN PRINT "DZ(";Y1;")",U[3*Y1-2],U[3*Y1-1],U[3*Y1]
1480   IF Y1=>I1+1 THEN PRINT "I(";Y1;")",U[3*Y1-2],U[3*Y1-1],U[3*Y1]
1490 NEXT Y1
1500 PRINT
```

```
1510 PRINT "DEFECT NO."," ","P.D.[H K L]"," ","R(ANGS.)"
1520 IF I1=<0 THEN GOTO 1590
1530 FOR Y1=1 TO I1
1540   READ H[Y1]
1550 NEXT Y1
1560 FOR Y1=1 TO I1
1570   LET F[Y1]=H[Y1]
1580 NEXT Y1
1590 FOR Y0=I1+1 TO I1+I3
1600   PRINT
1610   IF I1=<0 THEN GOTO 2240
1620   FOR Y2=1 TO I1
1630     LET C1=10
1640     LET H[Y2]=F[Y2]+C1*ABS(A[(Y0-1)*I1+Y2])
1650     LET V4=0
1660     LET H2=9
1670     LET H1=U[3*Y0-2]-U[3*Y2-2]
1680     LET K1=U[3*Y0-1]-U[3*Y2-1]
1690     LET L1=U[3*Y0]-U[3*Y2]
1700     LET R=SQR(H1↑2+K1↑2+L1↑2)
1710     LET W1=H1
1720     LET W2=K1
1730     LET W3=L1
1740     LET X0=90
1750     FOR Y1=1 TO 26
1760       GOSUB 5620
1770       GOSUB 6700
1780       GOSUB 6930
1790     NEXT Y1
1800     IF H2=9 THEN PRINT "I(";Y0;")-DE(";Y2;")- 0"; TAB(28);"[";H1;K1
;L1;"]"; TAB(56);INT(S1+.5)
1810     IF H2><9 THEN PRINT "I(";Y0;")-DE(";Y2;")- 0"; TAB(28);"[";H2;K
2;L2;"]"; TAB(56);INT(S1+.5)
1815     GOTO 2230
1820     LET V4=9
1830     FOR Y3=1 TO 2
1840       LET W1=0
1850       LET H2=9
1860       LET K2=9
1870       LET L2=9
1880       LET W2=(-1)↑Y3*L1
1890       LET W3=(-1)↑(Y3+1)*K1
1900       LET A1=H[Y2]*2/D8/(SQR(W2↑2+W3↑2))
1910       LET W1=W1+H1
1920       LET W2=W2*A1+K1
1930       LET W3=W3*A1+L1
1940       LET X0=90
1950       FOR Y1=1 TO 26
1960         GOSUB 5620
1970         GOSUB 6700
1980         GOSUB 6930
1990       NEXT Y1
2000       IF H2=9 THEN PRINT "I(";Y0;")-DE(";Y2;")-";Y3; TAB(28);"[";H1
;K1;L1;"]"; TAB(56);INT(S1+.5)
```

```
2010 IF H2><9 THEN PRINT "I(";Y0;")-DE(";Y2;")-";Y3; TAB(28);"[";H2;K2;L
2;"]"; TAB(56);INT(S1+.5)
2020 NEXT Y3
2030 FOR Y3=1 TO 2
2040   LET H2=9
2050   LET K2=9
2060   LET L2=9
2070   LET W1=(-1)↑(Y3+1)*(K1↑2+L1↑2)
2080   LET W2=(-1)↑Y3*H1*K1
2090   LET W3=(-1)↑Y3*H1*L1
2100   LET A1=H[Y2]*2/D8/SQR(W1↑2+W2↑2+W3↑2)
2110   LET W1=A1*W1+H1
2120   LET W2=A1*W2+K1
2130   LET W3=A1*W3+L1
2140   LET X0=90
2150   FOR Y1=1 TO 26
2160     GOSUB 5620
2170     GOSUB 6700
2180     GOSUB 6930
2190   NEXT Y1
2200   IF H2=9 THEN PRINT "I(";Y0;")-DE(";Y2;")-";Y3+2; TAB(28);"[";H1;K
1;L1;"]"; TAB(56);INT(S1+.5)
2210   IF H2><9 THEN PRINT "I(";Y0;")-DE(";Y2;")-";Y3+2; TAB(28);"[";H2;
K2;L2;"]"; TAB(56);INT(S1+.5)
2220 NEXT Y3
2230 NEXT Y2
2240 LET Y2=Y0
2250 FOR Y1=1 TO 26
2260   GOSUB 5620
2270   GOSUB 7700
2280 NEXT Y1
2290 LET C1=C[1]
2300 FOR Y1=2 TO 6
2310   IF C[Y1]<C1 THEN LET C1=C[Y1]
2320 NEXT Y1
2330 FOR Y1=1 TO 6
2340   IF ABS(C[Y1]-C1)=<.001 THEN LET V1=INT(Q[Y1]*100)/100
2350 NEXT Y1
2360 LET C2=C[7]
2370 FOR Y1=8 TO 18
2380   IF C[Y1]<C2 THEN LET C2=C[Y1]
2390 NEXT Y1
2400 FOR Y1=7 TO 18
2410   IF ABS(C[Y1]-C2)=<.001 THEN LET V2=INT(Q[Y1]*100)/100
2420 NEXT Y1
2430 LET C3=C[19]
2440 FOR Y1=20 TO 26
2450   IF C[Y1]<C3 THEN LET C3=C[Y1]
2460 NEXT Y1
2470 FOR Y1=19 TO 26
2480   IF ABS(C[Y1]-C3)=<.001 THEN LET V3=INT(Q[Y1]*100)/100
2490 NEXT Y1
2500 LET V1=ABS(V1)
```

```
2510 LET V2=ABS(V2)
2520 LET V3=ABS(V3)
2530 LET C1=INT(C1+.5)
2540 LET C2=INT(C2+.5)
2550 LET C3=INT(C3+.5)
2560 PRINT "I(";Y2;")-IRR.SUR. (";V1;")"; TAB(28);"[ 1 0 0 ]"; TAB(56);C
1
2570 PRINT "I(";Y2;")-IRR.SUR. (";V2;")"; TAB(28);"[ 1 1 0 ]"; TAB(56);C
2
2580 PRINT "I(";Y2;")-IRR.SUR. (";V3;")"; TAB(28);"[ 1 1 1 ]"; TAB(56);C
3
2590 NEXT Y0
2600 STOP
2610 LET I6=1
2620 LET I7=I1+I3+4*I9+8*I8
2630 LET I7=I7+I1
2640 GOSUB 5300
2650 GOSUB 5460
2660 INPUT "PLOT AGAIN(1) OR PAPER TAPE(2)?",Y4
2670 ON Y4 THEN GOTO 2680, 2700
2680 GOSUB 4570
2690 GOTO 2660
2700 GOTO 2740
2710 REM
2720 REM ARRANGE AND PUNCH DATA ON PTR FOR ORTEP PROGRAM IN MSC CENTER
2730 REM
2740 FOR Y1=I6 TO I7
2750   LET Y4=ABS(U[3*Y1-2]-INT(U[3*Y1-2]+.01))
2760   LET Y5=ABS(U[3*Y1-1]-INT(U[3*Y1-1]+.01))
2770   LET Y7=ABS(U[3*Y1]-INT(U[3*Y1]+.01))
2780   IF Y4<.01 THEN IF Y5<.01 THEN IF Y7<.01 THEN GOTO 2800
2790   GOTO 2870
2800   FOR Y2=0 TO 2
2810     LET V1=U[3*Y1-Y2]
2820     IF V1=0 THEN LET U[3*Y1-Y2]=.222222
2830     IF V1/10=>.099 THEN IF V1/10=<.95 THEN LET U[3*Y1-Y2]=V1+.22222
2840     IF V1/100=>.095 THEN IF V1/100=<.995 THEN LET U[3*Y1-Y2]=V1+.22
22
2850     IF V1/1000=>.0995 THEN IF V1/1000=<.9995 THEN LET U[3*Y1-Y2]=V1
+.222
2860   NEXT Y2
2870 NEXT Y1
2880 FOR Y1=1 TO 1000
2890   GOTO 2900
2900 NEXT Y1
2910 PRINT "DEPLETED ZONE(";I1;") - SIA(";I3;")"
2920 GOSUB 4180
2930 GOSUB 4480
2940 GOSUB 4220
2950 GOSUB 4420
2960 FOR Y1=I6 TO I7
2970   IF Y1=<I1 THEN PRINT "DZ(";Y1;")";
2980   IF Y1=>I1+1 THEN IF Y1=<I1+I3 THEN PRINT Y1-I1;
2990   GOSUB 4270
3000   IF Y1=<I1 THEN GOTO 3020
```

```
3010 GOTO 3060
3020 PRINT  TAB(1);.6*F[Y1];
3030 PRINT  TAB(11);"0.00000"; TAB(20);"0.00000"; TAB(29);"0.00000";
3040 PRINT  TAB(38);"0.00000"; TAB(47);"0.00000"; TAB(61);"6."
3050 GOTO 3090
3060 IF Y1=<I7-1 THEN GOTO 3080
3070 PRINT "1";
3080 GOSUB 4310
3090 NEXT Y1
3100 LET K1=101
3110 GOSUB 4060
3120 LET K1=201
3130 GOSUB 4060
3140 PRINT  TAB(6);"301"; TAB(12);"16.000"; TAB(21);"11.000"; TAB(30);"5
00.00";
3150 PRINT  TAB(39);"0.5000"; TAB(48);"0.0000"; TAB(57);"0.0000"; TAB(66
);"0.0000"
3160 LET K1=303
3170 GOSUB 4060
3180 LET K1=401
3190 GOSUB 4350
3200 LET K1=501
3210 GOSUB 4530
3220 PRINT  TAB(6);"502"; TAB(17);"1"; TAB(24);"30."; TAB(35);"2"; TAB(4
2);"30.";
3230 PRINT  TAB(53);"3"; TAB(60);"30."
3240 PRINT  TAB(6);"604"; TAB(12);"0.0000"; TAB(21);"0.0000"; TAB(30);"0
.0000";
3250 PRINT  TAB(39);"5.0000"; TAB(48);"0.0000"; TAB(57);"0.0000"; TAB(66
);"0.0000"
3260 PRINT  TAB(6);"611"; TAB(12);"0.0000"; TAB(21);"0.0000"; TAB(30);"0
.8000";
3270 PRINT  TAB(39);"0.0000"; TAB(48);"0.0000"; TAB(57);"0.0000"; TAB(66
);"0.0000"
3280 PRINT  TAB(6);"704"; TAB(12);"0.0000"; TAB(21);"0.0000"; TAB(30);"0
.0000";
3290 PRINT  TAB(39);"0.0000"; TAB(48);"0.1000"; TAB(57);"0.0500"; TAB(66
);"0.0500"
3300 LET K1=802
3310 GOSUB 4100
3320 GOSUB 4140
3330 LET K1=202
3340 GOSUB 4060
3350 LET K1=202
3360 GOSUB 4060
3370 LET K1=-1
3380 GOSUB 4380
3390 END
3400 STOP
3410 FOR Y1=I7 TO I6 STEP -1
3420   FOR Y2=I6 TO Y1-1
3430     IF U[3*Y2]>U[3*Y1] THEN GOTO 3450
3440     GOTO 3540
3450     LET W1=U[3*Y2-2]
3460     LET W2=U[3*Y2-1]
3470     LET W3=U[3*Y2]
3480     LET U[3*Y2-2]=U[3*Y1-2]
3490     LET U[3*Y2-1]=U[3*Y1-1]
3500     LET U[3*Y2]=U[3*Y1]
```

```
3510 LET U[3*Y1-2]=W1
3520 LET U[3*Y1-1]=W2
3530 LET U[3*Y1]=W3
3540 NEXT Y2
3550 NEXT Y1
3560 RETURN
3570 STOP
3580 LET C1=SQR(A1*A1+A2*A2+A3*A3)
3590 LET C2=SQR(A4*A4+A5*A5+A6*A6)
3600 LET C3=SQR(A7*A7+A8*A8+A9*A9)
3610 LET E[1,1]=A1/C1
3620 LET E[2,1]=A2/C1
3630 LET E[3,1]=A3/C1
3640 LET E[1,2]=A4/C2
3650 LET E[2,2]=A5/C2
3660 LET E[3,2]=A6/C2
3670 LET E[1,3]=A7/C3
3680 LET E[2,3]=A8/C3
3690 LET E[3,3]=A9/C3
3700 RETURN
3710 STOP
3720 LET B1=E[2,2]*E[3,3]-E[2,3]*E[3,2]
3730 LET B2=E[2,3]*E[3,1]-E[2,1]*E[3,3]
3740 LET B3=E[2,1]*E[3,2]-E[2,2]*E[3,1]
3750 LET B4=E[1,3]*E[3,2]-E[1,2]*E[3,3]
3760 LET B5=E[1,1]*E[3,3]-E[1,3]*E[3,1]
3770 LET B6=E[1,2]*E[3,1]-E[1,1]*E[3,2]
3780 LET B7=E[1,2]*E[2,3]-E[1,3]*E[2,2]
3790 LET B8=E[1,3]*E[2,1]-E[1,1]*E[2,3]
3800 LET B9=E[1,1]*E[2,2]-E[1,2]*E[2,1]
3810 LET C4=E[1,1]*B1+E[1,2]*B2+E[1,3]*B3
3820 LET E[1,1]=B1/C4
3830 LET E[1,2]=B4/C4
3840 LET E[1,3]=B7/C4
3850 LET E[2,1]=B2/C4
3860 LET E[2,2]=B5/C4
3870 LET E[2,3]=B8/C4
3880 LET E[3,1]=B3/C4
3890 LET E[3,2]=B6/C4
3900 LET E[3,3]=B9/C4
3910 RETURN
3920 STOP
3930 LET W1=E[1,1]*U[3*Y2-2]+E[1,2]*U[3*Y2-1]+E[1,3]*U[3*Y2]
3940 LET W2=E[2,1]*U[3*Y2-2]+E[2,2]*U[3*Y2-1]+E[2,3]*U[3*Y2]
3950 LET W3=E[3,1]*U[3*Y2-2]+E[3,2]*U[3*Y2-1]+E[3,3]*U[3*Y2]
3960 LET U[3*Y2-2]=W1
3970 LET U[3*Y2-1]=W2
3980 LET U[3*Y2]=W3
3990 RETURN
4000 STOP
```

```
4010 LET V1=E[1,1]*W1+E[1,2]*W2+E[1,3]*W3
4020 LET V2=E[2,1]*W1+E[2,2]*W2+E[2,3]*W3
4030 LET V3=E[3,1]*W1+E[3,2]*W2+E[3,3]*W3
4040 RETURN
4050 STOP
4060 PRINT  TAB(5);K1; TAB(12);"0.0000"; TAB(21);"0.0000"; TAB(30);"0.00
00";
4070 PRINT  TAB(39);"0.0000"; TAB(48);"0.0000"; TAB(57);"0.0000"; TAB(66
);"0.0000"
4080 RETURN
4090 STOP
4100 PRINT  TAB(2);"2"; TAB(5);K1; TAB(11);"0.00000"; TAB(20);"0.00000";
 TAB(29);"0.00000";
4110 PRINT  TAB(38);"0.00000"; TAB(47);"0.00000"; TAB(56);"0.00000"; TAB
(65);"0.00000"
4120 RETURN
4130 STOP
4140 PRINT  TAB(2);"0"; TAB(11);"2"; TAB(13);"00"; TAB(17);"2"; TAB(19);
"00"; TAB(23);"1";
4150 PRINT  TAB(25);"1.500"; TAB(31);"1.900"; TAB(37);"0.040"
4160 RETURN
4170 STOP
4180 PRINT  TAB(2);"2.00000"; TAB(11);"2.00000"; TAB(20);"2.00000";
4190 PRINT  TAB(29);"0.00000"; TAB(38);"0.00000"; TAB(47);"0.00000"
4200 RETURN
4210 STOP
4220 PRINT "1"; TAB(6);"0.0000000"; TAB(17);"1"; TAB(20);"0"; TAB(23);"0
"; TAB(30);"0.0000000";
4230 PRINT  TAB(41);"0"; TAB(44);"1"; TAB(47);"0"; TAB(54);"0.0000000";
4240 PRINT  TAB(65);"0"; TAB(68);"0"; TAB(71);"1"
4250 RETURN
4260 STOP
4270 PRINT  TAB(11);"0.00000"; TAB(20);"0.00000"; TAB(28);U[3*Y1-2];
4280 PRINT  TAB(37);U[3*Y1-1]; TAB(46);U[3*Y1]; TAB(61);"2."
4290 RETURN
4300 STOP
4310 PRINT  TAB(2);"0.50000"; TAB(11);"0.00000"; TAB(20);"0.00000"; TAB(
29);"0.00000";
4320 PRINT  TAB(38);"0.00000"; TAB(47);"0.00000"; TAB(61);"6."
4330 RETURN
4340 STOP
4350 PRINT  TAB(5);K1; TAB(12);"255502"; TAB(18);"-   55502"
4360 RETURN
4370 STOP
4380 PRINT  TAB(7);K1; TAB(12);"0.0000"; TAB(21);"0.0000"; TAB(30);"0.00
00";
4390 PRINT  TAB(39);"0.0000"; TAB(48);"0.0000"; TAB(57);"0.0000"; TAB(66
);"0.0000"
4400 RETURN
4410 STOP
4420 PRINT  TAB(11);"0.00000"; TAB(20);"0.00000"; TAB(29);"0.00000";
4430 PRINT  TAB(38);"0.00000"; TAB(47);"0.00000"; TAB(61);"2."
4440 PRINT  TAB(2);"0.50000"; TAB(11);"0.00000"; TAB(20);"0.00000"; TAB(
29);"0.00000";
4450 PRINT  TAB(38);"0.00000"; TAB(47);"0.00000"; TAB(61);"6."
4460 RETURN
4470 STOP
4480 PRINT  TAB(6);"0.0000000"; TAB(17);"1"; TAB(20);"0"; TAB(23);"0"; T
AB(30);"0.0000000";
4490 PRINT  TAB(41);"0"; TAB(44);"1"; TAB(47);"0"; TAB(54);"0.0000000";
TAB(65);"0";
4500 PRINT  TAB(68);"0"; TAB(71);"1"
```

```
4510 RETURN
4520 STOP
4530 PRINT  TAB(5);K1; TAB(12);"155502"; TAB(21);"155500"; TAB(30);"1655
00"; TAB(39);"155500";
4540 PRINT  TAB(48);"156500"; TAB(57);"0.0000"; TAB(71);"1"
4550 RETURN
4560 STOP
4570 INPUT "WHAT IS THE VIEW DIRECTION , (1) OR (2) ?",K7
4580 INPUT "FRONT(1), R-H SIDE(2), OR TOP VIEW(3) ?",V0
4590 INPUT "WHICH D.Z. OR SIA DO YOU LIKE TO LABEL, H(1) TO H(4)?",H[1];
H[2],H[3],H[4]
4600 ON K7 THEN GOTO 4640, 4610
4610 LET S1=0
4620 LET S2=0
4630 GOTO 4660
4640 LET S1=2/3
4650 LET S2=1/3
4660 LET V4=150
4670 LET V5=80
4680 IF Y6=1 THEN LET V6=2
4690 IF Y6=2 THEN LET V6=3
4700 ON V0 THEN GOTO 4810, 4710, 4760
4710 IF 975/(Y9+S1*X9)>780/(Z9+S2*X9) THEN GOTO 4740
4720 LET W6=950/(Y9+S1*X9)
4730 GOTO 4850
4740 LET W6=700/(Z9+S2*X9)
4750 GOTO 4850
4760 IF 975/(X9+S1*Z9)>780/(Y9+S2*Z9) THEN GOTO 4790
4770 LET W6=950/(X9+S1*Z9)
4780 GOTO 4850
4790 LET W6=700/(Y9+S2*Z9)
4800 GOTO 4850
4810 IF 975/(X9+S1*Y9)>780/(Z9+S2*Y9) THEN GOTO 4840
4820 LET W6=950/(X9+S1*Y9)
4830 GOTO 4850
4840 LET W6=700/(Z9+S2*Y9)
4850 LET W6=.8*W6
4860 PRINT "<27><12>"
4870 ON K7 THEN GOTO 4930, 4880
4880 CALL 20,45,0,1020,0
4890 CALL 20,1020,0,1020,780
4900 CALL 20,1020,780,45,780
4910 CALL 20,45,780,45,0
4920 GOTO 5090
4930 CALL 20,45,0,630,0
4940 CALL 20,630,0,630,585
4950 CALL 20,630,585,45,585
4960 CALL 20,45,585,45,0
4970 CALL 20,630,0,1020,195
4980 CALL 20,1020,195,1020,780
4990 CALL 20,1020,780,435,780
5000 CALL 20,1020,780,630,585
```

```
5010 CALL 20,435,780,45,585
5020 FOR Y1=0 TO 38 STEP 2
5030   CALL 20,45+390*Y1/39,195*Y1/39,45+390*(Y1+1)/39,195*(Y1+1)/39
5040 NEXT Y1
5050 FOR Y1=0 TO 44 STEP 2
5060   CALL 20,435+Y1*585/45,195,435+(Y1+1)*585/45,195
5070   CALL 20,435,195+Y1*585/45,435,195+(Y1+1)*585/45
5080 NEXT Y1
5090 FOR Y2=I6 TO I7
5100   ON V0 THEN GOTO 5170, 5110, 5140
5110   LET W1=W6*U[3*Y2-1]+V4+W6*S1*U[3*Y2-2]
5120   LET W2=W6*U[3*Y2]+V5+W6*S2*U[3*Y2-2]
5130   GOTO 5190
5140   LET W1=W6*U[3*Y2-2]+V4+W6*S1*U[3*Y2]
5150   LET W2=W6*U[3*Y2-1]+V5+W6*S2*U[3*Y2]
5160   GOTO 5190
5170   LET W1=W6*U[3*Y2-2]+V4+W6*S1*U[3*Y2-1]
5180   LET W2=W6*U[3*Y2]+V5+W6*S2*U[3*Y2-1]
5190   GOTO 5200
5200   CALL 20,W1,W2,W1,W2
5210   FOR Y3=1 TO 4
5220     IF Y2=H[Y3] THEN PRINT Y2
5230   NEXT Y3
5240 NEXT Y2
5250 FOR Y1=1 TO 40
5260   PRINT
5270 NEXT Y1
5280 RETURN
5290 STOP
5300 LET X0=U[3*I6-2]
5310 LET X9=U[3*I6-2]
5320 LET Y0=U[3*I6-1]
5330 LET Y9=U[3*I6-1]
5340 LET Z0=U[3*I6]
5350 LET Z9=U[3*I6]
5360 FOR Y2=I6 TO I7
5370   IF U[3*Y2-2]<X0 THEN LET X0=U[3*Y2-2]
5380   IF U[3*Y2-2]>X9 THEN LET X9=U[3*Y2-2]
5390   IF U[3*Y2-1]<Y0 THEN LET Y0=U[3*Y2-1]
5400   IF U[3*Y2-1]>Y9 THEN LET Y9=U[3*Y2-1]
5410   IF U[3*Y2]<Z0 THEN LET Z0=U[3*Y2]
5420   IF U[3*Y2]>Z9 THEN LET Z9=U[3*Y2]
5430 NEXT Y2
5440 RETURN
5450 STOP
5460 IF X0/2><INT(X0/2) THEN LET X0=X0-1
5470 IF Y0/2><INT(Y0/2) THEN LET Y0=Y0-1
5480 IF Z0/2><INT(Z0/2) THEN LET Z0=Z0-1
5490 FOR Y1=I6 TO I7
5500   LET U[3*Y1-2]=U[3*Y1-2]-X0
```

```
5510 LET U[3*Y1-1]=U[3*Y1-1]-Y0
5520 LET U[3*Y1]=U[3*Y1]-Z0
5530 NEXT Y1
5540 LET X9=X9-X0
5550 LET Y9=Y9-Y0
5560 LET Z9=Z9-Z0
5570 LET X0=0
5580 LET Y0=0
5590 LET Z0=0
5600 RETURN
5610 STOP
5620 ON Y1 THEN GOTO 5650, 5690, 5730, 5770, 5810, 5850, 5890, 5930, 597
0, 6010
5630 ON Y1-10 THEN GOTO 6050, 6090, 6130, 6170, 6210, 6250, 6290, 6330,
6370, 6410
5640 ON Y1-20 THEN GOTO 6450, 6490, 6530, 6570, 6610, 6650
5650 LET H=1
5660 LET K=0
5670 LET L=0
5680 GOTO 6680
5690 LET H=-1
5700 LET K=0
5710 LET L=0
5720 GOTO 6680
5730 LET H=0
5740 LET K=1
5750 LET L=0
5760 GOTO 6680
5770 LET H=0
5780 LET K=-1
5790 LET L=0
5800 GOTO 6680
5810 LET H=0
5820 LET K=0
5830 LET L=1
5840 GOTO 6680
5850 LET H=0
5860 LET K=0
5870 LET L=-1
5880 GOTO 6680
5890 LET H=1
5900 LET K=1
5910 LET L=0
5920 GOTO 6680
5930 LET H=-1
5940 LET K=-1
5950 LET L=0
5960 GOTO 6680
5970 LET H=-1
5980 LET K=1
5990 LET L=0
6000 GOTO 6680
```

```
6010 LET H=1
6020 LET K=-1
6030 LET L=0
6040 GOTO 6680
6050 LET H=0
6060 LET K=1
6070 LET L=1
6080 GOTO 6680
6090 LET H=0
6100 LET K=-1
6110 LET L=-1
6120 GOTO 6680
6130 LET H=0
6140 LET K=-1
6150 LET L=1
6160 GOTO 6680
6170 LET H=0
6180 LET K=1
6190 LET L=-1
6200 GOTO 6680
6210 LET H=1
6220 LET K=0
6230 LET L=1
6240 GOTO 6680
6250 LET H=-1
6260 LET K=0
6270 LET L=-1
6280 GOTO 6680
6290 LET H=-1
6300 LET K=0
6310 LET L=1
6320 GOTO 6680
6330 LET H=1
6340 LET K=0
6350 LET L=-1
6360 GOTO 6680
6370 LET H=1
6380 LET K=1
6390 LET L=1
6400 GOTO 6680
6410 LET H=-1
6420 LET K=-1
6430 LET L=-1
6440 GOTO 6680
6450 LET H=-1
6460 LET K=1
6470 LET L=1
6480 GOTO 6680
6490 LET H=1
6500 LET K=-1
```

```
6510 LET L=-1
6520 GOTO 6680
6530 LET H=1
6540 LET K=-1
6550 LET L=1
6560 GOTO 6680
6570 LET H=-1
6580 LET K=1
6590 LET L=-1
6600 GOTO 6680
6610 LET H=1
6620 LET K=1
6630 LET L=-1
6640 GOTO 6680
6650 LET H=-1
6660 LET K=-1
6670 LET L=1
6680 RETURN
6690 STOP
6700 LET S1=SQR(W1↑2+W2↑2+W3↑2)
6710 LET S2=SQR(H↑2+K↑2+L↑2)
6720 LET R=SQR(H1↑2+K1↑2+L1↑2)
6730 LET W4=(W1*H+W2*K+W3*L)/S1/S2
6740 IF V4=0 THEN LET W6=R/SQR(R↑2+(2*H[Y2]/D8)↑2)
6750 IF V4><0 THEN LET W6=(W1*H1+W2*K1+W3*L1)/S1/R
6760 LET W5=(H*H1+K*K1+L*L1)/S2/R
6770 IF W4=<0 THEN GOTO 6910
6780 IF W5=<0 THEN GOTO 6910
6790 LET Y5=SQR((1-W5)/(1+W5))
6800 LET W5=2*ATN(Y5)*180/3.14159
6810 LET Y5=SQR((1-W6)/(1+W6))
6820 LET W6=2*ATN(Y5)*180/3.14159
6830 IF W5-W6>5 THEN GOTO 6910
6840 LET Y5=SQR((1-W4)/(1+W4))
6850 LET W4=2*ATN(Y5)
6860 LET W4=W4*180/3.14159
6870 IF W4<X0 THEN LET H2=H
6880 IF W4<X0 THEN LET K2=K
6890 IF W4<X0 THEN LET L2=L
6900 IF W4<X0 THEN LET X0=W4
6910 RETURN
6920 STOP
6930 LET W5=(H2*H1+K1*K2+L1*L2)/SQR(H1↑2+K1↑2+L1↑2)/SQR(H2↑2+K2↑2+L2↑2)
6940 LET W4=X0
6950 IF H2=9 THEN LET S1=S1*D8/2
6960 IF H2><9 THEN LET S1=R*D8/2/W5
6970 LET S1=INT(S1+.5)
6980 RETURN
6990 STOP
7000 IF Y1=<I1 THEN PRINT "DZ(";Y1;")","(";H4;K4;L4;")",I2
```

```
7010 IF Y1>I1+I3 THEN GOTO 7030
7020 IF Y1=>I1+1 THEN PRINT "I(";Y1;")","(";H4;K4;L4;")",I2
7030 LET S9=SQR(H4↑2+K4↑2+L4↑2)
7040 LET A1=(H1*H4+K1*K4+L1*L4)/S1/S9
7050 LET B1=I4*Y0
7060 LET B2=(S0-S)*2/D8
7070 LET B1=B1+B2
7080 LET A9=SQR(B1↑2+B2↑2-2*B1*B2*A1)
7090 LET A9=(A9↑2+B1↑2-B2↑2)/2/A9/B1
7100 ON Y6 THEN GOTO 7110, 7200
7110 IF H4/2=INT(H4/2+.001) THEN GOTO 7150
7120 IF K4/2><INT(K4/2+.001) THEN IF L4/2><INT(L4/2+.001) THEN GOTO 7180
7130 LET E0=1/S9
7140 GOTO 7190
7150 IF K4/2=INT(K4/2+.001) THEN IF L4/2=INT(L4/2+.001) THEN GOTO 7180
7160 LET E0=1/S9
7170 GOTO 7190
7180 LET E0=2/S9
7190 GOTO 7240
7200 IF H4+K4+L4=2*INT((H4+K4+L4)/2+.001) THEN GOTO 7230
7210 LET E0=1/S9
7220 GOTO 7240
7230 LET E0=2/S9
7240 LET B7=S*2/D8
7250 LET E9=A1*A9-SQR(1-A1↑2)*SQR(1-A9↑2)
7260 IF I2=0 THEN LET B5=0
7270 IF I2><0 THEN LET B5=I2*E0/E9
7280 LET A7=B7*A1/S1
7290 LET A8=B7/S9
7300 LET H=A8*H4-A7*H1
7310 LET K=A8*K4-A7*K1
7320 LET L=A8*L4-A7*L1
7330 IF A1=1 THEN GOTO 7350
7340 IF ABS(H*H1+K*K1+L*L1)=>.01 THEN STOP
7350 LET B9=SQR(H↑2+K↑2+L↑2)
7360 IF A1=1 THEN LET A2=1
7370 IF A1><1 THEN LET A2=(H2*H+K2*K+L2*L)/S2/B9
7380 IF B9=0 THEN LET A4=1
7390 IF B9><0 THEN LET A4=(H*H3+K*K3+L*L3)/B9/S3
7400 IF A4=>0 THEN LET B2=SQR(1-A2↑2)
7410 IF A4<0 THEN LET B2=-SQR(1-A2↑2)
7420 LET B6=SQR(B5↑2+B7↑2-2*B5*B7*E9)
7430 LET A3=(B6↑2+B7↑2-B5↑2)/2/B7/B6
7440 LET A6=A1*A3-SQR(1-A1↑2)*SQR(1-A3↑2)
7450 LET B8=SQR(1-A6↑2)
7460 LET U[3*Y1-2]=B6*B8*A2
7470 LET U[3*Y1-1]=B6*B8*B2
7480 LET U[3*Y1]=B6*A6
7490 LET A9=INT(U[3*Y1-2]*D8/2+SQR(B7↑2-U[3*Y1-1]↑2-U[3*Y1]↑2)*D8/2+.5)
7500 IF Y1=<I1 THEN PRINT "THE DAMAGE DEPTH IS";A9;"A"
```

```
7510 LET Y2=Y1
7520 RETURN
7530 STOP
7540 LET A1=H2
7550 LET A2=K2
7560 LET A3=L2
7570 LET A4=H3
7580 LET A5=K3
7590 LET A6=L3
7600 LET A7=H1
7610 LET A8=K1
7620 LET A9=L1
7630 GOSUB 3580
7640 GOSUB 3930
7650 LET U[3*Y1-2]=INT(U[3*Y1-2]+.5)
7660 LET U[3*Y1-1]=INT(U[3*Y1-1]+.5)
7670 LET U[3*Y1]=INT(U[3*Y1]+.5)
7680 RETURN
7690 STOP
7700 LET H2=H
7710 LET K2=K
7720 LET L2=L
7730 LET S1=SQR(H2↑2+K2↑2+L2↑2)
7740 LET S2=SQR(U[3*Y2-2]↑2+U[3*Y2-1]↑2+U[3*Y2]↑2)
7750 LET S3=SQR(G[7]↑2+G[8]↑2+G[9]↑2)
7760 LET A2=U[3*Y2-2]*H2+U[3*Y2-1]*K2+U[3*Y2]*L2
7770 LET A2=A2/S2/S1
7780 LET A3=SQR(1-S2↑2*(1-A2↑2)/(S*2/D8)↑2)
7790 LET C[Y1]=S*A3+S2*D8*A2/2
7800 LET W1=U[3*Y2-2]-C[Y1]*H2/S1
7810 LET W2=U[3*Y2-1]-C[Y1]*K2/S1
7820 LET W3=U[3*Y2]-C[Y1]*L2/S1
7830 LET A1=G[1]
7840 LET A2=G[2]
7850 LET A3=G[3]
7860 LET A4=G[4]
7870 LET A5=G[5]
7880 LET A6=G[6]
7890 LET A7=G[7]
7900 LET A8=G[8]
7910 LET A9=G[9]
7920 GOSUB 3580
7930 GOSUB 3720
7940 GOSUB 4010
7950 IF V1=<0 THEN IF V3+S*2*COS(3.14159/3)/D8=>0 THEN GOTO 7980
7960 LET C[Y1]=99999
7970 GOTO 8150
7980 LET S4=SQR(W1↑2+W2↑2+W3↑2)
7990 IF V1=0 THEN IF V2=0 THEN LET A9=1
8000 IF V1><0 THEN LET A9=V1/SQR(V1↑2+V2↑2)
```

```
8010 IF V2><0 THEN LET A9=V1/SGR(V1↑2+V2↑2)
8020 LET A1=(W1*G[7]+W2*G[8]+W3*G[9])/S4/S3
8030 LET A2=(S0-S)/(I4*V9*D8/2+S0-S)
8040 IF A1<A2 THEN GOTO 8070
8050 LET O[Y1]=SGR(1-A1↑2)*A9
8060 GOTO 8150 -
8070 LET O[Y1]=SGR(1-A2↑2)*A9
8080 LET A3=SQR(1-A1↑2)*SGR(1-A2↑2)+A1*A2
8090 LET A4=S*SQR(2*(1-A3))
8100 LET A5=S*SQR(1-A3↑2)/A4
8110 LET A6=(-1)*(H2*G[7]+V2*G[8]+L2*G[9])/S3/S1
8120 LET A7=SGR(1-A6↑2)*SGR(1-A2↑2)+A2*A6
8130 LET A8=A4*A5/A7
8140 LET C[Y1]=C[Y1]+A8
8150 RETURN
```